Vilnius University

Semiconductor Physics Institute of
Center for Physical Sciences and Technology

Ramūnas Nedzinskas

MODULATED REFLECTANCE AND PHOTOLUMINESCENCE SPECTROSCOPY OF EPITAXIAL InGaAs QUANTUM DOT STRUCTURES

Doctoral dissertation

Physical Sciences, Physics (02 P), Semiconductor Physics (P 265)

Vilnius, 2012

Doctoral dissertation was prepared during 2007–2012 at Semiconductor Physics Institute of Center for Physical Sciences and Technology, Vilnius, Lithuania.

Scientific supervisor:
Prof Dr Habil Gintaras Valušis (Center for Physical Sciences and Technology, Semiconductor Physics Institute, Physical Sciences, Physics – 02 P, Semiconductor Physics – P 265)

Scientific adviser:
Dr Vytautas Karpus (Center for Physical Sciences and Technology, Semiconductor Physics Institute, Physical Sciences, Physics – 02 P, Semiconductor Physics – P 265)

Vilniaus universitetas

Fizinių ir technologijos mokslų centro
Puslaidininkių fizikos institutas

Ramūnas Nedzinskas

EPITAKSINIŲ InGaAs KVANTINIŲ TAŠKŲ DARINIŲ MODULIUOTO ATSPINDŽIO IR FOTOLIUMINESCENCIJOS SPEKTROSKOPIJA

Daktaro disertacija

Fiziniai mokslai, fizika (02 P), puslaidininkių fizika (P 265)

Vilnius, 2012

Disertacija rengta 2007–2012 metais Fizinių ir technologijos mokslų centro Puslaidininkių fizikos institute, Vilnius, Lietuva.

Mokslinis vadovas:
prof. habil. dr. Gintaras Valušis (Fizinių ir technologijos mokslų centro Puslaidininkių fizikos institutas, fiziniai mokslai,
fizika – 02 P, puslaidininkių fizika – P 265)

Konsultantas:
dr. Vytautas Karpus (Fizinių ir technologijos mokslų centro Puslaidininkių fizikos institutas, fiziniai mokslai,
fizika – 02 P, puslaidininkių fizika – P 265)

Acknowledgements

I would like to express my sincere gratitude to my scientific supervisor Prof Gintaras Valušis, who inspired and guided me thoughout my thesis with his patience and knowledge whilst allowing me to work in my own way. I could not have imagined having a better mentor for my PhD study.

A very special thanks goes out to my scientific advisers Dr Vytautas Karpus, Dr Julius Kavaliauskas, and Dr Bronislovas Čechavičius, who carefully taught me and raised me as a physicist, and made it possible to carry out experimental and theoretical work. I doubt that I will ever be able to convey my appreciation fully, but I owe them my eternal gratitude and pay their love forward.

Also I would like to thank in advance my Doctoral Dissertation Committee for their insightful comments and hard questions.

I am very grateful to my associates from laboratories of Semiconductor Optics and Terahertz Photonics, Prof Gintautas Jurgis Babonas, Algirdas Kindurys, Dr Alfonsas (Liudvikas) Rėza, Dr Dalius Seliuta, Dr Irmantas Kašalynas, Dr Artūras Suchodolskis, and Saulius Tumėnas, who created a warm working atmosphere.

I am indebted to my senior and student colleagues from Semiconductor Physics Institute for providing a rousing environment in which to learn and grow. Also I wish to thank the administration of Semiconductor Physics Institute for providing favourable working conditions.

Finally, I want to thank my family for their loving support and understanding through my entire life, especially to my mother. For her I dedicate this thesis.

Abbreviations

0-D	–	Zero-dimensional
CER	–	Contactless Electroreflectance
DOP	–	Degree of Polarization
DWELL	–	Dots-in-a-well
EMA	–	Effective Mass Approximation
ER	–	Electroreflectance
ES	–	Excited-state
FKO	–	Franz-Keldysh Oscillations
FM	–	Frank-van der Merwe
FWHM	–	Full-width at Half-maximum
GS	–	Ground-state
HH (hh)	–	Heavy-holes
Imp.	–	Impurity
LH (lh)	–	Light-holes
MBE	–	Molecular Beam Epitaxy
MD	–	Multiple-dot
PL	–	Photoluminescence
PR	–	Photoreflectance
PZR	–	Piezoreflectance
QCSE	–	Quantum-Confined Stark Effect
QD	–	Quantum Dot
QDIP	–	Quantum Dot Infrared Photodetector
QD-SL	–	Dots-in-a-superlattice
QR	–	Quantum Rod
QW	–	Quantum Well
RHEED	–	Reflection High-energy Electron Diffraction
RT	–	Room Temperature
SI-QD	–	Strain-induced Quantum Dot
SK	–	Stranski-Krastanow
SL	–	Superlattice
SOA	–	Semiconductor Optical Amplifier
TEM	–	Transmission Electron Microscopy
THz	–	Terahertz, 10^{12} Hz
VW	–	Volmer-Weber
WL	–	Wetting Layer

Table of Contents

Abstract

Epitaxial InGaAs quantum dot (QD) structures is the topic of this doctoral dissertation. The QD structures are studied using modulated reflectance and photoluminescence spectroscopy techniques. Such nanostructures are the key-ingredients in many novel photonic devices, operating in infrared and terahertz spectral range. Hence, a comprehensive knowledge of optical properties and electronic energy spectrum of these QD structures is essential in order to define their optimal design parameters and favorable growth conditions.

The doctoral thesis is organized as follows. Detailed motivation, main aims together with scientific novelty along with statements for defence and list of publications are given in the **Introduction**. Then, **Chapter 1** presents principles and examples of modulation spectroscopy, a very sensitive tool for optical characterization, followed by a brief introduction to molecular beam epitaxy and Stranski-Krastanow self-assembling growth mode for realization of QD nanostructures. Moreover, an extensive literature overview, regarding main achievements of QD-based nanostructures investigated, can be found here. In **Chapter 2**, details of QD samples studied and experimental set-up of spectroscopic techniques employed are given. **Chapters 3** and **4** covers original results of the dissertation. In particular, **Chapter 3** contains comprehensive investigation of electronic structure and optical properties of InAs/GaAs/AlAs dots-in-a-superlattice, InAs/InGaAs/GaAs/AlAs dots-in-a-well and epitaxial InGaAs quantum rod (QR) structures. Moreover, an intriguing optical anisotropy properties of InGaAs QRs are revealed therein. **Chapter 4** is devoted to original analytical approach, based upon separation of variables approximation, for energy spectrum calculations of cylindrical self-assembling QDs and QRs. Finally, **Chapter 5** underlines the main results and presents conclusions of the work.

Santrauka

Puslaidininkinių kvantinių taškų (*quantum dot,* QD) dariniai yra patraukliūs objektai tiek optoelektronikai, tiek ir fotonikai, o šių darinių energijos lygmenų spektras yra pamatas jų funkcionalumui analizuoti. Įdomu tai, kad keičiant QD matmenis ir/ar įterpiant juos į kvantinę duobę ar supergardelę galima suprojektuoti norimų spektrinių savybių aktyvius optinius komponentus. Praktiniams taikymams būtina žinoti, gerai suprasti tokių nanodarinių elektroninę sandarą lemiančius veiksnius — auginimo sąlygų įtaką, vidinių elektrinių laukų, defektų bei legiruojančių priemaišų poveikį.

Šioje disertacijoje pristatomi InAs QD sistemų — taškų supergardelėje ir sudėtinėje kvantinėje duobėje — bei InGaAs kvantinių strypelių spektroskopiniai ir teoriniai tyrimai. Disertacijoje parodoma, kad QD darinių energijos spektrui tirti galima sėkmingai taikyti moduliuoto atspindžio — fotoatspindžio (*photoreflectance*, PR) ir bekontakčio elektrinio atspindžio (*contactless electroreflectance*, CER) — spektroskopiją. Savo ruožtu, teoriškai modeliuojant energijos lygmenis galima išsamiai apibendrinti ir prognozuoti kvantinių taškų ir strypelių fotoatsaką aktualių taikymų reikmėms.

Disertacijos **Įvade** pagrindžiamas darbo aktualumas, o tolesniuose skyreliuose suformuluojami darbo tikslas ir uždaviniai, aptariamas disertacijos naujumas bei praktinė vertė, pristatomi ginamieji teiginiai ir pateikiamas mokslinių publikacijų disertacijos tema ir tikslinių pranešimų tarptautinėse bei nacionalinėse konferencijose sąrašas. **I-ajame skyriuje** pateikiama darbe tirtų QD struktūrų eksperimentinės metodologijos (bendroji apžvalga), jų epitaksinio auginimo ir aktualios literatūros apžvalga, **II-ajame skyriuje** aprašomi tiriamieji QD bandiniai, pateikiamos nanodarinių schemos, juostinės diagramos bei auginimo protokolai. Šiame skyriuje taip pat išsamiau supažindinama su naudota eksperimentine metodika — moduliuoto atspindžio (PR ir CER) bei fotoliuminescencijos (PL) spektroskopijos stendais. **III-iasis ir IV-asis skyriai** sudaro originaliąją disertacijos dalį. **III-iajame skyriuje** pristatomi kombinuotų InGaAs QD darinių — InAs kvantinių taškų, įterptų į GaAs/AlAs supergardelę (SL) [QD-SL], o taip pat į sudėtinę InGaAs/GaAs/AlAs kvantinę duobę (*dots-in-a-well*, DWELL), bei InGaAs kvantinių strypelių, įterptų į InGaAs duobę — optinių savybių ir elektroninės sandaros tyrimai. **IV-ajame skyriuje** aprašomas sukurtas analitinis cilindrinio QD energijos spektro skaičiavimų modelis, paremtas kintamųjų atskyrimo artiniu. Disertacijos pabaigoje pateikiami pagrindiniai rezultatai ir išvados (**V-asis skyrius**) bei cituojamos literatūros sąrašas.

Introduction and Motivation

Semiconductor quantum (or nano-) structures — two-dimensional (2-D) quantum wells, 1-D wires, 0-D dots, rods, rings — are the essential ingredients in modern optoelectronic and photonic devices. Indeed, by means of shape engineering and/or by varying the design of such a "bare" nanoelement, e.g., including it into a quantum well (QW) or superlattice (SL), one can obtain artificial optical components with desired spectral properties and carrier transport features. Self-assembling quantum dots (QDs) attract a particular attention, due to their large potential for applications in novel optoelectronic devices and quantum information processing. Furthermore, electronic structure of such QD-based systems depends both on size/shape of the dot, as well as on material parameters of the surrounding media. Thus, variation of the QD shape and size, along with parameters of barriers may qualitatively change QD electronic structure and, in turn, significantly alter the optical properties of QDs. Therefore, for applications one needs to get a comprehensive knowledge of optical properties and electronic layout of these nanostructures, including the effect of internal electric fields and/or doping impurities, etc.

In this thesis, self-assembling InGaAs QDs, embedded within GaAs-based quantum wells and superlattices, are studied experimentally using spectroscopic techniques and theoretically by numerical and analytical methods. In this work, the choice of QD structures for optical investigation is motivated by possible new QD applications in optoelectronic devices. Due to a well-developed molecular beam epitaxy (MBE) growth method, composite QD systems (e.g., QDs within quantum wells or superlattices) provide a great advantage over other types of nanostructures, such as quantum wells and wires, providing additional options to engineer material properties [1, 2]. On the other hand, developement of novel semiconductor QD devices is closely related to optical non-destructive characterization, which gives an invaluable feedback to designers and growers about the quality and fine material composition of the nanostructure. In particular, modulation spectroscopy techniques, such as photoreflectance (PR) and contactless

electroreflectance (CER), offer a possibility to investigate the full-extent of optical transitions with a perfect sensitivity even at room temperature.

Non-trivial strain relaxation mechanisms usually result in formation of flat (low aspect ratio), lens-shaped and inhomogeneous dots, scattered as two or more families in size, represented by a broad (Gaussian) lines in experimental spectra. An approach to reduce the inhomogeneity of self-assembled InAs dot structures is the fabrication of multilayer island stacks, in particular by growing dots-in-a-superlattice (QD-SL) structures. Moreover, InAs/GaAs quantum dot infrared photodetector (QDIP) has a huge advantage over quantum well infrared photodetector (QWIP), allowing normal incidence detection [3–6]. In order to define operation range, the desired resonant wavelength was achieved by covering self-assembling InAs/GaAs QDs with a strain-reducing $In_xGa_{1-x}As$ layer. Such an advanced dots-in-a-well (DWELL) design, based on transition between a QD state and a QW state offers additional tuning possibilities: Partly by varying the QD energy levels and, partly, by adjusting the width and composition of the QW. Moreover, such a design of QDIP offers, for instance, a bias-tunable spectrally adaptive response.

The typical lens-shape of Stranski-Krastanow (SK) QDs permits use of only transverse-electric (TE) polarized light, restricting their applicability in semiconductor optical amplifiers (SOAs). These limitations are governed by the asymmetric potential profile and compressive strain, which induce characteristic splitting of heavy- (HH) and light-hole (LH) states. Thereby, to modify the polarization-dependent optical gain function, QD shape and composition engineering has been proposed [7]. In particular, high aspect ratio columnar QDs, also referred to as quantum rods (QRs), were realized by depositing a short period InAs/GaAs superlattice (SL) on top of a seed SK QD layer by MBE. It is worth mentioning that QR morphology can be affected greatly by the growth parameters, including growth temperature, growth interrupts, the number of SL periods, and the type of As source used.

Transmission electron microscopy (TEM) structural analysis of elongated QR nanostructures brings a clear evidence of in-plane shape anisotropy of QRs. While the previous studies of polarization response of QDs provide only one value of degree of polarization (DOP), corresponding to a chosen direction for the TE mode, multidirectional measurements and calculations of the DOP revealed a unique property of InAs QRs that the TE response is anisotropic in the plane of the stacks. Therefore, a single value of the

DOP is not sufficient to fully characterize the polarization response.

In a context of aforementioned developments, there remains an everlasting demand to optimize the growth parameters and implement new designs of these unique quantum structures. Therefore, an in-depth knowledge of their optical and electronic properties is required. This was extensively addressed in our recent studies, where modulated reflectance spectroscopy, in particular, PR and CER techniques, alongside photoluminescence (PL) has been successfully employed to characterize low-dimensional systems and nanostructures, including two types of InAs QD- (QD-SL and DWELL) and various morphology epitaxial InGaAs QR-structures.

The doctoral dissertation is organized as follows. **Chapter 1** presents principles and examples of modulation spectroscopy. It also contains a brief introduction to molecular beam epitaxy and Stranski-Krastanow self-assembling growth mode. Moreover, **Chapter 1** includes an extensive literature overview, regarding the main acievements of QD-based nanostructures. In **Chapter 2**, details of QD samples studied and experimental set-up of spectroscopic techniques employed are given. **Chapters 3 and 4** cover original results of the dissertation. In particular, **Chapter 3** contains comprehensive investigation of electronic structure and optical properties of InAs/GaAs/AlAs dots-in-a-superlattice, InAs/InGaAs/GaAs/AlAs dots-in-a-well and InGaAs quantum rod structures. Moreover, an intriguing optical anisotropy properties of InGaAs quantum rods are revealed therein. **Chapter 4** described in details original analytical approach, based upon separation of variables approximation, for energy spectrum calculations of cylindrical self-assembling quantum dots and rods. Finally, **Chapter 5** underlines the main results and presents conclusions of the work.

Major Goal

In order to define the optimal physical parameters, essential for the fabrication technology of novel micro- and opto-electronic devices based on composite InGaAs quantum dot structures (dots-in-a-superlattice, dots-in-a-well; quantum dot shape engineering — quantum rods), one needs to know in detail optical properties and electronic layout of these nanostructures. Thereby, it is projected:

♢ to study the full-extent of interband optical transitions in differently designed InGaAs quantum dot structures by employing modulated reflectance and photoluminescence spectroscopy techniques;

♢ to determine the influence of dot's morphology and the impact of the surrounding matrix parameters on optical properties and electronic states in InGaAs quantum dots.

Quantum Structures Studied

The work is concerned specifically with composite InGaAs quantum dots (QD), embedded into quantum well (QW) or superlattice (SL), and different in morphology columnar InGaAs quantum dots, also referred to as quantum rods (QR), structures:

a) InAs QDs, embedded in GaAs QW or GaAs/AlAs SL (QD-SL);

b) InAs QDs with and without InGaAs layer, embedded into GaAs/AlAs QW (DWELL);

c) As_2- or As_4-grown InGaAs QRs, immersed in a 2-D InGaAs layer.

Tasks of the Work

To reach the main goal of the work, the following tasks were set:

i) to upgrade modulated reflectance (photoreflectance, contactless electroreflectance) and photoluminescence spectroscopy measurement set-up with relevant optical equipment/facilities (laser sources, detectors, monochromator gratings, etc.) in order to investigate the semiconductor device-like nanostructures;

ii) to study the interband transitions and determine of electronic structure of the InAs QD-SL and InAs DWELL structures;

iii) to investigate optical properties, polarization anisotropy and energy structure of different in morphology InGaAs QRs, grown using As_2 or As_4 sources;

iv) to carry out a numerical simulations and develop an analytical model, in order to analyze electronic states and optical transitions in spectroscopically investigated QD structures.

Scientific Novelty

In this work, modulation spectroscopy is applied to study a variety of InGaAs quantum dot structures. Spectroscopic study of composite InAs quantum dot structures (QD-SL and DWELL) for the first time revealed:

a) a decrease of InAs wetting layer thickness and the subsequent increase of QD size accross the stacks (growth direction);

b) the impact of surrounding material — GaAs/AlAs SL and InGaAs strain-reducing layer — on electronic energy states and interband transitions of InAs QDs.

Optical investigation of epitaxial InGaAs quantum rod structures for the first time disclosed:

a) the effect of the As source (As_2 or As_4) on optical properties and electronic structure of InGaAs QRs;

b) a strong (up to 60%) in-(001)-plane polarization anisotropy of the ground-state optical transitions within InGaAs QRs.

Statements for Defence

I. Blue-shifts and enhancement in intensity of InAs wetting layer-related optical transitions, observed in InAs/GaAs/AlAs dots-in-a-superlattice structure, are due to off-center position of the dot layers in the wells, while the spectral splitting is associated with a variation of the wetting layer thickness along the growth direction.

II. Red-shift of the InAs quantum dot ground-state interband transitions in InAs/InGaAs/GaAs/AlAs dots-in-a-well structures is caused by partial strain relaxation and increase in effective dot size.

III. InGaAs quantum rods grown using As_4 source exhibit a stronger photoluminescence intensity, a longer emission wavelength, and a larger energy spacing between the ground- and excited-states, as compared to As_2-grown nanorods, due to enhanced carrier confinement. These features are attributed to an increase of indium composition contrast between InGaAs quantum rods and the surrounding InGaAs well.

IV. Transverse magnetic mode dominates from the $(1\bar{1}0)$-surface, while transverse electric mode is larger from the (110)-surface owing to a high in-(001)-plane polarization degree ($\approx 60\%$) of ground-state optical transitions in InGaAs quantum rod structures. These features are ascribed to hole wavefunction orientation along $[1\bar{1}0]$ direction together with light- and heavy-hole subband intermixing.

V. Analytical approach for electron energy spectrum calculations of cylindrical quantum dots is proposed. The method is based on the separation of variables approximation and provides reliable results both for ground- and excited-states of various InGaAs quantum dot structures.

List of Publications and Conference Reports

The dissertation is based on the following scientific publications and conference reports, given in the chronological order.

List of publications

[1.§] R. Nedzinskas, B. Čechavičius, J. Kavaliauskas, V. Karpus, G. Krivaitė, V. Tamošiūnas, G. Valušis, F. F. Schrey, K. Unterrainer, and G. Strasser, *Energy Spectrum of InAs Quantum Dots in GaAs/AlAs Superlattices*. Acta Phys. Pol. A **113**, 975 (2008).

[2.§] R. Nedzinskas, B. Čechavičius, J. Kavaliauskas, A. Čerškus, J. Kundrotas, V. Karpus, V. Tamošiūnas, G. Valušis, G. Fasching, K. Unterrainer, and G. Strasser, *Optical study of InAs quantum dot stacks embedded in GaAs/AlAs superlattices*. Phys. Status Solidi C **6** (12), 2710 (2009).

[3.§] R. Nedzinskas, B. Čechavičius, J. Kavaliauskas, V. Karpus, D. Seliuta, V. Tamošiūnas, G. Valušis, G. Fasching, K. Unterrainer, and G. Strasser, *Modulated reflectance study of InAs quantum dot stacks embedded in GaAs/AlAs superlattice*, J. Appl. Phys. **106**, 064308 (2009).

[4.§] R. Nedzinskas, B. Čechavičius, J. Kavaliauskas, V. Karpus, D. Seliuta, V. Tamošiūnas, G. Valušis, F. F. Schrey, K. Unterrainer, and G. Strasser, *Electronic Structure of InAs Quantum Dots in GaAs/AlAs Superlattice*. AIP Conf. Proc. **1199** (1), 283 (2010).

[5.§] R. Nedzinskas, V. Karpus, B. Čechavičius, J. Kavaliauskas, G. Valušis, L. H. Li, S. P. Khanna, and E. H. Linfield, *Photoreflectance of Epitaxial InGaAs Quantum Rods*. Acta Phys. Pol. A **119** 164 (2011).

[6.§] R. Nedzinskas, B. Čechavičius, V. Karpus, J. Kavaliauskas, G. Valušis, L. H. Li, S. P. Khanna, and E. H. Linfield, *Photoreflectance and photoluminescence studies of epitaxial InGaAs quantum rods grown with As_2 and As_4 sources*. J. Appl. Phys. **109**, 123526 (2011).

[7.§] R. Nedzinskas, B. Čechavičius, A. Česnauskas, J. Kavaliauskas, V. Karpus, G. Valušis, L. H. Li, S. P. Khanna, and E. H. Linfield, *Electronic structure and optical anisotropy of InGaAs quantum rods studied by photoreflectance and photoluminescence*. Phys. Status Solidi C **9** (7), 1640 (2012).

International conferences

[1.i] R. Nedzinskas, B. Čechavičius, J. Kavaliauskas, V. Karpus, G. Krivaitė, V. Tamošiūnas, G. Valušis, F. F. Schrey, K. Unterrainer, and G. Strasser, *Energy Spectrum of InAs Quantum Dots in GaAs/AlAs Superlattices.* // 13th International Symposium on Ultrafast Phenomena in Semiconductors (UFPS-2007). August 26–29, 2007. Vilnius, Lithuania.

[2.i] R. Nedzinskas, B. Čechavičius, J. Kavaliauskas, V. Karpus, D. Seliuta, V. Tamošiūnas, G. Valušis, F. F. Schrey, K. Unterrainer, and G. Strasser, *Electronic Structure of InAs Quantum Dots in GaAs/AlAs Superlattice.* // 29th International Conference on the Physics of Semiconductors (ICPS-2008). July 27 – August 1, 2008. Rio de Janeiro, Brazil.

[3.i] R. Nedzinskas, B. Čechavičius, J. Kavaliauskas, A. Čerškus, J. Kundrotas, V. Karpus, V. Tamošiūnas, G. Valušis, G. Fasching, K. Unterrainer, and G. Strasser, *Optical study of InAs quantum dot stacks embedded in GaAs/AlAs superlattices.* // 15th Semiconductor and Insulating Materials Conference (SIMC-2009). June 15–19, 2009. Vilnius, Lithuania.

[4.i] R. Nedzinskas, V. Karpus, B. Čechavičius, J. Kavaliauskas, G. Valušis, L. H. Li, S. P. Khanna, and E. H. Linfield, *Photoreflectance of epitaxial InGaAs quantum rods.* // 14th International Symposium on Ultrafast Phenomena in Semiconductors (UFPS-2010). August 23–25, 2010. Vilnius, Lithuania.

[5.i] R. Nedzinskas, B. Čechavičius, A. Česnauskas, J. Kavaliauskas, V. Karpus, G. Valušis, L. H. Li, S. P. Khanna, and E. H. Linfield, *Electronic structure and optical anisotropy of InGaAs quantum rods.* // 16th Semiconducting and Insulating Materials Conference (SIMC-2011). June 19–23, 2011. Stockholm, Sweden.

[6.i] R. Nedzinskas, B. Čechavičius, J. Kavaliauskas, G. Valušis, L. H. Li, and E. H. Linfield, *Modulation spectroscopy of epitaxial InGaAs nanorods.* // COST (European Cooperation in Science and Technology) Training School on "Epitaxy and Structural Analysis of III-V-N Semiconductor Nanostructures", April 29 – May 2, 2012. Heraklion-Crete, Greece.

[7.i] R. Nedzinskas, B. Čechavičius, J. Kavaliauskas, V. Karpus, G. Valušis, L. H. Li, S. P. Khanna, and E. H. Linfield, *Polarized photoreflectance and photoluminescence spectroscopy of InGaAs/GaAs quantum rods grown*

with As_2 and As_4 sources. // 17th International Conference on Superlattices, Nanostructures, and Nanodevices (ICSNN-2012). July 22–27, 2012. Dresden, Germany.

[8.i] R. Nedzinskas, B. Čechavičius, J. Kavaliauskas, V. Karpus, G. Valušis, L. H. Li, S. P. Khanna, and E. H. Linfield, *Photoreflectance and photoluminescence study of InAs dots-in-a-well nanostructures.* // 31st International Conference on the Physics of Semiconductors (ICPS-2012). July 29 – August 3, 2012. Zurich, Switzerland.

[9.i] R. Nedzinskas, B. Čechavičius, J. Kavaliauskas, V. Karpus, G. Valušis, L. H. Li, S. P. Khanna, and E. H. Linfield, *Comparative optical study of epitaxial InGaAs quantum rods grown with As_2 and As_4 sources* // 31st International Conference on the Physics of Semiconductors (ICPS-2012). July 29 – August 3, 2012. Zurich, Switzerland.

National conferences

[1.n] R. Nedzinskas, B. Čechavičius, J. Kavaliauskas, V. Karpus, G. Valušis, L. H. Li, S. P. Khanna, and E. H. Linfield, *Photoreflectance study of electronic energy levels in InAs quantum dot structures.* // 39th Lithuanian National Physics Conference. Vilnius University, Vilnius, October 6–8, 2011.

[2.n] R. Nedzinskas, R. Paulauskas, B. Čechavičius, and V. Karpus. *Interband optical transitions in a composite quantum well.* // 39th Lithuanian National Physics Conference. Vilnius University, Vilnius, October 6–8, 2011.

[3.n] R. Nedzinskas, V. Karpus. *Adiabatic model for energy spectra calculations of cylindrical quantum dots and rods.* // 39th Lithuanian National Physics Conference. Vilnius University, Vilnius, October 6–8, 2011.

Student and PhD student conferences

[1.s] R. Nedzinskas, V. Karpus, *Adiabatic model for energy spectrum calculations of self-assembling quantum dots.* // 12th Conference for Lithuanian Young Researchers "Science — the Future of Lithuania". Physics and Computational Physics. Vilnius Gediminas Technical University, Vilnius, April 2, 2009.

[2.s] R. Nedzinskas, B. Čechavičius, and G. Valušis, *Optical Properties of InGaAs Nanorods.* // 13th Conference for Lithuanian Young Researchers "Science — the Future of Lithuania". Physics and Computational Physics. Vilnius Gediminas Technical University, Vilnius, April 23, 2010.

[3.s] R. Paulauskas, R. Nedzinskas, and B. Čechavičius, *Selection Rules for Optical Transitions in Composite Quantum Wells.* // 13th Conference for Lithuanian Young Researchers "Science — the Future of Lithuania". Physics and Computational Physics. Vilnius Gediminas Technical University, Vilnius, April 23, 2010.

[4.s] A. Česnauskas, R. Nedzinskas, *Modulated photoreflectance spectra of InGaAs quantum rods.* // Student Scientific Works. Lithuanian Research Council, Vilnius, May 14–15, 2010.

[5.s] R. Paulauskas, B. Čechavičius, and R. Nedzinskas, *Optical features of composite quantum wells.* // Student Scientific Works. Lithuanian Research Council, Vilnius, May 14–15, 2010.

[6.s] R. Nedzinskas, B. Čechavičius, *Photoreflectance spectroscopy of InGaAs quantum rods.* // 1st Conference for PhD students and Young Researchers (FizTeCh-2010). Center for Physical Sciences and Technology, Vilnius, November 18–19, 2010.

[7.s] R. Nedzinskas, B. Čechavičius, and J. Kavaliauskas, *Energy spectrum and optical anisotropy of InGaAs nanorods.* // 2nd Conference for PhD students and Young Researchers (FizTeCh-2011). Center for Physical Sciences and Technology, Vilnius, November 24–25, 2011.

Other publications and conference reports

[‡.§] B. Čechavičius, R. Nedzinskas, J. Kavaliauskas, V. Karpus, G. Valušis, B. Sherliker, M. Halsall, P. Harrison, E. Linfield, and M. Steer, *Study of Excitonic Transitions in δ-doped GaAs/AlAs Quantum Wells.* Lith. J. Phys. **49** (3), 291 (2009).

[‡.n] B. Čechavičius, R. Nedzinskas, J. Kavaliauskas, V. Karpus, G. Valušis, B. Sherliker, M. Halsall, P. Harrison, E. Linfield, and M. Steer, *Study of Excitonic Transitions in δ-doped GaAs/AlAs Quantum Wells.* // 38th Lithuanian National Physics Conference. Vilnius University, Vilnius, June 8–10, 2009.

1 Semiconductor Quantum Dot Structures — an Overview

In this Chapter, firstly, the introductory fundamentals from the common 3-D down to 0-D electron confinement is given. The following Section is devoted to modulation spectroscopy, which is a powerful tool in characterization of the quantum nanostructures. Afterwards, a realization of nanostructures by molecular beam epitaxy under self-assembling regime is explained in detail. The Chapter ends with a literature overview of QD-based structures for modern optoelectronics. The relevant milestones (significant papers) in the literature was selected so that the Reader find her-/himself confident to progress with the original part of the dissertation.

1.1 Modulation Spectroscopy of Semiconductor Nanostructures

Modulation spectroscopy, since its inception in 1964, is a powerful method for the study and characterization of a large number of semiconductor configurations, including bulk/thin film, micro- and nanostructures (heterojunctions, quantum wells, superlattices, quantum dots, etc.) in addition to semiconductor processing. Modulation spectroscopy deals with the measurement and interpretation of changes in the optical response of a sample which are caused by modifying in some way the measurement conditions. This can easily be accomplished by periodically modulating (i) some parameter applied to the sample ("external" modulation) or (ii) the measurement conditions themselves ("internal" modulation). Thereby, the influence of external perturbations such as temperature, electric fields, hydrostatic pressure, uniaxial stress, etc. can be investigated.

This optical technique utilizes a very general principle of experimental physics, in which a periodically applied perturbation leads to sharp, derivative-like spectral features in the optical response of the system. The

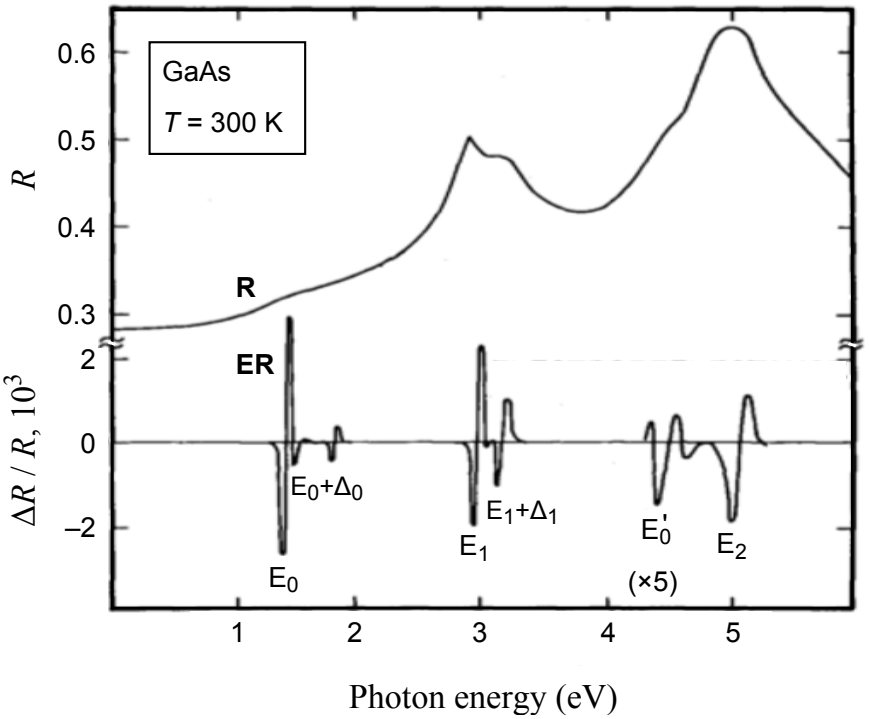

Figure 1.1 Comparison of room temperature reflectivity (R) and electric field-modulated reflectivity (ER) spectra of bulk GaAs. [Reproduced from [8]]

derivative nature of modulation spectroscopy emphasizes structure localized in the photon energy region of interband (intersubband) transitions of semiconductors (semiconductor micro- and nanostructures) and suppresses uninteresting background effects. Also, weak features that may not have been detected in the absolute spectra are often enhanced. Because of this derivative-like nature a large number of sharp spectral features can be observed, even at room temperature.

Therefore, owing to the richness of the derivative-like spectra, the information in the lineshape fits, room temperature performance and relative simplicity of operation, modulation spectroscopy is an indispensable tool to study novel materials and structures down to a nanoscale for advanced micro- and opto-electronics. Hereinafter, this Section reviews main principles and examples of modulation spectroscopy.

1.1.1 Basic concepts of modulation spectroscopy

The power of modulation spectroscopy is illustrated by Fig. 1.1. Here, a comparison of the reflectivity (R) and electric-field modulated, or electroreflectance (ER) spectra of bulk GaAs at 300 K are shown. While the reflectivity is characterized by broad features, the ER trace has zero as a base and is dominated by a series of very sharp, derivative-like features,

corresponding to specific optical transitions.

Moreover, the great advantage of modulation spectroscopy is the ability to perform a lineshape fit. Since, for the modulated signal, the features are localized in photon energy it is possible to account for the lineshapes to yield accurate values (within a few meV) of energies and broadening parameters of interband transitions even at room temperature. Hence, the effects of static external perturbations (electric and magnetic fields, temperature, hydrostatic pressure, uniaxial stress, composition, etc.) can be conveniently studied.

Besides the possibility to directly measure sharp, derivative-like peaks, as shown in Fig. 1.1, there is also important information in other modulation variables, such as phase, modulation frequency, modulation amplitude, etc. Certain types of modulation spectroscopy can be depth-selective and thus act as probes of specific spatial regions of the sample being studied, as will be illustrated for dots-in-a-superlattice structures in the original part of the dissertation.

1.1.2 Modulation spectroscopy techniques

Electroreflectance and contactless electroreflectance

Periodic variation in the dielectric function of the structure investigated can be carried out by alternating electric field applied, realized by electroreflectance (ER) technique. There are different ways how to apply this electric field. The modulating electric field can be produced by depositing a thin metalic gate on the semiconductor sample, thereby forming a Shottky contact. In such a way, the voltage is applied between the gate and the Ohmic contact on the bottom of the sample. Another approach to attain the field is to use an interface semiconductor or electrolyte instead of Shottky contact. A specific type of ER, contactless electroreflectance (CER), utilizes a condenser-like system, where the sample is mounted between a transparent (usually indium-tin-oxyde, ITO) and metalic contacts. Thereby, a high modulating voltage can be applied on the sample. Moreover, one is encouraged to use a p-i-n system by placing the sample in the insulating region. The advantage of such configuration is that the same electric field can be applied, as compared to position-dependant field when Shottky contact is used.

Photoreflectance

Photoreflectance (PR), instead of using modulating electric field as in ER, employs coherent light source (laser) and optical chopper. Therefore, with PR a special preparation of the sample (doping, deposition of Shottky contact, etc.) is not needed. PR utilizes a Fermi level, which is pinned to the surface of the sample. The pinning, thus, produces a built-in electric field, which can be easily modulated by photoexcitation of the carriers. The measurements of PR are performed by exciting the sample with a laser of higher energy than the bandgap or interband transition energies being investigated. One should note, however, that a good filter at the laser frequency is required, since the laser beam is modulated at the same chopper frequency as the recovered signal. Moreover, laser light produces bandgap photoluminescence, which may significantly affect the detected signal. This unwanted luminescence can be avoided e.g., by using two-monochromator system along with long focal length optics.

Wavelength-modulated reflectance

In wavelength-modulated reflectance (WMR) spectroscopy, the modulating parameter is the wavelength of a probe light beam. A small variations of wavelength, $\Delta\lambda$, typically can be accompolished by using a vibrating plate mounted within a monochromator before the exit slit. As a result, the recovered signal is the reflectance spectra differentiated by the probe beam wavelength, $\Delta R/\Delta\lambda$.

Piezoreflectance

Piezoreflectance (PZR) spectroscopy employs the physical property of semiconductor — the change in optical transition energy under an applied uniaxial or biaxial stress. For example, in the experimental setup providing uniaxial sress, sample is mounted on a piezoelectric transducer, which in turn produces a uniform strain in the sample plane.

Thermoreflectance

Thermoreflectance (TR) method relies on the temperature modulation of the sample, and usually similar results as that from PZR can be obtained. Dielectric function changes are thus indued by temperature modulation, which on the other hand evokes the change in the bandgap energy and

broadening parameter of the associated spectral feature. Temperature modulation can be realized simply by wraping a heater wire around the sample, however care must be taken so that not to overheat it. Moreover, as one can expect, the temperature modulation frequency is limited to certain value (depends on a sample material) owing to the finite heat dissipation speed. Therefore, only comparatively low-frequency TR mesurements can be performed.

1.1.3 Line shape analysis

The relationship between the reflectance modulation and the corresponding modulation of real and imaginary parts of the dielectric function, $\varepsilon(\omega) = \varepsilon_r + \mathrm{i}\varepsilon_i$, can be linearized by introducing the so-called Seraphin coefficients β_r and β_i ,

$$\frac{\Delta R}{R} = \beta_r \Delta\varepsilon_r + \beta_i \Delta\varepsilon_i \,, \tag{1.1}$$

with

$$\beta_r = \frac{\partial \ln R}{\partial \varepsilon_r}, \qquad \beta_i = \frac{\partial \ln R}{\partial \varepsilon_i}. \tag{1.2}$$

Since the normal-incidence reflection coefficient, or reflectance, R of a semi-infinite isotropic medium in vacuum is given as a function of complex refractive index $\tilde{n}$ by

$$R = \left| \frac{\tilde{n} - 1}{\tilde{n} + 1} \right|^2 , \tag{1.3}$$

the coefficients β_r and β_i can be obtained by differentiation of Eq. (1.3) employing the relation between complex dielectric function and refractive index, $\varepsilon(\omega) = \tilde{n}^2$.

1.2 Molecular Beam Epitaxy

All of the nanostructures studied were grown on a semi-insulating GaAs (001) wafers by molecular beam epitaxy (MBE), in which epitaxial growth occurs via a vapor phase. One of the main advantages of MBE-growth is that layer thickness can be controlled down to the monolayer (owing to very slow deposition rate, typically $< 1\,\mu$m per hour), which is of great importance for growing and developing novel heterostructures, e.g., where the electrons are fully confined in space or forced to stream down a potential staircase and emit photons at each step/cascade, as is the case in quantum dots (QDs) and quantum cascade lasers (QCLs), respectively. One can

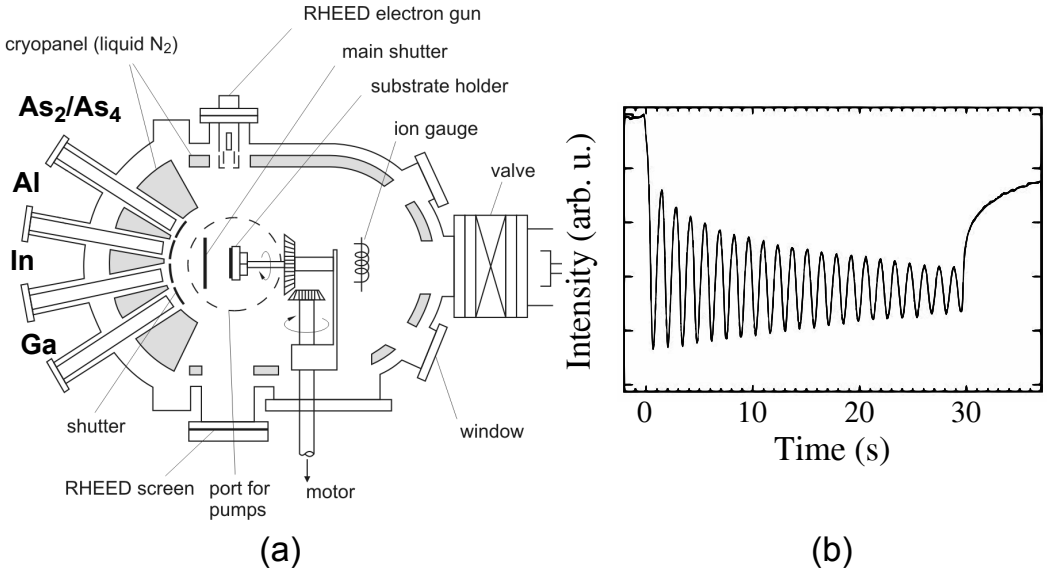

Figure 1.2 The main components and rough layout and concept of the main chamber in a MBE system (a) and typical RHEED oscillations for GaAs growth on GaAs (001) indicating the layer-by-layer growth.

achieve high purity of grown sample and minimal surface roughness by means of MBE. Indeed, nearly perfect mono-crystal with hardly any defects can be grown by this technique.

Molecular beam epitaxy requires ultra-high vacuum chambers (10^{-8} Pa). Scheme of a typical MBE system is given in Fig. 1.2(a). In solid-source MBE, pure elements such as Ga and As are heated in separate effusion cells until they begin to slowly sublimate. Effusion cells are the sources of needed material. They are filled e.g., with In, Ga, As, Al, and Si (for n-doping). For the growth of arsenides, the group III elements are always supplied as monomers, while group V elements can be supplied as tetramers (As_4) or as dimers (As_2) by dissociating the tetrameric molecule in a two-zones furnace (arsenic cracker). It is possible to control the flux of material within 1% of accuracy. A computer controls shutters in front of each furnace, allowing precise control of the thickness of each layer, down to a single layer of atoms. The gaseous elements are evaporated from the effusion cells and then condense on the wafer, where they may react with each other. In the example of Ga and As, single-crystal GaAs is formed. Both constituent elements of GaAs have almost the same lattice constant (see Fig. 1.3), therefore no stress is introduced. If only As is evaporated, it will not stick to the wafer properly. Ga is required to build a stable crystal. Since effusion cells are mounted eccentrically, there will be a thickness gradient from one end of the wafer to the other. To solve this, the wafer is rotated with a constant speed during the growth process. Evaporated atoms do

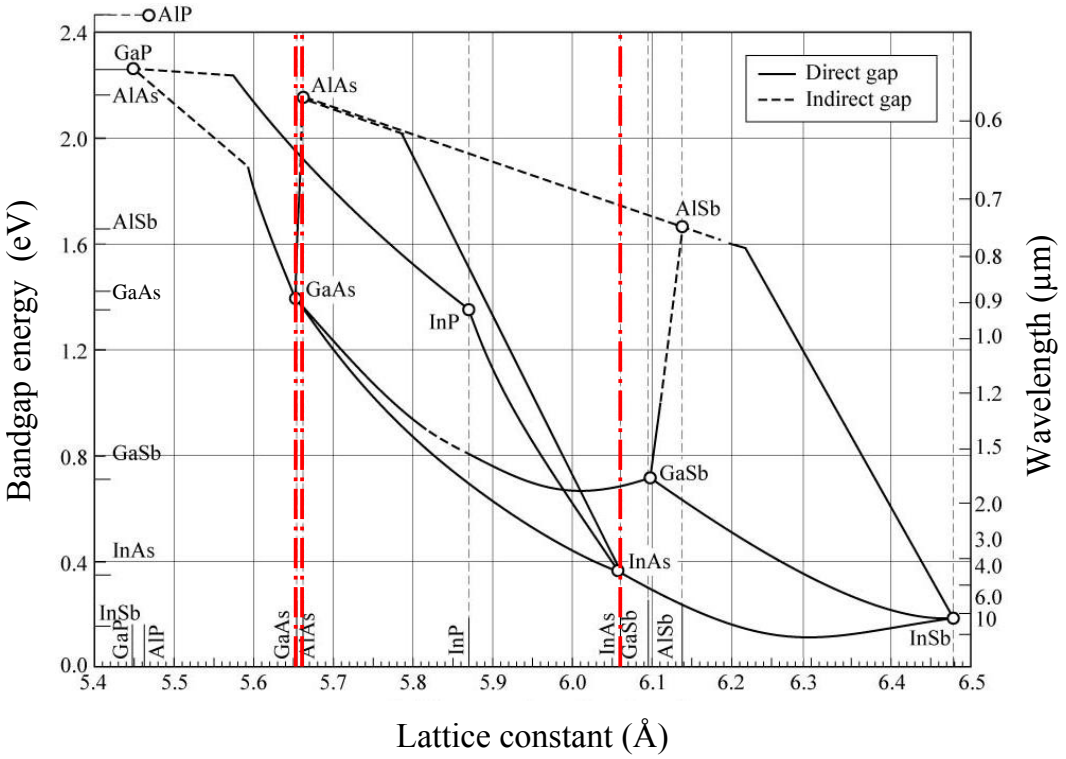

Figure 1.3 Bandgap energy and lattice constant of various III-V semiconductor compounds at room temperature. Materials of consideration — GaAs, AlAs and InAs — are denoted by vertical dash-dot lines.

not interact with each other or vacuum chamber gases until they reach the wafer, due to the long mean free paths of the atoms.

In systems where the substrate needs to be cooled, the ultra-high vacuum environment within the growth chamber is maintained by a system of cryopumps, and cryopanels, chilled using liquid nitrogen or cold nitrogen gas to a temperature close to 77 K. Cryogenic temperatures act as a sink for impurities in the vacuum, so vacuum levels need to be several orders of magnitude better to deposit films under these conditions. On the other hand, the wafers, on which the crystals are grown may be mounted on a rotating platter, which can be heated to several hundred degrees Celsius during operation.

For live-monitoring the growth of the crystal layers, reflection high energy electron diffraction (RHEED) is often used, gathering information from the surface layer of the grown sample. The electron gun generates a beam of electrons, which strike the sample at a very small angle relative to the sample surface. Incident electrons diffract from atoms at the surface of the sample, and a small fraction of the diffracted electrons interfere constructively at specific angles forming regular patterns on the detector. The electrons interfere according to the position of atoms on the sample surface,

so the diffraction pattern at the detector is a function of the sample surface. Each peak in RHEED intensity oscillations with time (see Fig. 1.2(b)) represents the formation of a new monolayer. Since the degree of order is at a maximum once a new monolayer has been formed, the spots in the diffraction pattern have maximum intensity owing to the maximum number of diffraction centers of the new layer contributing to the diffracted beam. The overall intensity of the oscillations is dropping with the more layers being grown.

Since MBE of self-assembled QDs relies on the formation of coherently strained epitaxial islands, after depositing a thin (or epi-) layer of one semiconductor material of larger lattice constant on a substrate, having smaller constant. Therefore, the choice of materials for forming the self-assembled dot arrays is limited to those, which have a relatively small (1–8%) lattice mismatch with the substrate or cladding layer materials (see Fig. 1.3). Too large mismatch could produce a dislocated epitaxial layer prior to the formation of coherently strained islands. Thus, for growing QDs one can use dot-cladding (or dot-substrate) material pairs: InAs/GaAs, InGaAs/GaAs, InGaAs/AlGaAs, AlInAs/AlGaAs, InGaAs/AlGaAs and InP/InGaP. On the other hand, if the deposited layer on a substrate is too thick, above its critical thickness (which is usually above 10 nm), no 3-D islands synthesize and this layer relaxes into unstrained one forming dislocations, which drastically reduce optical properties.

In the following subsection the self-assembling nature of QDs is explained in terms of Stranski-Krastanow growth regime, which is the case for A_3B_5 dots.

1.2.1 Stranski-Krastanow mode

Stranski–Krastanow (SK) growth is one of the primary modes by which thin films grow epitaxially at a crystal surface or interface. The SK mode (also known as "layer+island" growth) follows a two step process: initially, complete films of adsorbates, up to several monolayers thick, grow in a layer-by-layer fashion on a crystal substrate. Beyond a critical layer thickness, which depends on strain and the chemical potential of the deposited film, growth continues through the nucleation and coalescence of adsorbate "islands". Therefore, Stranski–Krastanow growth is an intermediary process characterized by both 2-D layer and 3-D island growth. The essential steps in epitaxial growth of InAs QD on GaAs under Stranski-Krastanow mode is depicted in Figs. 1.4(a)–(c). Note, that wetting layer (WL) is always

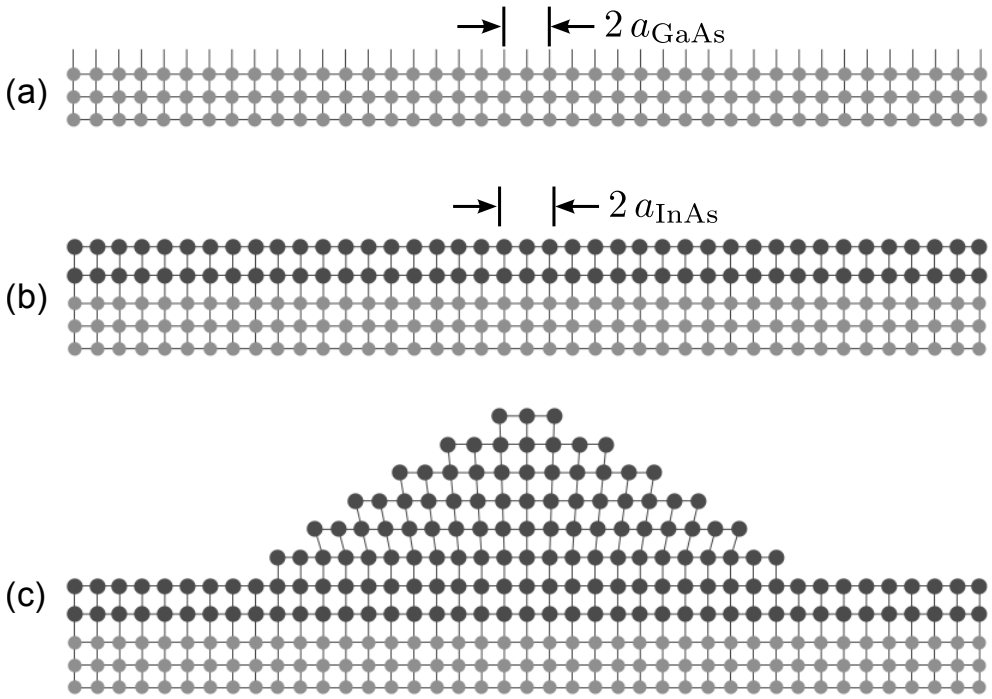

Figure 1.4 Epitaxial growth of InAs quantum dot on GaAs substrate under Stranski-Krastanow mode: GaAs (001) substrate (a) is covered by a strained InAs wetting layer, which mimics the lattice constant of GaAs (b). After reaching a critical thickness, the strained InAs layer undergoes relaxation minimizing its surface energy by spontaneous formation of randomly-distributed 3-D nanoislands (c). On the top of QD lattice parameter is fully that of InAs.

present, no matter how densely or loosely dots assemble. Transition from the layer-by-layer to island-based growth occurs at a critical layer thickness which is highly dependent on the chemical and physical properties, such as surface energies and lattice parameters, of the substrate and film.

This growth mechanism was first noted by I. Stranski and L. Krastanow in 1938 [9]. It wasn't until 1958, however, in a seminal work by E. Bauer published in Zeitschrift für Kristallographie, that the SK, Volmer-Weber (VW), and Frank-van der Merwe (FM) mechanisms were systematically classified as the primary thin-film growth processes [10]. Since then, SK growth has been the subject of intense investigation, not only to better understand the complex thermodynamics and kinetics at the core of thin-film formation, but also as a route to fabricate novel nanostructures for application in the micro- and later in the opto-electronics industry.

Stranski–Krastanow growth initially follows a FM mechanism, when surface adhesive force is stronger than adatom cohesive force (chemical potential derivative with respect to coverage n is positive, $\mathrm{d}\mu(n)/\mathrm{d}n > 0$) and non-trivial amounts of strain energy accumulate in the deposited layers. At a critical thickness, this strain induces a sign reversal in the chemical

potential (adatom cohesive force is stronger than surface adhesive force, $\mathrm{d}\mu(n)/\mathrm{d}n < 0$), leading to a switch in the growth mode. At this point it is energetically favorable to nucleate islands and further growth occurs by a VW type mechanism.

Heteroepitaxy is a process in which a film of a certain material is deposited on substrate of a different material. The typical examples of film substrate combinations include Ge/Si, InAs/GaAs and InP/GaAs. The lattice mismatch between the film and substrate can lead to the growth of a strained film. The film often grows in a layer-by-layer fashion until a certain critical thickness, beyond which 3-D islands form through what is known as the Stranski-Krastanow transition. In a strained film, the formation of islands is energetically favorable, as it reduces the strain energy in the crystal. The thickness of the wetting layer at which island nucleation initiates, called the critical thickness h_{c}, is strongly dependent on the lattice mismatch between the film and substrate, with a greater mismatch leading to smaller critical thicknesses. Values of h_{c} can range from sub-monlayer coverage to up to several monolayers thick [11].

The principle associated with the growth of self-assembled QDs is based on the formation of coherently strained islands and requires controlling the 2-D to 3-D growth transition that is induced by a misfit strain built into the epitaxial structure [12,13]. The strain induced origin of the 2-D to 3-D transition is illustrated in Fig. 1.5(a) for the InGaAs/GaAs system. As expected, the larger misfit strain, expressed as $2(a_{\mathrm{InAs}} - a_{\mathrm{GaAs}})/(a_{\mathrm{InAs}} + a_{\mathrm{GaAs}})$, leads to a thinner layer prior to the formation of the 3-D islands. Figure 1.5(b) shows self-assembled QD density *versus* the estimated total InAs coverage. For this plot an extensive data in the coverage range of 1.6 ML was obtained, corresponding to a QD density of $1 \times 10^9\,\mathrm{cm}^{-2}$. Below this coverage the low probability of measuring a single QD caused less precise determination of the density. The QD density is essentially zero until a certain critical coverage, at which the value increases sharply. The data are fit with a function of the form $\rho_{\mathrm{QD}} = \rho_0(\Theta - \Theta_{\mathrm{c}})^{\alpha}$. In this case ρ_{QD} is the QD density, and Θ is the estimated InAs coverage in monolayers (MLs). This functional behavior is that of a first-order phase transition, with QD density representing an order parameter. The critical InAs coverage $\Theta_{\mathbf{c}} = 1.5\,\mathrm{ML}$, the exponent $\alpha = 1.76$, and the normalization density $\rho_0 = 2 \times 10^{11}\,\mathrm{cm}^{-2}$ were obtained from a least-squares fit shown by the solid line. The exponential increase in the dot density also suggests the use of very slow growth rates for a better control of the size uniformity and QD density.

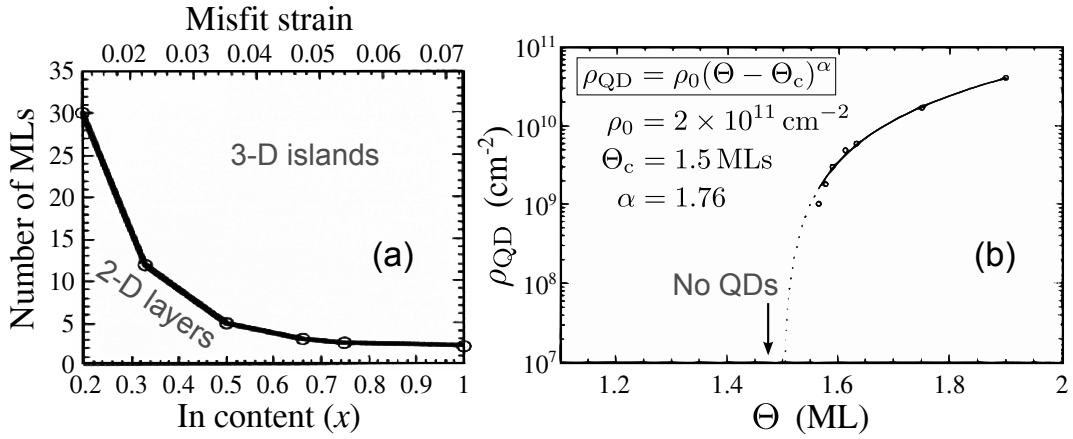

Figure 1.5 Formation of self assembled $In_xGa_{1-x}As/GaAs$ QDs. The number of InGaAs monolayers (MLs) required for the transition from 2-D layers to 3-D islands (dots) as a function of composition or strain (a). The evolution of InAs island density as a function of InAs coverage (b). Treating (b) data as a first-order phase transition gives a critical thickness of 1.50 MLs. [Adapted from Ref. [12].]

In case of InAs/GaAs QDs, temperature-driven diffusion and migration of indium on the surface due to stress induce a slowing in the growth rate of larger islands. This can be regarded as a self-organization of the InAs quantum dots, leading to a very good uniformity of the coherent island size distribution, as shown in the scanning electron micrography (SEM) image in Fig. 1.6. As a rule, self-assemled QDs have a flat circular and lens-like (lenticular) geometry (although pyramidal shape has been proposed and widely investigated by theoretical calculations too), as can be seen from another SEM image of uncapped QD structure in Figs. 1.7(a) and (b). The narrow distribution of dot sizes can be also deduced for the buried (embedded) QDs from optical spectroscopy, e.g., photoluminescence (PL) spectra. Figure 1.7(c) shows a very narrow (small full-width at half-maximum, FWHM) PL peak, proving high uniformity of QD size. Indeed, size (height/width, or aspect ratio), shape (geometry), material composition (e.g., In content within InGaAs) are the key parameters to analyze the experimental spectra and/or carry out simulations. However, one can not count solely on structural analysis of the uncapped structures. It is long-known that size, shape, composition and surface density of self-assembled QDs change significantly during the overgrowth (capping) process and thereby shape anisotropy should be considered usually. One can use TEM for capped structures, however it is a disruptive (killing the sample) tool. Therefore, various optical methods are widely implemented providing a sensitive, non-destructive analysis. Particularly, modulation spectroscopy, by which one can directly measure the derivative of the energy spectrum.

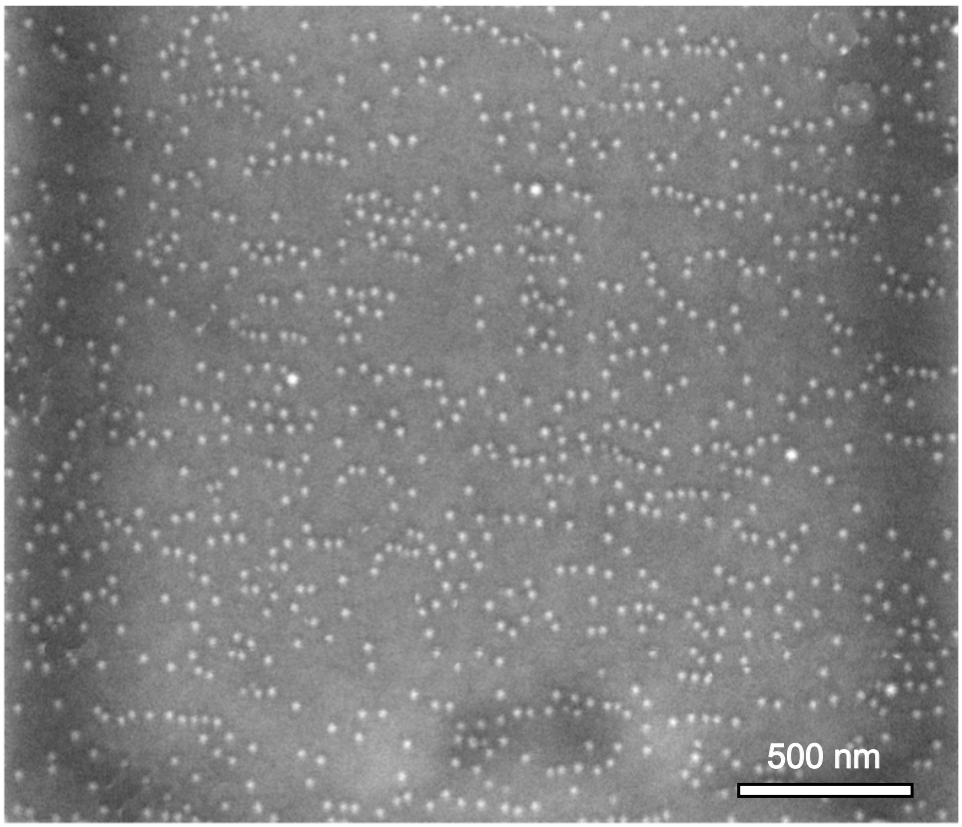

Figure 1.6 Micrograph of self-assembled InAs QDs, formed on GaAs by MBE under SK growth conditions, showing uniform island size distribution. Dots of 20 nm width, 7–9 nm height clearly predominate, yielding $2 \times 10^{10}\,\mathrm{cm}^{-2}$ areal density.

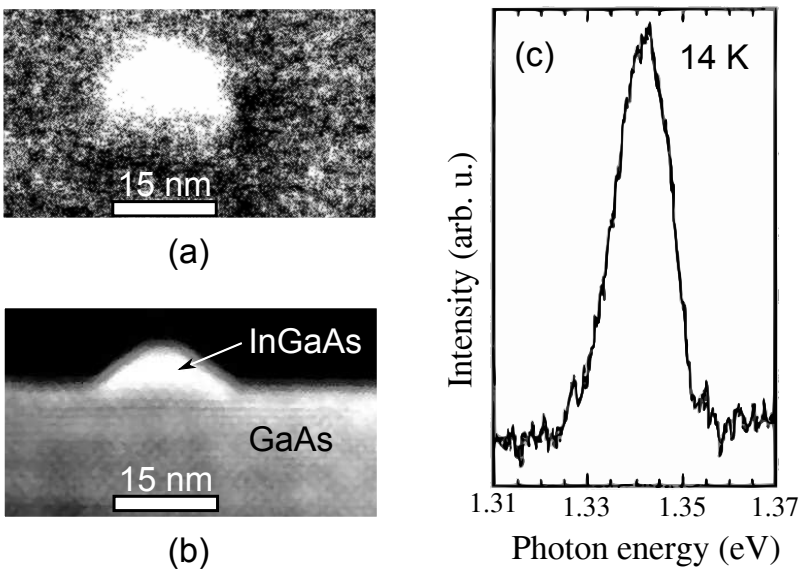

Figure 1.7 High resolution SEM images of the self-assembled lens-like InGaAs/GaAs QD in plane-view (a) and cross section (b). High uniformity of QD size was confirmed by narrow PL peak (c). [Adapted from Ref. [14].]

1.3 Literature Overview — Quantum Dot Structures for Novel Optoelectronics

One should note in advance that the nanostructures studied within this dissertation include:

- ◇ InAs quantum dots (QDs), embedded in GaAs and GaAs/AlAs superlattices (SLs);
- ◇ InAs quantum dots with and without InGaAs cap layers, embedded within GaAs/AlAs QWs;
- ◇ InGaAs quantum rods (QRs), embedded within InGaAs QW, and sandwiched between GaAs barrier layers.

Therefore, prior to moving into original part — the spectroscopic results and their theoretical analysis of the InGaAs QD and QR nanostructures studied — achievements and the coexisting (expanding) problematics of the semiconductor QDs, which are the top candidates for modern micro- and optoelectronics, are briefly introduced hereinafter. Literature overview covers the investigations of similar (or even the same) nanostructures and aims to highlight the difference in methodology approaching the features, which are observed and properly discussed in the original part of dissertation. Finally, new ideas (pathways) towards developement and characterization of the QD structures are suggested and realized revealing the full-extent of electronic structure and various optical properties of QD and QR structures, studied in the following Chapter.

Semiconductor nanotechnology based upon material (band gap) engineering and state-of-the-art growth technology (e.g., molecular beam epitaxy, metal-organic chemical vapour deposition, etc.) allows to develop materials by design with a great potential to adjust/tune their optical and electronic properties. The functionality of semiconductor nanostructures in a wide spectral region from ultraviolet (UV) to far-infrared, or terahertz (THz) is directly related to their energy level spectrum. In particular, there is a great demand for light sources (such as lasers, optical amplifiers) in the telecom spectral ranges of 1.26–1.36 μm and 1.5–1.6 μm (see Fig. 1.8). (Infrared light with wavelengths of 850 nm, 1.310 nm and 1.550 nm is mostly used for laser applications.) In case of detectors for infrared applications, the operation in the atmosperic spectral windows of MWIR (3–5 μm) and LWIR (8–12 μm) is needed (see Fig. 1.9). Thus, knowledge of electronic

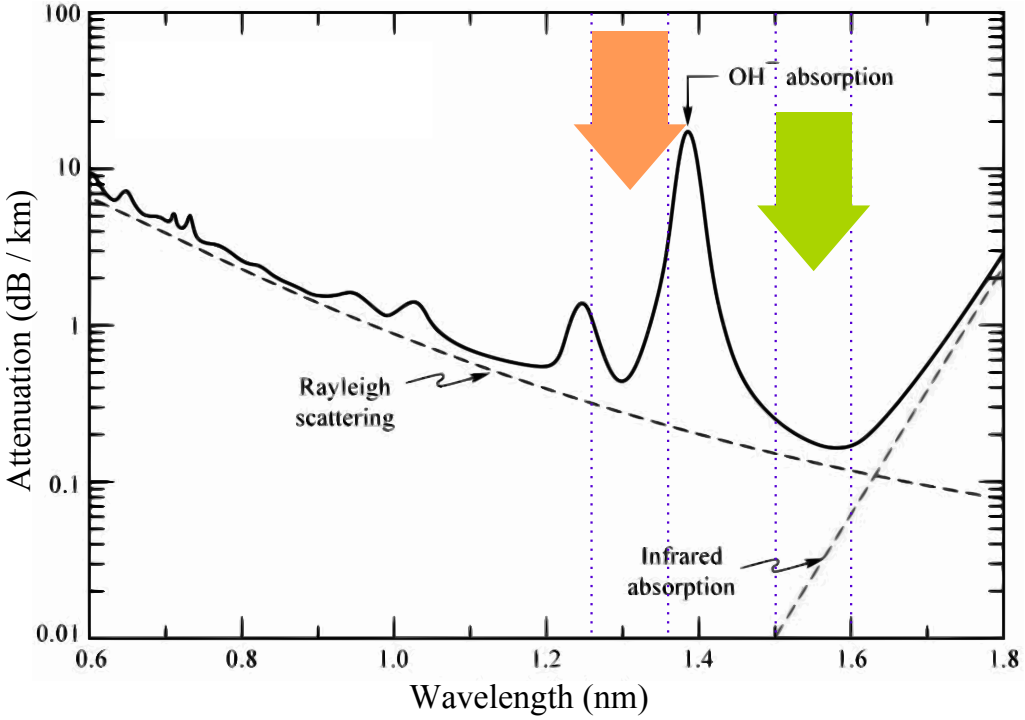

Figure 1.8 Infrared light attenuation in SiO_2 fiber. Measured (solid line) and theoretical (dashed lines) limits given by Rayleigh scattering in the short-wavelength (near-IR) region, and by infrared absorption (due to molecular vibrations) in the long-wavelength (middle-IR) region.

structure and optical properties is crucial, in order to analyze and design new/advanced semiconductor quantum heterostructures for middle-IR and even far-IR (or THz) photonics and optoelectronics.

In the meantime the permanent interest in 2-dimensional (2-D) semiconductor quantum well heterostructures already yield a generation of new devices, exploiting these "quaint" quantum mechanical properties, attention is now turning towards low-dimensional solid state systems, providing higher degree of carrier confinement. The impetus at the moment is to understand the electronic and optical properties of 1-D quantum wires, 0-D quantum dots and even nanosystems, representing an exiting interjacent confinement, such as "quasi" 0-D quantum rods and quantum rings. The knowledge of low-dimensional electron behaviour would naturally reveal the potential of such semiconductor nanostructures to be incorporated into next generation electronic and photonic devices. Moreover, separate "pure" quantum systems can be combined, e.g. quantum ring on a quantum rod, expanding the degree of freedom and hiding numerous striking effects to be discovered someday...

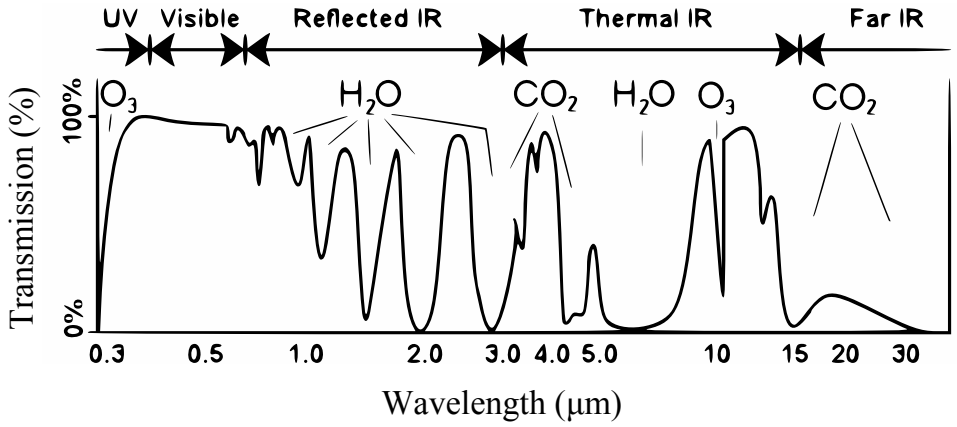

Figure 1.9 Ambient air transmission spectra showing infrared atmospheric windows for IR detection between 3–5 μm and 8–12 μm.

1.3.1 Vertically coupled InAs quantum dots

Very elegant alternative to engineer modern functional elements at nanoscale is to use self-assembling (or Stranski-Krastanov, SK) quantum dots. Semiconductor heterostructures, embedding SK quantum dots have been studied extensively, owing to their intriguing atomic-like quantum confinement, which lead to a broad range of possible applications (see e.g. [1]). In particular, self-assembled InAs QDs, whose intersublevel transition energies lie in mid- and far-infrared spectral range (3–25 μm), have attracted particular interest as active elements of infrared photodetectors [15–23]. One should note that in case of quantum well (QW) based photodetectors (quantum well infrared photodetector, QWIP), which were well-elaborated previously, selection rules of optical transitions allowed only the facet-incidence (lateral) detection making QWIPs a complex and unpractical system. Here with QD infrared detectors (QDIPs), a normal-incidence detection due to a three-dimensional carrier confinement is permitted [24], which considerably simplifies the layout of potential photodetectors and sensor applications. In addition, QD structures are expected to provide higher photocurrents and lower dark currents than quantum well structures due to the longer lifetime of the excited states. Moreover, the desired wavelength operation of QDIPs can be tuned/obtained by changing dots parameters along with their surrounding matrix, offering a great freedom for heterostructure designers. In particular, QD electronic structure can be adjusted by varying the dots size, shape [25], along with/or their environment, like by incorporating an AlAs layer close to the QDs [26]. These features make QDs as a very potential option in creation of photoelectronic devices with a desired spectral range.

Non-trivial strain relaxation mechanisms usually result in formation of

flat (low aspect ratio), lens-shaped and inhomogeneous dots, scattered as two or more families in size, represented by a broad (Gaussian) lines in experimental spectra. An approach to reduce the inhomogeneity of self-assembled InAs dot structures is the fabrication of multilayer island stacks. In this geometry strain fields of underlying islands penetrate into the spacer layer, create a strain energy modulation at the surface, and induce stacks of vertically aligned and laterally more homogeneous islands in upper layers. The growth conditions of self-assembled InAs islands can be chosen in such a way that both the island-related and the wetting layer (WL) related energy transitions are equally well-resolved in PL experiments.

The structural and therefore electronic and optical properties of self-assembled QD multilayer structures, obtained by alternating deposition of few monolayers (ML) InAs on GaAs surfaces, are strongly influenced by strain fields during growth. Indeed, for sufficiently thin spacer layers, the strain fields of underlying islands create a strain energy modulation at the spacer surface (tensile above the islands and compressive in neighboring regions). Atoms forming the next island layer migrate to regions of lower lattice mismatch (tensile strained region), and as a result stacks of vertically aligned QDs are obtained. One should note that the dot size is larger and the strain-induced material intermixing is more pronounced for the upper dots.

Wetting layer thickness variation accross the QD stacks

It is evident that strain modulation should also be reflected in WL-related properties. For the Ge/Si system, TEM microscopy proved a reduction of the WL thickness in the upper layers, while PL yielded a blueshift for the optical transitions. Indeed, such effect was first revealed in Ge/Si dots, because self-assembling III/V islands are much harder to evaluate due to extremely small sizes. Recently, it was found experimentally for a simple two-fold InAs/GaAs QD structure in Ref. [27], that the strain field modulation induced by an initial InAs island layer causes a reduction of the WL thickness Δ_{WL} in all but the initial layer and induces an energy separation ΔE of the WL related energy transition. In the next few paragraps Winzer *et al.* [27] paper is reviewed, since the WL-related effects of InAs dots-in-a-superlattice systems are discussed properly in the original part of the dissertation.

Recently, Winzer *et al.* [27] elaborated optical transitions of the WLs in two-fold self-assembled InAs/GaAs quantum dot samples, having different

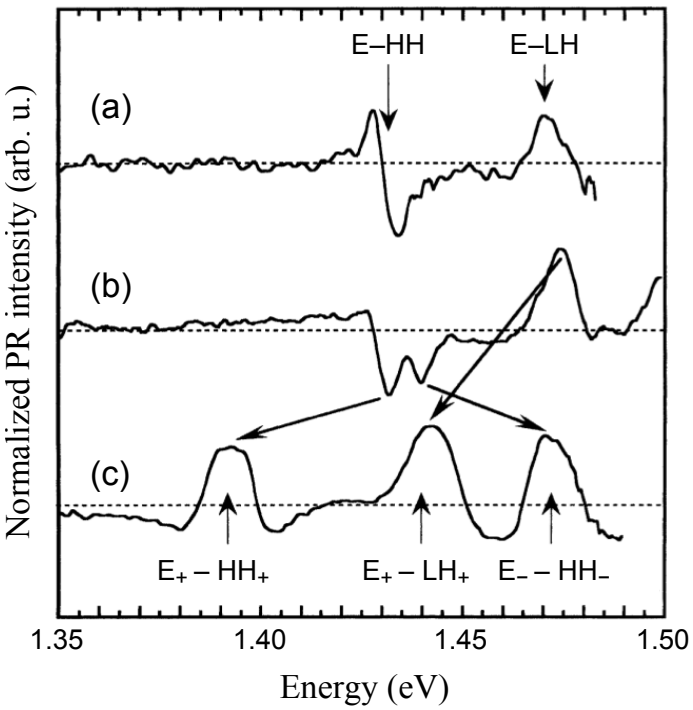

Figure 1.10 Liquid nitrogen (80 K) temperature PR spectra of WL-related interband transitions in a two-fold InAs QD structures with single layer of dots (a) and two layers of dots having $d_S = 20$ nm (b) and $d_S = 3$ nm (b) spacers. Two heavy- and light-hole excitons `E-HH` and `E-LH` of the reference structure (a) develop into three below about 15 nm of GaAs spacer thickness. Coupled WLs show transitions between symmetric-like (+) and antisymmetric-like (−) states. [Adapted from Ref. [27].]

GaAs spacer thickness d_S. Here, PR and selective PL excitation (PLE) spectroscopy in combination with layer removal by anodic oxidation, which allows an unambiguous assignment of WL transitions for two-fold stacked InAs QDs as a function of GaAs spacer thickness, revealed two energetically separated heavy-hole transitions already for thick barriers, for which coupling effects can be excluded, as is illustrated in Fig. 1.10. This splitting indicates the formation of two wetting layers during growth with a 10% difference in width and refects strain field interaction between the island layers. Thin spacer layer samples show in addition the expected WL coupling as confirmed by subband calculations.

The formation of an InAs WL in a GaAs matrix produces a confining potential on the length scale of about 1 ML, which introduces electron (`E`), heavy-hole (`HH`), and light-hole (`LH`) bound states in the GaAs bandgap giving rise to the formation of `E-HH` and `E-LH` excitons. It is obvious that if both WL widths for two-fold stacked samples are different one should observe two energetically separated transitions of each type. However, below 15 nm thickness of GaAs barriers, the WLs couple with each other, and electron and hole states become symmetric-like (+) or antisymmetric-like

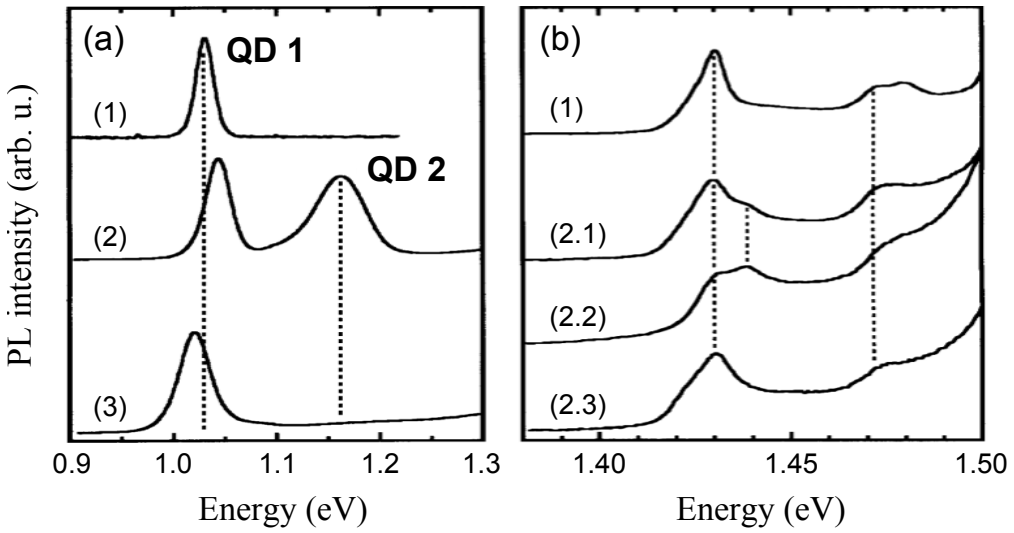

Figure 1.11 Liquid nitrogen (80 K) temperature PL (a) and PLE (b) spectra for the reference QD sample (1) and two-fold (2, 3) QD structure before (2) and after (3) top QD layer removal. In PLE-excited two-fold InAs QD sample with $d_S = 20$ nm-thick GaAs spacer (b) QD1 (curves 1, 2.1 and 3) or QD2 (curve 2.2) emission was monitored. [Adapted from Ref. [27].]

(−). It is worth noting that the size of level splitting is determined by spacer thickness rather than by the WL widths. However, it was suggested that the second E-HH transition in Fig. 1.10(b) and (c) arises from the upper WL characterised by a smaller width. As expected for coupling of WLs the energy separation between the three transitions is enlarged, and the E_+-HH_+ contribution is strongly red-shifted with decreasing d_S.

The luminescence studies provide further insight into the basic properties. Curves (1) and (2) in Fig. 1.11(a) show the PL spectra of the reference and the as-grown $d_S = 20$ sample, respectively. For the former one, the single QD emission is found while the latter one shows two emission bands. The high-energy band arises from emission in the upper layer (QD2) despite the larger dot size in this layer, owing to intermixing of these dots with the GaAs matrix. The assignment of PL bands is emphasized from the spectrum taken after removing by anodic oxidation all upper layers so that only GaAs spacer remains on top of QD1 (curve 3 in Fig. 1.11(a)).

While in determination of WL absorption by PLE, the QD emission was monitored, allowing the use of low excitation intensities. Typical PLE results for the WL are presented in Fig. 1.11(b). The reference sample (curve 1) is characterised by a strong E-HH and a weaker E-LH excitonic resonance. Because the stacked sample shows two emission bands, the detection energy can be set to either QD1 (curve 2.1) or QD2 (curve 2.2). In both cases two E-HH transitions are observed, however, with different intensity ratio. It is

obvious that QD2 emission yields higher intensity if the directly connected wetting layer (WL2) is resonantly excited than exciting WL1. The assignment of the peaks is emphasized by the spectra measured after layer removal (curve 3). Only the lower energetic E-HH resonance remains without any energy shift, i.e. the transition energy is not influenced by coupling.

As a result, the PR, PL and PLE study of optical properties in two-fold self-assembled InAs/GaAs quantum dot structures with different spacer thickness unambiguously proved strain field-induced WL reduction in the upper layers. Moreover, subband calculations (not shown) reproduced the observed transition energy splitting within the whole studied spacer thickness range if a 10% reduction of the upper WL is assumed, which is a result of a reduced critical thickness of the second layer during growth.

Intraband transitions in InAs dots-in-a-superlattice structures

In recent years, advanced method to design the energy level scheme of QD-based photodetectors was proposed by embedding QDs in a two-dimensional superlattice (SL) [4]. As both the electronic levels of the QDs and the minibands of the superlattice are not, or only slightly, coupled, dot energy levels and the extended states of the SL can be adjusted individually by varying the period of the SL as well as by changing the growth conditions of the dots [6]. Such scheme of photodetector was realized by embedding vertically stacked InAs QDs into a GaAs/AlAs SL [3–6]. The strong photocurrent signal was obtained under normal-incidence detection. Spectral peculiarities are related to intersublevel transitions in QD structure and subsequent vertical transport of photoexcited carriers through the stacked QD/SL structure. In addition, it was found that the dark current of these devices is reduced by one order of magnitude compared to the devices without GaAs/AlAs SL [6], which is of great importance regarding the possible use of such systems as photodetectors in the infrared spectral region. In the next few paragraps Rebohle *et al.* [3] paper is reviewed, since two of the InAs dots-in-a-superlattice systems studied there (structures MD-A and MD-C) are the same, which are investigated and discussed properly in the original part of the dissertation.

Three multiple-dot (MD) device structures, denoted as A, B, and C, were designed, grown, and characterized. Sketches of the different MD structures studied are given in Fig. 1.12 (left). Device A consists of periodically arranged InAs QD layers which are spaced by a 10 nm-thick GaAs matrix. Device B is additionally provided with 1 nm thick AlAs barriers at a dis-

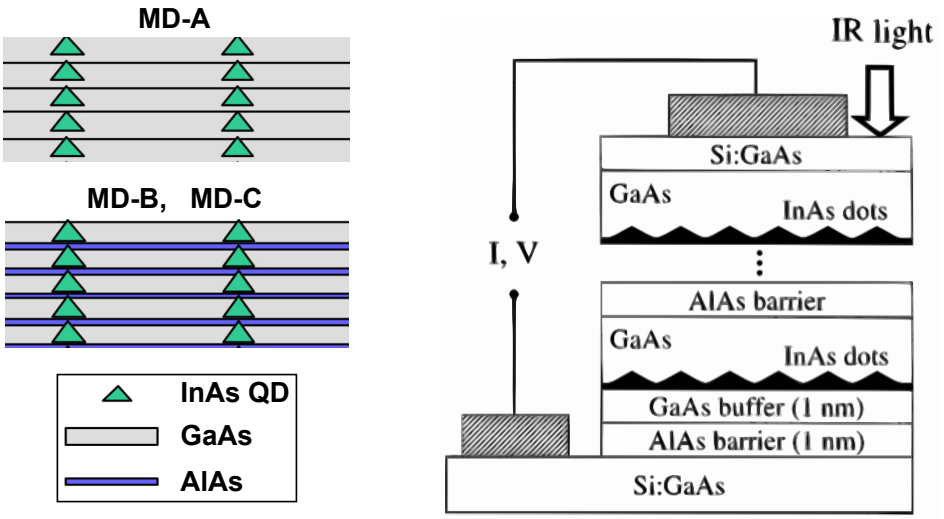

Figure 1.12 Sketches of the different multiple-dot structures studied (left) and schematic structure of a device with a QD stack embedded in the AlAs/GaAs superlattice (right), as it was processed for PC and I-V measurements. [Adapted from Refs. [3, 6].]

tance of 1 nm from the InAs dots, resulting in a superlattice period of 11 nm and an enhancement of the absorption energy in comparison with device A. The superlattice period, which is necessary to shift the absorption energy of device B back to the original energy value of device A, was calculated to be 14 nm and was applied to device C.

Energy level system and the dark current behavior of the nanostructures was studied by PL, photocurrent (PC) [see Fig. 1.12 (right)] and current-voltage (I-V) measurements.

PL spectra of the devices at 300 K (RT) and 4 K are shown in Fig. 1.13(a) and (b), respectively. As expected, PL peaks of devices B and C (with AlAs barriers) in RT spectra are blue-shifted by more than 100 meV as compared to device A. Therefore the energy level system of the InAs dots is quite similar for the B and C devices. All PL peaks are asymmetric with a shoulder on the high-energy side, and a second peak of lesser intensity has to be assumed. At 4 K, the situation becomes more complex. First, the main PL peak is shifted to higher energies at 1072 meV (device A), 1105 meV (B), and 1100 meV (C). Furthermore, a second PL feature at the high-energy side becomes visible at 1182 meV (B) and 1178 meV (C). While the peak positions for both devices coincide well, the intensity ratio for device C has changed in favor of the high-energy peak.

Liquid helium (4 K) temperature unbiased PC spectra spectra of the QD devices studied are given in Fig. 1.14(a). While the main PL peaks are situated at around 225 meV (devices A and C) and at 247 meV (B), the

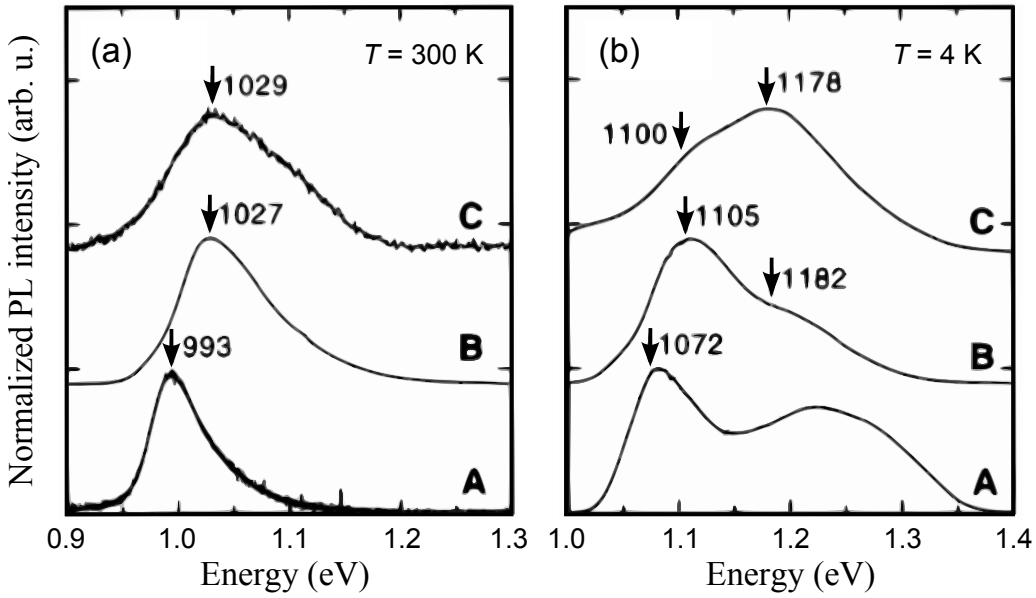

Figure 1.13 PL spectra of the devices A, B, and C at room (a) and at 4 K (b) temperatutes. The numbers indicate PL peak energies, given in meV. [Adapted from Ref. [3].]

FWHM of the main PC peak amounts approximately to 13 meV (A), 16 meV (B), and 11 meV (C), owing to size distribution of QDs. Similar to the PL analysis, a smaller second PC peak has to be assumed on the high-energy side of the main peak. The main peaks are assigned to the transition from the dot `GS` to the GaAs continuum (device A) or to the first miniband (`MB1`) of the GaAs/AlAs SL (devices B and C). The I-V characteristics, on the other hand, exhibits an asymmetric diode-like behavior. It can be clearly seen in Fig. 1.14(b) that the dark current for the devices B and C (with AlAs barriers) is remarkably lower than that of device A (without AlAs barriers). Moreover, the strong PC signal obtained under normal incidence underlines the good suitability of the proposed dots-in-a-superlattice system for infrared photodetectors.

Whereas the calculation of the dot energy levels is rather complex and depends on many details, the energetic position of the minibands (MBs) of the superlattice can be easily estimated by numerically solving the 1-D Schrödinger equation in growth direction. Based on the experimental results, the basic energy level system of the devices was reconstructed and is schematically drawn in Fig. 1.15. In the following discussion, the ground-states of InAs QD for heavy-hole and electron are denoted as `HH0` and `E0`, whereas the first-excited states — as `HH1` and `E1`. (The first miniband of the AlAs superlattice is indicated by `MB1`.)

In case of the sample A, the GS transition in QD at 4 K of 1072 meV

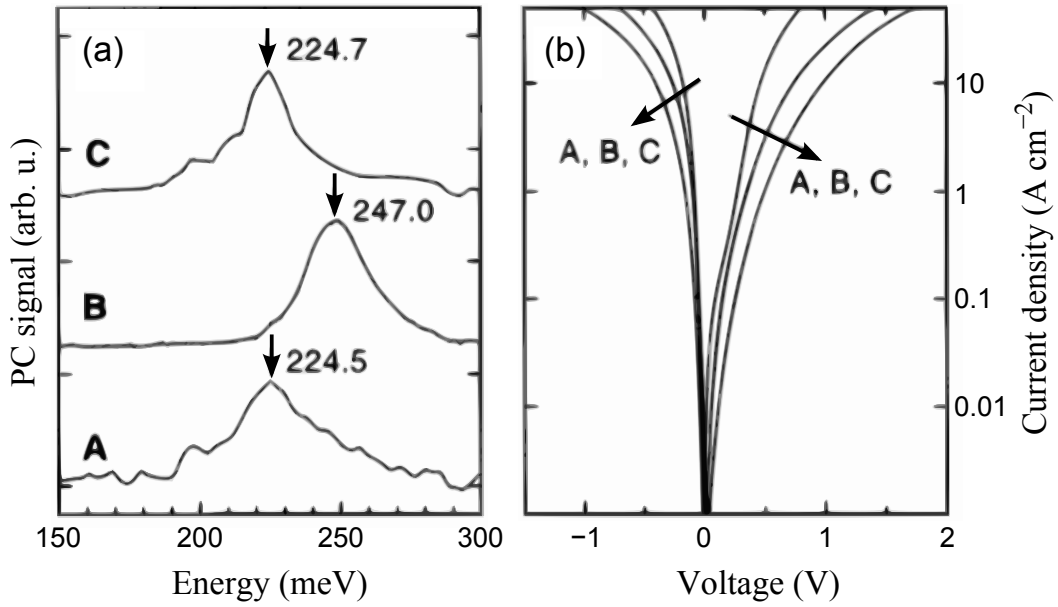

Figure 1.14 Liquid helium (4 K) temperature unbiased PC spectra spectra of the devices A, B, and C (a). The numbers indicate PL peak energies, given in meV. The *I-V* characteristics of the studied devices at 4 K (b). The current density decreases in the order of A, B, and C. [Adapted from Ref. [3].]

is found (see Fig. 1.13(b)). Although the high-energy shoulder of the PL peak is often attributed to the excited-state transition, `HH1` → `E1`, from PL data alone it can not be distinguished, whether it belongs to the transition `HH1` → `E1` or if it reflects a bimodal size distribution of the QDs [28]. Moreover, the PC peak at 224 meV is attributed to the transition from `E0` to the GaAs conduction band (CB).

Although the dot growth conditions are the same for all the samples, the GS transition for device B presents an enhanced energy spacing of 1105 meV as compared to device A, resulting in a blue-shifted PL peak by 33 meV (see Fig. 1.13(b)). Then, the transition energy `E0` → `MB1` was estimated from PC data to be of 247 meV (Fig. 1.14(a)). This value can be now split into an energy of 191 meV for the distance `E0` → `CB` and an energy of 56 meV (`CB` → `MB1`). It was calculated withn 1-D band structure approximation that the position of `MB1` should expand between 48.6–53.2 meV above CB. The small difference of 3 meV can be easily explained by the rough assumption of an unchanged `HH0` state. In fact, the `HH0` state approaches the GaAs valence band by a few meV. It should be noted, that the introduction of a QW between the AlAs barriers (a rough approximation of the QD) does not change significantly the results of the calculation, as long as the width of the well is small compared to the SL period.

Furthermore, the larger SL period of device C lowers and narrows its

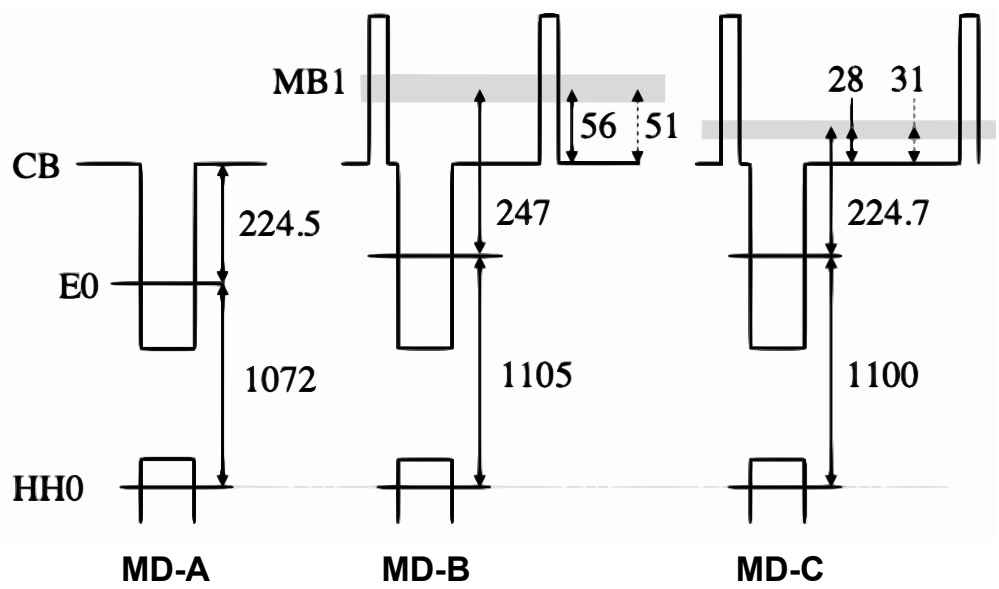

Figure 1.15 Basic energy level scheme of devices A–C. Distances between energy levels are given in meV. Solid arrows indicate values estimated from the experiment, while dashed ones present calculation results within 1-D band structure approximation. [Adapted from Ref. [5].]

MB1, which extends between 30.1–32.3 meV above CB, according to the calculations. With the small PL peak red-shift by 5 meV in respect of device B, and the PC peak at 225 meV, the experimental value of 28 meV for the CB $\rightarrow$ MB1 distance was found. As a result, device C has the same absorption peak as device A, but the dark current has been decreased by more than one order of magnitude, according to Fig. 1.14(b).

Finally, to optimize operation of dots-in-a-superlattice devices, one need to know in detail their optical properties and electronic structure. Previous works on determining electronic structure of InAs/GaAs/AlAs QD/SL have been primarily focused on intersublevel transitions in InAs QDs with little emphasis on the wetting layer properties [3–6]. The information needed can be obtained by modulated reflectance spectroscopy, in particular, by photoreflectance (PR) and contactless electroreflectance (CER). These methods have been shown to be efficient and successful for characterization of low-dimensional systems and nanostructures [29, 30], including delta-doped GaAs/AlAs QWs, and InAs dots-in-a-superlattice structures [1–4.§].

1.3.2 InAs dots-in-a-well

Recently, a new type of detector has been proposed for detection of IR radiation — a quantum dot infrared photodetector (QDIP). The QDIP is a natural extension of the development of QWIPs, since only the active ma-

terial in the detector is changed from QWs to QDs. The QDIPs employ intersubband transitions between different discrete (bound) energy states of the electrons in quantum dots (QDs), similarly to a QWIP, to detect radiation in the infrared wavelength region. In QDIPs, absorption at all angles of incidence occurs, whereas in QWIPs only infrared light polarised in the confinement direction can be detected. Light coupling by means of processed gratings, which normally are used in QWIPs to enhance the absorption, will thus not be needed. As compared to QWIPs, where the electrons are confined only in the growth direction, the electrons in quantum dots are confined in three dimensions, which reduces the dark current and offers higher photoelectric gain. This in turn enables higher operation temperatures without sacrificing performance. Furthermore, for practical applications an increase of operating temperature would make the camera system cheaper and the detector lifetime longer.

In this Section, an introduction to the detection mechanisms and tuning possibilities of QDIPs will be given. Results from a study of a specific type of QDIP, a quantum dots-in-a-well infrared photodetector (DWELL QDIP), will be presented, including an energy level scheme of the DWELL structure as deduced from interband PC measurements.

Detection principle

The design of a QDIP is based on the fact that the energy difference between the electron ground-state and an excited-state in the dot corresponds to the desired detection wavelength. Electrons populating the ground-state can thus absorb photons with that specific energy and be excited to higher energy states. If an external bias is applied, the energy band diagram is tilted, which enables tunneling from the excited-state to the barrier (see Fig. 1.16(a)). The excited electrons can be swept out of the quantum dot, contributing to the photocurrent. In order to get an efficient electron transport out of the well, the final state of the electron should be situated close to the band edge.

Tuning of the detection wavelength

There are several variable parameters which determine the detection wavelength. The detection wavelength can be adjusted by changing the size of the quantum dot, since the energy separation between the discrete states is size-dependent. The composition of the dot will have influence on the depth of the quantum dot potential well, which also plays a major role for

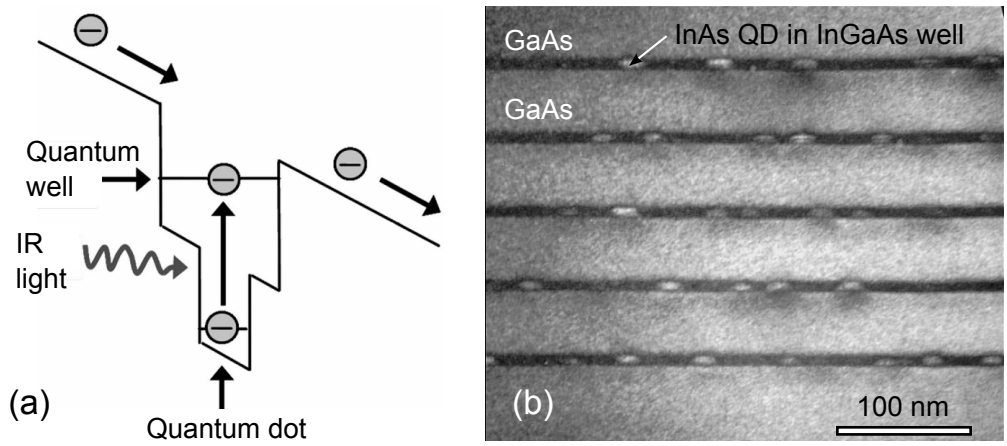

Figure 1.16 Schematic of the detection principle of a quantum dots-in-a-well infrared photodetector (a) and cross-sectional TEM view of typical DWELL active region (b).

the energy structure, and thus for the detection range. InAs quantum dots surrounded by a GaAs barrier (InAs/GaAs) forms a potential well in the conduction band which approximately corresponds to the MWIR (3–5 μm) detection range, while InGaAs quantum dots in a GaAs barrier is better suited for detection in the LWIR (8–12 μm) detection range, due to the shallower potential well.

Typically, InAs/GaAs QDs emit a PL peak around 1050 nm. Therefore, to achieve the important 1300 nm or 1550 nm laser operation or detect within 3–5 μm and/or 8–12 μm atmospheric windows, an effective method to tune the resonant wavelength was proposed — to cover self-assembling InAs/GaAs QDs by a thin capping or strain-reducing $In_xGa_{1-x}As$ layer. Such an advanced dots-in-a-well (DWELL) design, which typical cross-sectional TEM-view of active region is given in Fig. 1.16(b), allows a detection in the LWIR region. Here, the detected wavelength corresponds to a transition between a QD state and a quantum well (QW) state (Fig. 1.16(a)). This method can accordingly offer additional tuning possibilities — partly by varying the QD energy levels and partly by adjusting the width and composition of the QW.
In particular, InGaAs layers can red-shift the QD emission by:

† incrementing of QD size;

† reduction of the residual compressive strain;

† strain-driven decomposition of the InGaAs layer;

† lowering of the lateral confinement (barrier lowering).

As a result, the dots-in-a-well design, in which InAs quantum dots are placed

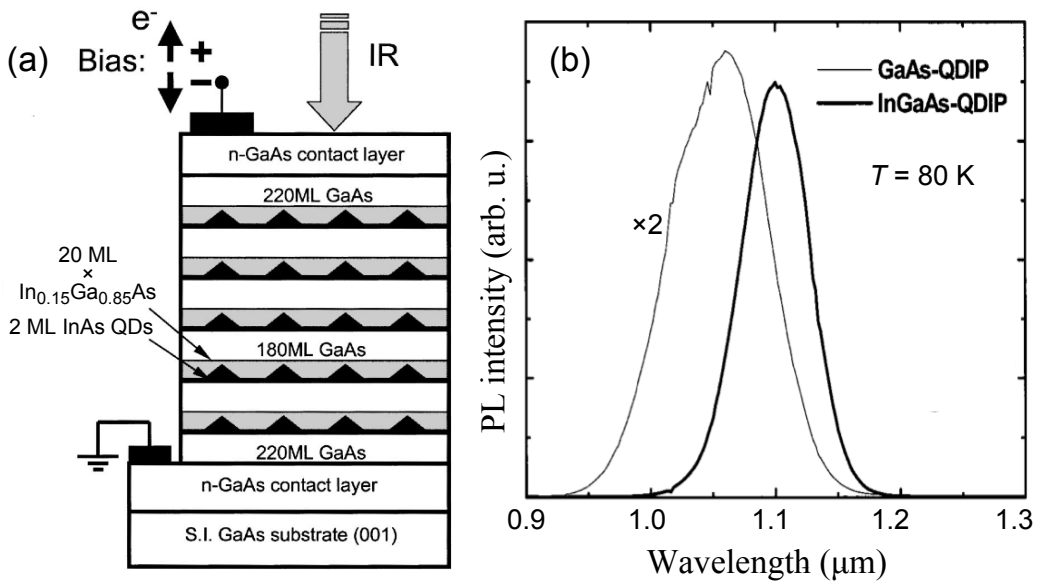

Figure 1.17 Schematic of InGaAs-QDIP growth and device structure (a) and PL spectra of the GaAs- and InGaAs-QDIPs at 80 K. [Adapted from Ref. [15].]

in an InGaAs/GaAs (DWELL) or an InGaAs/GaAs/AlGaAs (DDWELL) quantum well allows precise control of the PC peak wavelength by simply changing the width of the quantum well. Moreover, such a design of QDIP offers a bias-tunable spectrally adaptive response.

In the following few paragraphs a brief overview of the literature considering DWELL nanostructures, a combination of 0-D (QD) and 2-D (QW) systems for QDIPs is presented. Firstly, a paper by Kim *et al.* [15] is reviewed, where the detection bands of InAs QDIPs was tailored by using $In_xGa_{1-x}As$ strain-relieving capping layers that also act as QWs. Authors report results of the effect of an $In_xGa_{1-x}As$ capping layer on the LWIR photoresponse arising from electron intraband transitions.

Tailoring detection bands of InAs QDIP by InGaAs layer

Replacing GaAs capping layers by $In_xGa_{1-x}As$ layers allows partial strain relief and modification of confinement potential to realize longer-wavelength interband transitions in InAs QDs, of value for near-IR detector and laser applications. Therefore, QDIP structures in the n–i(QD)–n configuration were grown (see Fig. 1.17(a)) with the objective of realizing the LWIR photoresponse in the important 8–12 μm window.

Figure 1.17(b) shows the PL spectra of the GaAs and InGaAs QDIPs at 80 K. The GaAs QDIP has a peak at 1.06 μm with a FWHM of 100 meV. The PL peak position of the InGaAs QDIP is red-shifted to 1.10 μm with FWHM of 65 meV, owing to a lower potential confinement effect and the

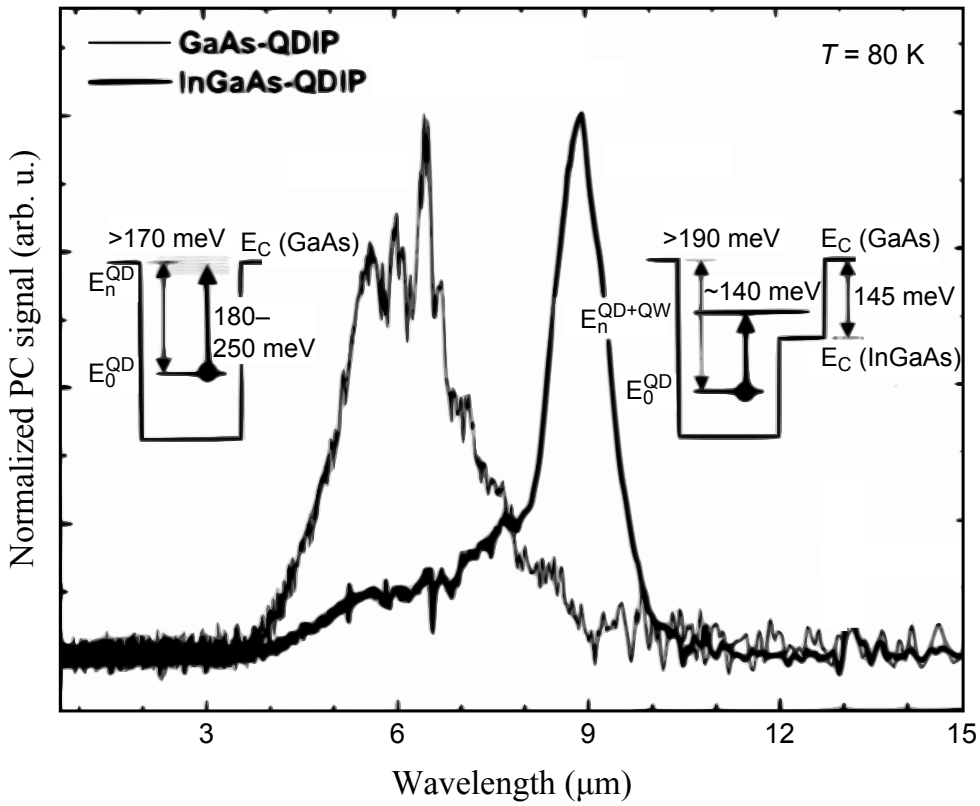

Figure 1.18 Intraband PC spectra of the GaAs- and InGaAs-QDIPs at 80 K. Insets show schematic energy-band diagrams of GaAs- and InGaAs-QDIPs at biases of +10.42 V and −10.4 V at 80 K, respectively. [Adapted from Ref. [15].]

strain relaxation effect of the 20 ML $In_{0.15}Ga_{0.85}As$ cap layer.

Normal-incidence FTIR intraband photocurrent spectra of the GaAs and InGaAs QDIPs were measured as a function of bias. The PC behavior at a bias of +10.42 V and −10.4 V at 80 K, respectively, is given in Fig. 1.18. It was found that QDIPs with InAs QDs capped by a 20 ML $In_{0.15}Ga_{0.85}As$ QW show a sharp photoresponse at $\approx 9\,\mu m$ with a FWHM of only 16 meV. While the counterpart QDIPs without QWs show broad photoresponse in the 5–7 μm range (actually, there are a few PC peaks rather than a single broad peak). The experiental data was analyzed and a summary is schematically indicated in the band diagrams for the InAs QDs in the GaAs QDIPs and in InGaAs QDIPs shown as insets in Fig. 1.18. It was suggested that the $In_{0.15}Ga_{0.85}As$ QW electron energy states contribute to the LWIR intraband transitions in the InGaAs QDIPs through coupling with QD electron excited-states.

Moreover, it was found that the dark current of the InGaAs QDIPs is two to four orders of magnitude smaller than that of the GaAs QDIPs (not shown). This is a combined effect of the larger binding energy for the QD electron ground-state with respect to the GaAs band edge in the InGaAs

QDIP as compared to in the GaAs QDIP and the thicker spacer layers in the former.

Finally, the results obtained by Kim *et al.* [15] also indicate one of the ways to exploit a combination of 0-D (QD) and 2-D (QW) systems for specific applications.

1.3.3 Columnar InGaAs quantum dots for laser applications

Low-dimensional structures have been studied extensively, and are used in modern electronic and optoelectronic devices. Self-assembled quantum dots are particularly attractive both for fundamental research and applications, owing to their unique, atomic-like quantum confinement, which leads to a broad range of optical phenomena [1,31–34]. Recent interest in QDs as functional elements for semiconductor optical amplifiers (SOAs) has stimulated technological developments to improve QD homogeneity and polarization insensitivity [32, 35]. The typical lens-shape of Stranski-Krastanow (SK) grown QDs permits use of only transverse-electric (TE) polarized light, restricting their applicability in SOAs. These limitations are governed by the asymmetric potential profile and compressive strain, which induce characteristic splitting of heavy- and light-hole states. Indeed, light-hole states are pushed away from the band edge and thus in-plane polarized ground-state transitions with large heavy-hole component are predominant. To modify the polarization-dependent optical gain function, QD shape and composition engineering has been proposed [7, 36–38].

Optical properties in terms of polarization insensitivity and size (volume of confinement) control can be significantly improved realizing high aspect ratio, or columnar quantum dots and quantum rings, respectively. In particular, columnar QDs, also referred to as quantum rods (QRs) or quantum posts, were realized by depositing a short period InAs/GaAs superlattice (SL) on top of a seed SK QD layer by means of molecular beam epitaxy (MBE). The quantum confined structure thus consists of vertically oriented InGaAs QRs immersed in a two-dimensional InGaAs layer. By carefully choosing the growth parameters, tall QRs with aspect ratios (height/diameter) significantly > 1 were obtained [7, 37]. Very recently, it was demonstrated both theoretically [39] and experimentally [40, 41] that a critical indium composition contrast between the $In_xGa_{1-x}As$ QR and the surrounding 2-D $In_xGa_{1-x}As$ layer, or quantum well (QW), $x_{QR}/x_{QW} > 3$ is needed to alter the polarization properties in favour of the transverse-

magnetic (TM) mode. Moreover, as was deduced in [39], this composition contrast is more important than the aspect ratio in achieving zero net axial strain at the centre of an elongated dot, and hence enhancing the intensity of TM light with respect to TE components. Such elongated nanostructures, following optimization of both their composition and geometry, already appear very attractive for fabrication of polarization-insensitive SOAs. Furthermore, alongside such practical applications, QR structures are a model system for fundamental research, because they present a crossover between zero-dimensional and one-dimensional quantum confinements.

QR formation can be affected greatly by the growth parameters, including growth temperature, growth interrupts, the number of SL periods, and the type of As source used [42]. To optimize the growth parameters and implement new designs of these unique quantum structures, an in-depth knowledge of their optical and electronic properties is required. In recent studies, modulated reflectance spectroscopy, in particular photoreflectance (PR) and contactless electroreflectance (CER), alongside photoluminescence (PL) [42], has been successfully employed to characterize low-dimensional systems and nanostructures [29, 33] including QRs [43].

In the following Subsections, advanced QD shape, composition and surrounding matrix engineering regarding the growth and characterization of InGaAs quantum rods is presented. The target of the QR growth is to modify the shape anisotropy of conventional asymmetric QDs and consequently the optical polarization. A brief literature overview of very similar QR structures studied in the original part of the dissertation is given hereinafter.

Firstly, a recent announcement by Li *et al.* in Ref. [7], where InGaAs QRs with a high aspect ratio of 4.1 were synthesized by MBE, indicating the feasibility of artificial shape engineering of QDs, is presented. Here, the InGaAs QRs were formed by depositing a 1.8 ML InAs seed dot layer followed by a short period GaAs/InAs SL.

Growth and characterization of InGaAs quantum rods

Recently, Li *et al.* demonstrated [7] that the growth of the InGaAs QRs (in a paper denoted as columnar quantum dots, CQDs) is very sensitive to growth interruption (GI) and growth temperature. Both longer GI and higher growth temperature impact the size dispersion of the QRs, which causes the broadening of PL spectrum and the presence of the additional PL peak tails. By properly choosing the GI and the growth temperature,

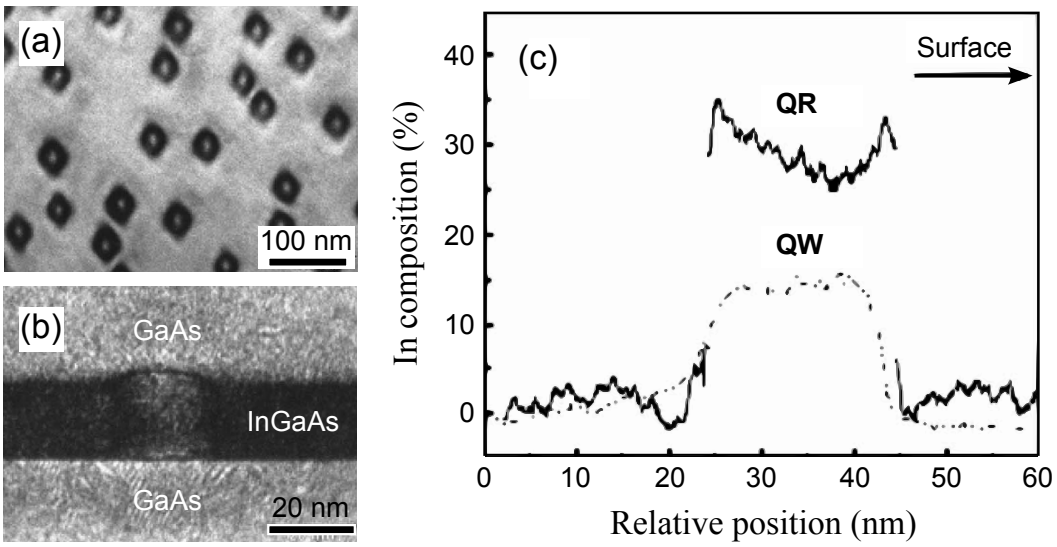

Figure 1.19 TEM of the sample including a 16-period SL. Bright-field (001)-plan-view image (a), magnified dark-field cross-sectional image (b), and In composition profiles across the center of the InGaAs QRs and InGaAs QW layer. [Adapted from Ref. [7].]

QRs including GaAs/InAs (3 ML/0.7 ML) SL with period number up to 35 without plastic relaxation were grown. As a result, the corresponding equivalent thickness of the SL was 41 nm, which is twice as high as the theoretical critical thickness of the strained InGaAs layer with the same average In composition of 16%.

The formation of nanorods was confirmed by TEM data, as shown in Fig. 1.19(a) and (b). QRs with nearly isotropic cross-section (20 nm × 20 nm dimensions) and $1.7 \times 10^{10}\,\mathrm{cm}^{-2}$ density were formed by depositing a 16-period GaAs/InAs (3 ML/0.62 ML) SL on an InAs seed dot layer. The CQDs have a parallelogram shape with the diagonals exactly along the $[1\bar{1}0]$ and [110] directions of the growth plane (Fig. 1.19(a)). The average ratio between the long diagonal and the short one is 1.22 (with a standard deviation of 0.05). From the observations of the cross-sectional images (Fig. 1.19(b)), the whole structure consists of two parts, i.e., the QRs and a 2-D layer around them. The 2-D layer consists of an InGaAs QW with an average thickness of about 20 nm. Its composition is uniform and has an average value of about 16%. According to In composition profile measurements across the center of the InGaAs QRs and InGaAs QW layer (Fig. 1.19(c)), it was found, that In content in QRs is around three times higher ($\approx 45\%$) as compared to QW. Therefore, the whole quantum region is comprised of In-rich QRs, surrounded by In-reduced QW.

Figure 1.20(a) shows the room temperature PL spectra of the reference sample with 1.8 ML InAs QDs (having no SL) and the QRs including 10-

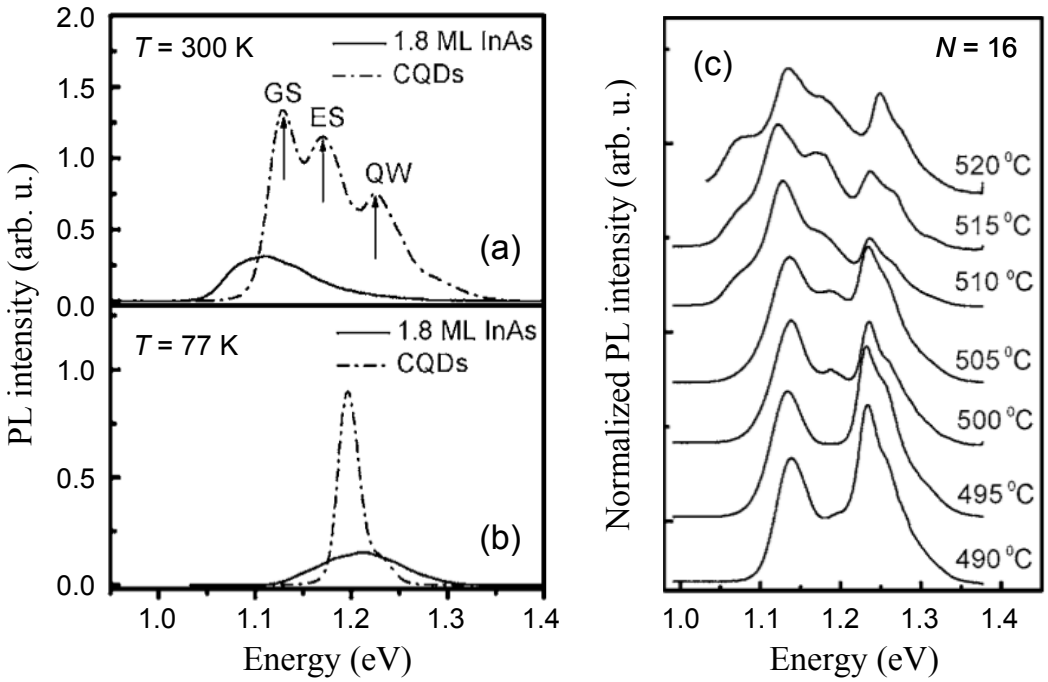

Figure 1.20 Room (a) and liquid nitrogen (b) temperature PL spectra of the reference sample with 1.8 ML InAs QDs (no SL) and the CQDs (QRs) including a 10-period GaAs/InAs (3 ML/0.7 ML) SL, grown at 500 °C. In (c): Room temperature PL spectra (normalized to the QR GS transition peak) of the QR samples with 16-period GaAs/InAs (3 ML/0.62 ML) SL, grown at different temperatures. [Adapted from Ref. [7].]

period GaAs/InAs (3 ML/0.7 ML) SL. The PL spectral width of the reference QD sample is very broad, which is a typical feature of the conventional SK growth of QDs. The broad PL spectrum can be attributed to the large QD size inhomogeneity and to thermal population of close-spaced excited-states (ES). When the 1.8 ML InAs QDs were capped by the GaAs/InAs SL, a well-developed PL spectrum with three distinct peaks along with a strong increase in PL intensity was observed (Fig. 1.20(a)). The first two peaks at low photon energy were assigned to the ground-state (GS) and the first ES transitions in InGaAs QRs. The high-energy peak was attributed to the transitions from the 2-D InGaAs QW, surrounding the QRs. The observed strong emission from the QW was due to the thermal population of the high 2-D density of states.

Figure 1.20(b) shows the PL spectra of the same samples at 77 K. PL spectral width of the QR sample drastically decreases due to the suppressed thermal population of the QD ES and the QW, whereas the PL spectral width of the 1.8 ML InAs QDs is nearly the same as at RT. The PL spectral width of QRs is very small (only $\approx$ 26 meV) compared to the reference QD sample and, thereby, demonstrates a relatively small inhomogeneous broadening. The small inhomogeneous broadening was related partly to the

uniform size distribution evidenced by TEM (see Fig. 1.20(a)), and partly to the large QD dimensions and small confinement energy, which make the energy levels less sensitive to size fluctuations.

The temperature-dependent surface diffusion of the adatoms affects the structural and the optical properties of the QDs. In order to investigate these effects, a set of QR samples were grown at different growth temperatures ranging from 490 to 520 °C. Normalized room temperature PL spectra for the relevant QR samples are shown in Fig. 1.20(c). The QR-related PL peaks slightly red-shift with increasing substrate temperature up to 515 °C and then blue-shift at the growth temperature of 520 °C. The red-shift was attributed to the increasing size of QRs, which is the consequence of the increased diffusion length of the adatoms at higher growth temperature. The blue-shift was explained by the enhanced In desorption. It was suggested that the material exchange among different QR during the GI may be accelerated due to the increasing growth temperature, which induces dot size dispersion. This explains the appearance of the low-energy peak tail and the spectral broadening at higher growth temperature.

In order to modify the shape (and thereby the optical) anisotropy of conventional asymmetric QDs, the different in height QRs were realized, adjusting the GaAs/InAs SL period number. Indeed, the number of SL periods unambiguously determines the height of the QR, a property unique to QRs. While with increasing period number N, polarized emission along the growth direction (TM-mode) overtakes the in-plane polarized emission (TE-mode), it is interesting to investigate the effects of SL period number. For this purpose, a series of QR samples including a different number of periods ($N = 0$–50) was grown at 500 °C. Normalized room temperature PL spectra of these samples are shown in Fig. 1.21(a), whereas in Fig. 1.21(b) the dependences of the PL peak energies and the PL integrated intensities on the number of SL periods are summarized. With increasing number of periods, the QW-related PL peak red-shifts and then keeps nearly constant after a certain number, indicating the evolution of the SL equivalent thickness; whereas the QR-related PL peaks first blue-shift and then red-shift systematically. It was proposed that the In composition of the initial (small aspect ratio) In-rich QDs is decreased, thereby a PL peak blue-shift from the QRs was observed. However, with increasing the stacking number, the vertical electronic coupling in the system becomes more effective and the equivalent island height increases, both red-shifting the PL peak energy and increasing the PL integrated intensity. Finally, the drastic decrease of

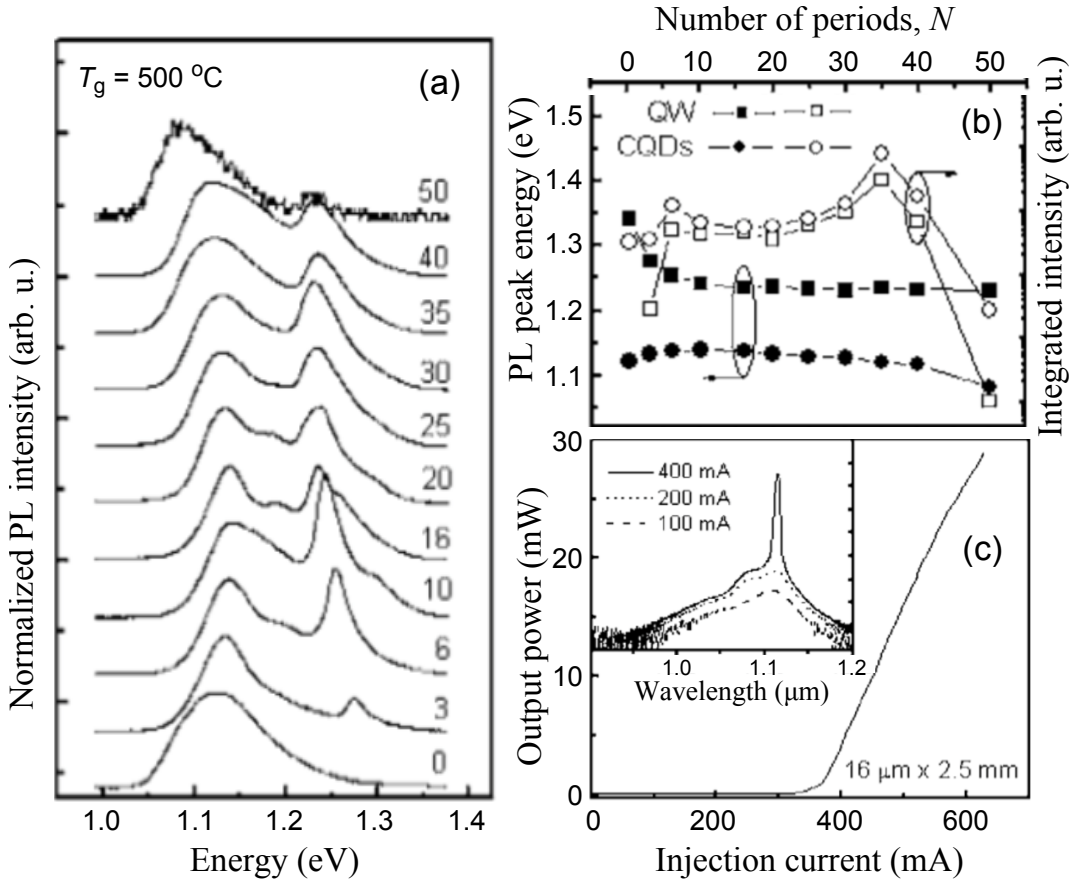

Figure 1.21 Room temperature PL spectra (normalized to the QR GS transition peak) of the CQD samples including different number of periods (N) of the GaAs/InAs (3 ML/0.62 ML) SL, grown at 500 °C. The number of periods N was varied from 0 (reference) to 50. In (b): Variation of PL peak energies and integrated intensities from the InGaAs QW and the InGaAs CQDs (QRs) as the function of the SL period number N. In (c): Output power against drive current (L-I) characteristic from a 16 μm × 2.5 mm QR laser stripe under pulsed operation at RT. Inset in (c) shows the emission spectra (logarithmic scale) of the same device at different injection currents. [Adapted from Ref. [7].]

the PL integrated intensity for the $N = 50$ sample are attributed to the plastic relaxation due to the total equivalent thickness of the SL exceeding the corresponding critical value.

To validate the device applications of the QRs, laser diodes, based on a five-stack QR active region and emitting around 1120 nm at room temperature were demonstrated indicating a high material quality. Figure 1.21(c) shows the output power *versus* drive current characteristic for a QR laser device. The laser operates in pulsed mode with a threshold current of 360 mA, corresponding to a threshold current density around 900 A/cm^2 . The emission spectra of the same device at different injection currents are shown in the inset.

Finally, it is expected that such a novel QR structure will be very promis-

ing for the polarization insensitive semiconductor optical amplifiers (SOAs) and other specific applications requiring the control of the QD aspect ratio.

Effects of using As_2 and As_4 sources on optical properties of InGaAs quantum rods

Extending the review of a QR study in Ref. [7], a very recent work by Li *et al.* (Ref. [42]), considering the technological effect of arsenic source (As_2 and As_4) on optical and electronic properties of MBE-grown InGaAs QR structures, is presented. It should be noted, that a very similar study (although using far more different experimental techniques and tools of analysis) on identical QR structures was carried out by our group (see Refs. [5–7.§]) and, thereby, it is again of great importance for a Reader to get familliar with the another Li *et al.* work [42]. The overview of a relevant paper is given in the following few paragraphs.

The report by Li *et al.* (Ref. [42]) demonstrated that the PL peak energies of the QR samples depend strongly on the As source when similar growth conditions are used. Different optical properties of As_2- and As_4-grown QRs were mainly caused by different In and Ga diffusion lengths under the corresponding arsenic fluxes. A marked improvement in the PL intensities from QR samples grown using As_4 was recorded. However, for both As_2 and As_4, an increase of the As overpressure resulted in a PL intensity degradation, probably due to the formation of nonradiative recombination centers.

Within the growth scheme of nanorods (InAs QD + InAs/GaAs SL) proposed by Li *et al.* [7, 37, 41, 42], large aspect ratio QRs, which are much sought for polarization control of SOAs, can be achieved straightforwardly by increasing the number of SL periods N. Therefore, to investigate the effects of the As source on QR optical properties a two sets of As_2- and As_4-grown QR structures with $N = 10$, 20, and 35 periods were grown at the optimum growth temperature of 500 °C. It was noted that the lower thickness of InAs in the SL increases the number of SL periods (N) that could be achieved without the creation of strain-related defects. As a result, higher aspect ratio QRs can be synthesized.

Figure 1.22 shows the PL spectra of the samples, with the dependencies of the PL peak energy and intensity on SL period number N being shown in the inset. As the N is increased, the PL peak energy of these QRs first blue-shifts and then red-shifts. The blue-shift is attributed to In–Ga atoms intermixing and In segregation during the QR growth, whereas the red-

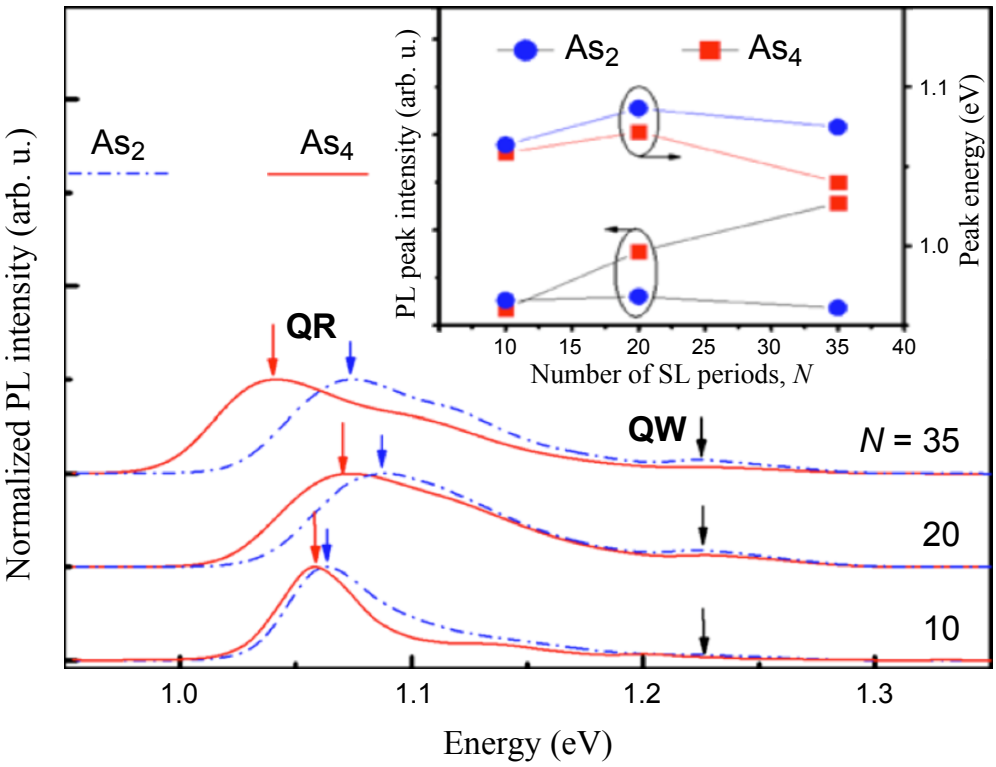

Figure 1.22 Normalized PL spectra of the QR samples with different numbers of SL periods grown at 500 °C. The samples consist of GaAs/InAs (3 ML/0.64 ML) SL with N = 10, 20, and 35 periods. Inset: Dependencies of the PL peak energy and intensity on SL period number N. [Adapted from Ref. [42].]

shift — to enhanced vertical electronic coupling with increasing QR length. Moreover, a higher PL peak energy of the As_2-grown QR samples was observed, particularly for samples with increased SL period number. It was proposed that, during growth, there is a first order interaction between the incident As_2 molecules and the Ga atoms on the surface, whereas there is a second order interaction with incident As_4 molecules. This causes the reaction between Ga and As_2 being faster than that between Ga and As_4. Ga adatoms on the surface are therefore more mobile under an As_4 flux than under an As_2 flux. Using an As_4 source during QR growth will therefore accelerate Ga migration and consequently lead to a more In-rich QR structure and, thereby, to a lower energy PL emission. Finally, the experiments, in which the growth temperature and SL period number have been varied, suggested that low temperature QR growth is Ga-diffusion-dominated, whereas at higher QR growth temperatures In-diffusion dominate.

Furthermore, the PL intensity drastically improved for the As_4-grown QRs with large SL period number, which is similar to the observation from the growth temperature study (not shown). The improvement was attributed to lower impurity incorporation into the epitaxial layer during

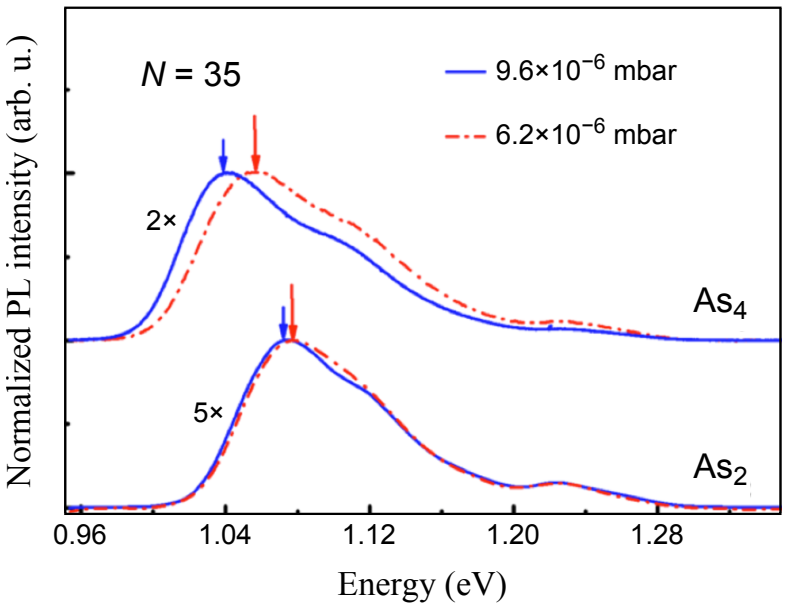

Figure 1.23 Normalized PL spectra of the QR samples grown at 500 °C, with different As overpressures. The samples consist of a $N = 35$ period GaAs/InAs (3 ML/0.64 ML) SL. Ga and In beam equivalent pressures were kept constant with values of 5.2×10^{-7} mbar and 1.9×10^{-7} mbar, respectively. [Adapted from Ref. [42].]

growth, owing to the lower cracking temperature used for the As_4 source.

Additionally, the effect of As overpressure on the QRs was investigated, since the As overpressure is a key growth parameter and plays a major role in the MBE growth of III–V semiconductor materials. Figure 1.23 shows the PL spectra of the $N = 35$ QR samples grown at 500 °C using two As overpressures. The PL peak energies of the QR samples red-shift with the increase of As overpressure used during the MBE-growth. This effect is more evident for the As_4-grown QRs. It was suggested that higher As overpressure suppresses surface diffusion of In/Ga adatoms. As discussed above, enhanced In/Ga surface diffusion/migration results in In-rich QR structures. On the contary, suppressed In/Ga surface diffusion/migration results in In-reduced QR structures and consequently higher energy PL emission. Moreover, PL intensities of the QR samples grown at the higher As overpressure are reduced by factors of about 2 and 5 with As_4 and As_2 sources, respectively. It is believed that the formation of nonradiative recombination centers at higher As overpressure, such as As antisite defects, is responsible for such degradation.

Finally, it was deduced that PL peak energies of QR samples grown under given growth conditions strongly depend on the As source used and, thereby, remarkable improvements of the PL intensities from the QR samples grown by using an As_4 source were achieved.

Although Li *et al.* [42] study provide technological — optimized GI and

temperature — parameters through an in-depth analysis in terms of the mechanisms involved during the MBE-growth of QR structures, there is no deeper insight into QR electronic structure and optical properties, such as optical anisotropy.

1.3.4 Optical polarization properties of InGaAs quantum rods

The atom-like density of states in semiconductor QDs is quite promising to design optical devices such as lasers, SOAs, etc., with high saturation powers and fast response. Recently, bilayer and multilayer quantum-dot (QD) stacks have attracted strong interests because of their operating wavelengths within the telecommunication range of interest (1.3–1.5 μm). However, for practical design of optical devices, polarization-insensitive optical spectra are needed. Therefore, controlling polarization response in QD systems is a critical issue, since in-plain optical anisotropy is common figure of merit for InGaAs-based nanostructures due to better mobility (longer migration length) of In adatoms in [001] direction on the GaAs [44, 45].

Recent experimental measurements, without any theoretical guidance, showed that isotropic polarization response can be achieved by increasing the number of quantum-dot (QD) layers in a QD stack, where the QD layers are geometrically separated by thin GaAs spacers [46, 47]. Such multilayer QD stacks have a twofold advantage over columnar QDs (i.e. QRs):

† moderately thick GaAs spacer between the QD layers allows precise control of overall QD shape and size;

† reduced strain accumulation results in isotropic polarization response with fewer QD layers in the stack.

Very recently, Usman *et al.* (Ref. [48]) analyzed the polarization response of multilayer QD stacks containing up to nine QD layers by linearly polarized PL measurements and by carrying out a systematic set of multimillion atom simulations. The atomistic modeling and simulations allowed to include correct symmetry properties in the calculations of the optical spectra, a factor critical to explain the experimental evidence. The values of the degree of polarization (DOP) calculated follows the trends of the experimental data. Detailed physical insight by examining strain profiles, band edges diagrams, and wave function plots is given therein. While the previous studies of polarization response of QDs provide only one value of DOP

corresponding to a chosen direction for the TE mode [40], multidirectional PL measurements and calculations of the DOP revealed a unique property of InAs QD stacks that the TE response is anisotropic in the plane of the stacks. Therefore, a single value of the DOP is not sufficient to fully characterize the polarization response. This is explained by the anisotropy of the TE-modes due to orientation of hole-wave functions along the $[\bar{1}10]$ direction. It was suggested that isotropic polarized PL (PPL) response is due to two factors:

(i) HH-LH band mixing favors the increase of TM_{001}-mode intensity;

(ii) hole wavefunction $[\bar{1}10]$-alignment reduces TE_{110}-mode intensity.

Finally, it was found that the QD stacks with identical layers will exhibit lower values of the DOP than the stacks with nonidentical layers. In the following few paragraphs the relevant paper is presented.

Degree of polarization from multilayer InAs/GaAs quantum dots

The polarization response of QDs is measured in terms of DOP, defined as

$$\mathrm{DOP} = \frac{\mathrm{TE}_{\perp\text{-growth}} - \mathrm{TM}_{\parallel\text{-growth}}}{\mathrm{TE}_{\perp\text{-growth}} + \mathrm{TM}_{\parallel\text{-growth}}}. \tag{1.4}$$

Here $\mathrm{TE}_{\perp\text{-growth}}$ refers to traverse electric mode in a direction perpendicular to the growth direction ([001]), whereas $\mathrm{TM}_{\parallel\text{-growth}}$ refers to traverse magnetic mode along the growth direction. The DOP is associated with the direction of TE mode, i.e., $\mathrm{TE}_{110} \rightarrow \mathrm{DOP}_{110}$, $\mathrm{TE}_{\bar{1}10} \rightarrow \mathrm{DOP}_{\bar{1}10}$, $\mathrm{TE}_{100} \rightarrow \mathrm{DOP}_{100}$, and $\mathrm{TE}_{010} \rightarrow \mathrm{DOP}_{010}$. It is shown hereinafter that the value of DOP depends highly on the chosen direction for the TE mode in the plane of QD and only one DOP value is not sufficient to fully characterize the polarization response of QD systems.

Further, the experimental results are provided for QD stacks containing three (`L3`), six (`L6`), and nine (`L9`) QD layers along with a reference sample of single QD layer (`L1`). The results indicate that the DOP_{110} takes up the values of $+0.46$ and -0.60 for the `L6` and `L9` structures, respectively. A change of sign for the DOP_{110} implies that an isotropic polarization response ($\mathrm{DOP} \sim 0$) can be achieved by engineering the number of QD layers in the stack.

The polarization-dependent PL spectra are shown in Fig. 1.24 for a single QD layer [panels (a)–(c)] and nine QD layers [panels (d)–(f)]. Figures 1.24(a)–(c) indicate for a single QD (`L1`) that TE_{110} and $\mathrm{TE}_{\bar{1}10}$ show a

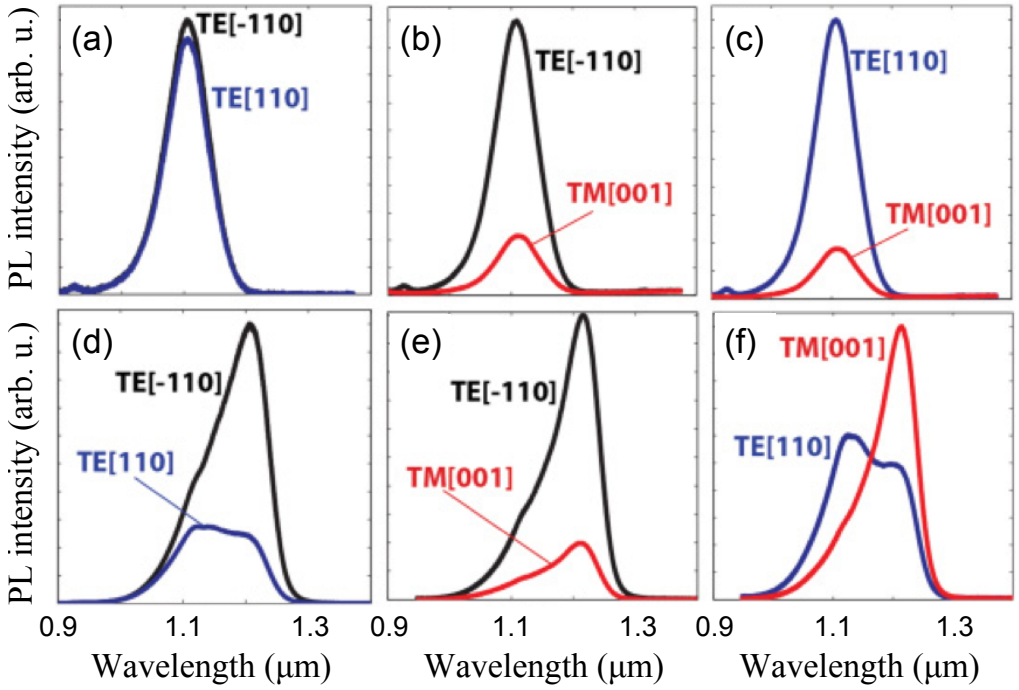

Figure 1.24 Normalized linearly polarized PL measurements for TE_{110}, $TE_{\bar{1}10}$ and TM_{001} modes for a single-QD-layer (a–c) and a nine-QD-layers (d–f) samples. [Adapted from Ref. [48].]

similar magnitude, and that TM_{001} has a much smaller response than both in-plane TE modes. This is typical for InAs QDs, since the compressive biaxial strain splits the HH-LH band edges, resulting in HH-type valence band states close to band gap.

On the contrary, the PL spectra revealed an interesting and unique property of the InAs/GaAs QD stacks (L9) that the TE_{110} response is significantly less than the $TE_{\bar{1}10}$ one, as illustrated in Figs. 1.24(d)–(f). The measured difference between the two TE modes is such that even the DOP for the same QD stack could have different signs when measured along the [110] and [$\bar{1}$10] directions.

Electron and hole wavefunctions To investigate the reasons for such a nonintuitive TE-mode anisotropy, modeling and simulations of these large QD structures was carried out. Figures 1.25(a) and (b) show the plots of the lowest conduction band state E1 for all of the four QD systems studied. Here, the horizontal dotted lines are to guide the eye and indicate the base of the QD layers in the stack, whereas the intensity of the color indicates the magnitude of the wavefunction. From the top views of the wavefunctions (Fig. 1.25(b)), it is evident that the lowest electron state is of s-type symmetry. The side views of the wave functions (Fig. 1.25(a)) show that the

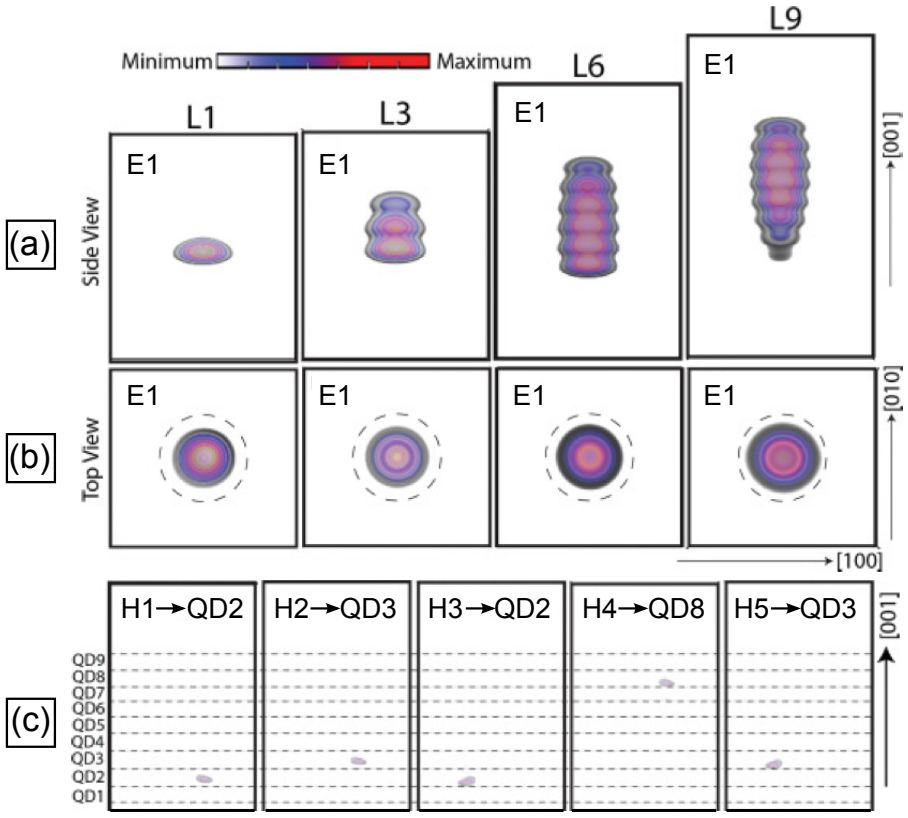

Figure 1.25 Side- (a) and top-view (b) of the lowest electron state (`E1`) for QD systems `L1`, `L3`, `L6`, and `L9`. In row (c): The highest five hole states, `H1`, `H2`, `H3`, `H4` and `H5`, for `L9` QD system. [Adapted from Ref. [48].]

electron state forms a hybridized (molecular) state in `L3`, `L6` and `L9` stacks and is spread over all of the QDs, owing to a strong coupling of QDs. The presence of the `s`-like electron wavefunction in all of the QDs implies that only the details of hole-wave functions inside the QD stack will determine the optical activity of a particular QD inside the stack. It was observed for `L3` and `L6` systems that strain tends to push the electron states toward the lower QDs. However, this was no longer true for `L9` QD stacks, where the electron wavefunction `E1` vanishes around the edges of the stack due to the larger strain magnitude there.

Although the electrons (lighter-mass particles) are strongly influenced by the interdot electronic and strain couplings and exhibit tunneling across the QDs forming molecular-like hybridized states, the holes due to their heavier mass remain well-confined inside the individual dots and do not show any hybridization. Such a behaviour of holes is evident from Fig. 1.25(c), where the lowest five hole wavefunctions (side views) in the `L9` system are ploted. The horizontal dotted lines are plotted to mark the positions of the base of the QDs and helps to determine the location of a particular hole wavefunction inside the stack. In this system, `H1` and `H3` are inside `QD2`,

H2 and H5 are in QD3, and H4 is in QD8. The location of a hole state inside a QD stack is strongly influenced by geometry of the QD stack (QD base diameter, height, interdot layer separation, etc.).

Hydrostatic and biaxial strains Thereby, the strain profile, which controls the strength of the coupling between the QD layers inside the stack and determines the position of the hole states inside the stacks, was calculated. The plots of hydrostatic $\epsilon_H = \epsilon_{xx}+\epsilon_{yy}+\epsilon_{zz}$ (dotted lines) and biaxial strain $\epsilon_B = \epsilon_{xx} + \epsilon_{yy} - 2\epsilon_{zz}$ (solid lines) profiles along the [001] direction through the center of the L1 and L9 QDs is given in Figs. 1.26(a) and (b), respectively. The hydrostatic strain exhibits a very slight change from L1 to L9. The hydrostatic component is dominantly negative inside the QD, indicating strong compression of the InAs and almost zero outside the QD. The biaxial strain, however, significantly changes as the QD stack height increases.

In more detail, the biaxial strain in the QD evolves from highly negative for a single QD (Fig. 1.26(a)) to zero for the L9 stack (Fig. 1.26(b)) with a small increase in positive contributions in the capping layer. It was suggested that a highly negative biaxial strain observed for L1 QD was due to InAs unit cells inside the QD region, which tend to fit over the GaAs matrix by an in-plane compression and an elongation along the [001] direction. However, when the size of the stack increases, the unit cells of InAs around the center of the stack feel lesser and lesser compressive force from the surrounding GaAs. Thereby, the vertical lattice constant of the InAs starts matching with the GaAs and hence the biaxial strain tends to change its sign around the middle of the QD stack, as shown for L9 QD sample in Fig. 1.26(b).

Heavy- anf light-hole subband intermixing The minor change in the magnitude of the hydrostatic strain (as L1 $\rightarrow$ L9) implies that the lowest CB edge will experience very small change as they are only affected by the hydrostatic component. However, the VB edges are affected by both the hydrostatic, and the biaxial strains. The impact of strain on HH- and LH-band edges is analytically expressed as

$$\delta E_{\mathrm{HH}} = a_v\epsilon_H + \frac{b_v\epsilon_B}{2}, \qquad \delta E_{\mathrm{LH}} = a_v\epsilon_H - \frac{b_v\epsilon_B}{2}. \tag{1.5}$$

Here a_v and b_v are deformation potential constants for HH- and LH-band edges, and the values for these constants for InAs systems are $a_v = 1.0\,\mathrm{eV}$

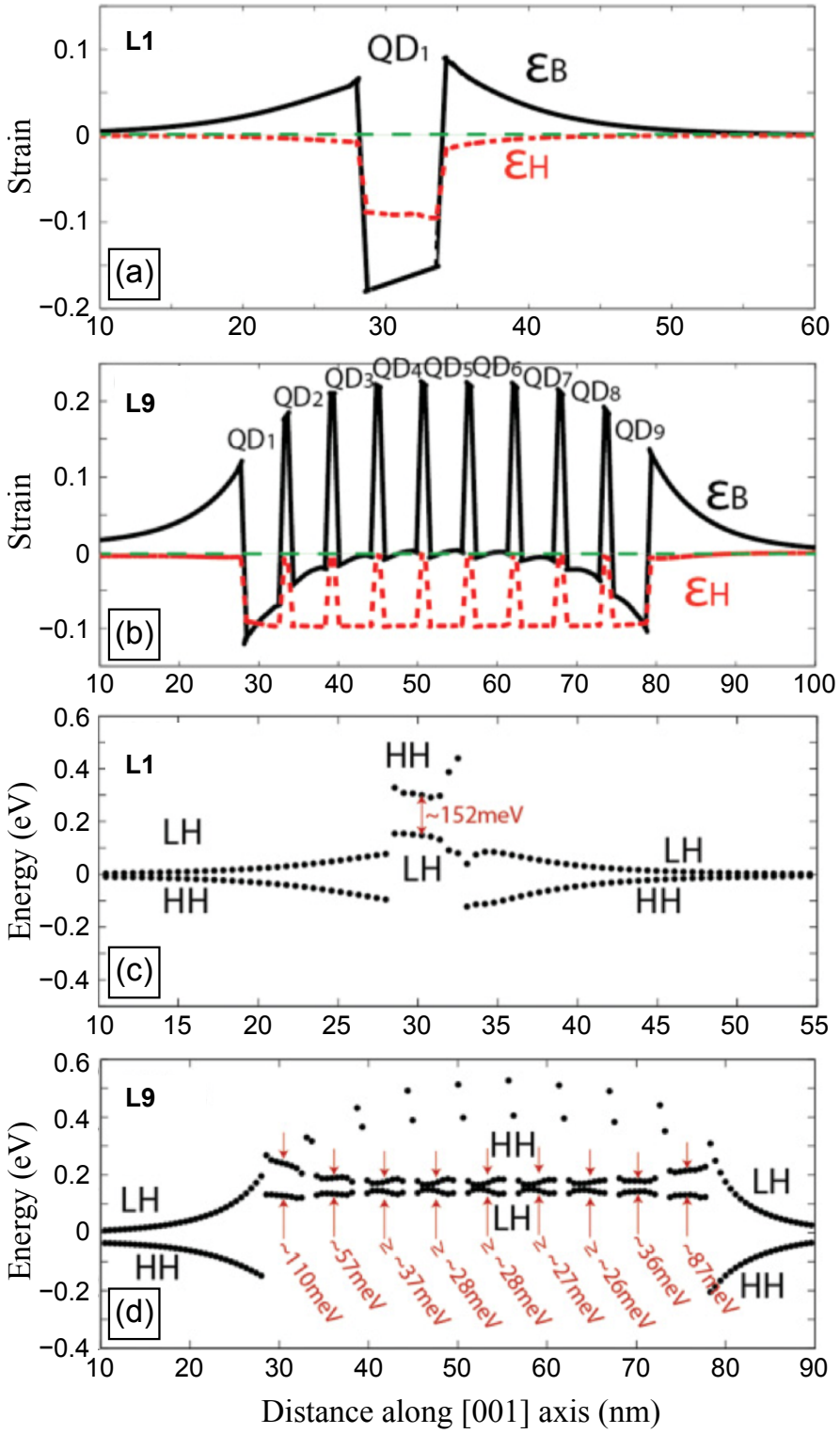

Figure 1.26 The plots of hydrostatic (ϵ_H) and biaxial strain (ϵ_B) components (a, b), and local band edges for the highest two heavy- (HH) and light-hole (LH) bands (c, d) through the center of the QD along the [001] direction for `L1` (a, c) and `L9` (b, d) QD systems. [Adapted from Ref. [48].]

and $b_v = -1.8\,\text{eV}$. From Eq. (1.5), it is evident that the magnitude of the ϵ_B determines the HH-LH splitting. For a single QD layer, `L1`, due to large negative value of ϵ_B, the HH and LH band edges will be considerably separated inside the QD region. This will induce dominant HH character in the highest few VB states. As the magnitude of ϵ_B decreases, the HH-LH splitting reduces, increasing the LH component in the VB states. For the `L9` system, the nearly zero magnitude of the ϵ_B around the center of the stack implies that the HH and LH bands will be nearly degenerate around the center of the QD stack. The VB states will therefore be of highly mixed character, consisting of contributions from both the HH, and the LH bands.

Figures 1.26(c) and (d) show the highest two local VB edges, HH and LH, along the [001] direction through the center of the `L1` and `L9` QDs, rspectively. Highly negative biaxial strain in `L1` results in $\sim 152\,\text{meV}$ splitting of HH and LH bands within the QD region (Fig. 1.26(c)). As the biaxial strain around the center of QD stack decreases toward zero, the HH-LH splitting around the center of the stack also decreases to $\sim 74\,\text{meV}$, $\sim 32\,\text{meV}$ (not shown) and $\sim 28\,\text{meV}$ (Fig. 1.26(d)) for the `L3`, `L6` and `L9` QD systems, respectively. As a result, the reduction in the magnitude of biaxial strain favours in larger HH-LH intermixing (lesser separation) as the size of the stack increases.

Since in a QD system, the HH states consist of contributions from p_x and p_y orbitals and the LH states — of p_x, p_y and p_z ones, the TM-mode (which is along the z direction) will only couple to the LH states. The large splitting of the HH-LH bands (see Fig. 1.26(c)) resulting in a weak LH contribution in the `L1` system, therefore, yields a very weak TM_{001} mode (see Figs. 1.24(b) and (c)). Thus, according to Eq. (1.4), the DOP is nearly 1.0 and the polarization response is highly anisotropic. As the size of the QD stack increases, the larger HH-LH intermixing increases LH contribution in the VB states. This results in an increase of TM_{001} mode of optical transitions reducing the anisotropy of DOP (DOP $\rightarrow$0).

According to the optical intensity function calculations (not given), it was found that the increase in the TM_{001} mode only partially helps toward an isotropic polarization response. This is in contrast to a general notion, where it is described that the increase in the TM_{001} mode is mainly responsible for the isotropic polarization. The reason for such understanding is that the previous studies [40,46,47] of the DOP have assumed only one direction for the TE mode. Indeed, PL measurements in Figs. 1.24(d)–(f) show that the TE modes along the [110] and [$\bar{1}$10] have significant anisotropy in the

plane of the QD stack. It was shown by theoretical model that, in fact, a major contribution to achieve isotropic polarization response in these systems stems from a suppressed TE_{110} mode rather than an increased TM_{001} mode.

Indeed, the TE mode is highly anisotropic in the plane of the QD with the magnitudes of the TE_{110} and $TE_{\bar{1}10}$ modes becoming very different as the QD stack size increases. For a single QD system, `L1`, $TE_{110} \approx TE_{\bar{1}10}$, and TM_{001} is very weak. Hence, the measured and calculated DOP is highly anisotropic (close to 1.0) irrespective of the direction for the TE mode. As the QD stack size increases, the TM_{001} mode also increases, partially contributing to reduction in the DOP. However, the TE_{110} mode simultaneously decreases considerably such that for `L6` and `L9` it becomes smaller than the TM_{001} mode. It was proposed that such a drastic decrease in the TE_{110} mode is due to the orientation of hole-wave functions along the $[\bar{1}10]$ direction for the `L6` and `L9` systems.

Hole wavefunction polarization along [110] **and** $[\bar{1}10]$ **axis** Top views of the highest five VB states (`H1`, `H2`, `H3`, `H4` and `H5`) for `L1`, `L3`, `L6` and `L9` QD systems are given in Fig. 1.27. All the five hole wavefunctions for the `L1` system have an almost uniform distribution inside the QD region with nearly symmetric shape. Such symmetry results in approximately equal magnitude of TE mode along the [110] and $[\bar{1}10]$ directions, as evident in the first row of the Fig. 1.27. For the `L3`, `L6` and `L9` QD stacks, the distribution of the hole wavefunctions is clearly oriented along the [110] and $[\bar{1}10]$ directions. Such a symmetry was verified numerically and attributed to the strain and piezoelectric potentials that lower the overall symmetry of the QD system and favor these two directions.

Furthermore, the orientation of the hole wavefunctions determines the magnitude of the TE_{110} and $TE_{\bar{1}10}$ modes, since the lowest electron wave function (see Fig. 1.24(b)) is symmetrically distributed. For `L3`, the hole wavefunctions `H1`, `H2` and `H5` are oriented along the $[\bar{1}10]$ direction, while `H3` and `H4` — along the [110] direction. The orthogonal distributions of the hole wavefunctions in `L3` therefore result in similar [110] and $[\bar{1}10]$ TE modes.

Moreover, all of the highest five hole wavefunctions are polarized along the $[\bar{1}10]$ direction in the cases of the `L6` and `L9` QD systems. This yields a strong reduction of the TE_{110} mode, which becomes smaller than the magnitude of TM_{001} mode. This change in relative magnitude ($^{TE_{110}}/_{TM_{001}}$)

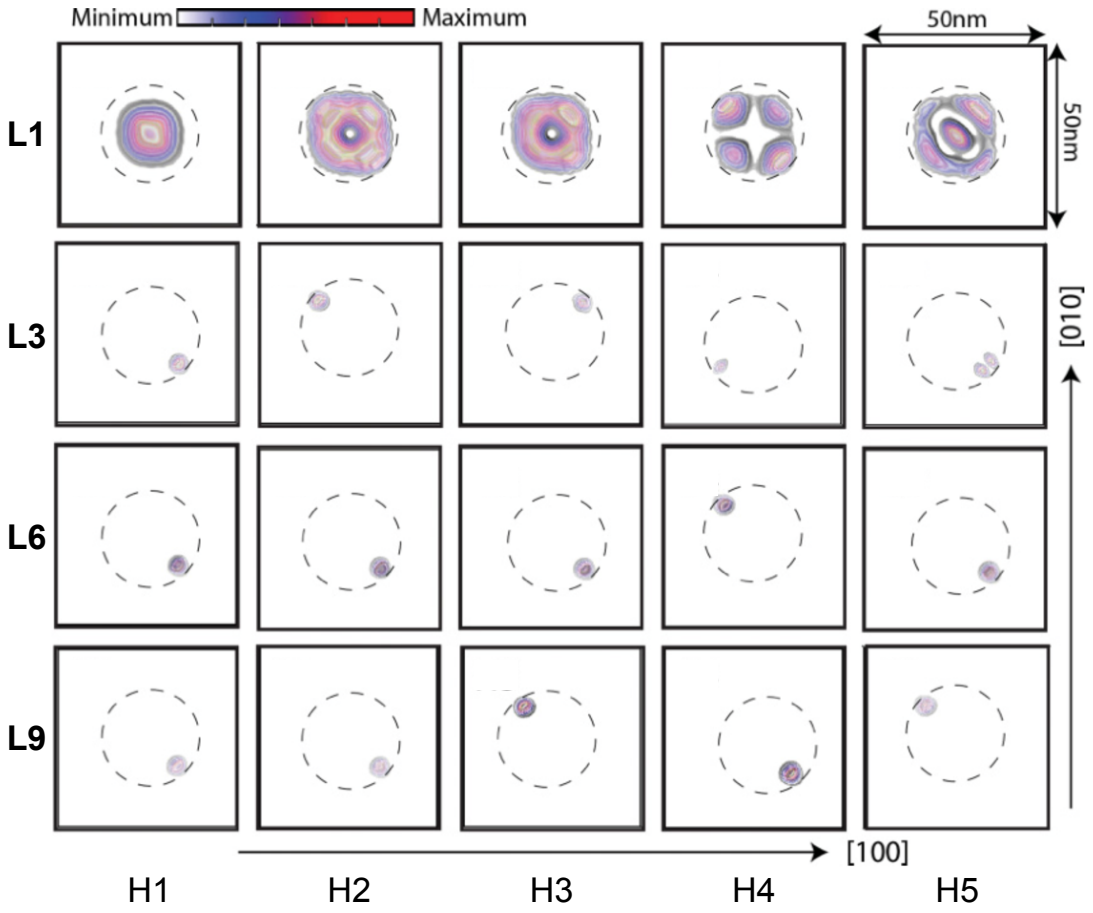

Figure 1.27 Top view of the wavefunctions of the highest five hole states (`H1`, `H2`, `H3`, `H4` and `H5`) for `L1`, `L3`, `L6` and `L9` QD systems. Dashed circles indicate the boundary of the QD bases. [Adapted from Ref. [48].]

results in a flip of sign ($+ \rightarrow -$) for DOP_{110}, as indeed measured in the experiment (see Figs. 1.24(c) and (f)).

It was emphasized that the relative magnitude of the $\mathrm{TE}_{\bar{1}10}$ mode does not reduce as the size of the QD stack is increased. Even for the largest system under study, `L9`, the $\mathrm{TE}_{\bar{1}10}$ mode was much stronger than the TM_{001} mode. Thereby, the PL data for $\mathrm{DOP}_{\bar{1}10}$ still show anisotropy, as illustrated in Fig. 1.24(e). In more detail, PL measurements on `L9` QD system indicate a positive value for the $\mathrm{DOP}_{\bar{1}10}$ ($\mathrm{TE}_{\bar{1}10} > \mathrm{TM}_{001}$) and a negative value for the DOP_{110} ($\mathrm{TE}_{110} < \mathrm{TM}_{001}$).

Finally, it was suggested that the isotropic polarization response demonstrated by the experiment is a result of two factors: (i) increase in the TM_{001} mode due to enhanced HH-LH intermixing and (ii) the reduction of TE_{110} mode due to orientation of holes along the $[\bar{1}10]$ direction.

2 Samples and Experimental

2.1 Quantum Structures Studied

The various type of quantum dot nanostructures studied, including

- ◇ InAs quantum dots (QDs), embedded in GaAs matrix and GaAs/AlAs superlattice (SLs) [stacked dots; dots-in-a-superlattice structures];
- ◇ InAs quantum dots with and without InGaAs cap layer, embedded in GaAs/AlAs quantum well (QW) [dots-in-a-well (or DWELL) structures];
- ◇ InGaAs columnar quantum dots, or quantum rods (QRs), embedded within InGaAs QW, and sandwiched between GaAs barrier layers [QR structures],

represent, as well, the historical path of scientific pursuits in achieving better (in terms of linewidth and intensity), more controllable (taylorable absorption/emission energy) optical response, structural quality (interfaces, purity, stacking, etc.), uniformity (homogeneity) and optical polarization properties of QDs. To improve QD size homogeneity and polarization insensitivity, quantum rod structures were proposed. Here an emphasis is put on the effect of technological conditions (As_2 and As_4 sources used during MBE-growth) on optical properties and electronic structure of ORs.

2.1.1 InAs dots-in-a-superlattice structures

The samples of InAs quantum dot stacks in GaAs matrix and GaAs/AlAs superlattice were MBE-grown by G. Strasser in the Institut für Festkörperelektronik, Technische Universität Wien, Floragasse 7, 1040 Wien, Austria (Univ.Prof. Mag.rer.nat. Dr.rer.nat. Gottfried Strasser group).[1]

The studied QD structures (samples `#469` and `#577`) were grown on a semi-insulating GaAs (001) substrate. Figure 2.1 shows a basic band structure (conduction band) schemes and corresponding active region layout

[1] Websites: http://fke.tuwien.ac.at/; http://zmns.tuwien.ac.at/; http://www.mbelab.at/
E-mail: gottfried.strasser@tuwien.ac.at

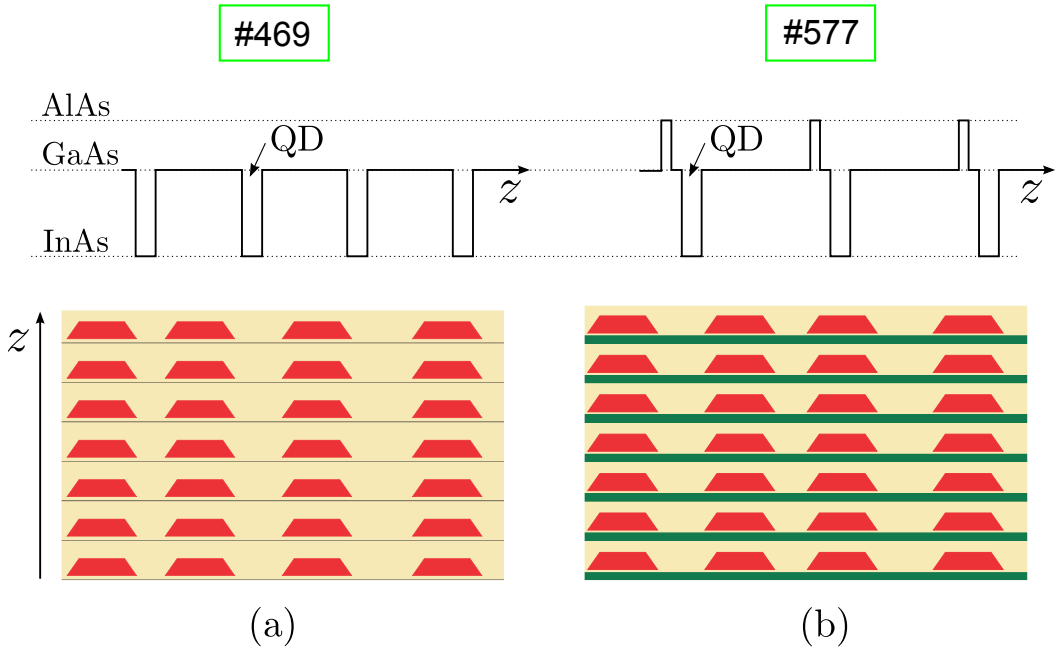

Figure 2.1 Conduction band diagrams (top) and corresponding active region (few periods) layout sketches (bottom) for the stacked dot structures investigated, #469 (a) and #577 (b).

sketches for both stached QD structures investigated. Growth protocol for the InAs QDs embedded into GaAs matrix (sample #496) is given in Table 2.1, whereas that for the nanostructure with InAs QDs embedded into GaAs/AlAs supperlattice (sample #577) — in Table 2.2. Main parameters of both investigated multiple dot samples are summarized in Table 2.3.

The superlattice period for QD structure #577 was designed so that the absorption energies of both #469, and #577 structures would match. After depositing a 650 nm thick Si-doped GaAs layer the superlattice structure is formed. Here, the vertical spacing between subsequent dot layers is small enough to guarantee vertical alignment (stacking) of QDs due to strain minimization.

The #469 multiple dot structure contain 30 stacked layers with InAs QDs embedded in GaAs matrix, and has a period of 10 nm. The #577 multiple dot structure consist of 20 InAs QD stacked layers, embedded in a GaAs/AlAs SL, with a period of 14 nm. In the latter case every dot layer is placed 1 nm apart from AlAs barrier of 1 nm thick. Dots were grown by the Stranski-Krastanow mechanism by depositing two monolayers (MLs) of InAs. Whereas the bottom contact layer (Si: GaAs) was grown at 600 °C, all subsequent layers were deposited at 485 °C in order to avoid Al, Ga and In intermixing. The dots were modulation doped with one electron per QD. Transmission electron microscopy (TEM) was used to control the quality of

Table 2.1 Growth protocol for the InAs/GaAs multiple dot sample #496.

No.	layer (substrate→surface)	thickness (nm)	doping (Si) (cm^{-3})
1.	S.I. GaAs Substrate (001)	508 ± 20 μm	–
2.	Si: GaAs	600	1.5 E18
3.	Si: GaAs	50	3.0 E16
4.	**start loop**: 30×		
	InAs QDs (5.0 E10 dots/cm^{-2})	2 ML	(1 electron/dot)
	GaAs cap	10	
	end loop		
5.	Si: GaAs	50	3.0 E16
6.	Si: GaAs	200	1.5 E18

Table 2.2 Growth protocol for the InAs/GaAs/AlAs multiple dot sample #577.

No.	layer (substrate→surface)	thickness (nm)	doping (Si) (cm^{-3})
1.	S.I. GaAs Substrate (001)	350 ± 20 μm	–
2.	Si: GaAs	600	1.5 E18
3.	Si: GaAs	50	3.0 E16
4.	**start loop**: 20×		
	AlAs	1	
	GaAs	1	
	InAs QDs (5.0 E10 dots/cm^{-2})	2 ML	(1 electron/dot)
	GaAs cap	12	
	end loop		
5.	Si: GaAs	50	3.0 E16
6.	Si: GaAs	150	1.5 E18

Table 2.3 Parameters of the investigated multiple dot samples #496 and #577.

sample	SL period (nm)	InAs QD layers	AlAs barrier width (nm)
#469	10	30	–
#577	14	20	1

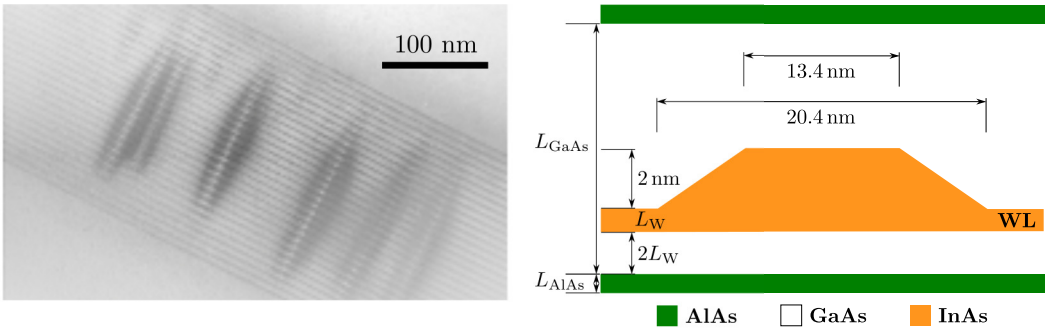

Figure 2.2 Transmission electron microscopy (TEM) of the structure #469, showing vertical stacking of InAs dots (a) and schematic representation of the supercell including the dot and its WL (b). Sample #469: $L_{GaAs} = 10\,nm$, no AlAs layer; Sample #577: $L_{GaAs} = 13\,nm$, $L_{AlAs} = 1\,nm$. $L_W = 0.5\,nm$ is the thickness of InAs WL (scheme reproduced from [6]).

the layer stack and to corroborate the vertical alignment of the InAs dots (Fig. 2.2(a)).

It is well-known that overgrown InAs QDs within GaAs matrix exhibit a flat, lens-like shape with a typical aspect ratio (height to base radius) h/r_0 of 2–3 nm/10 nm, and therefore one can use a geometric simplification of the QD by modeling them as truncated cones. The proposed geometry for a QD supercell is adapted to stacked QD structures under consideration and is presented in Figure 2.2(b) with parameters given in the caption.

As-grown QD active layers, surrounded by 50 nm low-doped (10^{16} cm^{-3}) GaAs layers, were sandwiched between highly n^+-doped ($n \sim 10^{18}$ cm^{-3}) GaAs contact layers. For optical measurements, the top n^+-GaAs layer was etched off to expand surface depletion region into the QD ensemble. Thereby, it is expected to deplete the QDs by the surface potential and to increase the modulation efficiency. Simulations done using G. Snider code reveal dramatic changes in band structure, comparing as-grown and etched QD nanostructures. The effect for the sample #577 is presented in Fig. 2.3.

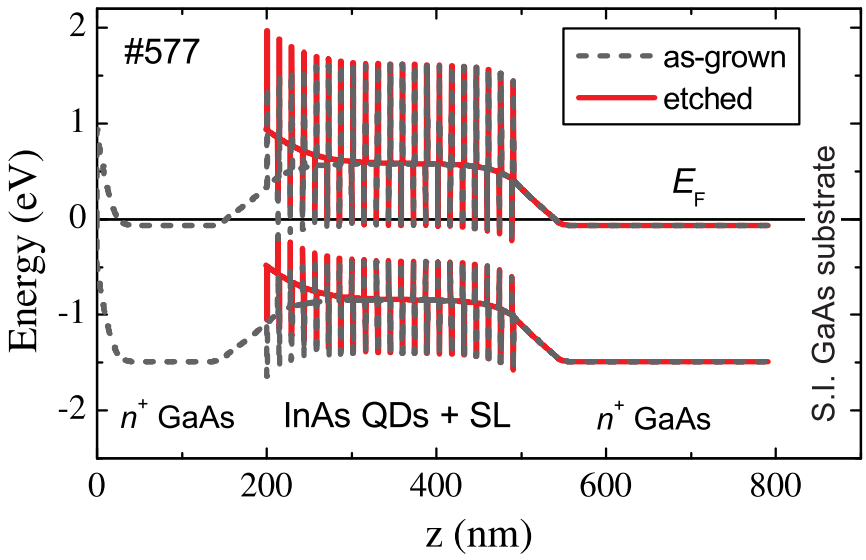

Figure 2.3 Simulation of band diagram for as-grown and etched nanostructures of InAs QDs within GaAs/AlAs SL.

2.1.2 InAs dots-in-a-well structures

The samples of InAs quantum dots with and without InGaAs cap layer, embedded within GaAs/AlAs quantum well, were MBE-grown by L. H. Li in the School of Electronic and Electrical Engineering, University of Leeds, Leeds LS2 9JT, United Kingdom (Prof. Edmund Linfield group).[2]

The quantum dots-in-a-well (DWELL) systems studied is comprised of $N = 10$–15 periods of InAs dots embedded within GaAs/AlAs QW. To investigate the effects of the InGaAs capping layer on optical properties and electronic states of QDs, a set of two DWELL structures — samples `L442` and `L444` — was grown with and without 5 nm-thick InGaAs cap layer, covering SK dots, respectively. Main parameters of both investigated DWELL samples are summarized in Table 2.4. Dots were grown by the Stranski-Krastanow mechanism by depositing 2.4 monolayers (MLs) of InAs. The lenticular self-assembled dots with an aspect ratio of about 0.25 (see Fig. 2.4) were modulation doped with one electron per QD.

The studied DWELL structures (samples `L442` and `L444`) were grown on a semi-insulating GaAs (001) substrate. The whole quantum system is comprised of N periods of dots-in-a-well layers. Here, InAs QDs are embedded asymmetrically within InGaAs/GaAs/AlAs (sample `L442`) or GaAs/AlAs (sample `L444`) quantum well (QW). Figure 2.4 shows a basic band structure (conduction band) schemes, corresponding active region layouts and

[2]Website: http://www.engineering.leeds.ac.uk/electronic/
E-mail: e.h.linfield@leeds.ac.uk

Table 2.4 Parameters of the investigated DWELL samples L442 and L444.

sample	QD density (cm^{-2})	doping (cm^{-2})	InGaAs cap width (nm)
L442	1.7 E10	2 E10	5
L444	3.0 E10	3 E10	–

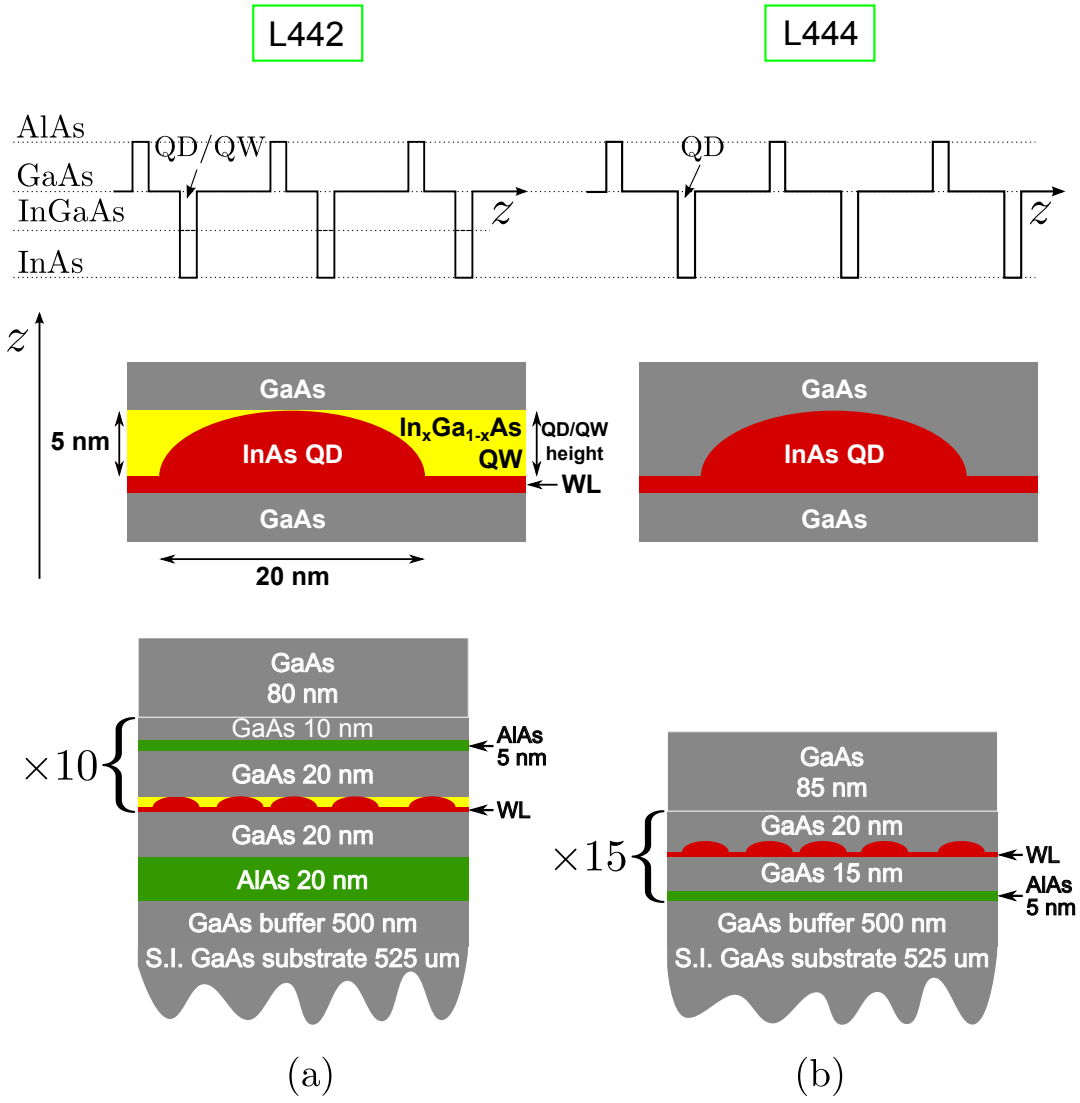

Figure 2.4 Conduction band diagrams (top), active region layouts (middle) and full-sample sketches (bottom) corresponding to the DWELL nanostructures investigated, L442 (a) and L444 (b).

Table 2.5 Growth protocol for the InAs/InGaAs/GaAs/AlAs DWELL structure (sample `L442`). Sheet doping was 2 E10 cm^{-2}.

No.	layer (substrate→surface)	thickness (nm)
1.	S.I. GaAs Substrate (001)	525 μm
2.	GaAs	500
3.	AlAs	20
4.	GaAs	20
5.	**start loop**: 10×	
	InAs QDs (1.7 E10 dots/cm^{-2})	2.4 ML
	$In_xGa_{1-x}As$ ($x = 0.15$) cap	5
	GaAs	20
	AlAs	5
	GaAs	10
	end loop	
6.	GaAs	80

full-sample sketches for both DWELL structures investigated. Growth protocol for the capped InAs/InGaAs/GaAs/AlAs DWELL structure (sample `L442`) is given in Table 2.5, whereas that for the DWELL nanostructure with uncapped InAs QDs — InAs/GaAs/AlAs (sample `L444`) — in Table 2.6.

2.1.3 Epitaxial InGaAs quantum rod structures

The samples of InGaAs columnar quantum dots, or *so called* quantum rods (QRs), embedded within InGaAs quantum well were MBE-grown by L. H. Li in the School of Electronic and Electrical Engineering, University of Leeds, Leeds LS2 9JT, United Kingdom (Prof. Edmund Linfield group).

The use of QDs as active elements for semiconductor optical amplifiers (SOAs) requires both for an improvement of QD homogeneity, and for polarization insensitivity. To modify polarization dependent optical gain, quantum rods were realized by growing Stranski-Krastanow (SK) InAs QD layer followed by a short period InAs/GaAs superlattice [7]. A growth interruption (GI) after each InAs layer was applied in order to make the QD size more uniform. As a result, the active region of such structures consists of vertically oriented QRs immersed into a 2-D quantum well (see

Table 2.6 Growth protocol for the InAs/GaAs/AlAs DWELL structure (sample `L444`). Sheet doping was 3 E10 cm^{-2}.

No.	layer (substrate→surface)	thickness (nm)
1.	S.I. GaAs Substrate (001)	525 μm
2.	GaAs	500
3.	**start loop**: 15×	
	AlAs	5
	GaAs	15
	InAs QDs (3.0 E10 dots/cm^{-2})	2.4 ML
	GaAs	20
	end loop	
4.	GaAs	85

cross-sectional TEM image in Fig. 2.5(a)). Plan-view TEM micrograph (Fig. 2.5(b)), however, shows that these nanorods do not possess cylindrical, or cubic symmetry (contrary to one's intuitive judgment). Instead, (001)-plane TEM image presents a rhombus-like plan-view of QRs. From the plan-view, the size of the QRs is very uniform and the dot density is about $1.7 \times 10^{10}\,\mathrm{cm}^{-2}$. The QRs have a parallelogram shape with the diagonals exactly along the [110] and [$0\bar{1}1$] directions of the growth plane. The length of these two diagonals is anisotropic and the average ratio between long and short diagonals is 1.22 with a standard deviation of 0.05. Such a shape anisotropy of InGaAs QRs suggested an optical anisotropy to be considered.

All of the samples studied were epitaxially grown on (001)-oriented GaAs substrate by using solid-source molecular beam epitaxy. Full-sample layout sketch is given in Fig. 2.5(c). After a GaAs buffer layer, 200 nm thick $Al_{0.2}Ga_{0.8}As$ and 100 nm thick GaAs layers were grown. The self-assembled QRs were then formed by first depositing 1.8 monolayers (MLs) of InAs, which relaxed under SK conditions into a QD seed layer, and then a short period SL of alternating GaAs (3 ML) and InAs (0.64 ML) epilayers. A 100 nm thick GaAs capping layer completed the structure. The GaAs buffer layer was grown at 600 °C, whereas all the subsequent layers were grown at lower temperature. The growth rates of GaAs and InAs were 0.7 and 0.1 ML/s, respectively. Arsenic beam equivalent pressure (As overpressure)

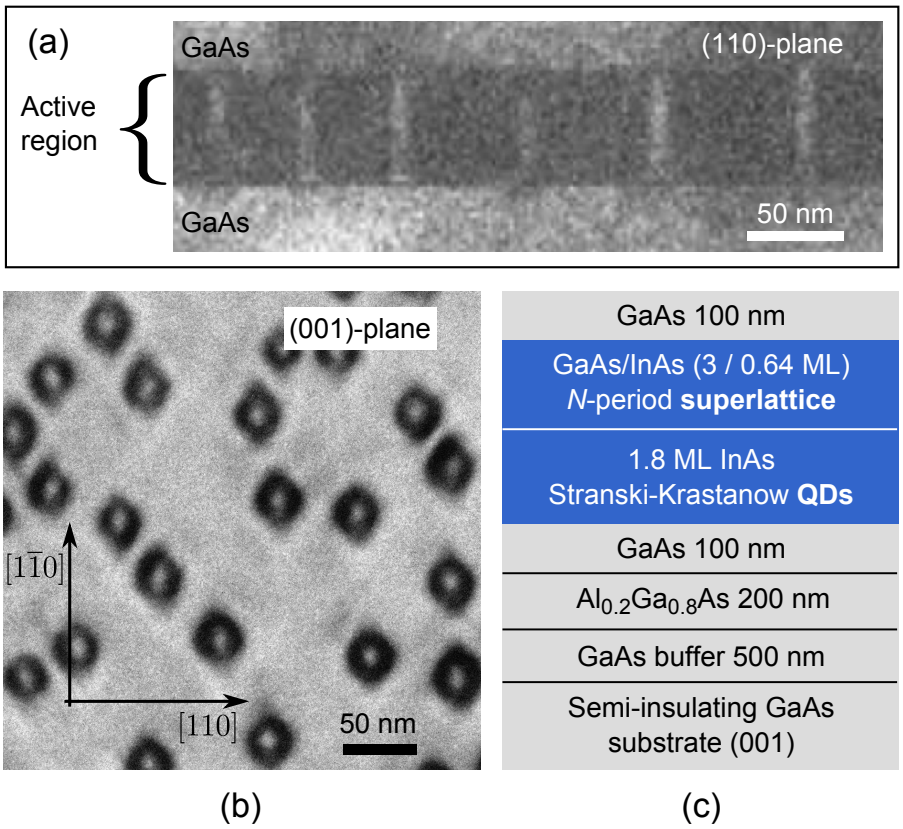

Figure 2.5 Cross-sectional (110)-plane TEM image (a) of nanorod structures, grown by MBE. The whole quantum region consists of vertically oriented InGaAs QRs, surrounded by InGaAs QW, and sandwiched between GaAs layers. In-plane view of the structure [across (001)-plane] with QRs having assymetric rhombus-like shape (b), suggesting an optical anisotropy to be considered. Full-sample layout sketch with active region picked out (c). QRs studied rely on a two step (QD+SL) growing proccess.

and number of SL periods were varied for each case. The growth temperatures were calibrated using reflection high energy electron diffraction. The temperature required to remove the surface oxide on the GaAs substrate, and the temperature at which the GaAs surface reconstruction switches from (2×4) to $c(4 \times 4)$ were determined as references.

The QD evolution was monitored *in situ* by reflection high-energy electron diffraction (RHEED). After growth of the 1.8 ML InAs QD layer, characteristic chevrons along the $[0\bar{1}1]$ direction are observed. They evolve into short and streaky diffraction rods during the growth of the 3 ML GaAs layers. When the subsequent InAs layers are grown, the RHEED pattern changed back and during GI = 5 s clear chevrons redevelop. Generally, the redeveloped characteristic chevron is a very important hint in obtaining a high quality material.

From the observations of the cross-sectional images, the whole structure consists of two parts, i.e., the QRs and a 2-D layer around them. The 2-D

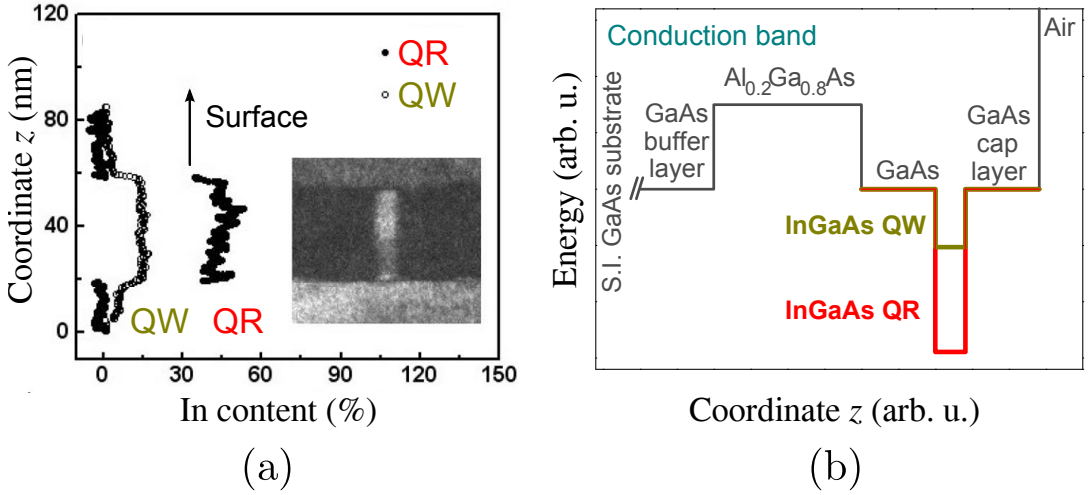

Figure 2.6 In composition profiles across the center of the QR and QW layer (a). It was estimated that QRs have high In content – about 45%, whereas In percent within QW is only about 15%. Inset: Magnified dark-field cross-sectional TEM micrograph in (110)-plane of the QR sample including a 35-period SL. Conduction band diagram for QR structures studied is given in (b).

layer consists of an InGaAs QW with an average thickness of about 20 nm. Its composition is uniform and has an average In percentage value of about 16%. The achieved highly uniform In composition across the QW is mainly due to the In-Ga intermixing during the growth. Therefore, the whole quantum structure comprises of InGaAs QRs within InGaAs QW. Although the nanorods are slightly higher than the QW, the interfaces between GaAs and the QW layer are sharp and planar, no dislocation and QD plastic relaxation were observed, indicating an excellent material quality.

Although, the In composition across the center of the QRs is not uniform and a vertical composition modulation was observed [7, 37, 41, 42], the obtained unique shape of the QRs is very different from that of the conventional SK growth of QDs, indicating the feasibility of artificial shape engineering of QDs. The in-plane strain distribution created by the first QD layer favors In incorporation on top of QDs, thereby resulting in an In-rich column-shaped nanostructure. As a result, QRs with an increased In compositional contrast $x_{\mathrm{QR}}/x_{\text{2-D}} > 3$, along with a large aspect ratio of up to 4.1, were obtained (see Fig. 2.6(a)). The In composition across the center of the QRs has an average value of about 45% with a vertical composition fluctuation of about 10%. No vertical short-range composition modulation related to the cycled deposition mode was observed, indicating that In composition of the QR is homogeneous [49]. This should be compared to the growth of closely stacked InAs QDs, where distinct InAs islands are observed.

Table 2.7 Parameters of the investigated InGaAs QR samples L396, L397, L398, L399, L400 and L402.

sample	SL periods, N	QR height (nm)	As source
L396	20	32	As_4
L397	35	41	As_4
L398	10	20	As_2
L399	10	20	As_4
L400	35	41	As_2
L402	20	32	As_2

The initial highest In composition at the bottom of the QR is related to the In-rich seed QDs. The in-plane diameter of the QR is about 10 nm, which is set by the diameter of the seed QD layer and can be controlled by varying the growth parameters such as InAs coverage, GI, growth temperature, InAs growth rate, and arsenic overpressure, as is well known in SK growth mode. The height of the QR was tuned by varying the number of SL periods. The aspect ratios of the QR structures studied — 2, 3.2 and 4.1 — are extremely large, and it is impossible to achieve for the conventional SK growth of QDs. Since, geometrical and material parameters are set, one can draw band diagram of the heterostructure. Conduction band diagram for QR structures studied are presented in Fig. 2.6(b)

To investigate the effects of the As source on the optical properties of the QR structures, two sets of QR samples were grown with SL periods $N = 10$, 20, and 35; these are designated QR10, QR20, and QR35, respectively. Both sets of structures were grown with As_2 and As_4 sources, using the same growth conditions. The main parameters of the investigated InGaAs QR structures (samples L396, L397, L398, L399, L400 and L402) are given in Table 2.7.

The height of the QRs is explicitly controlled by d_{InAs} and d_{GaAs}, as well as by the number of periods (N) in the SL; the indium content of the QW, x_{QW}, can be roughly estimated by $d_{\mathrm{InAs}}/(d_{\mathrm{InAs}} + d_{\mathrm{GaAs}})$, where, d_{InAs} and d_{GaAs} are thicknesses of InAs and GaAs layers in the SL, respectively. On this basis, we estimate the height of the QRs with $N = 10$, 20, and 35 period SLs to be 20, 32, and 41 nm, respectively, and the indium content (x_{QW}) to be ≈ 0.16 (see Fig. 2.7). Further details about the growth of the

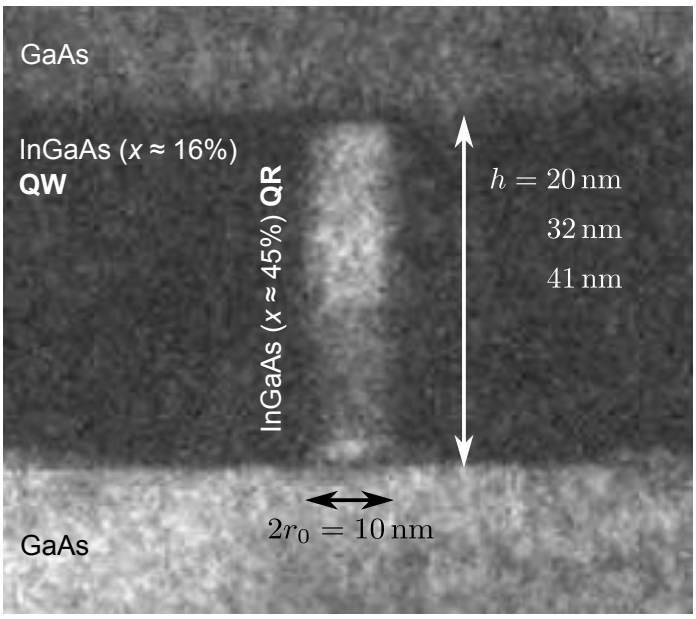

Figure 2.7 Cross-sectional (110)-plane TEM image showing three different geometries of QR structures studied. In-rich InGaAs nanorods are embedded within InGaAs QW of lesser In content and both are sandwiched between GaAs cladding layers. QRs are different in heigths and MBE-grown with different arsenic sources — As_2 and As_4.

QR structures and the precise determination of the indium content of x_{QW} and x_{QR} can be found elsewhere [7, 42].

2.2 Experimental Techniques Employed

We have employed modulated reflectance techniques to study the optical interband transitions of quantum dot (QD) and rod (QR) heterostructures at room (300 K) and liquid nitrogen (80 K) temperatures. Also photoluminescence (PL) spectroscopy was used for comparison and analysis of the spectra. PL measurements were performed in 3.6–300 K temperature range. Various lasers as the modulation and excitation sources and photodeterctors along with a lock-in system were employed for experimental measurements.

2.2.1 Modulated reflectance spectroscopy

We have mainly employed modulated reflectance techniques — photoreflectance and contactless electroreflectance — in order to explore the optical interband transitions of QD structures at 300 K and 80 K temperatures. Indeed, by using modulation spectroscopy methods, one can directly measure the derivate of the spectra and thus obtain very sharp transition peaks. These approaches were found as well-suitable for optical characterization of nanostructures studied with perfect sensitivity even at room temperature. All the measurements were performed in Semiconductor Optics Laboratory (Semiconductor Physics Institute of Center for Physical Sciences and Technology; SPI/CPST).

Photoreflectance

Photo-modulated reflectance or photoreflectance (PR) experimental spectra of nanostructures studied were measured using setup, sketched in Fig. 2.8(a). Two optical beam lines — probe and pump (modulating) — are present in the PR setup. Quartz-tungsten-halogen lamp (12 V; 100 W) was used as a probe beam (white light) source, whereas various laser sources [He-Ne: 632.8 nm (red; 1.96 eV; 5 mW) and diode-pumped solid-state (DPSS): 532 nm (green; 2.33 eV; 200 mW) and 473 nm (blue; 2.62 eV, 15 mW)] together with optical chopper (SR-540, Stanford Research) were employed in order to photo-modulate sample (excite electrons from valence band far above its bandgap energy). Pump beam chopping frequency Ω_m in a range of 0.5 Hz up to 4 kHz was used. It is important to note, that the probe beam dispersed by a step-motor driven monochromator (SPM-2; Carl-Zeiss, Jena, Germany) and focused on the sample should be fully covered by the pump beam (the area of a probe beam on a sample surface should be smaller than

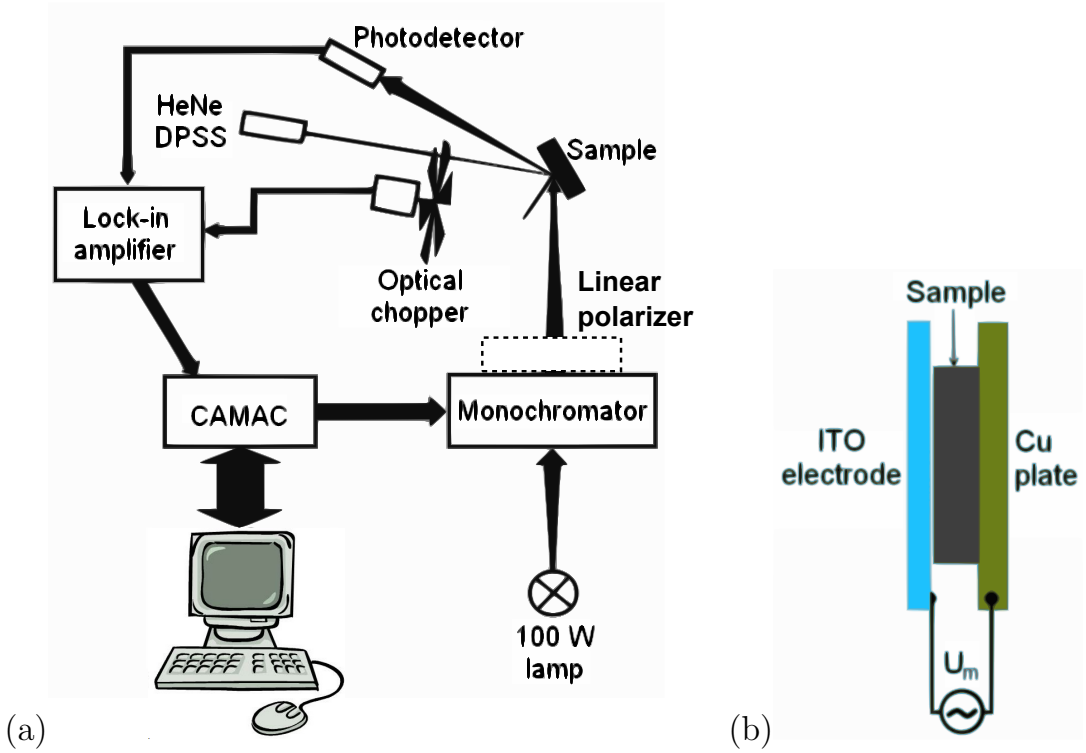

Figure 2.8 Schemes of the PR setup (a) and a condenser-like CER system (b). In CER experiment modulating electric field U_m was applied on a sample via transparent (ITO) and metal electrodes. In optical anisotropy experiments linear polarizer was used.

pump beam). For a light, which reflected from the sample, detection we used a thermoelectrically cooled (TEC; with a Peltier element) InGaAs or low noise Si *p-i-n* diode detectors. The light striking/reflected into detector contains/carries two different signals — DC component $I_0\,R$ and modulated AC signal $I_0\,\Delta R$. A very sensitive phase-locked (or phase-sensitive) detection of a modulated (AC) signal from photodetector output was analysed by a lock-in amplifier (Ametek DSP-7270, Stanford Research SR-830, Unipan 232-B), connected with optical chopper that provided reference (REF) input (at Ω_m frequency). Lock-in amplifier enables a detection of a pure modulated AC component $I_0\,\Delta R$. A signal of interest, $\Delta R/R$, can be found by various normalization procedures, e.g., one can perform two separate measurements of $I_0\,\Delta R$ and $I_0\,R$ signals and then simply divide them. Another way to get a needed quantity $\Delta R/R$ can be accompolished by driving a photodetector amplification electronically, forcing the DC signal $I_0\,R$ to be constant. This procedure yields $\Delta R/R$ signal with DC component being at a constant level over all spectral range.

The signal (output) from the lock-in amplifier is connected to the personal computer via CAMAC modular system. Computer program LAB-

ORA (written in C-code) allowed a precise control of the monochromator scanning positions (by driving step-motor corresponding to $\leq$1 meV spectral steps) and collected the measurement data (lock-in recovered signal). The PR spectra were measured in-phase with the modulating field, although both components (X and Y) constituting the total signal (R) were usually registered (instead of $R = \sqrt{X^2 + Y^2}$ and phase θ).

It is worth to noting, that the use of various lasers is important, when considering the penetration depth of the light into sample. Indeed, the penetration depth is low for high-energy pump beam and, therefore, capped quantum structures are usually more effectively modulated, when exiting with a laser of longer wavelength, i.e. red laser penetrates deeper into the sample than blue one. One should note, that the bandgap energy of a material changes with a temperature and, therefore, to efectivelly study the optical transitions low-temperature measurements were carried out. For this purpose, we used a cryostat, inside which a sample was mounted on a cold head, and by filling in liquid nitrogen, the lattice temperature was kept at 80 K during measurements.

Contactless electroreflectance

Contactless electroreflectance (CER) measurements were carried out using the similar setup as that for PR experiment (Fig. 2.8(a)). Sample was mounted on a copper (Cu) plate and covered with a transparent ITO (indium-tin-oxide) glass electrode [50]. ITO was separated from the sample by a thin dielectric film (e.g., piece of paper). As a result, a condenser-like system was build (see Fig. 2.8(b)) and to provide modulating field, both ITO and Cu electrodes were connected to the high-voltage generator. Typically, a sinusoidal AC voltage of 1.3 kHz frequency and of U_m = 300–500 V peak-to-peak amplitude was being applied to the top transparent electrode. Measurements were performed down to liquid nitrogen (80 K) temperature with and without optical bias (constant unchopped laser exitation).

2.2.2 Photoluminescence

In experimental study of quantum nanostuctures, we have also used photoluminescence (PL) spectroscopy jointly with modulated reflectance techniques to analyse interband optical transitions, occuring within quantum dots and quantum rods.

Photoluminescence spectroscopy is a contactless, versatile, non-destructive

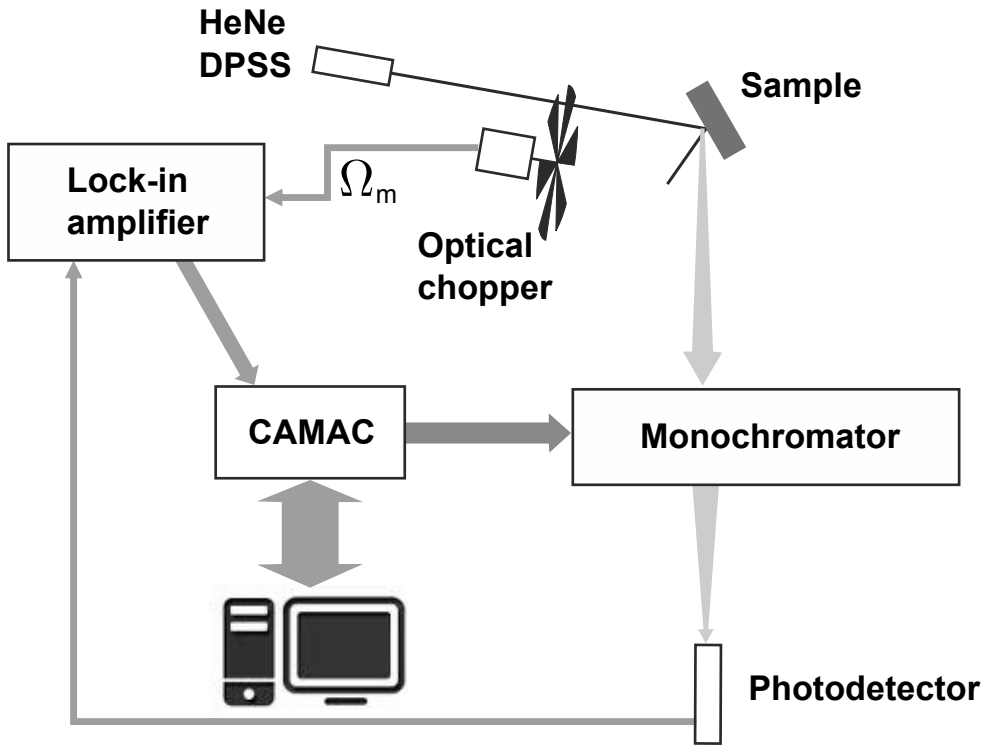

Figure 2.9 Principal scheme of the PL setup.

method of probing the electronic structure of a material. A sketch of a principal PL setup is given in Fig. 2.9. Typically, a laser beam impinges a sample, where it is absorbed. The excess energy brought to the material can be dissipated through the emission of light, or luminescence. As the excitation of the sample is performed by light, this luminescence is called "photoluminescence". Photoluminescence is thus the spontaneous emission of light from a material under optical excitation. This light can be collected and analyzed spectrally, spatially and also temporally. However, PL spectroscopy, athough often used as a main tool for optical characterization of quantum structures, has important shortcomings. Indeed, PL method allows to examine only lowest energy interband transtions, involving electron and hole ground-states (transition between lowest conduction band and highest valence band states, 11H), and sometimes also one or two excited-states (e.g., 22H, 11L). Moreover, PL lines are broad (especially for QDs, indicating Gaussian dispersion) and hence overlaping strongly, making it hard to distinguish between separate transition energies. Therefore, by using PL, one cannot investigate optical transitions between higher energy bound states, as well as numerous continuum/unbound states (which can be easily resolved by PR and CER methods) present in QD structures.

In fact, it is possible to overcome the limitations of PL and study the higher-energy optical transitions by means of photoluminescence excitation

spectroscopy (PLE). In this specific type of PL the detection is fixed on the recombination line of the semiconductor system while the excitation laser energy is tuned. When it matches the energy of an optical transition in the absorption spectrum of the semiconductor, the PL signal increases. PLE is thus analogous to absorption spectroscopy, and identical to it in the specific case where nonradiative relaxation processes are negligible. This technique is often used in the case of semiconductor heterostructures with a low absorption probability, less than 1%, where standard direct absorption spectroscopy is hard to implement.

In semiconductor systems, the most common radiative transition is between states in the conduction and valence bands, with the energy difference being known as the bandgap, E_{g}. During a PL spectroscopy experiment, excitation is provided by laser light with an energy much larger than the optical bandgap. The photo-excited carriers (electrons and holes) relax toward their respective band edges and recombine by emitting light at the energy of the bandgap. Moreover, radiative transitions in semiconductors may also involve localized defects or impurity levels. In that case, the analysis of the PL spectrum leads to the identification of specific defects or impurities, and the magnitude of the PL signal allows determining their concentration.

The recombination of the photo-excited carriers can involve both radiative and nonradiative processes. The respective rates of radiative and nonradiative recombination can be estimated from a careful analysis of the temperature variation of the PL intensity and PL decay time. In semiconductor systems like quantum wells or quantum dots, the photoluminescence quantum yield is approximately constant up to temperatures of about 50–70 K. At higher temperatures nonradiative recombination channels are activated and the PL intensity decreases exponentially. Apart the advantageous simplification of the underlying physics, low temperatures appear unavoidable for the optical study of semiconductor-based nanostructures.

In Semiconductor Optics Laboratory (SPI/CPST) we have measured PL for all the nanostructures studied at room (300 K) and liquid nitrogen (80 K) temperatures. Aditionally, in Semiconductor Compound Laboratory (SPI/CPST), PL study was carried out on QD stack in superlattice structures in the 3.6–300 K temperature range.

3 Optical Properties of Quantum Dot Structures

In this Chapter, the experimental data along with calculations carried out for the analysis and interpretation of the spectra for different quantum dot (QD) nanostructures, including

- ◇ InAs quantum dots (QDs), embedded in GaAs matrix and GaAs/AlAs superlattice [stacked dots; dots-in-a-superlattice structures],
- ◇ InAs quantum dots with and without InGaAs cap layers, embedded within GaAs/AlAs QWs [dots-in-a-well (or DWELL) structures],
- ◇ InGaAs columnar quantum dots, or quantum rods (QRs), embedded within InGaAs QW, and sandwithed between GaAs barrier layers [quantum rod structures],

is presented in detail.

To optimize operation of such novel nanostructures indended for advanced micro- and opto-electronic applications, one need to know their optical properties and electronic structure. The information needed can be obtained by modulated reflectance spectroscopy, in particular, by photoreflectance (PR) and contactless electroreflectance (CER). These methods along with photoluminescence (PL) have been shown to be efficient and successful for characterization of nanostructures.

To determine the optical transition energies and broadening parameters from the recorded PR/CER features, spectra were analyzed using Lorentzian-type functions [29, 30, 51, 52]

$$\Delta R/R = \mathrm{Re}\Big[C\, e^{\mathrm{i}\theta}(E - E_{\mathrm{ex}} + \mathrm{i}\Gamma)^{-m}\Big], \tag{3.1}$$

where C, θ, E_{ex} and Γ are the amplitude, phase, energy and broadening parameter of the spectral line, respectively. A value of $m = 3$ was used in calculations. It should be noted that in this case the expression (3.1) represents reasonably well the first derivative of an excitonic dielectric function

with a Gaussian absorption profile [53], and is appropriate for quantum systems with inhomogeneously broadened energy levels.

The modulus of individual PR/CER resonances (individual optical transitions) were evaluated from fitting the PR/CER spectra according to [54]

$$|\Delta\rho(E)| = \frac{C}{\left[(E - E_{\mathrm{ex}})^2 + \Gamma^2)^{m/2}\right]}. \tag{3.2}$$

Samples were experimentally investigated mainly at room (300 K) and liquid nitrogen (80 K) temperatures. All the measurements were performed in Semiconductor Optics Laboratory (Semiconductor Physics institute of Center for Physical Sciences and Technology; SPI/CPST). Aditionally, in Semiconductor Compound Laboratory (SPI/CPST), PL study was carried out on dots-in-a-superlattice structures in the 3.6–300 K temperature range.

Energy spectra calculations for the nanostructures studied were performed within the envelope function (effective mass) approximation, using nextnano^3 software.[1]

3.1 Energy Spectrum of InAs Quantum Dots in GaAs/AlAs Superlattice

Vertically stacked quantum dots (QDs) embedded in a two-dimensional superlattices (SL) are very attractive for developing of the infrared photodetectors with improved operation. In these devices the transition energies between the dot energy levels and the extended states of the SL can be adjusted by the period of the SL as well as by changing the growth conditions of the dots [6]. Such photodetector scheme was realized recently by embedding the vertically stacked InAs QDs into a GaAs/AlAs SL [3]. For deeper elaboration and forthcoming design of new structures the knowledge about optical and electronic properties of QD and wetting layer (WL) is essential.

In this Section, vertically stacked InAs quantum dot (QD) superlattices (SLs) with and without AlAs barriers are examined by the modulated reflectance and photoluminescence spectroscopies. The interband transitions corresponding to the QD, wetting layer (WL) and InAs/GaAs/AlAs SL have been identified. While previous works on determining electronic structure

[1] nextnano^3, next generation 3-D nanodevice simulator.
Website: http://www.nextnano.de/nextnano3

of InAs/GaAs/AlAs QD/SL have been primarily focused on intersublevel transitions in InAs QDs with little emphasis on the wetting layer (WL) properties [3–6], here attention has been paid mainly to the optical transitions in the WL-SL system formed by InAs WL and GaAs/AlAs SL. Modulated reflectance measurements were performed at 90 K and 300 K temperatures, while PL spectra were measured in the temperature range of 3.6–300 K.

Experimental data and numerical calculations show that blue-shifts and enhancement in intensity of WL-related optical transitions in InAs/GaAs/AlAs SL originate mainly due to off-center position of the QD layers in the wells. Furthermore, the QD size and WL thickness variation across the stacks is revealed and discussed.

3.1.1 Full optical view of dots-in-a-superlattice structures

Figure 3.1 shows the CER spectrum for the sample `#469` (upper curve) as well as CER (lower curve) and PR (middle curve) spectra for the sample `#577`, all measured at room temperature. Also, the PL spectra for both samples are shown for comparison. As one can see in modulated reflectance spectra, three major sets of spectral features, related to various optical transitions in the multiple QD structures, can be identified. *Firstly*, the features in the high photon energy region of 1.42–1.7 eV originate from the GaAs buffer layers and (samples `#469` and `#577`) InAs/GaAs/AlAs SL (samples `#577`). *Secondly*, the features observed in the spectral region just below the band gap of GaAs (1.42 eV) can be attributed to the optical transitions in the WL. *Finally*, in the low-energy region of 0.9–1.3 eV the PR and CER spectra exhibit several broadened peculiarities, labeled as `QD1`–`QD3`, which are related to the interband optical transitions in InAs QDs. This assignment is corroborated by PL data for interband ground-state transitions `QD1` only, however. The energies (indicated by arrows) and broadening parameters of optical transitions were determined from the fitting (solid curves) of the spectra to the first derivative of a Gaussian-type function. This line-shape model takes into account the inhomogeneous broadening [29, 30] related to the size fluctuations in QDs and the varying thickness of WL.

3.1.2 QD-related optical transitions

As can be seen in Fig. 3.1, low photon energy lines `QD1` (1.002 eV and 1.052 eV for the samples `#469` and `#577`, respectively) are located at the maxima of the broad PL bands and therefore correspond to the ground-

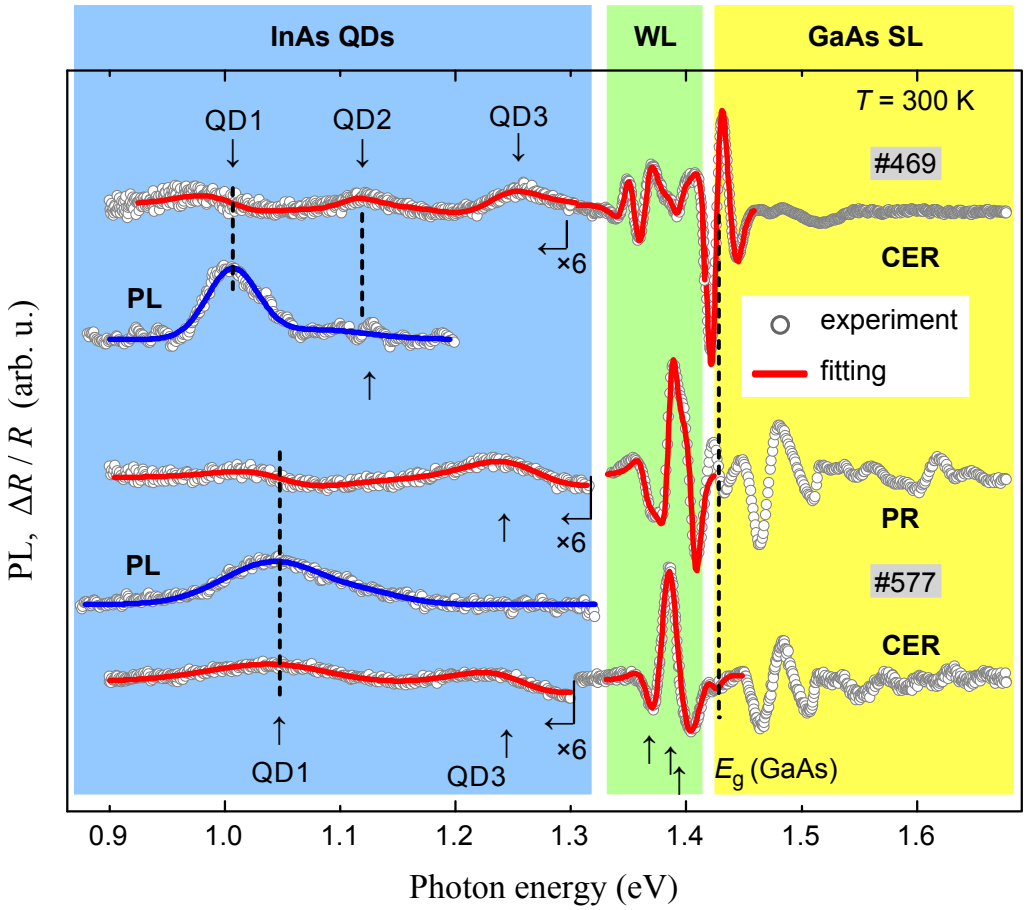

Figure 3.1 Room temperature CER spectrum for the InAs/GaAs QD structure #469 (uppermost curve), as well as PR and CER spectra for the InAs/GaAs/AlAs QD structure #577 (middle and lowermost curves). The arrows indicate the transition energies, estimated from the line shape analysis of modulated reflectivity spectra. PL spectra for the samples studied are also shown for comparison. Different background colors (shades of grey) signify three major sets of spectral regions.

state transitions in the QDs. Note, that for the sample #577 with AlAs barrier layers, PL peak and QD1 line are blue-shifted by ≈ 50 meV as compared with those from the sample #469 without AlAs barriers. The blueshift of the QD1 feature for #577 sample should not be due to different size distribution because the growth conditions of QDs in both samples were similar. Instead, the blue-shift of the QD1 feature for the sample #577 should be attributed to the QD energy level modification by the AlAs barrier layers [26]. The second CER line, QD2 (1.111 eV), for the sample #469 is close to the energy (1.08 eV) of high energy shoulder in PL spectrum and should be related to the excited-state transitions. Unfortunately, QD2 signature cannot be clearly resolved in the PR and CER spectra for the #577 nanostructure. Most probably, the aforesaid inhomogeneous broadening obscures an expected QD2 feature for this sample, because the average QD size changes across the stacks. The origin of the highest energy QD3 lines in modulated reflectance spectra is less evident. Measured spectral positions, 1.237 eV and 1.258 eV for the samples #469 and #577, respectively, suggest that they cannot be related to the higher order excited-state transitions of a single family of QD sizes. Instead, QD3 peak could be a result of ground-state transitions from QDs having significantly smaller size. Indeed, such small-sized QDs are expected to compose at the very initial growth stage of stacked QD layers by depositing 2 ML of InAs [55]. This is consistent with the transmission electron microscopy (TEM) obtained pictures for the studied QD structures in Refs. [3, 5].

Energy spectra calculations of InAs QD in GaAs matrix

In order to get deeper insight into electronic structure and optical properties of the dots-in-a-superlattice nanostuctures, the simulations of a strained InAs/GaAs QW were carried out by using nextnano^3 software. A fully 3-D QD system approach was considered, making use of the effective mass (or envelope function) approximation. The energy levels obtained for a lens-like dot with geometrical parameters — height $d = 3$ nm and base radius $r_0 = 12$ nm — are given in the Fig. 3.2. The energy values obtained (experimentally derived) for interband bound-state transitions are QD1 = 1.03 eV (1.002 eV), QD2 = 1.1 eV (1.111 eV) and QD3 = 1.2 eV (1.237 eV). All the calculated transitions obey Henry's selection rule, $n = n'$. Six electron and six hevy-hole eigenstates in InAs/GaAs QD along with InAs/GaAs wetting layer (WL) quantum well eigenvalues of electrons ($\mathtt{e}_{\mathrm{WL}}$) and heavy holes ($\mathtt{hh}_{\mathrm{WL}}$) were calculated. Moreover, the top view of the electron and heavy-

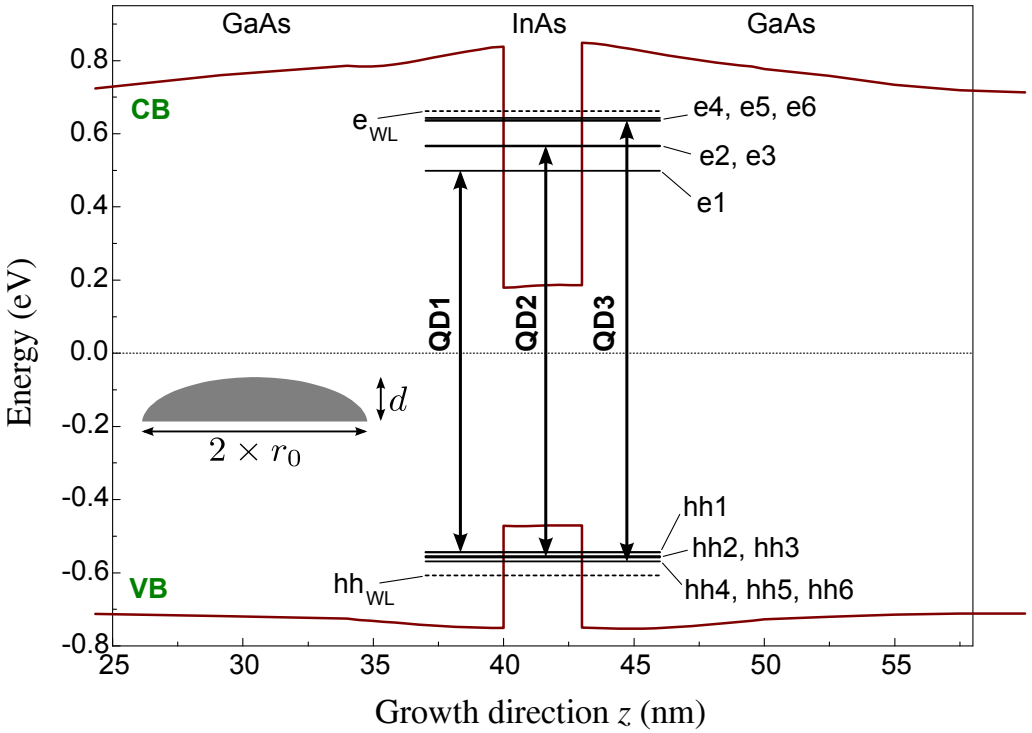

Figure 3.2 Potential profile along the growth direction (001) and eigenvalues (solid lines) of both electrons (`e1`–`e6`), and heavy holes (`hh1`–`hh6`), calculated for a lens-like ($d = 3\,\text{nm}$, $r_0 = 12\,\text{nm}$) InAs QD, embedded into GaAs matrix. Three lowest energy interband optical transitions are denoted by `QD1`, `QD2` and `QD3`. Aditionally, InAs/GaAs wetting layer (WL) quantum well eigenvalues of electrons ($\mathtt{e}_{\text{WL}}$) and heavy holes ($\mathtt{hh}_{\text{WL}}$) are given (in dashed lines). InAs WL thickness of 0.56 nm was used in calculations, performed under 3-D effective mass approximation by nextnano[3] simulation software.

hole wavefunctions for corresponding bound QD states were found. The squared electron and heavy-hole wavefunctions are illustrated in Figs. 3.3 and 3.4, respectively.

Photoluminescence under variable-λ excitation

In order to elaborate the formation of different-size QD ensembles across the QD stacks, a comparison of optical transition intensities in CER and PR spectra was done. Moreover, a variable-pump wavelength (variable-λ excitation) PL technique for this purpose was applied.

As it was stated previously, the origin of the highest energy `QD3` lines in modulated reflectance spectra is less evident (see Fig. 3.1). Their spectral positions, suggest that they should be not due to the excited states of a single family of QD sizes, but rather a result of the ground state transitions from QDs having significantly smaller size. Indeed, such small QDs are expected to compose at the very initial growth stage of stacked QD layers.

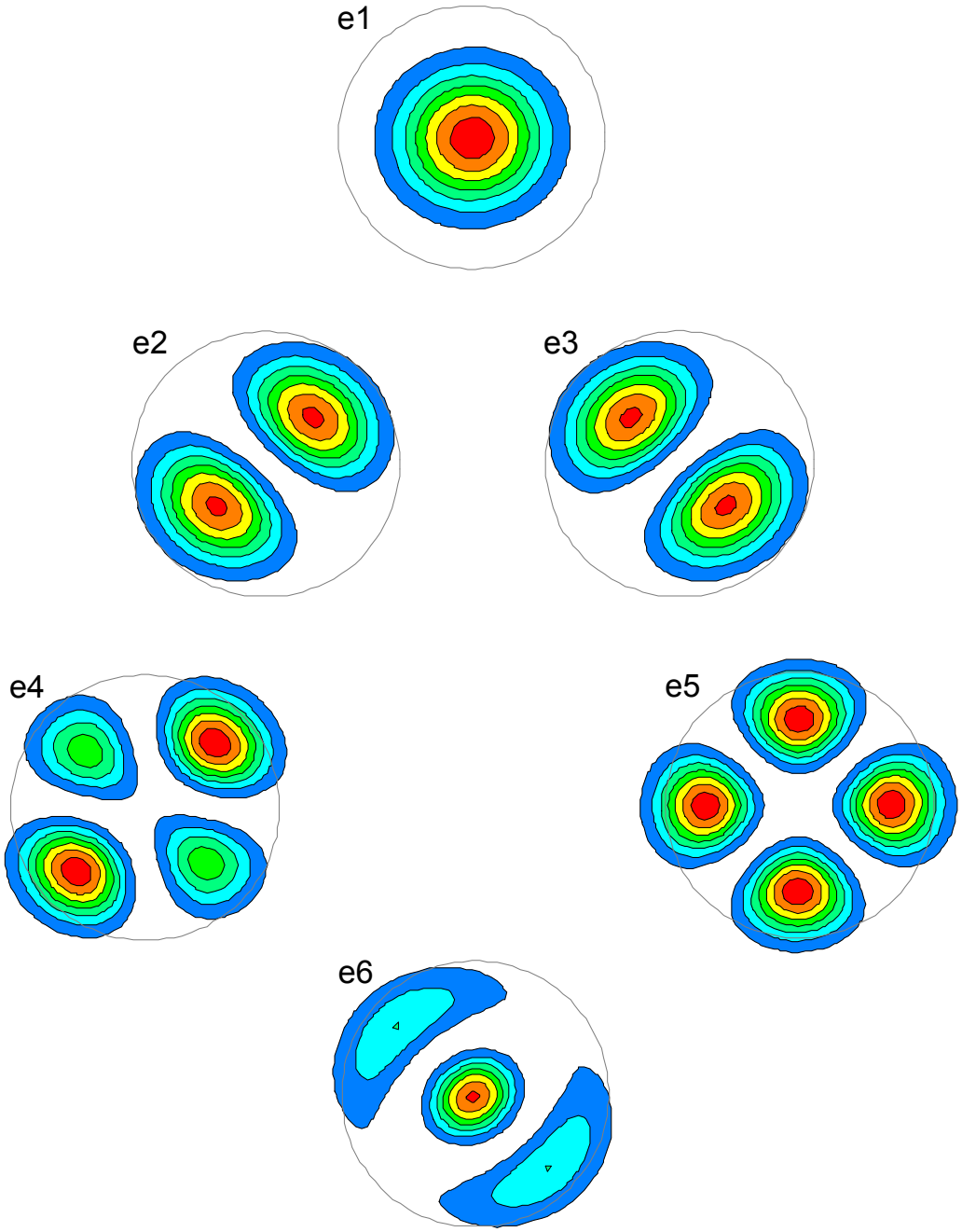

Figure 3.3 Top-view of squared electron wavefunctions, calculated for a lens-like ($d = 3\,\mathrm{nm}$, $r_0 = 12\,\mathrm{nm}$) InAs QD, embedded into GaAs matrix. Eigenstate `e1` is of **s** type, `e2`, `e3` — **p** type, `e4`, `e5` — **d** type.

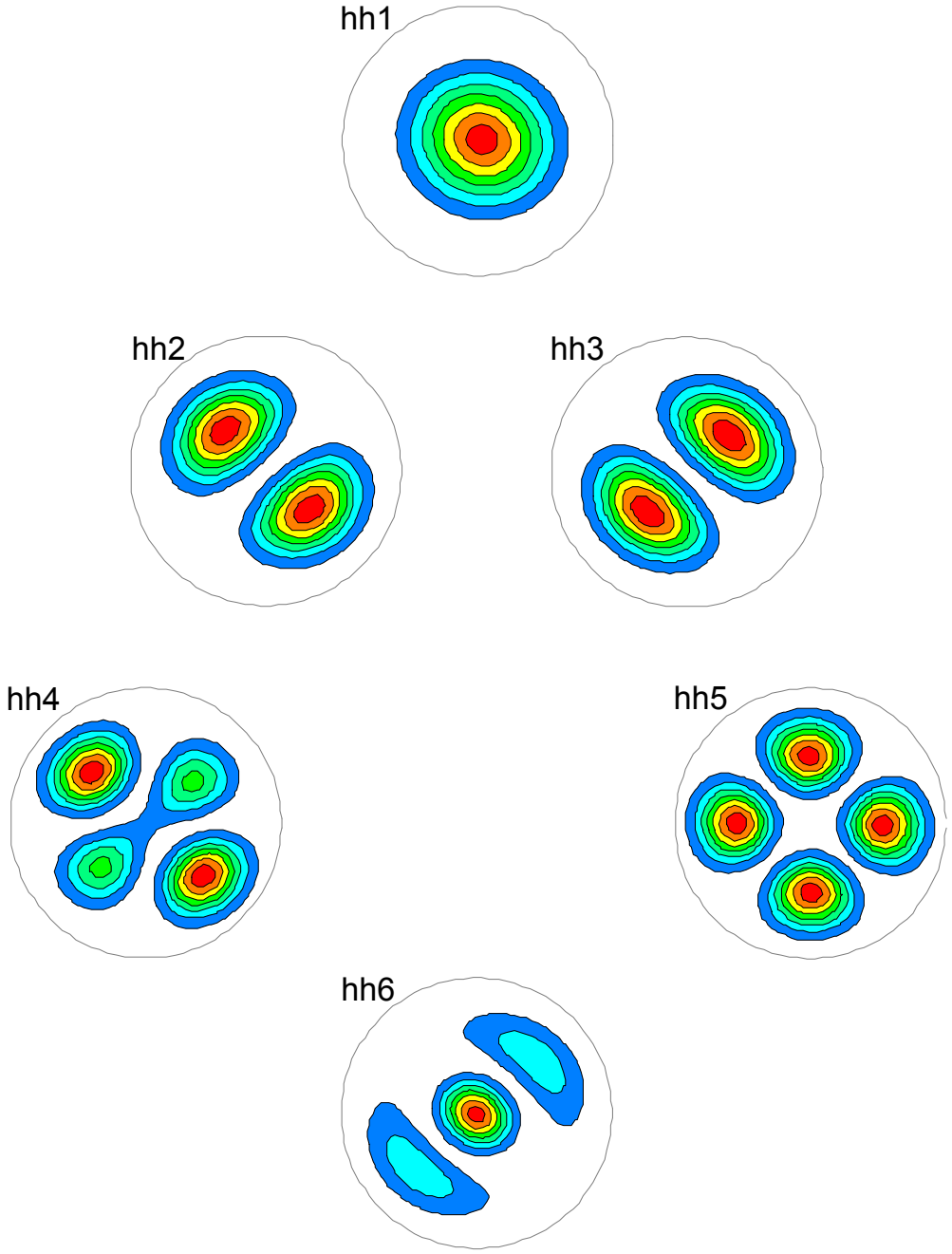

Figure 3.4 Top-view of squared heavy-hole wavefunctions, calculated for a lens-like ($d = 3\,\mathrm{nm}$, $r_0 = 12\,\mathrm{nm}$) InAs QD, embedded into GaAs matrix. Eigenstate `hh1` is of **s** type, `hh2`, `hh3` — **p** type, `hh4`, `hh5` — **d** type.

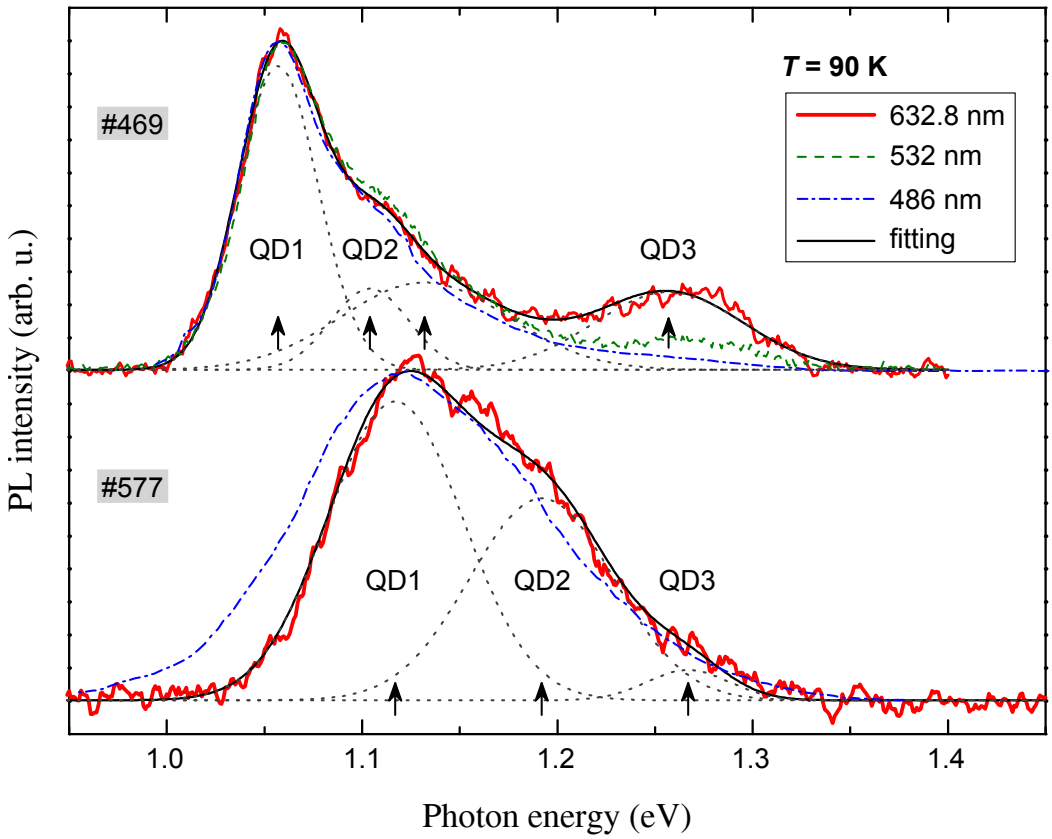

Figure 3.5 Three different laser excited PL spectra for the QD structure with GaAs matrix (sample #469; upper curves) and with GaAs/AlAs matrix (sample #577; lower curves) at 90 K. Arrows indicate obtained energy values for QD-related interband tranbsitions. The high photon energy features QD3 originate from small dots, grown in the bottommost layers of the nanostructures.

This is also consistent with the PL spectral properties shown in Fig. 3.5 under a variable wavelength excitation. As a result, one can trace a high photon energy feature QD3 extinction, particularly for the #469 sample. The high photon energy features QD3 that appear in low temperature (90 K) PL spectra at energies of 1.257 eV and 1.267 eV for the samples #469 and #577, respectively, is less pronouced under excitation with Ar^+ laser, as compared to HeNe laser having a longer penetration depth. Bearing this in mind, the feature QD3 should be atributed to emission from from small-sized QDs located in the bottommost layers of the nanostructures.

Note also, that the discrepancies between CER and PL data can arise due to the different spatial regions of multiple-dot structures probed by these two techniques. In particular, CER technique most effectively probe the QDs, which are under the influence of internal electric fields — dots located close to the surface and GaAs buffer layer. It should be noted as well, that the lowest energy CER feature for the nanostructure #577 at 90 K (not shown) is shifted to higher energies with respect to PL band and

could be associated with the excited-state transitions. The effect can be explained by the Moss-Burstein shift in QD absorption due to the filling of conduction band ground states at low temperature.

Low temperature PL spectra

The blue-shifted ground-state interband transition (QD1) for a #577 structure, as compared to #469 one, is obvious not only in the region of QD-related transitions (which were properly disscussed above), but also where the WL-related ones prevail. In fact, one can use PL technique to explore optical transitions within WL-QW even for undoped QDs. However, this usually demands for powerful laser and cryogenic temperatures. We have employed a Ar-ion (486 nm) laser in order to excite PL of dots-in-a-superlattice structures in a wide temperature range of 3.6–300 K.

Figure 3.6 shows the normalized PL spectra for a stacked InAs/GaAs QD structure with (sample #577) and without (sample 469) AlAs barriers, measured at different temperatures. The low photon energy interval (depending on temperature) of broad spectral feature is where the optical transition within InAs QDs occur, whereas the low energy shoulder could be attributed to some defect influence. The emission bands are complex and each can be reasonably deconvoluted by several Gaussian components. The main (most intensive) low photon energy component could be related to ground-state optical transitions in QDs stacks, whereas the folowing ones (below broad PL curves) are due to excited-states. (This assignment is corroborated by modulated reflectance data given above.) The high photon energy features just below the characteristict bandgap energy of GaAs (which increases decreasing the lattice temperature) are due to interband transitions within InAs WL-QW, however these were resolved only below the temperature of liquid nitrogen (77 K). Again, the temperature behaviour of the PL is different for the stacked dot structures studied.

The high photon energy tail of PL emission — where WL-retated optical transitions occur — is quenched with increase of the temperature. One can ascertain from Fig. 3.6 that for the nanostructure with AlAs barriers (#577) the quenching is less obvious. Reduction of thermal quenching of the QD luminescence band for sample #577 could be related to an increased bandgap of the barrier material.

We suggest that the unusual behavior observed can be understood owing to a transfer of thermally activated carriers from small to large quantum dots. It was found that in QD-SL structures, the carrier migration

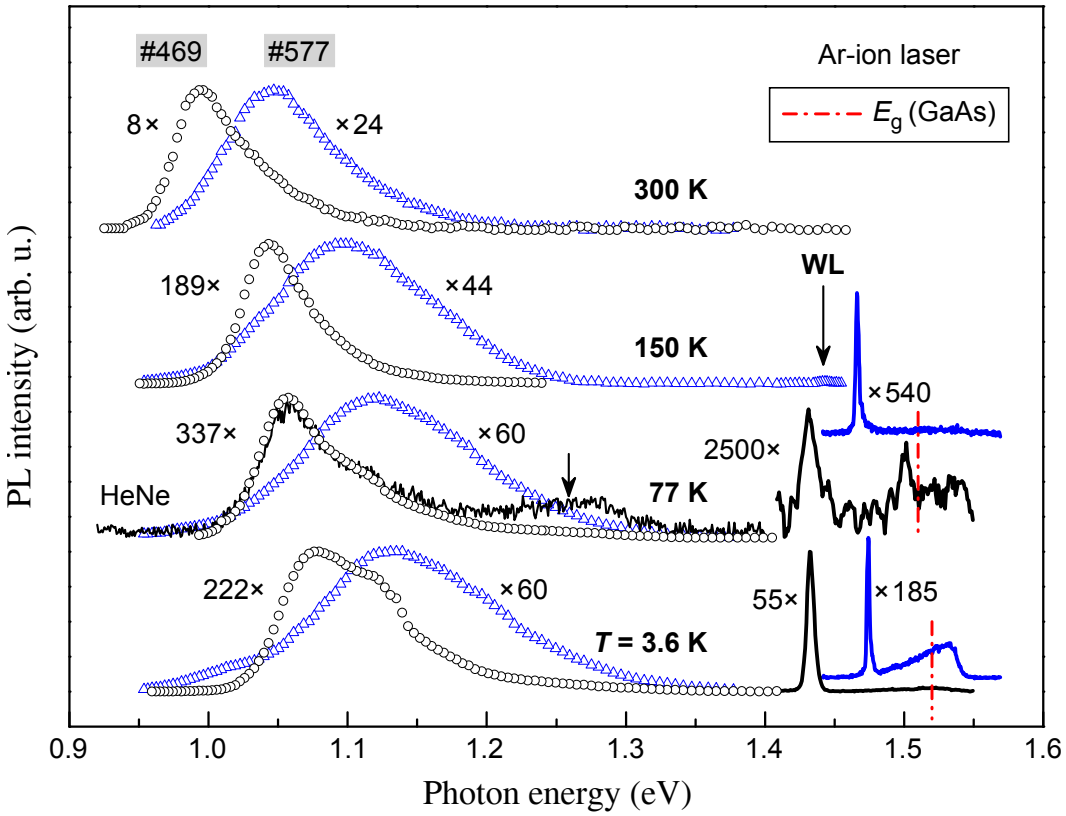

Figure 3.6 Ar-ion excited PL spectra for a stacked QD nanostructures #469 and #577 in a wide temperature range of 3.6–300 K. The HeNe excited spectrum of #469 stucture is also given at 77 K. The blue-shifted PL peak for #577 structure is obvious in both regions of QD- and WL-related interband transitions. PL pump power density was 6.8 W/cm^2.

becomes more intensive with rising the temperature among different QD layers through barrier layer. This results in a large decrease of PL peaks' full-width-at-half-maximum (FWHM) with temperature. In contrast, the migration is very weak for #577 sample with AlAs barriers, which results in little change of PL peaks' FWHM with temperature.

It is worth noting that the excited-states are observed even at very low excitation powers. This effect can be attributed to the fact that the ground-state may be partially occupied with carriers as a consequence of the intentional n-doping of the QDs (dots are doped with one electron). Besides, when the temperature is rised the integral (total) PL intensity weakly decreases. This decrease at higher temperature is related to exciton dissociation and the subsequent escape of electron-hole pairs from the QDs. However, the remarkable stability of the integral (total) PL intensity as a function of the temperature is indicating a strong carrier confinement and/or spatial localization due to AlAs barriers.

3.1.3 Optical transitions in InAs wetting layer

Now, let us move to the interesting optical properties, occurring in the energy range just below the bandgap of GaAs. Here we observe multiple (splitting of) spectral lines, as well as blue-shift and enhancement in intensity. Nature of such features is explained in detail hereinafter.

The sharp resonances in the spectral region of 1.35–1.41 eV, just below the energy bandgap of GaAs, should be related to the interband optical transitions in the InAs/GaAs WL-QW (sample #469) and InAs/GaAs/AlAs SL (sample #577). Usually, only two lines concerned with heavy-hole- (11H) and light-hole-like (11L) optical transitions are observed for a single layer QD structures [55]. However, as follows from more detailed analysis and contrary to what might be expected for a single-layer QDs, the CER and PR spectra for the stacked QDs present multiple lines, i.e., doublet-like splitting of 11H and 11L features, clearly resolved in Fig. 3.7. Therefore, a standard single line shape fitting cannot be satisfactorily used to evaluate 11H and 11L optical transitions. Thus, in order to reproduce the experimental spectra, additional optical lines should be included.

Additional features appearing in CER and PR spectra could be related to the SL miniband effects. Note, that due to a periodic arrangement WL forms a SL by itself and thus differs from a WL for diluted dots in GaAs. Furthermore, under built-in electric field F, which in our case composes after removing top n^+-GaAs layer, the minibands of the SL can transform to

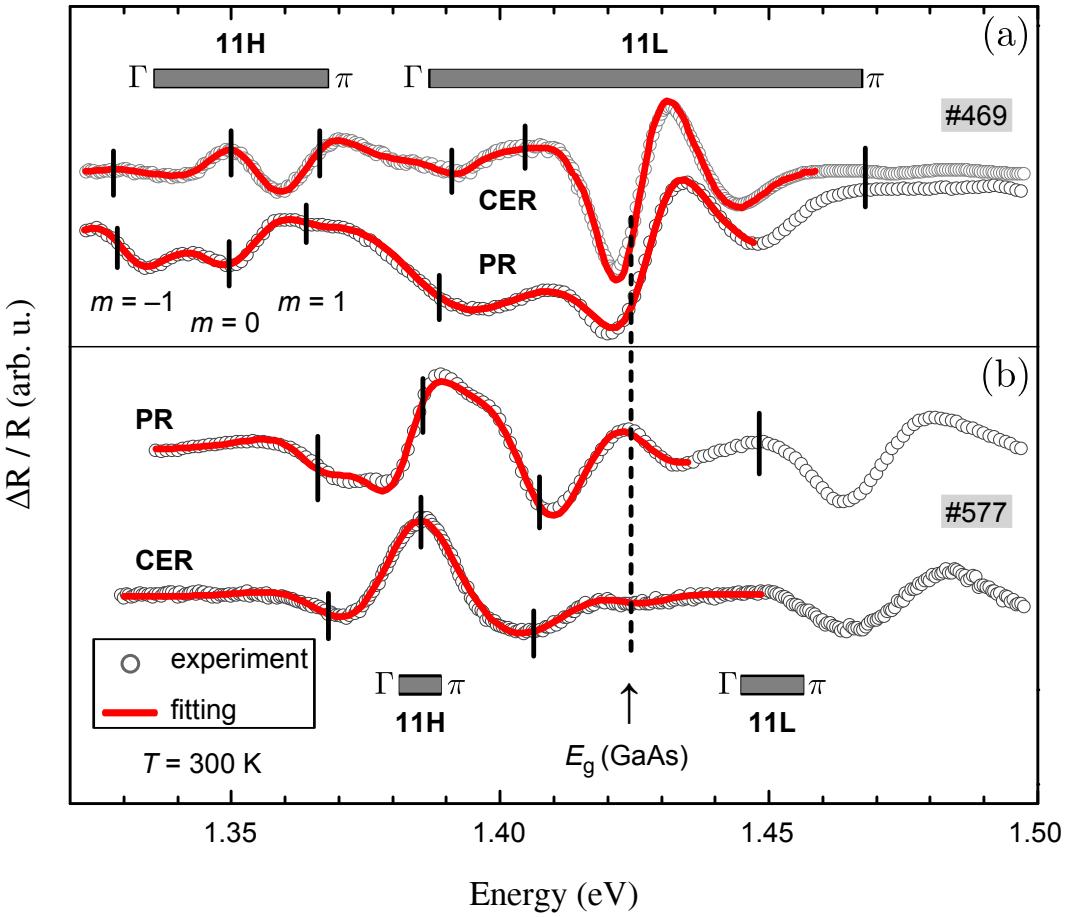

Figure 3.7 Room temperature CER and PR spectra for the samples #469 (a) and #577 (b) in the region of WL-related interband transitions. Vertical dashes indicate the transition energies estimated from the line shape analysis of the spectra. The calculated energy bandwidth (under zero electric field) for the heavy- (11H) and light-hole (11L) related ground-state transitions are indicated by horizontal bars. Designations Γ and π denote transitions at the minizone center and the edge, respectively. In calculations, WL thickness was assumed to be of 0.4 nm.

localized states [56–58], known as Wannier-Stark (WS) states, with energy spacing eFD, where D is a period of the SL. The WS localization leads to spatially indirect transitions between the WS levels and could be the origin of the additional lines in the spectra. Practically, however, the SL effects can be disturbed by the fluctuations in the growth parameters such as a layer width, as discussed in Ref. [59]. Therefore, another reason for the complex optical spectra could be related to the variation of WL thickness across the QD stacks.

In order to gain further information about the features in our experimental spectra, we have calculated the SL energy structure using the envelope function approximation. The calculations were done using the nextnano^3 simulator with material parameters taken from Ref. [60]. First electron miniband (`1e`) in InAs/GaAs and InAs/GaAs/AlAs superlattices, corespond to the structures `#469` and `#577`, are shown in Fig. 3.8. Energy dispersion $E(k_z)$ was calculated from the minizone center Γ to the edge π. Note that 11H SL bandwidth Δ is mainly determined by electron states and are of $\simeq 30\,\mathrm{meV}$ and $\simeq 5\,\mathrm{meV}$ for the samples `#469` and `#577`, respectively. In Fig. 3.7, the expected energy ranges for the 11H and 11L optical transitions under zero electric field (flat bands) are indicated by horizontal bars.

By comparing measured energy positions of the certain spectral lines with the calculated ones, it follows that the multiple features in 11H region cannot be satisfactory explained in terms of optical transitions at the minizone center, Γ point, and at the edge, π point. To get deeper understanding, we simulated also the effects of electric field by regarding the features observed in the spectra as transitions related to the WS localization. Calculations indicate that for the sample `#469`, the 11H spectral features could, in principle, account for the intrawell and first order Stark-ladder transitions. In this case, the energy separation between neighboring CER/PR components ($\simeq 20\,\mathrm{meV}$) correspond to a built-in field of about $20\,\mathrm{kV/cm}$ satisfying WS regime ($F < \Delta/eD$). However, for the sample `#577` the separation ($\simeq 18\,\mathrm{meV}$) between split-off components is too large to be correctly explained in terms of WS localization effect. Indeed, such splitting value requires the electric field strength of $\simeq 15\,\mathrm{kV/cm}$ ($F > \Delta/eD$) at which the electron wavefunctions are completely localized in individual wells. At that rate only the intrawell transitions are sustaining the effect as in the case of multiple-QWs.

Therefore, the most likely explanation of the complex WL features could

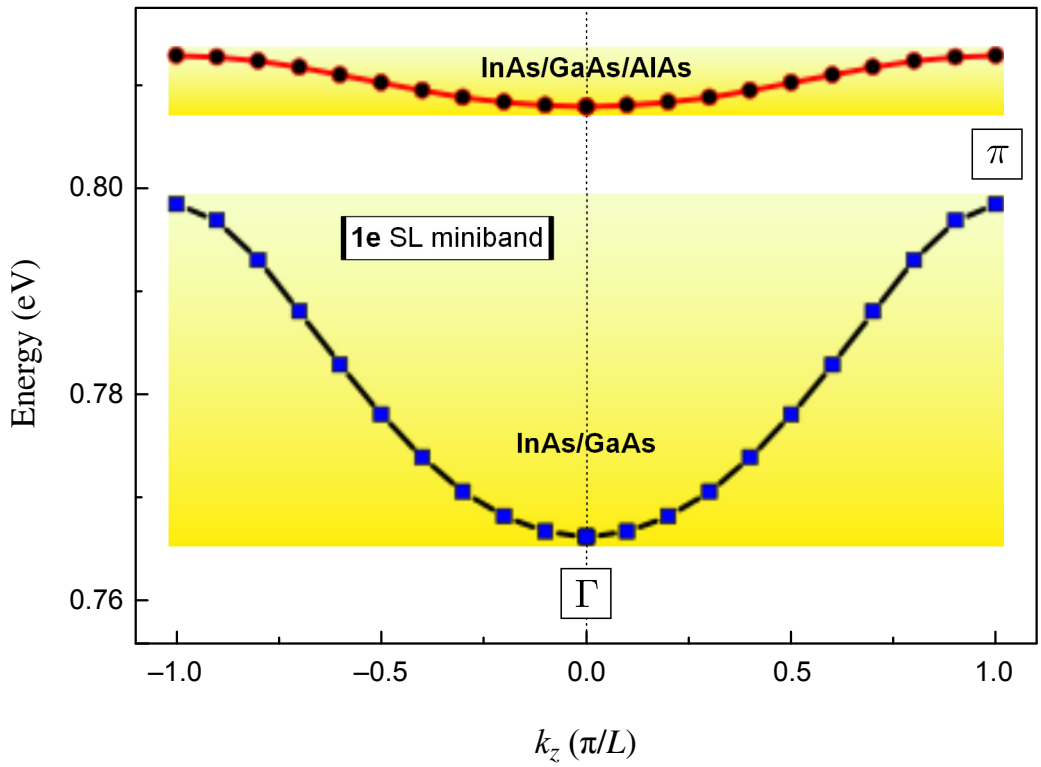

Figure 3.8 First electron miniband (**1e**) in InAs/GaAs and InAs/GaAs/AlAs superlattices (in gradient fill). Energy dispersion $E(k_z)$ calculated from the minizone center Γ to the edge π.

be related to the variation of WL (parameters) thickness across the QD stacks in our samples. Indeed, PR and CER signals are contributed from different depth of the sample. Bearing this in mind, such multiple optical lines may be the effect of the superposition of modulated reflectivity signals from the WL-QWs having different thicknesses. One can note that the strain-induced attenuation of the upper WLs in vertically stacked QD structures has previously been reported for Ge/Si [61] and InAs/GaAs QDs [27,62,63]. Furthermore, the appearance of the multiple WL-related features correlate with the existence of the large and small dot ensembles in the stacked structures, as this was predicted in the analysis of the QD-related spectra (see Subsection 3.1.2 and Figs. 3.1 and 3.5).

WL thickness variation across the multilayers

Based on the above analysis, the variation of WL thickness, Δ_{WL}, across QD stack layers was calculated. The simulations for 11H and 11L transition energies *versus* QW width were performed for the InAs/GaAs/AlAs heterostructure within the envelope function approximation. Again, the calculations were done using the nextnano^3 simulator with material pa-

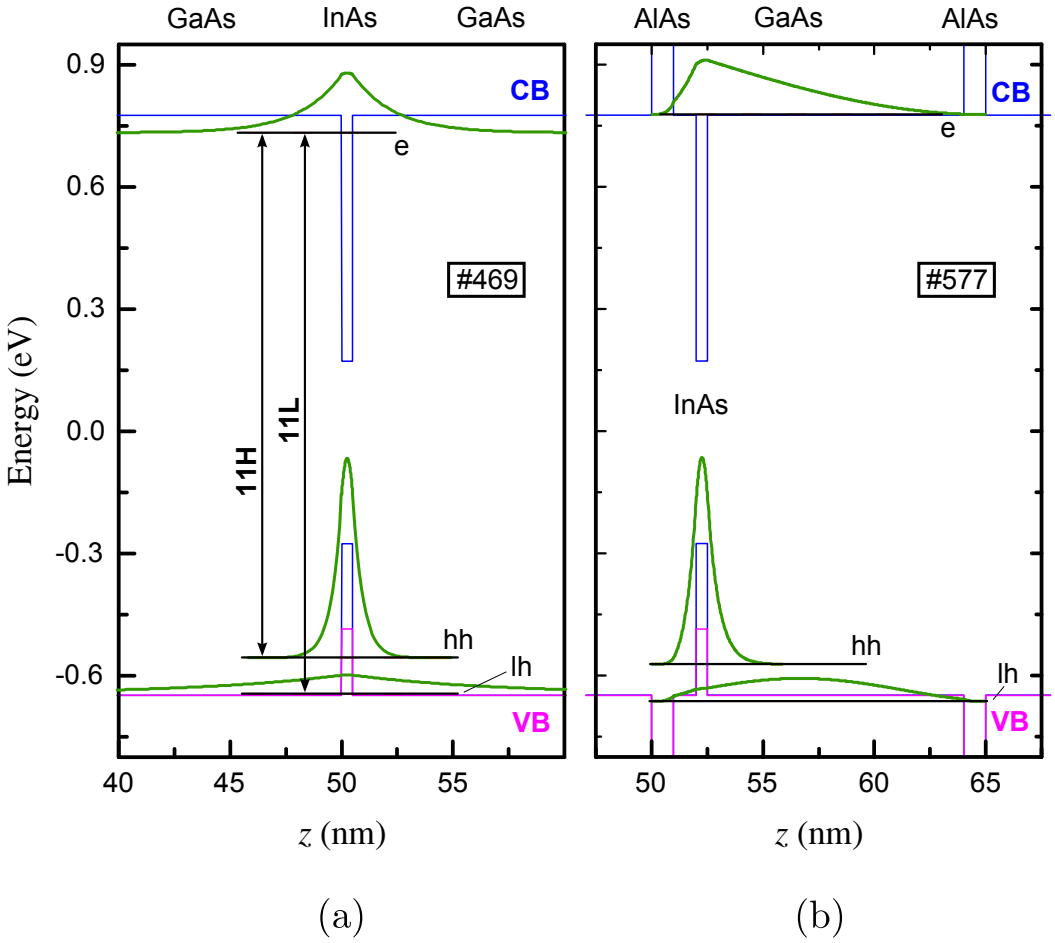

Figure 3.9 Potential profile along the growth direction z (001), squared electron, heavy- and light-hole wavefunctions, and corresponding eigenvalues of electrons (`e`), heavy- (`hh`) and light-holes (`lh`), calculated for InAs/GaAs wetting layer (WL) quantum well (a) and InAs/GaAs/AlAs wetting layer QW (b). Here, heavy- and light-hole related interband optical transitions are denoted by **`11H`**, and **`11L`**, respectively. Simulations carried out mimic the real QD nanostructures studied — `#469` (a) and `#577` (b) — only disregarding the presence of InAs QD. InAs WL thickness of 0.5 nm was used in calculations, performed by nextnano^3 simulation software.

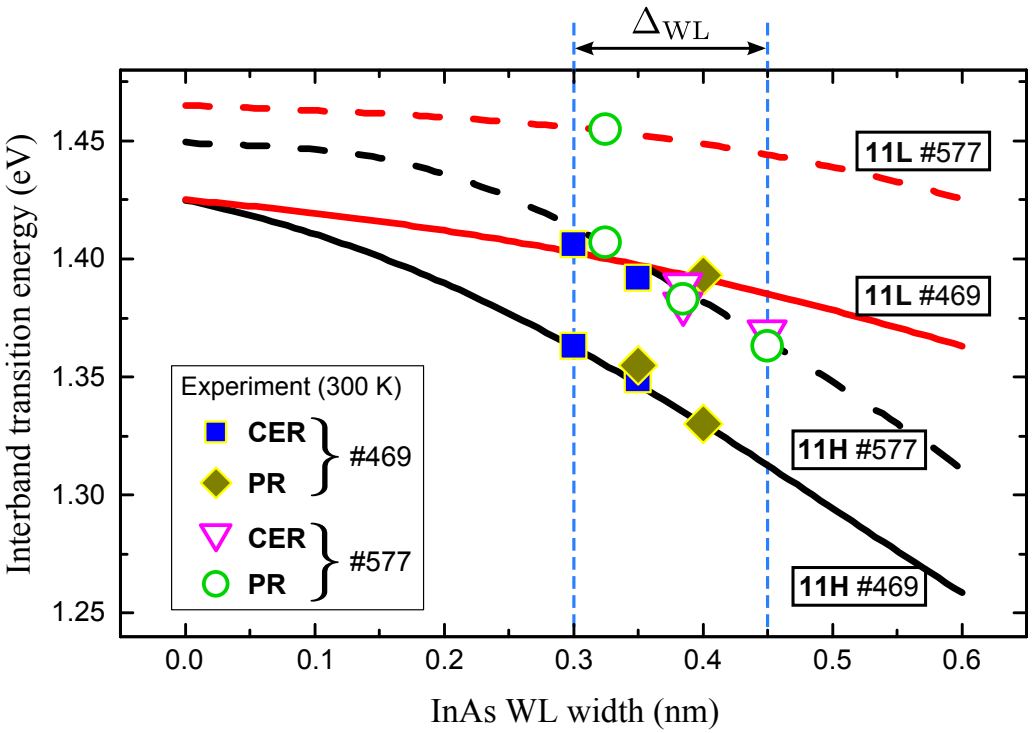

Figure 3.10 Experimental (symbols) and calculated (curves) transition energies in the InAs/GaAs WL-QW without (sample #469) and with (sample #577) AlAs barriers. The variation of WL thickness Δ_{WL} by about ± 0.25 MLs implies a shift of 11H transition energies by ± 25 meV. Bottommost layers of the QD structure, as compared to upper ones, have a thicker WLs and smaller dots.

rameters taken from Ref. [60]. The results of the calculations are presented in Fig. 3.9, which illustrates the potential profile along the growth direction z (001), squared electron, heavy- and light-hole wavefunctions, and corresponding eigenvalues of electrons (e), heavy- (hh) and light-holes (lh), calculated for InAs/GaAs wetting layer (WL) quantum well (a) and InAs/GaAs/AlAs wetting layer QW (b). The calculations of interband transition energies as a function of WL thickness (represented by curves in Fig. 3.10) yield that for narrow (0.4 nm) QWs, a variation in the thickness by ± 0.25 ML implies a shift or splitting of 11H transition energies by about ± 25 meV. Such splitting is close to the one detected in the CER/PR spectra (given by symbols in Fig. 3.10). Different probing depth between CER and PR techniques allows to distinguish experimentally the WL-related responses coming from various parts of the structure [64]. As can be seen in Fig. 3.7, low-energy components of the WL-related features are more pronounced in PR rather than CER spectra. This suggests that these spectral lines could be related to the thicker bottom WL-QWs.

Thus, it is likely that the variation in the size of the self-aligned QDs could be attributed to the changes in the thickness of the InAs WL. The

lower layers of the QD structure have a thicker WLs and smaller dots and *vice versa*. As follows from a comparison of experimental and calculated transition energies (Fig. 3.10), the thickness of the WL varies from about 1.5 ML to 1 ML with vertical ordering in favor of larger QDs as a consequence of gradual buildup of the internal strain [27, 62, 63]. However, in order to unambiguously confirm these findings, additional structural investigations are necessary.

AlAs barrier impact on electron states

Two more spectral properties are evident in Fig. 3.7 — a blue-shift and enhancement in intensity of 11H and 11L related transitions in the sample with AlAs barriers in respect of the sample without barriers. In order to understand the origin of these perturbations we made calculations as well. *Firstly*, the calculations were carried out in order to find out the impact of AlAs barrier on electronic states. We numerically evaluated the electron energy levels of the InAs/GaAs/AlAs SL combined from the 0.5 nm-thick InAs WL inserted into a GaAs/AlAs SL with a period of 14 nm. *Secondly*, after applying calculations on the heavy-holes, we found the intrawell 11H transition energies for the studied heterostructures under the applied electric field.

To illustrate AlAs barrier-induced spectral features of the structure, numerical calculations were carried out varying the distance (position), Δz, of the InAs layer from the AlAs barrier. The dependence of the electron energy levels at $k_z = 0$ (Γ-point) are presented in Fig. 3.11 (circle-line notation). The electron energy levels, together with their squared wavefunctions, calculated for the GaAs/AlAs SL (levels `e1`–`e3`) and the InAs WL-SL (level `e0`) alone are shown by dashed lines. From the diagram in Fig. 3.11, one can see that GaAs/AlAs QW is sensitive to the perturbation with InAs WL. Obviously, the electron energy spectrum of the SL essentially depends both on the presence of AlAs barriers, and on the WL insertion position, Δz. Characteristic, that due to an attractive potential of InAs layer [65], the electron energy levels exhibit oscillations with Δz, which in turn follow the oscillations of the squared wavefunctions of GaAs/AlAs SL.

In more detail, the highest shift in main energy level of InAs/GaAs QW happens, when WL is placed close to the AlAs barrier. Indeed, while approaching AlAs barrier, InAs WL continually shifts its electron energy level `e0` to higher energy and eventually coincides with the lowest electronic level of GaAs/AlAs SL, `e1` (Fig. 3.11). Alternatively, the largest shift of the elec-

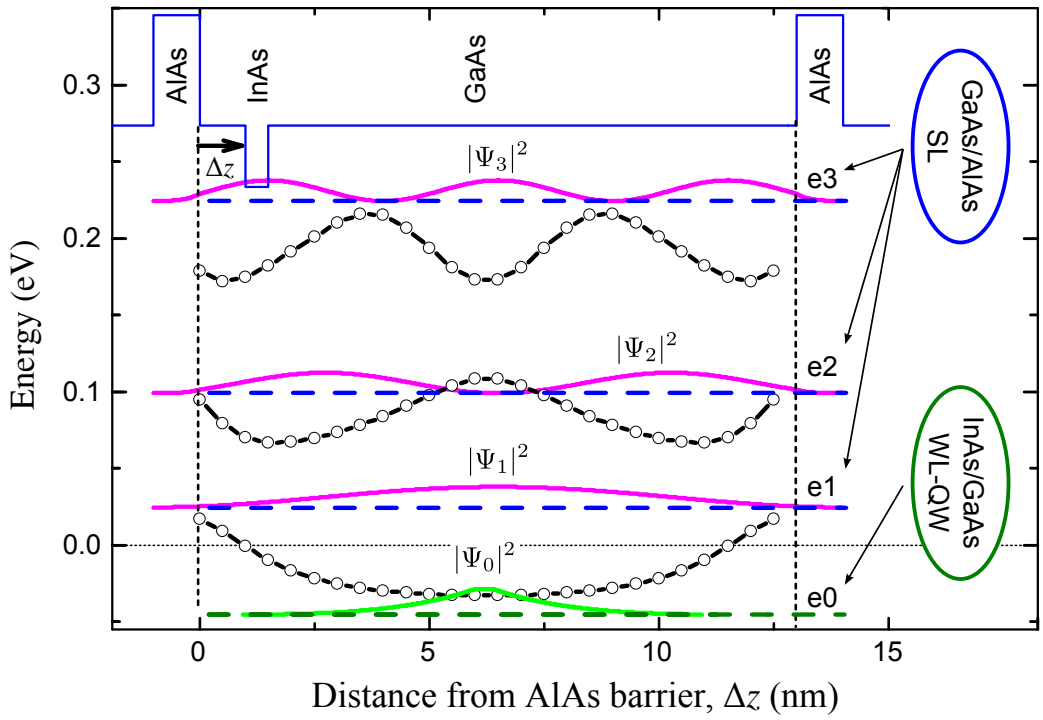

Figure 3.11 Calculated InAs/GaAs/AlAs QW electron energy levels as a function of a distance Δz of InAs WL from AlAs barrier (symbol+line). Squared wavefunctions together with energy levels `e1`–`e3` and `e0` correspond to the pure GaAs/AlAs QW-SL and the InAs WL-QW, respectively. The energy origin is taken at the conduction band (CB) edge of GaAs. Top: InAs/GaAs/AlAs CB scheme (not in the energy scale). Parameters used: AlAs barrier width 1 nm; InAs WL thickness 0.5 nm; GaAs/AlAs QW width 13 nm.

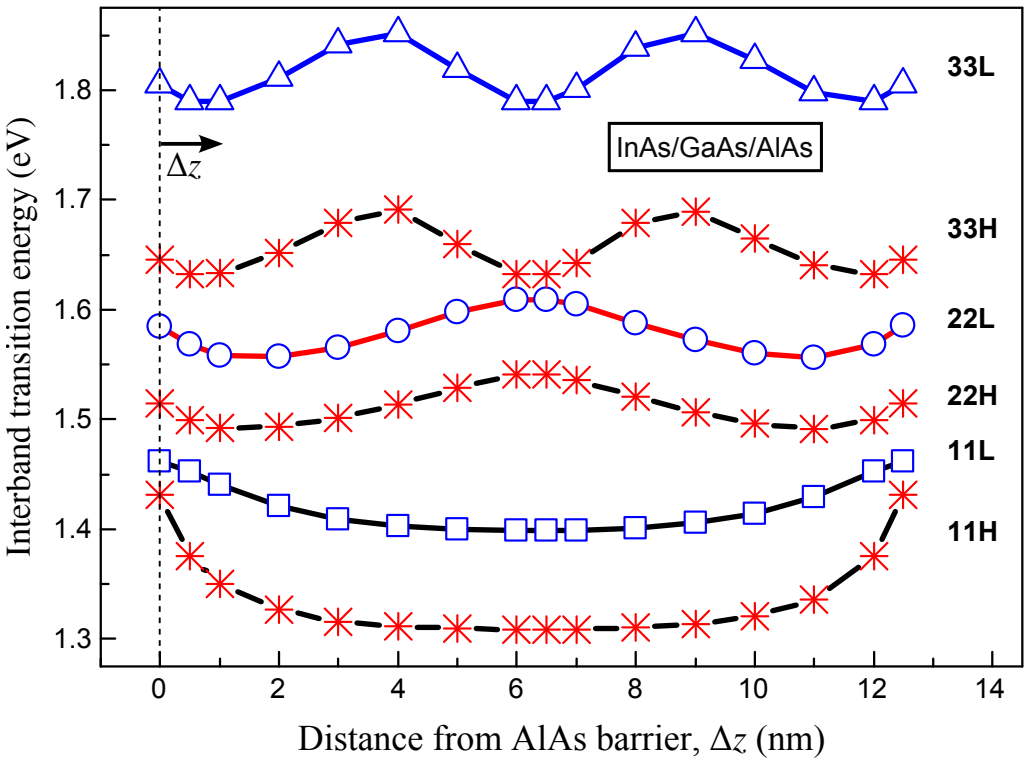

Figure 3.12 Optical interband transition energies in a combined InAs/GaAs/AlAs QW-SL system, calculated as function of the InAs WL layer insertion position Δz in the GaAs/AlAs QW. Heavy- (nmH) and light-hole (nmL) related optical transitions occur between n-th electron and m-th hole states. Parameters used: AlAs barrier width 1 nm; InAs WL thickness 0.5 nm; GaAs/AlAs QW width 13 nm.

tronic level `e1` to lower energy occurs, when InAs WL is placed at the center of GaAs/AlAs QW. Thus, simulations of the electronic states predicts the enhanced blue-shift by about 50 meV of WL-related optical transitions for InAs/GaAs/AlAs SL (the case of sample `#577`) with the off-center position of the QD layers in the wells.

In similar manner changes the energies of hole states (not shown). Calculated interband transition energies as a function of the InAs WL insertion position in the GaAs/AlAs well are shown in Fig. 3.12. Again, the blue-shift of the lowest energy heavy- (11H) and light-hole (11L) related transitions is evident when the insertion position of InAs layer approaches the high potential barrier of AlAs.

Signal intensity of WL-related features

Finally, we turn our attention to the signal intensity of the WL-related PR/CER features. In order to address the intensity enhancement, for low-dimensional structures two mechanisms should be taken into account. The first one is quantum-confined Stark effect (QCSE). This is an electroabsorp-

tive effect, when an electric field is applied, and which has no analog in bulk semiconductors. The quantum-confined Stark effect describes the effect of an external electric field upon the light absorption (or emission) spectrum of a QW. In the absence of an external electric field, electrons and holes within the QW may only occupy states within a discrete set of energy subbands. When an external electric field is applied, the electron states shift to lower energies, while the hole states shift to higher energies. This reduces the permitted light absorption (or emission) frequencies. Additionally, the external electric field shifts electrons and holes to opposite sides of the well, decreasing the overlap integral, which in turn reduces the recombination efficiency of the system. The spatial separation between the electrons and holes is limited by the presence of the potential barriers around the quantum well, meaning that excitons are able to exist in the system even under the influence of an electric field.

Briefly, the QCSE-induced shift of an energy level, ΔE , under applied electric field F can be described by formula

$$\Delta E = \mathbf{p}F + \beta F^2, \tag{3.3}$$

where $\mathbf{p}$ is the built-in dipole moment, whereas β measures the polarization of electron and hole states, i.e. QCSE. Here, both linear, and square terms are important, as for the nanostructures studied, QDs are embedded asymmetrically within QW.

The second mechanism, which can account for signal intensity enhancement of WL-related PR/CER features, is the squared overlap integral (matrix element) of the electron and heavy-hole wavefunctions [66], determined by

$$|M_{\mathrm{CV}}|^2 = \left| \int_{-\infty}^{+\infty} \mathrm{d}z \, \psi_{\mathrm{e}}(z) \psi_{\mathrm{h}}(z) \right|^2. \tag{3.4}$$

Figure 3.13 shows the calculated field dependencies of the 11H interband transition energies and overlap integral, $|M_{\mathrm{CV}}|^2$, for WL-QW without (sample `#469`) and with (sample `#577`) AlAs barriers. As it is evident from Fig. 3.13, the 11H transitions for the sample `#577` exhibit an enhanced nearly linear Stark shift and strong variation of $|M_{\mathrm{CV}}|^2$ with an electric field. Furthermore, in contrast to the sample `#469`, these characteristics are asymmetric with respect to the applied electric field direction. On the basis of these calculations, the observed intensity enhancement of the WL-related PR/CER features for the sample `#577` (see Fig. 3.7) may be ex-

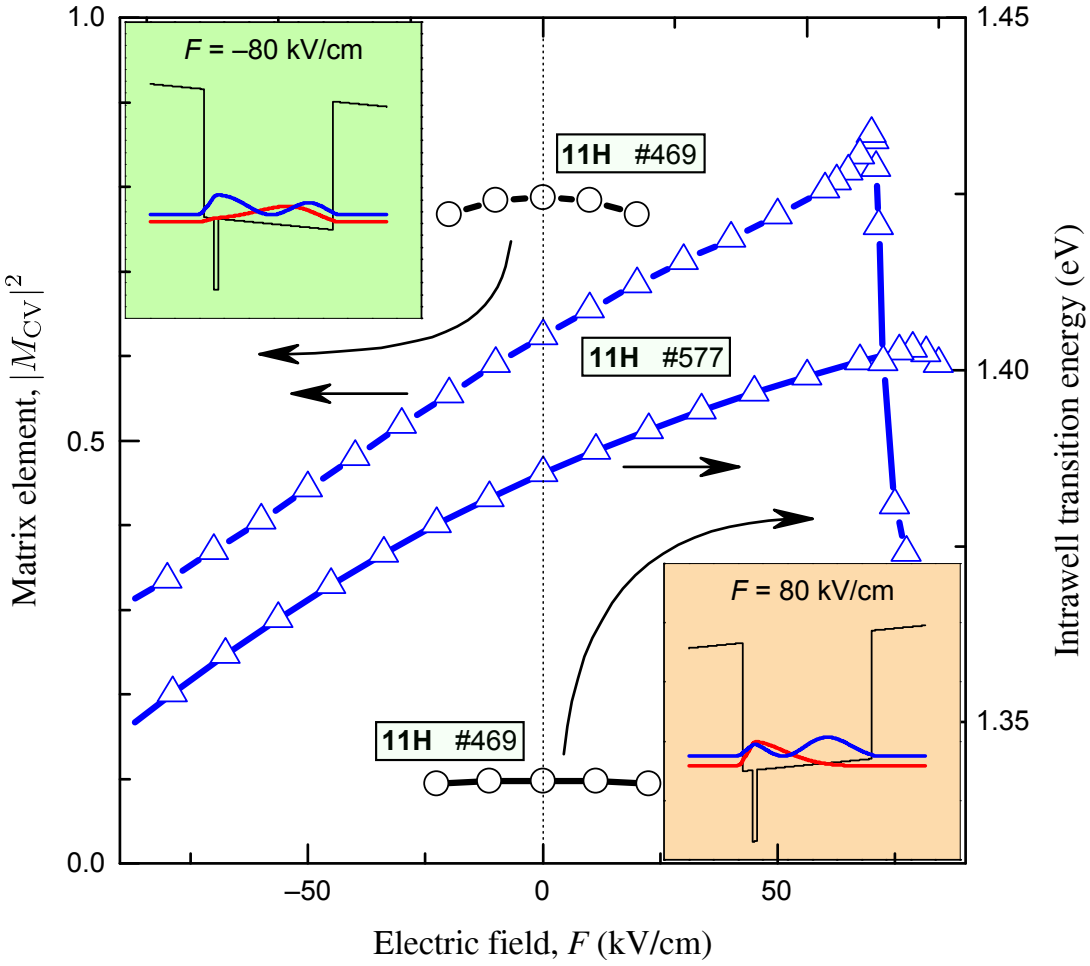

Figure 3.13 The electric field dependencies of the 11H intrawell transition energies and the squared overlap integral of the electron and heavy-hole wavefunctions, $|M_{CV}|^2$, for the samples `#469` (circle-line) and `#577` (triangle-line). Insets show the potential profile and squared modulus of the two lowest-state electron wavefunctions for different directions of the electric field $F = \pm 80\,\mathrm{kV/cm}$. The positive F values represent the growth direction of the QW structure.

plained by the enlarged Stark shift of the ground-state interband transitions 11H. Aforesaid Stark shift is caused by the asymmetry of the structure, an off-center position of the QD layers in the GaAs/AlAs wells (see the insets in Fig. 3.13). These results clearly show that WL-related electronic states in asymmetric QWs may be controlled by the external electric field.

3.1.4 Conclusions

In summary, interband optical transitions and electronic structure of vertically stacked InAs QD multilayers within GaAs and GaAs/AlAs matrix (i.e. with and without AlAs barriers) were explored and examined by PR and CER techniques, supported by PL spectroscopy. The optical transitions related to the QD ground and excited states, as well as the interband transitions in InAs/GaAs/AlAs SL were revealed. Spectroscopic results and numerical calculations show that the electronic structure of considered system is strongly affected by parameters of InAs QDs, WL and GaAs/AlAs SL. In particular, it was found that

- ✓ blue-shift by about 50 meV of InAs WL-related interband transitions in InAs/GaAs/AlAs QD-SL originate mainly due to off-centre position of the QD layers in the wells;

- ✓ the intensity enhancement of the WL-related PR/CER features for the structure with AlAs barriers may be explained by the enlarged Stark shift of the ground-state interband transitions 11H;

- ✓ the appearance of multiple InAs WL-related features in the modulated reflectance spectra could be attributed to the variation of the WL thickness in the stacked QD structures. In particular, the thickness of the WL varies from about 1.5 ML to 1 ML with vertical ordering in favor of larger QDs as a consequence of gradual buildup of the internal strain.

The aforementioned findings allowed to formulate the following *statement for defence*

Blue-shifts and enhancement in intensity of InAs wetting layer-related optical transitions, observed in InAs/GaAs/AlAs dots-in-a-superlattice structure, are due to off-center position of the dot layers in the wells, while the spectral splitting is associated with a variation of the wetting layer thickness along the growth direction.

3.2 Energy Spectrum of InAs Quantum Dots in a Composite InGaAs/GaAs/AlAs Quantum Well

QD structures are the foremost candidates for numerous applications in optoelectronics, such as in QD infrared photodetectors (QDIPs). Particularly, size, shape and compositional engineering (e.g., incorporation of capping and/or barrier layer) allows to taylor optical transition energies of QD structures. Recently, novel dots-in-a-well (DWELL) designs, where InAs QDs are embedded in an InGaAs/GaAs/AlGaAs quantum well (QW), were proposed by Barve *et al.* in Ref. [67]. This novel detector design allows to control the photodetectivity peak wavelength through changing the QW width. Understanding the optical properties, and gaining knowledge of the electronic spectrum of such nanostructures, are key issues for potential micro- and opto-electronic applications.

In this Section, the effects of a 5 nm-thick InGaAs cap layer (covering the dots) on electronic and optical properties of MBE-grown DWELL infrared photodetector structures are investigated using modulated reflectance spectroscopy techniques — photoreflectance (PR) and contactless electroreflectance (CER). The photoluminescence (PL) spectra were also measured for a comparison.

The quantum system studied comprised $N = 10$–15 periods of InAs dots (with and without InGaAs cap layers) embedded within GaAs/AlAs QWs. Hereinafter, interband optical transitions within the InAs QDs and InGaAs QW for two different structures are disclosed and discussed. We show that modulated reflectance spectroscopy can successfully be employed to reveal the full-extent of the optical transitions of DWELL nanostructures, even at room temperature. Results obtained from our study offer a pathway to shift the photodetectivity towards longer wavelengths for QDIPs, based on self-assembled InAs QDs.

3.2.1 Full optical view of dots-in-a-well structures

Room temperature PR and PL spectra of the InAs/GaAs/AlAs DWELL structures with (sample `L442`) and without (sample `L444`) 5 nm-thick InGaAs capping layer (covering the dots) are given in Fig. 3.14 (a) and (b), respectively. Optical study reveals three principal sets of spectral features, which are numbered for ease of use. *Firstly*, the low energy interval of

0.85–1.2 eV corresponds to the ground- (1) and excited-state (2–4) optical transitions within lenslike (of $d = 5$ nm height and $r_0 = 10$ nm base radius) self-assembled InAs QDs. *Secondly*, with the increase of a photon energy, in the region between 1.2–1.42 eV, nanostructure `L442` (with InGaAs cap layer) present a sharp and intensive PR line (5), which is due to interband ground-state optical transition in InAs/InGaAs QW. The following two optical features (6, 7) for the stucture `L442` originate also from the asymmetric binary-well (bi-QW), formed by InAs wetting and InGaAs cap layers, and their origin is due to the excited states in bi-QW. On the other hand, PR spectrum of the DWELL nanostructure `L444` (without InGaAs cap layer) in the photon energy region just below the bandgap energy of GaAs (1.424 eV at 300 K) show two lines (5, 6), which correspond to interband transitions within InAs WL-QW. Note also, that for the sample `L444`, fitting of a PR spectrum yields additional line (4*), which cannot be assigned neither to QD-related optical interband transitions, nor to InAs WL-QW-related ones, however, and its possible origin is discused in more detail later. *Finally*, the high photon energy features above the GaAs bandgap energy are ascribed to interband transitions within a wide GaAs/AlAs QW.

Insets in a Fig. 3.14 show a schematic band diagram of then nanostructures studied with electron and hole energy levels along with corresponding interband transitions (numbered), which were revealed experimentally. Experimental data — interband transition energies and their intensities — were interpreted by calculations using the effective mass approximation, using nextnano[3] software. Numerical simulation results are represented by vertical bars in a Fig. 3.14. Vertical bar position and amplitude denote calculated interband transition energy and intensity, respectively, for heavy- (nmH) and light-hole (nmL) related optical transitions. Interband transition energies were extracted by fitting the PR spectra to the first derivate of a Lorentzian-type function. Table 3.1 shows the obtained energy values for DWELL nanostructures investigated.

As a result, spectroscopic PR and PL data was verified and interpreted by numerical calculations. Up to seven different interband optical transitions were revealed, which were identified (by numbers in Fig. 3.14) as transitions between energy levels from the valence and the conduction bands, involving

(1) InAs QD ground-states (`GS`, both samples);

(2–4) InAs QD excited-states (`ES`, both samples);

(4*) Strain-induced QD (`SI-QD`) states (only sample `L444`);

Table 3.1 Fitting results of the room temperature (300 K) PR and PL spectra along with the corresponding calculated interband transition energies for two DWELL nannostructures studied — samples `L442` and `L444`. All the energy values are given in electronvolts (eV).

optical feature		sample `L442`			sample `L444`		
		RP	PL	calc	RP	PL	calc
	`Imp`					0.997	
1	`GS`	0.956	0.951		1.085	1.073	
2	`ES1`	1.016	1.008		1.137	1.128	
3	`ES2`	1.066	1.062		1.195	1.190	
4	`ES3`	1.123	1.122				
4*	`SI-QD`				1.302	1.304	
5	`bi-QW`	1.248	1.250	1.251			
		(1.263)					
6		1.318		1.321			
7		1.358		1.360			
		1.372		1.373			
5	WL-QW				1.349		1.348
6					1.385		1.384
					1.399		1.401
GaAs/AlAs	`QW1`	1.418		1.420	1.441	1.435	1.439
QW		1.442		1.443	1.458		1.453
	`QW2`	1.458		1.459	1.482	1.484	1.489

(5) InAs/InGaAs bi-QW (`bi-QW`, sample `L442`) or InAs WL-QW (sample `L444`) ground-states;

(6, 7) InAs/InGaAs bi-QW (`bi-QW`, sample `L442`) or InAs WL-QW (sample `L444`) excited-states.

3.2.2 Optical transitions in InAs quantum dots

In order to explore interband optical transitions within InAs QDs of capped (sample `L442`) and uncapped (sample `L444`) by 5 nm-thick InGaAs layer DWELL nanostructures in detail, PL measurements were carried out. Room temperature PL spectra for both DWELL structures studied are given in Fig. 3.15. Interband optical transition parameters for QD structures stud-

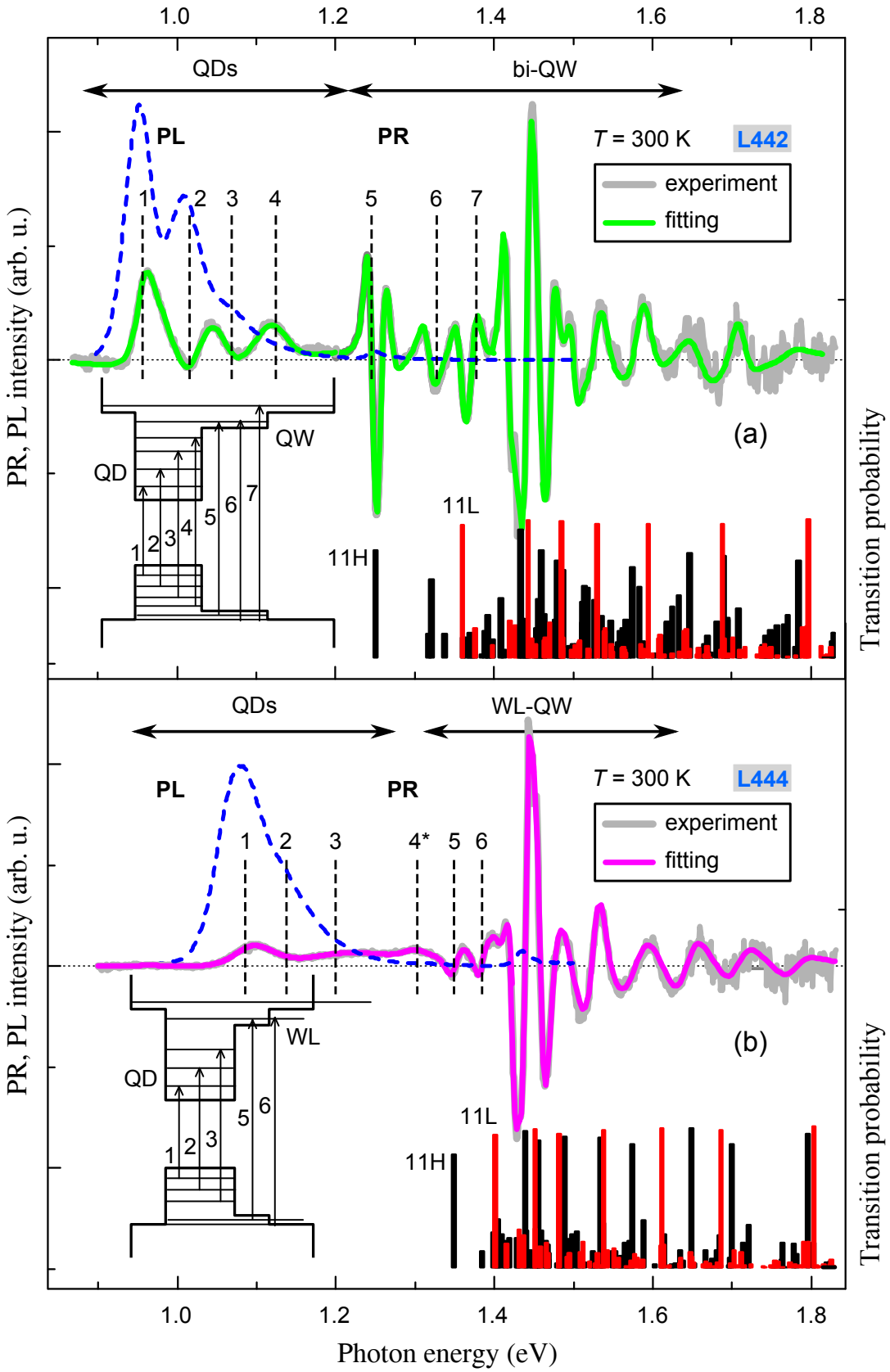

Figure 3.14 Room temperature PR and PL spectra for the DWELL structures with (sample L442; (a)) and without (L444; (b)) InGaAs cap layer. The position and amplitude of vertical bars represent calculated transition energies and intensities, respectively. Insets: band diagram of the structures studied with numbered interband transitions, revealed experimentally.

ied were extracted from PL spectra using a multi-Gaussian fit. Thereby, transition energies (and intensities) between ground- (GS) or excited- (ES) states were obtained.

It was found that the shift of the GS transitions to lower energies (red-shift) by about 100 meV is characteristic for the L442 DWELL structure as compared to L444 one. In particular, the InGaAs-capped structure L442 presented QD-related optical transitions of GS = 0.951 eV, ES1 = 1.008 eV, ES2 = 1.062 eV and ES3 = 1.122 eV, along with ground-state optical transition in InAs/InGaAs bi-QW, bi-QW1 = 1.250 eV. The uncapped DWELL structure L444, on the other hand, presented QD-related optical transitions of GS = 1.073 eV, ES1 = 1.128 eV and ES2 = 1.190 eV together with valence band to conduction band transitions $VB_2 \rightarrow CB_2$ and $VB_4 \rightarrow CB_4$ within GaAs/AlAs QW of QW1 = 1.435 eV and QW2 = 1.484 eV, respectively. Moreover, there are two more interband transitions for the stucture L444, resolved by PL. One is in the very low photon energy region, most probably associated with impurity levels, Imp = 1.003 eV. Another one is situated in between QD-related and WL-QW-retated transitions [see experimental PR spectra in Fig. 3.14(b)], and is attributed to the interband transition occuring in strain-induced QD, SI-QD = 1.304 eV.

Indeed, in case of DWELL sample without InGaAs capping layer the fitting of a PR spectrum yields additional line (numbered as 4* in Fig. 3.14(b)), which cannot be assined neither to QD-related optical interband transitions, nor to GaAs/AlAs QW-related ones, however. It is supposed, that an additional spectral band revealed below the energy of the InGaAs QW exciton should be assigned to the emission of a strain-induced QD layer created by the InAs stressors within the InGaAs QW, as was discussed for similar DWELL nanostructures in Ref. [68].

The burying of InAs QDs results in strain reducing, which changes QD properties and creates new states in the InGaAs QW. While the InGaAs cap layer lowers the energy of the QD ground-state transition, it maintains the strong quantization of the QD electronic states which develop into a series of excited states transitions in PL under increased excitation intensity (and which will be discussed furthermore later). An additional PL band is revealed below the energy of InGaAs QW exciton, and is tentatively assigned to the emission of the strain-induced QDs, created by the InAs stressors in the InGaAs QW. Such bound state does not appear (or is obscured) in the InAs/InGaAs/GaAs/AlAs DWELL stucture, but arise in the uncapped InAs/GaAs/AlAs, possibly due to the asymmetry in the strain distribution

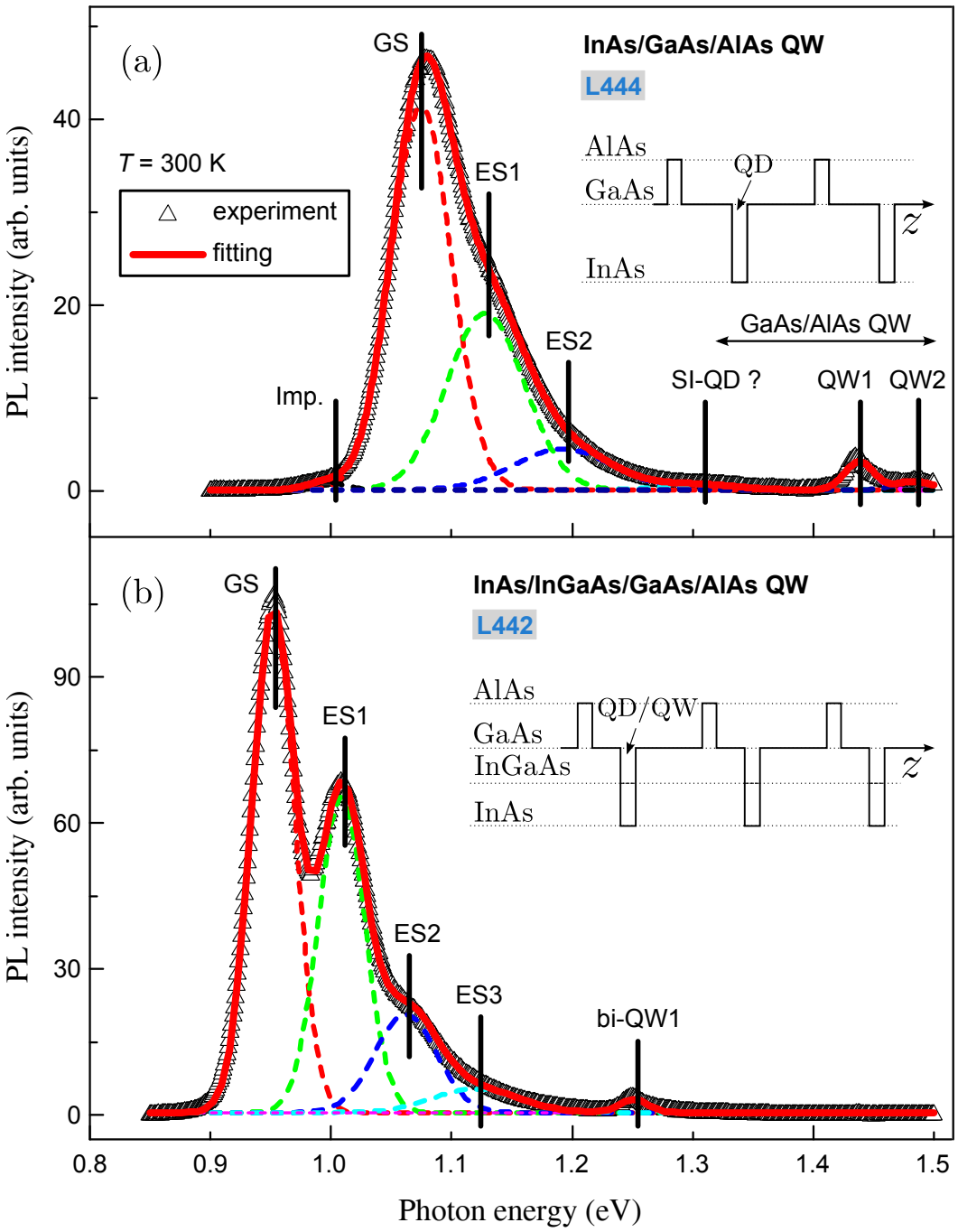

Figure 3.15 Room temperature photoluminescence (PL) spectra for the DWELL structures without (sample `L444`; (a)) and with (sample `L442`; (b)) InGaAs capping layer. PL spectra are deconvoluted by Gaussian lines, each representing an optical transition between ground- (`GS`) or excited- (`ES`) states. Insets show a schematic band diagram of the DWELL nanostructures studied.

around a dot.

QD energy spectra *versus* PL pump power

In order to verify the excited-states observed in modulated reflectance and PL spectra above, we have excited both DWELL structures varying PL pump power. Figure 3.16 shows room temperature PL intensity spectra for the DWELL structures studied [samples L444; (a)) and L442; (b)] as a function of the excitation power. Indeed, PL measurements at different excitation powers confirms the presence of QD excited states. In particular, at the lowest excitation power the emission mainly originates from the ground-state (GS) transition. While increasing excitation power, the GS transition saturates and subsequent excited-state (ES) transitions gain intensity. Emission from InGaAs and GaAs/AlAs QW leads to a weak peaks around 1.25 eV and 1.43 eV for samples L442 and L444, respectively. Interband optical transition parameters for QD structures studied were extracted from PL spectra using a multi-Gaussian fit. The red-shift of the GS transitions to lower energies (by about 100 meV) is characteristic for the L442 DWELL structure, capped by InGaAs layer, in respect of uncapped sample L444.

Low temperature PL spectra

At liquid nitrogen temperature (80 K) PL features, as expected, are shifted to higher energies owing to the increase in a bandgap energy with reducing the temperature. Low temperature PL spectra for both DWELL stuctures investigated are shown in Fig. 3.17. In more detail, InGaAs-capped structure L442 presented QD-related optical transitions at 80 K of GS = 1.012 eV, ES1 = 1.071 eV, ES2 = 1.125 eV and ES3 = 1.186 eV, along with ground-state optical transition in InAs/InGaAs bi-QW of bi-QW1 = 1.319 eV. Bandgap transition of GaAs is also clearly visible for the sample L442 at E_{g}(GaAs) = 1.488 eV. Therefore, GS interband transitions for L442 DWELL structure are blue-shifted by about 60 meV, as compared to room temperature PL spectrum. In case of the uncapped DWELL structure L444, 80 K PL spectrum presented QD-related optical transitions of GS = 1.145 eV, ES1 = 1.199 eV and ES2 = 1.267 eV together with $\mathrm{VB}_2 \rightarrow \mathrm{CB}_2$ and $\mathrm{VB}_4 \rightarrow \mathrm{CB}_4$ transitions within GaAs/AlAs QW of QW1 = 1.507 eV and QW2 = 1.559 eV, respectively. Moreover, the impurity-related transition blue-shifted to Imp = 1.048 eV, while interband transition in strain-induced QD appeared at SI-QD = 1.371 eV. Therefore GS interband transitions for

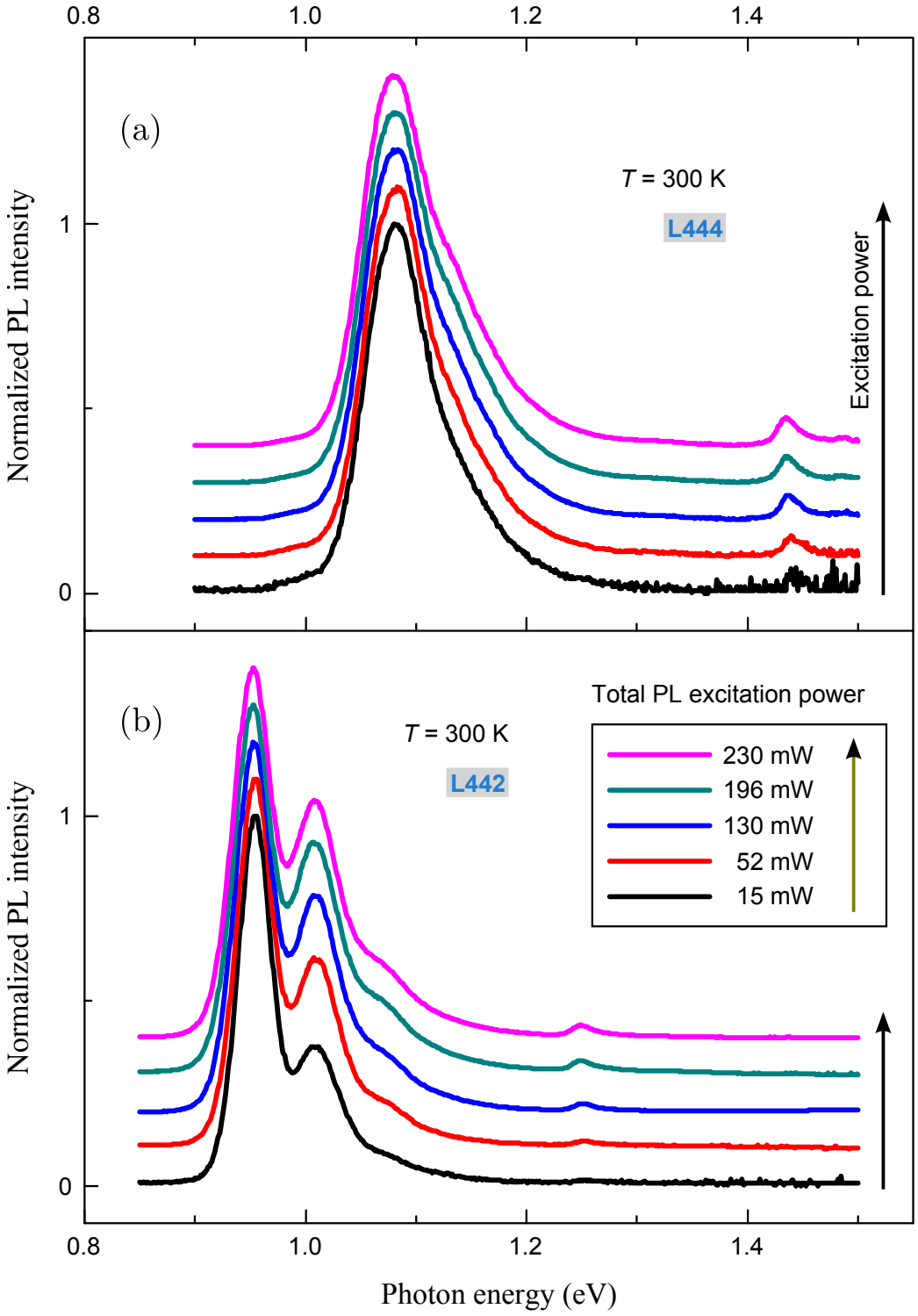

Figure 3.16 Room temperature photoluminescence (PL) spectra for the DWELL structures without (sample `L444`; (a)) and with (sample `L442`; (b)) InGaAs capping layer under variable excitation powers. Excited-states appear (develop) with the increase in PL pump power.

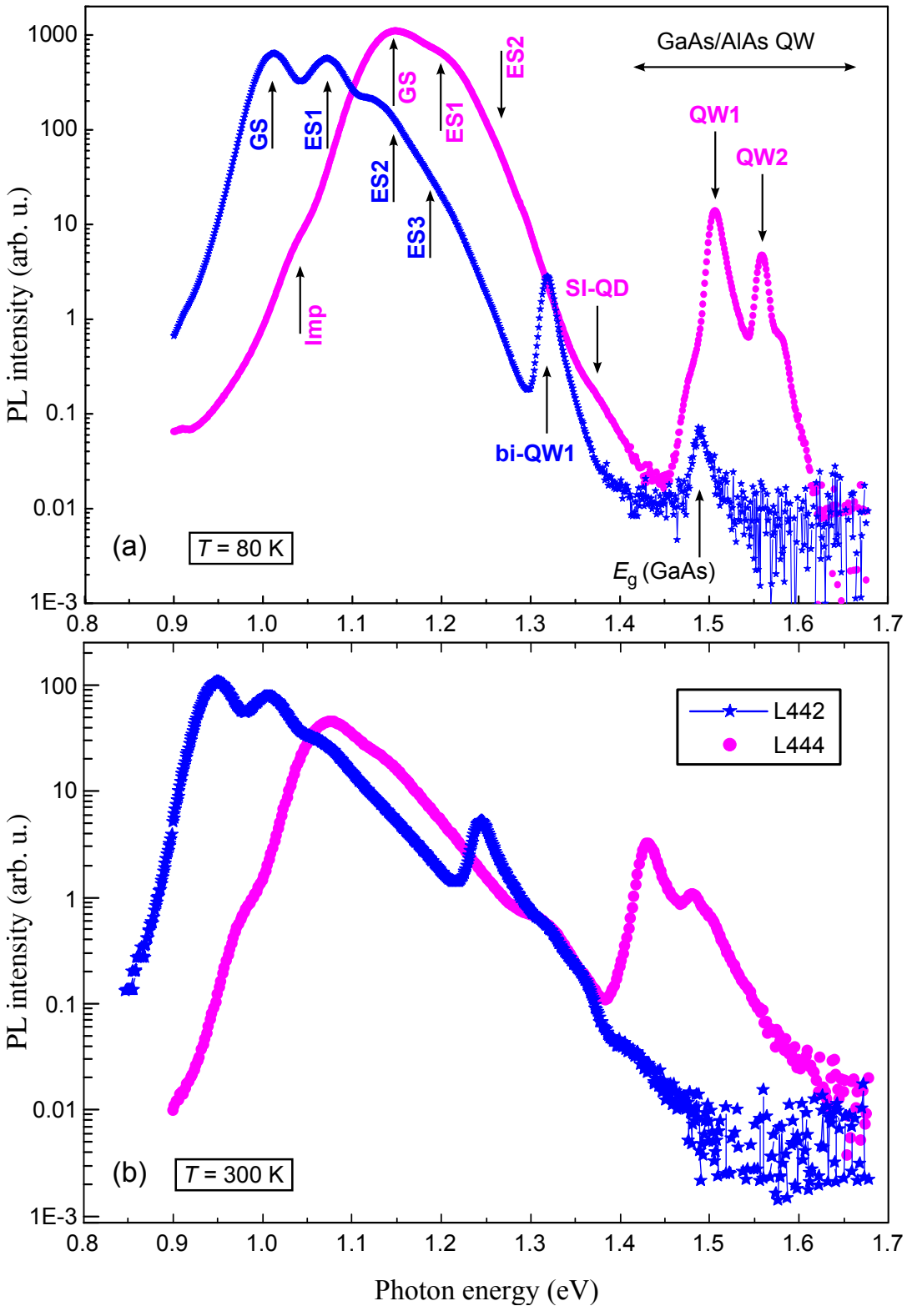

Figure 3.17 Photoluminescence (PL) spectra for the DWELL structures without (sample `L444`) and with (sample `L442`) InGaAs capping layer at liquid nitrogen (a) and room (b) temperatures. The low temperature interband transition energies for the sample `L442`: `GS` = 1.012 eV, `ES1` = 1.071 eV, `ES2` = 1.125 eV, `ES3` = 1.186 eV, `bi-QW1` = 1.319 eV and E_g(GaAs) = 1.488 eV, and for the sample `L444`: `Imp` = 1.048 eV, `GS` = 1.145 eV, `ES1` = 1.199 eV, `ES2` = 1.267 eV, `SI-QD` = 1.371 eV, `QW1` = 1.507 eV and `QW2` = 1.559 eV. Interband optical transition parameters for QD structures studied were extracted from PL spectra using a multi-Gaussian fit.

L444 DWELL structure are blue-shifted by about 70 meV as compared to room temperature PL spectrum.

Finally, experimental study revealed that InGaAs capping layer significantly improves PR and PL signal intensity, as well as shifts QD optical transitions to lower energies by about 100 meV. The red-shift of the QD ground-state could be ascribed mainly to the increasing QD sizes and decreasing strain in QDs. Strain-driven partial decomposition of the InGaAs cap layer increases the effective QD size during growth and the altered barrier composition leads to a partial strain relaxation within the capped InAs QD's. This offers a pathway to shift the photodetectivity wavelength of QDIPs, based on self-assembled InAs QDs, towards the infrared.

In content within InGaAs quantum well

Experimentally observed InAs/InGaAs bi-QW-related transition energies were exploited to estimate the actual In concentration (x) in the $In_xGa_{1-x}As$ capping layer. The experimental results were compared to calculations (based on effective mass approximation) for the model QW consisting of InAs WL and InGaAs layer. On the one part, Fig. 3.18 (top) illustrates PR moduli spectrum, which was obtained by fitting the PR data to the first derivate of a Lorentzian-type function. On the other part, vertical bars in Figure 3.18 (bottom) denote calculated energies and interband transition intensities (probabilities) for heavy- (hh$n$) and light-hole (lh$n$) related optical transitions. Additionally, squared wavefunctions of electrons and holes, calculated for the model complex InAs/InGaAs/GaAs/AlAs (having a 5 nm-thick InGaAs capping layer) and InAs/GaAs/AlAs (uncapped) QWs, are presented in Fig. 3.19, which simulate DWELL nanostructures L442 (Fig. 3.19(a)) and L444 (Fig. 3.19(b)), respectively.

According to the numerical calculations for a L444 structure, hh2 $\rightarrow$ e2 and hh4 $\rightarrow$ e4 optical transitions both have a huge matrix elements (transition probabilities) over 0.9, thus they clearly manifest themselves in optical spectra as QW1 and QW2 peaks, respectively. Moreover, by combining the results from PR and PL measurements with modeling for the InAs QDs in a complex InGaAs/GaAs/AlAs QW, an actual value of $x = 0.13$ for the $In_xGa_{1-x}As$ capping layer was was deduced.

By combining the results from the PR and the PL measurements a tentative electronic subband structure for the InAs QD, embedded in a complex InGaAs/GaAs/AlAs QW, structure was deduced, which is given in Fig. 3.18 inset. This was made by first calculating the energy difference between the

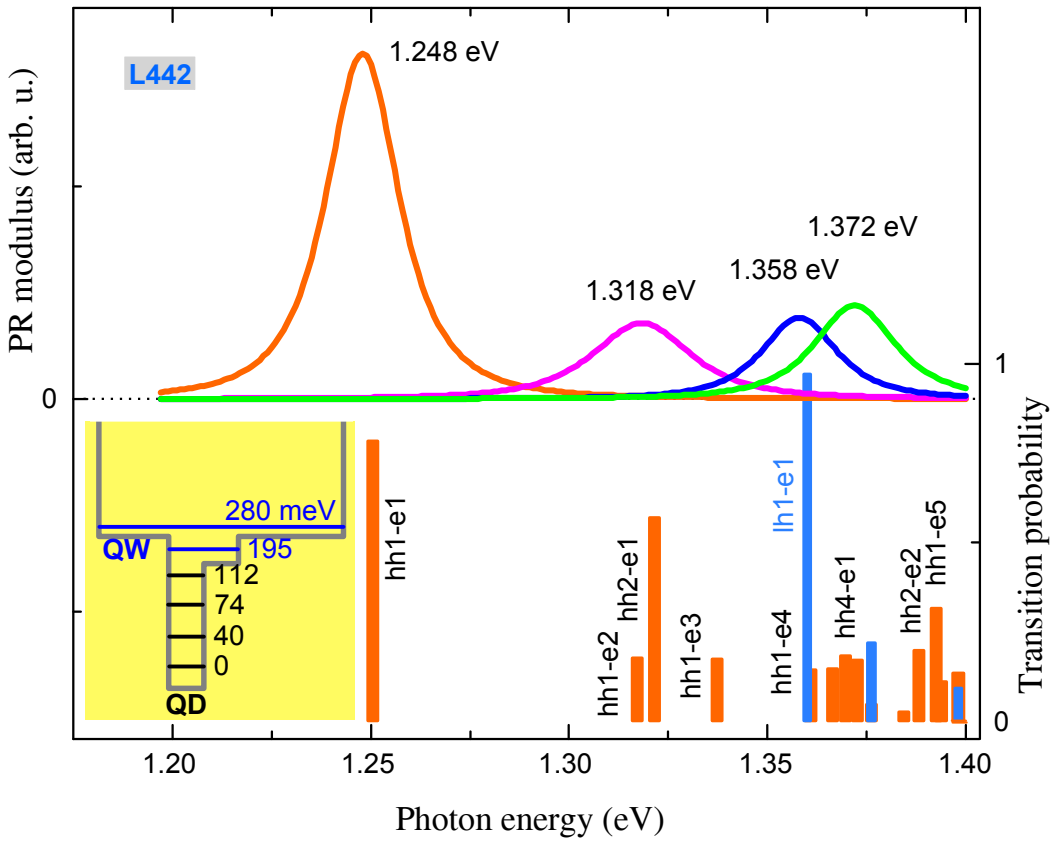

Figure 3.18 Moduli of PR lines with corresponding interband transition energies (top), obtained experimentaly from the line shape analysis of the spectra for the `L442` DWELL structure with strain-reducing InGaAs layer. Vertical bars (bottom) denote calculated energies and interband transition intensities (probabilities) for heavy- (`hh`n) and light-hole (`lh`n) related optical transitions (also presented in different colors/shades of grey). Inset: A tentative electronic subband structure for the InAs QDs in a complex InGaAs/GaAs/AlAs QW.

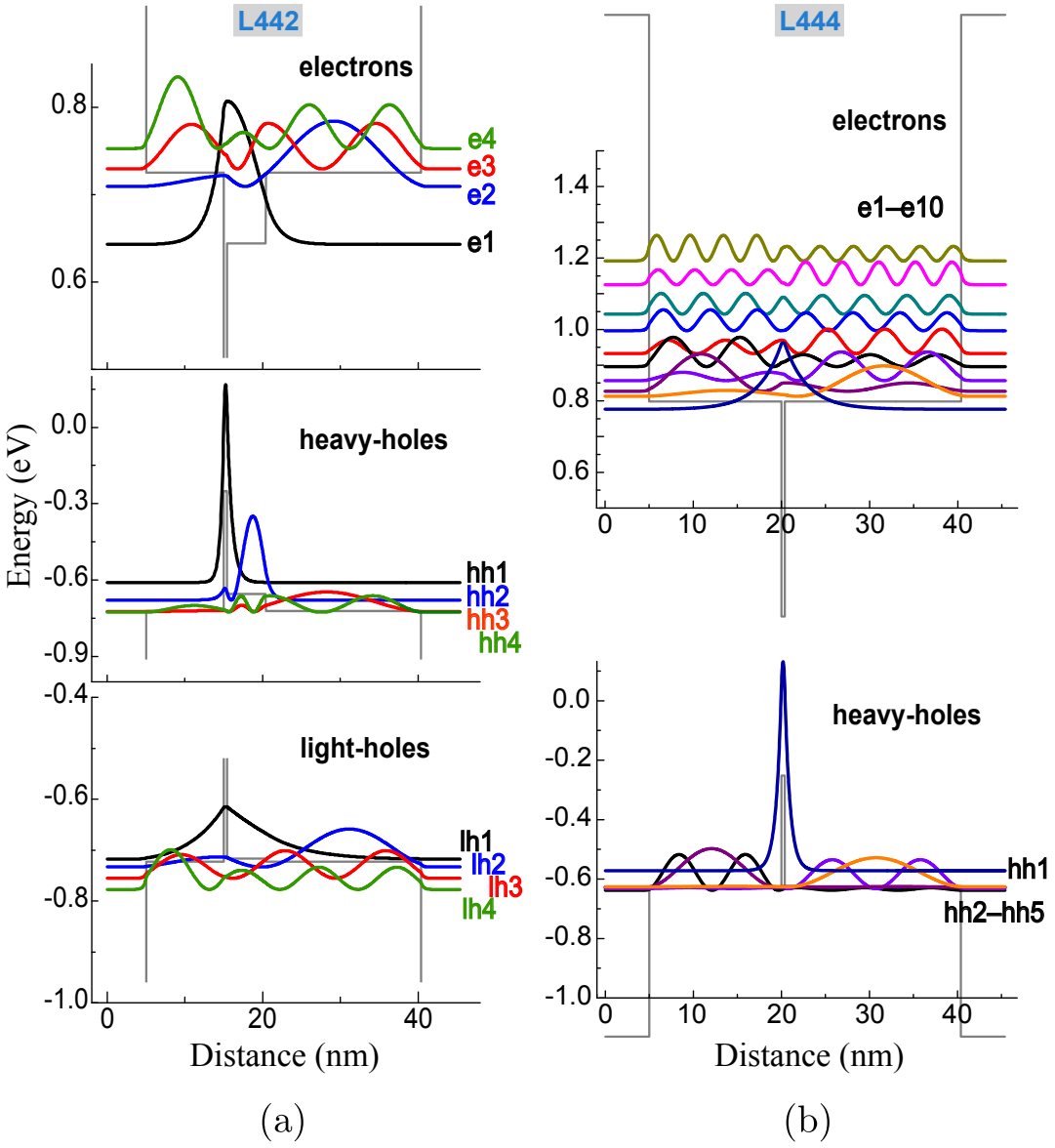

Figure 3.19 Electron and hole wavefunction calculations in the model complex InAs/InGaAs/GaAs/AlAs QW, having 5 nm-thick InGaAs capping layer (a) and InAs/GaAs/AlAs QW (b), which simulate the DWELL nanostructures `L442` and `L444`, respectively. InAs WL thickness of 0.4 nm was used.

interband transitions of higher energy and the ground state transition energy. This energy difference contains contributions both from the energy separation between the electrons in the conduction band and the holes in the valence band. To isolate the energy structure of the electrons in the conduction band, an approximate ratio between electron and hole contributions (conduction-to-valence band offset ratio) of 67% to 33% was used [69].

As one can see in Fig. 3.19, under zero electric field (the case of flat bands) electrons and holes are spatially separated due to the assymetry of DWELL structures investigated. One should remind that, despite the width and localizing potential of a QW (the depth of a well), there is always at least one electron level present in the well. In fact, effective mass ratio between electrons and heavy-holes (which enter the interband transitions at lower photon energies as compared to light-holes) along with the thickness of InAs WL — both are very small. Therefore, electron ground-state in InAs WL (there is only a single electron state in the WL) is already very shallow and its wavefunction is considerably spread in InAs/InGaAs bi-QW (see Fig. 3.19(a)), as well as in GaAs/AlAs QW (Fig. 3.19(b)), athough in the latter case the effect is not that evident. As a result of electron wavefunction spreading, while hole being tightly localized, the overlap between electron and hole wavefunctions decreases. However, the advantage (peculiarity, virtue) of asymmetrical DWELL structures is that one can observe forbidden interband transitions (i.e. the initial and final energy states having different quantum number) under applied electic field, as will be revealed in more detail in the following Subsubsection.

Interband transitions within bi-QW under electric field

As was discussed previously in Subsection 3.1.3 regarding InAs WL-related optical transitions (i.e. the intensity enhancement effect in particular) of dots-in-superlattice structures, the change in interband transition energy is induced both, by the built-in dipole moment (which is present in asymmetrical DWELL structures studied) along with the quantum-confined Stark effect (polarization of electron and hole states) under an applied electic field. To illustrate the Stark shift of optical interband transitions within DWELL nanostructures investigated, calculations were carried out. Interband transition energies in InAs/InGaAs bi-QW as a function of the applied electric field of the (capped) InAs/InGaAs/GaAs/AlAs DWELL nanostructure `L442` for a variety of heavy-hole related optical transitions is presented in Fig. 3.20.

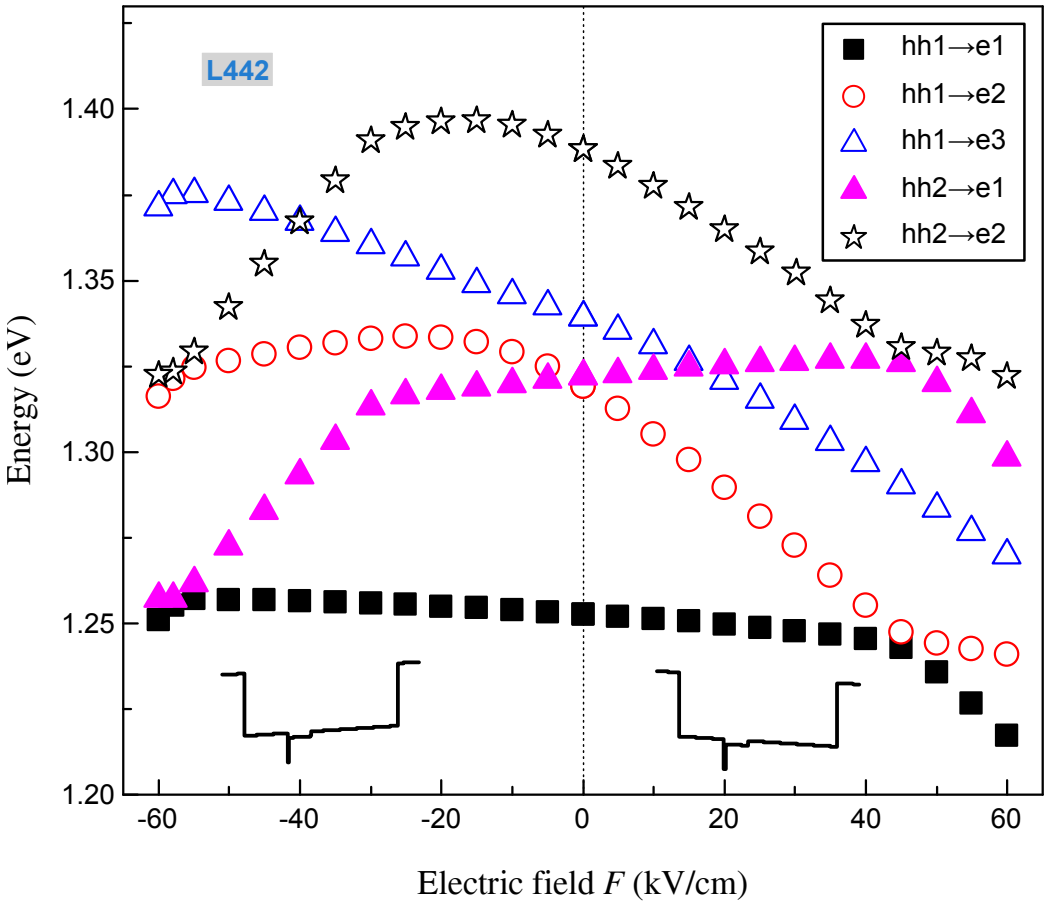

Figure 3.20 A varation of heavy-hole related interband transition energies in InAs/InGaAs bi-QW *versus* the applied electric field, calculated for the (capped) InAs/InGaAs/GaAs/AlAs DWELL nanostructure `L442`. Insets show the potential profile for different directions of the electric field $F = \pm 60\,\mathrm{kV/cm}$. The positive F values represent the growth direction of the nanostructure.

As one can see from Fig. 3.20 insets, applied electric field bends the potential profile and as a result may open even forbidden transitions, the ones, which have different initial and final quantum numbers ($n \neq m$). The presence of such non-direct interband transitions was verified by overlap integral between hole and electron wavefunctions, $|M_{\mathrm{CV}}|^2$, calculations (not shown). As it is evident from Fig. 3.20, the 11H transitions InAs/InGaAs bi-QW exhibit a small Stark shift and a small variation, as compared to 12H, 13K, 21H (which changes mostly among presented) and 22H interband transitions, athough having the highest probability of 0.7–0.8 to occur for a range of electric fields considered. Whereas, the second most intensive transition 21H has the probability of about 0.5 only. Here, the aforesaid Stark shift is caused by the asymmetry of the structure, an off-center position of the QDs within the InGaAs/GaAs/AlAs well, which can be also deduced from the asymmetrical dependence of the curves in Fig. 3.20.

These results clearly show that bi-QW-related electronic states in asymmetric QWs may be controlled by the external electric field.

3.2.3 Conclusions

Two different dots-in-a-well nanostructures — InAs QDs, embedded within InGaAs/GaAs/AlAs and GaAs/AlAs matrices — have been examined by spectroscopic PR and PL techniques together with the numerical calculations for the interpretation of the energy spectra. From the analysis of DWELL structures it was found, that

- ✓ the use of InGaAs capping layer tunes the QD ground state (GS) transition to lower energies by about 100 meV maintaining strong quantization of the electronic states;
- ✓ the changes in electronic properties (i.e. the red-shift of the QD ground-state interband transitions) could be ascribed mainly to the partial strain relaxation within the capped InAs QDs and the increase of effective QD size due to decomposition of InGaAs cap layer during growth process;
- ✓ by combining the results from PR and PL measurements with modelling, an actual value of $x = 0.13$ for the $In_xGa_{1-x}As$ cap layer was determined.

The aforementioned findings allowed to formulate the following *statement for defence*

Red-shift of the InAs quantum dot ground-state interband transitions in InAs/InGaAs/GaAs/AlAs dots-in-a-well structures is caused by partial strain relaxation and increase in effective dot size.

3.3 Energy Spectrum of Epitaxial InGaAs Quantum Rods in InGaAs Quantum Well

The typical lens-shape of Stranski-Krastanow (SK) grown QDs permits use of only transverse-electric (TE) polarized light, restricting their applicability in SOAs. These limitations are governed by the asymmetric potential profile and compressive strain, which induce characteristic splitting of heavy and light hole states. Light hole states are pushed away from the band edge and thus in-plane polarized ground state transitions (with large heavy hole component) are predominant. To modify the polarization-dependent optical gain function, QD shape and composition engineering has been proposed [7, 36–38]. Columnar QDs, also referred to as quantum rods (QRs) or quantum posts, were realized by depositing a short period InAs/GaAs superlattice (SL) on top of a seed SK QD layer by means of molecular beam epitaxy (MBE). The quantum confined structure thus consists of vertically oriented InGaAs QRs immersed in a two-dimensional InGaAs layer. By carefully choosing the growth parameters, QRs with aspect ratios (height/diameter) significantly > 1 were obtained [7, 37]. Very recently, it was demonstrated both theoretically [39] and experimentally [40, 41] that a critical indium composition contrast between the $In_xGa_{1-x}As$ QR and the surrounding $In_xGa_{1-x}As$ layer, or quantum well (QW), $x_{QR}/x_{QW} > 3$ is needed to alter the polarization properties in favour of the TM mode. Moreover, as was deduced in [39], this composition contrast is more important than the aspect ratio in achieving zero net axial strain at the centre of an elongated dot, and hence enhancing the intensity of TM light with respect to TE components. Such elongated nanostructures, following optimization of both their composition and geometry, already appear very attractive for fabrication of polarization-insensitive SOAs. Furthermore, alongside such practical applications, QR structures are a model system for fundamental research, because they present a crossover between zero-dimensional and one-dimensional quantum confinements.

QR formation can be affected greatly by the growth parameters, including growth temperature, growth interrupts, the number of SL periods, and the type of As source used [42]. To optimize the growth parameters and implement new designs of these unique quantum structures, an in-depth knowledge of their optical and electronic properties is required. In recent studies, modulated reflectance spectroscopy, in particular photoreflectance (PR) and contactless electroreflectance (CER), alongside pho-

toluminescence (PL) [42], has been successfully employed to characterize low-dimensional systems and nanostructures [29, 33] including QRs [43].

To investigate the effects of the As source on the optical properties of the QR structures, two sets of QR samples were grown with SL periods $N = 10$, 20, and 35; these are designated `QR10`, `QR20`, and `QR35`, respectively. Both sets of structures were grown with As_2 and As_4 sources, using the same growth conditions.

In this Section, modulated reflectance spectroscopy and photoluminescence (PL) have been used to explore the optical properties and electronic structure of InGaAs quantum rods (QRs) grown by molecular beam epitaxy. Different As sources — As_2 and As_4 — were used during epitaxial growth in order to evaluate their effect on the optical properties of the nanostructures. Spectral features associated with interband optical transitions taking place in the QR and the surrounding quantum well (QW) regions are examined. Experimental results are then compared with calculations performed within the envelope function approximation. It is found, that the optical properties of the samples grown under identical conditions depend strongly on the As source used during MBE growth. In particular, a red-shift of the QR- and a blue-shift of the QW-related optical transitions, along with a significant increase in PL intensity, have been observed if an As_4 source is used. These changes in optical properties are mainly attributed to quantum confinement effects related to a variation of indium content in the QR and QW regions, as well be discussed hereinafter in detail.

3.3.1 Full optical view of InGaAs quantum rod structures

Room temperature PR and PL spectra for the As_4- and As_2-grown `QR20` samples are shown in Fig. 3.21. These samples have a nominally identical structure with an $N = 20$ period SL. The PR spectra are typical for the QR samples investigated and show four principal sets of spectral features associated with the various interband optical transitions in QR structures. The sharp feature in the high-energy region at 1.67 eV (marked by vertical arrows) is attributed to a bandgap transition in the AlGaAs confining layer. Analysis of the spectrum suggested a 20.5% aluminium content, which agrees well with the nominal value of 20%. For energies above the characteristic GaAs bandgap energy at 1.42 eV, an oscillating signal, resembling that of Franz-Keldysh oscillations (FKO), appears. However, a plot of $4/3\,\pi(E_m - E_g)^{3/2}$ as a function of the extremum index number m (see Fig. 3.22) does not follow a straight line, as would be the case for the

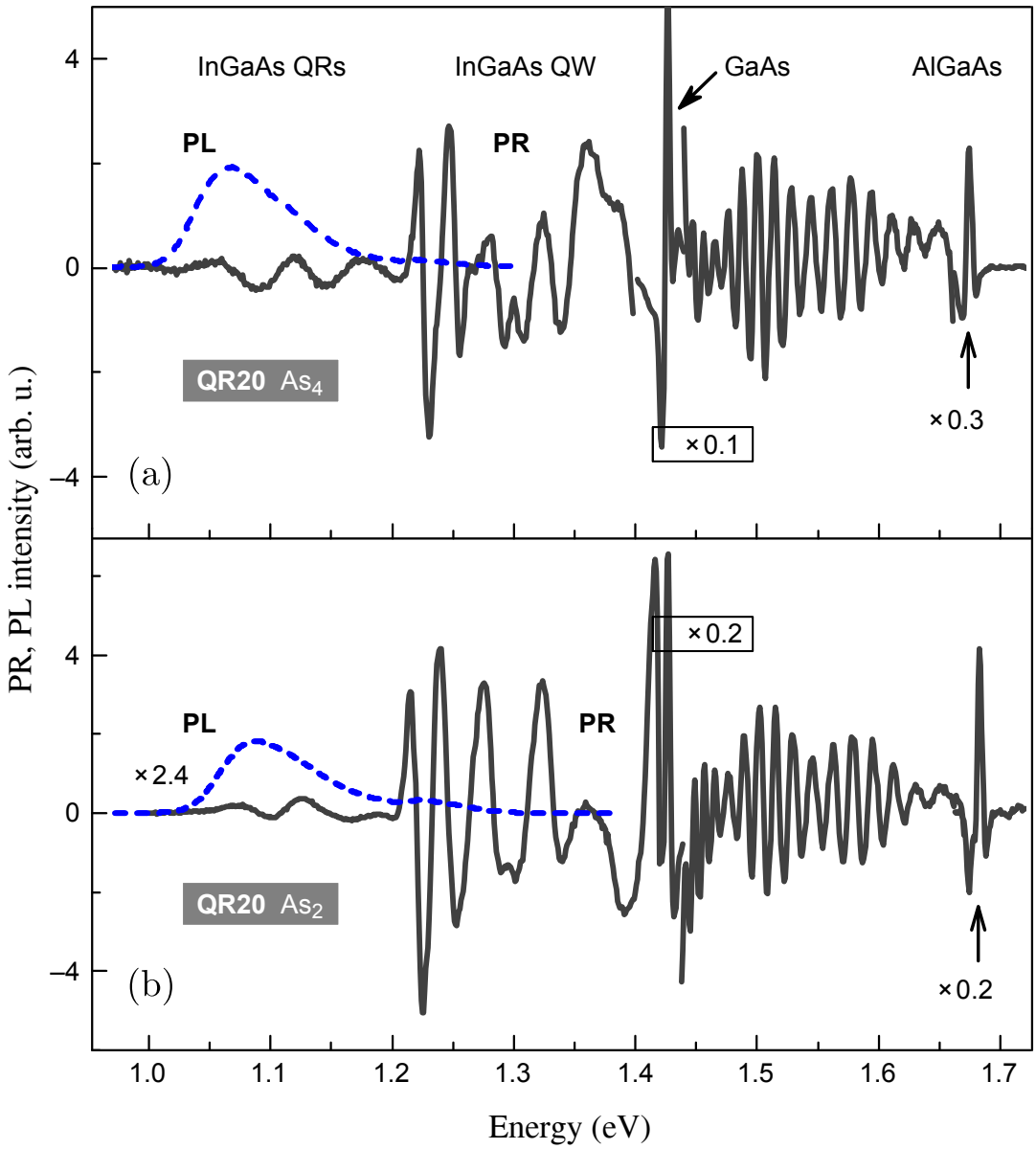

Figure 3.21 Room temperature photoreflectance (PR) and photoluminescence (PL) spectra (solid and dashed curves, respectively) of the QR20 samples grown using (a) As_4 and (b) As_2 sources. The QRs were grown as a 20 period GaAs/InAs (3 ML/0.64 ML) SL.

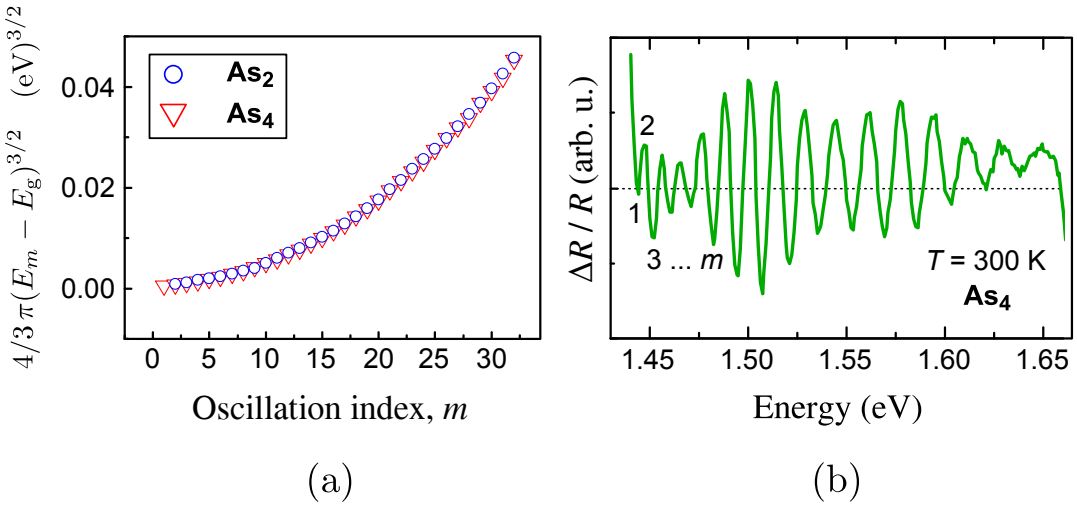

Figure 3.22 Plot of the quantity $4/3\,\pi(E_m - E_g)^{3/2}$ *versus* the extremum index number m for the As_4-grown QR20 sample (a), which oscillating part of room temperature PR spectra is given in (b). In case of FKO effect present, straight line behaviour of functionality (a) is expected.

FKO effect. Therefore, we deduce that the PR oscillating signal is related to optical transitions between the quantum states located above the GaAs barrier. Indeed, the inclusion of the AlGaAs layer for better carrier confinement supports the formation of quasi-bound above-barrier states. Note that similar optical transitions have been observed previously in PR [70] and electroreflectance [71] spectra of QWs, primarily at energies above the bandgap of the barrier material. A rich PR structure is then observed below the bandgap of GaAs, in the energy interval 1.2–1.42 eV. This corresponds to a number of optical transitions occurring in the InGaAs QW, surrounding the QRs. Finally, in the low-energy region of 1–1.2 eV, the PR spectrum exhibits broadened features related to interband transitions in the InGaAs QRs. This last assignment is supported by PL data (Fig. 3.21, dashed lines), as well as by contactless electroreflectance (CER) spectroscopy of similar QR structures [43]. Hereafter, we will consider the optical transitions in the QR and QW regions in more detail.

Figures 3.23 and 3.24 show a comparison of PR and PL spectra measured at room temperature for the QR20 and QR35 samples, respectively, grown with As_4 and As_2 sources. It should be noted that both QR20, and QR35 samples exhibit a significant enhancement in the photoluminescence intensity when the As_4 source was used in a growth process. It should be noted that the positions of the peaks in the PR modulus spectra correspond to the optical transition energies, whilst their heights are proportional to the intensity of the transitions.

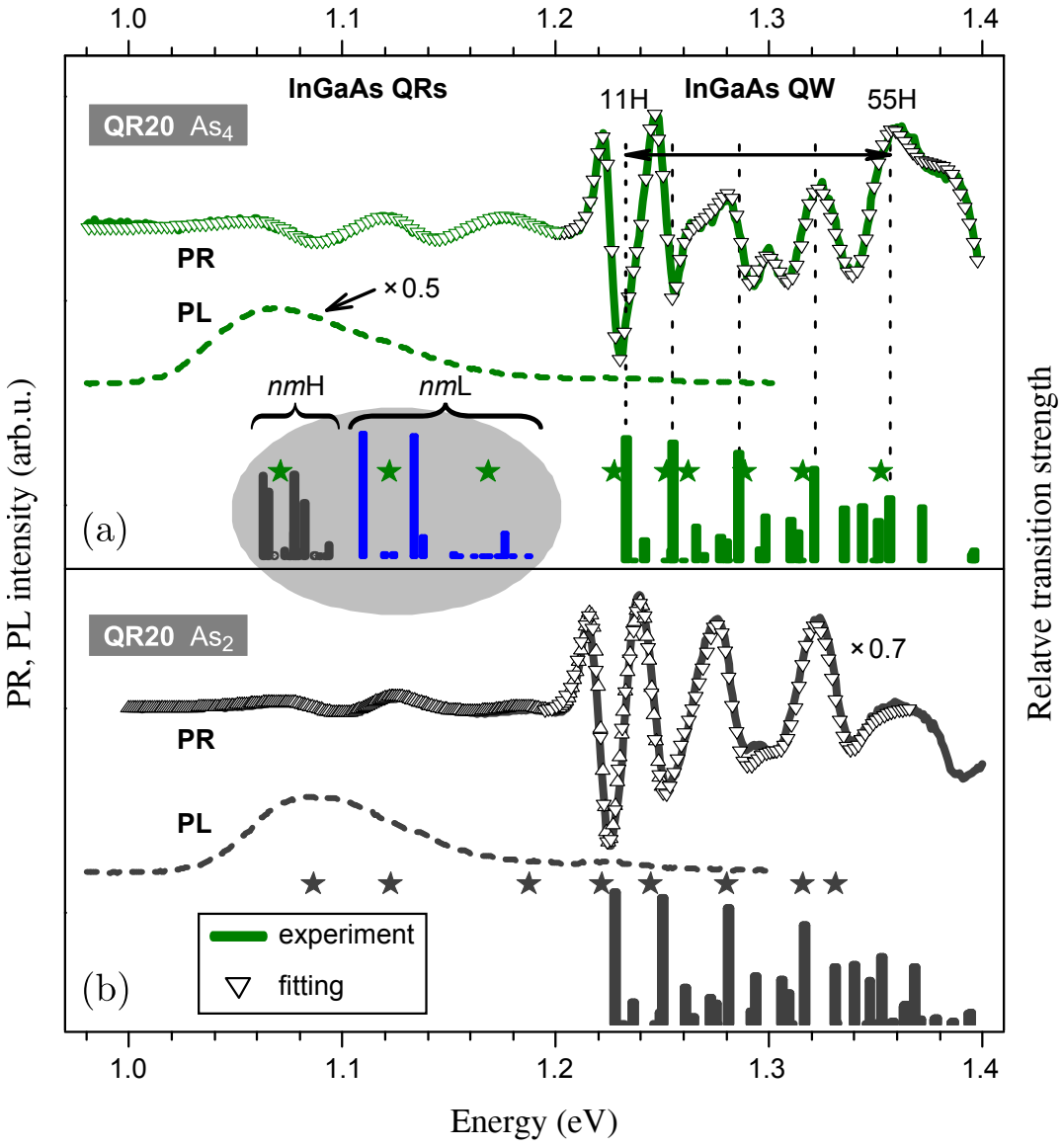

Figure 3.23 Room temperature PR and PL spectra for the InGaAs QR20 structures grown using As_4 (a) and As_2 (b) sources. Stars denote the interband transition energies determined from the fitting of the PR spectra to the first derivative of a Lorentzian-type function (open triangles). Vertical bar positions and amplitudes indicate numerically evaluated energies and relative strengths of the interband transitions in InGaAs QRs (only for As_4-grown structure) and the surrounding InGaAs QW.

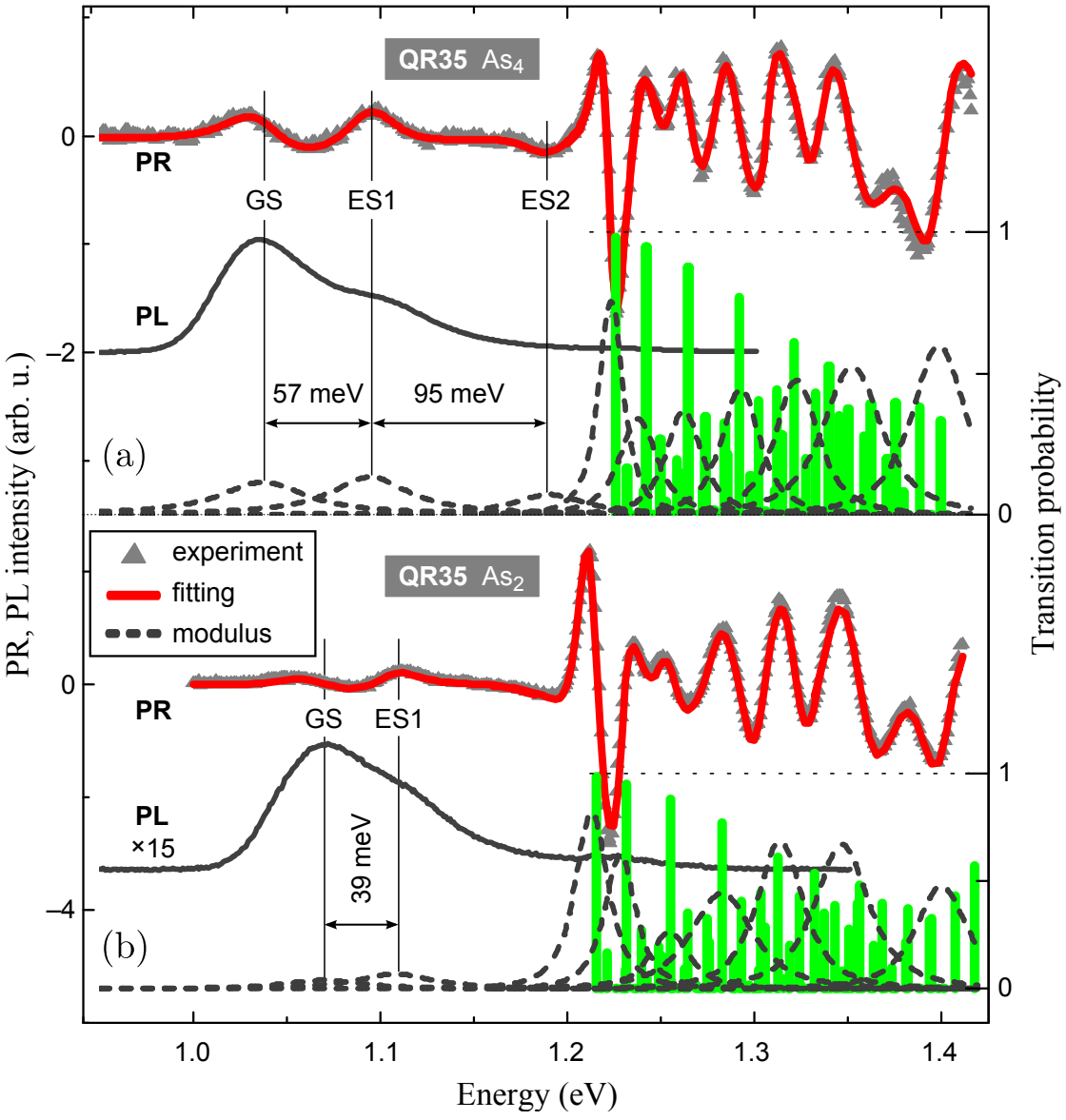

Figure 3.24 Room temperature photoreflectance (PR) spectra (triangles) for the InGaAs QR structures grown as a 35-period SL using (a) As_4 and (b) As_2 sources, together with the fitting curves (solid lines) and the modulus of the PR resonances (dashed lines). Vertical bars indicate numerically evaluated energies and relative strengths, M^2_{CV}, of the optical transitions in the InGaAs QW layer. Photoluminescence (PL) spectra are also shown for comparison. `GS`, `ES1` and `ES2` denote interband transitions from ground and two excited states, accordingly.

3.3.2 Optical transitions in InGaAs quantum well

It can be seen in Figs. 3.23 and 3.24 that PR spectra in the QW region exhibit a rich structure owing to the relatively wide (32 nm and 41 nm) wells, resulting in a large number of confined levels. To identify the spectroscopic features, calculations of the energy levels and interband transition energies in the strained InGaAs/GaAs QWs were carried out, using the nextnano[3] simulation package. The overlap integrals of electron and hole wavefunctions were also calculated. The calculations, based on an effective mass approximation, were performed with material parameter values taken from Ref. [60] and using the nominal values for QW widths. The In content, x_{QW}, was then determined by fitting the calculated transition energies to the experimental values. x_{QW} was found to be in the range of 0.175–0.19, depending on the precise QR sample being investigated, in reasonable agreement with the value of 0.16 estimated from the growth parameters. It was assumed that the indium content, x_{QW}, follows a Fermi function at the material interfaces (with a Fermi step at each interface), taking into account segregation-related interface grading [7].

The vertical bars in Figs. 3.23 and 3.24 indicate the calculated relative strengths (overlap integrals) of the optical transitions under zero electric field (flat band) conditions. It should be noted that due to a weak light-hole confinement, the PR spectra are dominated by the optical transitions mnH between the heavy-hole (n) and electron bound states (m) with the same quantum number ($n = m$). However, the transitions with $n \neq m$ are also allowed. In general, the calculated energies for the transitions mnH qualitatively match the spectral positions of the main PR features for the samples studied. A more complicated PR spectra was found for the `QR10` As_4-grown structure (not shown), which present as well the bimodal character of the lowest 11H transition (apparent also in Fig. 3.25(a) around 1.2 eV), probably associated with fluctuations in QW width. However, the sharp PR resonances of QW-related excitonic transitions reveal good structural uniformity of the QR structures grown with 20 and 35 period SLs, which is consistent with transmission electron microscopy (TEM) measurements [7, 42].

Figure 3.25(a) shows the dependencies of the experimental (large open symbols) and calculated (small full symbols) transition energies on the SL period number, N, for QR samples grown with As_2 and As_4. As can be seen from the figure, the energies of optical transitions in the QW region depend strongly on the number of SL periods, as well as on the As source

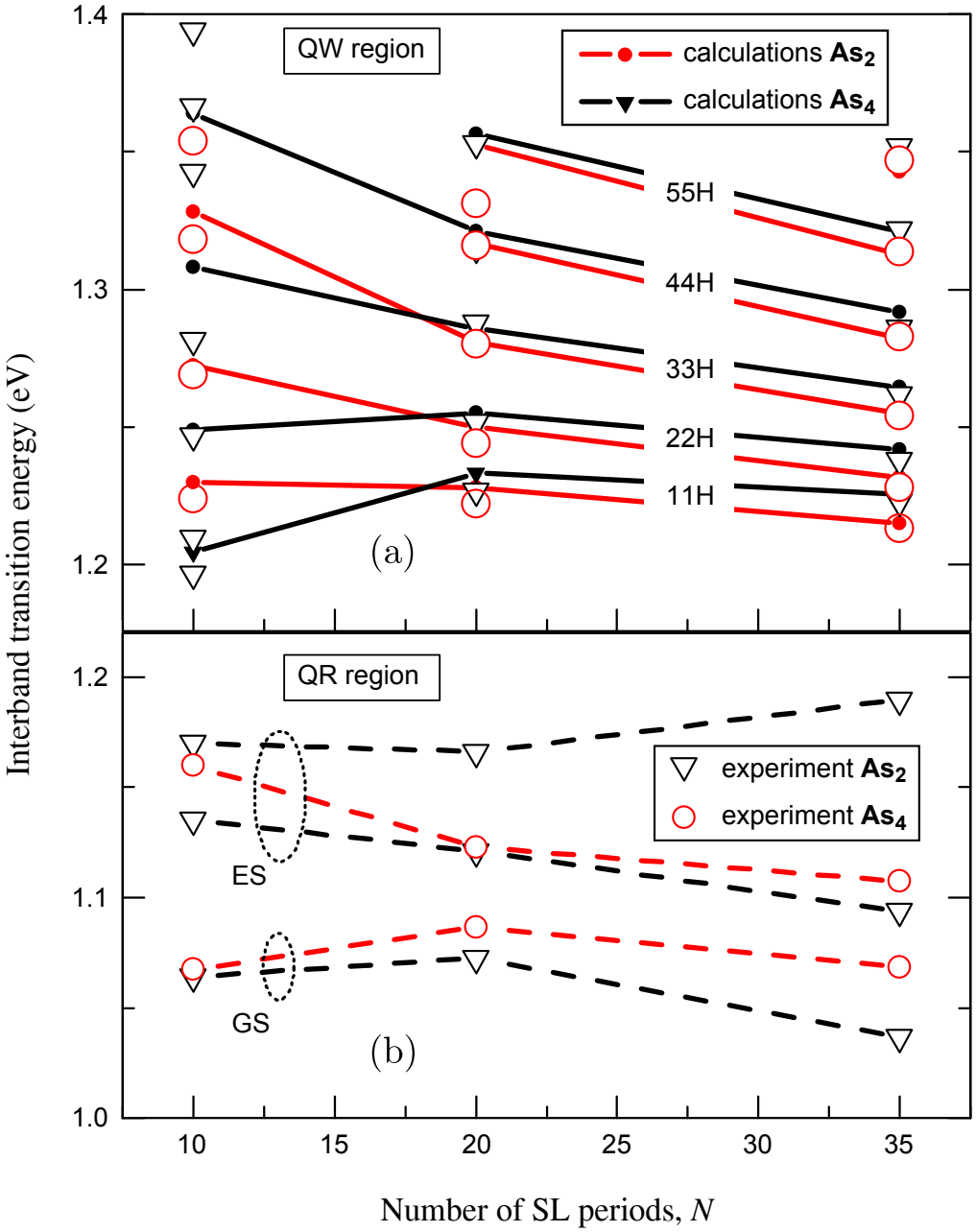

Figure 3.25 Dependencies of the experimental (large open symbols) and calculated (small full symbols) interband transition energies as a function of the SL period number for QR samples grown using As_4 and As_2 sources: (a) QW-, and (b) QR-related optical transitions. GS and ES denote QR-related interband optical transitions from ground and excited states, respectively. The solid lines in (a) and the dashed lines in (b) are drawn as a guide for the eye only. Experimental data is obtained from analysis of the PR spectra.

used. For the QR10 data set, the ground-state optical transitions, 11H, for the As_4-grown sample occur at lower energy, compared with the As_2-grown sample. However, the converse is true for the QR20 and QR35 sets of samples. Here, both the experimental results, and calculations, demonstrate that the use of an As_4 source results in a noticeable blueshift of the QW-like ground (11H) and excited (22H, 33H, 44H, 55H) optical transitions. According to the calculations, the observed blue shift of the QW-related optical features for the As_4-grown samples is attributed to a decrease of indium content, x_{QW}.

3.3.3 Optical transitions in InGaAs quantum rods

As can be seen in Figs. 3.23 and 3.24, low-energy PR features at 1.04 eV (1.07 eV) and 1.07 eV (1.09 eV) for As_4- and As_2-grown samples QR35 (QR20) respectively, are located at the maxima of the broad PL bands and therefore correspond to the ground-state (GS) transitions in the QRs. Furthermore, the higher energy PR features, appearing close to the high energy shoulders of the PL spectra should be related to the QR excited state (ES) interband optical transitions. The optical transitions in the QR region also depend strongly on the SL period number, N, and the growth mode (As_2 or As_4) of the QR samples. One can ascertain from Fig. 3.25(b), that the ground-state PR/PL features (GS) first experience a blue-shift and then a red-shift with increase of SL period number in a similar manner to the 11H QW-related optical transitions. The principal reason for the blue-shift can be attributed to In-Ga atom intermixing and In segregation during the QR growth, whilst the red-shift can be explained by enhanced vertical electronic coupling with increasing QR length [7]. When considering the effect of the As source on the relative energy of the ground-state transitions, however, it is important to emphasize that the behaviour of the $N = 20$ and $N = 35$ data is opposite to that of the QW-related 11H transitions. There is now a red shift of QR-related optical transitions for the As_4-grown samples compared with the As_2-grown samples, as shown by the data presented in Fig. 3.25(b). One can assume that this is due to a variation of the indium content, x_{QR}, caused by the different growth kinetics when using the two sources. It was argued previously that the formation of In-rich QRs, together with In-reduced InGaAs QW layers, is related to the different In and Ga diffusion lengths under As_2 and As_4 fluxes [42]. Indeed, due to the higher reactivity of As_2 to Ga adatoms, the lateral flow of Ga atoms is enhanced with an As_4 flux [72]. Under these circumstances, more In-rich QRs are grown under an

As_4 flux. This supposition is confirmed by scanning-TEM measurements, i.e. the In content of QRs grown using As_4 is larger than that of samples grown under an As_2 flux [42].

To analyze the effect of indium content, x_{QR}, on optical transitions originating from the QRs, we calculated the electronic states based on a model QR. Calculations were performed using a fully 3-D approach taking into account strain and piezoelectric effects. The QR was assumed to have a cuboid shape with a height h and a square base of length d. The key parameters were then varied as follows: $30 \leq h \leq 35\,\text{nm}$, $8 \leq d \leq 14\,\text{nm}$, $0.45 \leq x_{QR} \leq 0.6$ and $0.16 \leq x_{QW} \leq 0.2$. From the simulations, which for the structure `QR20` is presented in Fig. 3.23(a) by vertical bars (within grey ellipsis background), the calculated energies were typically from 60 meV to 140 meV above the measured energies for a given input set of parameters. [In Fig. 3.23(a) the calculated energy values of the `QR20` nanostructure are therefore red-shifted by 130 meV to match experimental ones.] The slight discrepancy between the calculated and measured transition energies could be attributed to limitations of the effective mass approximation and excitonic effects. However, the behavior of calculated optical transitions agrees, in general, with the experimental observations well. In particular, it was found that the lowest-energy PR and PL features are due to transitions between heavy-hole and electron states, whilst higher-energy QR features involve light-hole related transitions. Finally, it is worth noting that the calculations predict the red shift of QR-related optical features owing to the formation of more indium-rich QR structure under an As_4 flux.

In addition to the above-mentioned spectral peculiarities, associated with the `GS` interband optical transitions in InGaAs QR, another striking feature is that the energy spacing between `GS` and `ES` transitions strongly depends on As source used, as discussed hereinafter.

3.3.4 Carrier confinement effects

The relative red shift of QR-like and blue shift of QW-like ($N = 20$, 35) optical transitions for samples grown with an As_4 flux indicates that the carrier confinement, defined as the energy spacing ΔE between lowest QW-related transition and the QR ground-state transition, is enhanced in As_4-grown QRs. This is clearly seen in Fig. 3.26(a), where the energy spacing ΔE is plotted as a function of the SL period number. Here, ΔE increases with SL period N from 134 meV to 186 meV for As_4-grown QRs. In contrast, there is little change in ΔE for As_2-grown samples. This increase of carrier

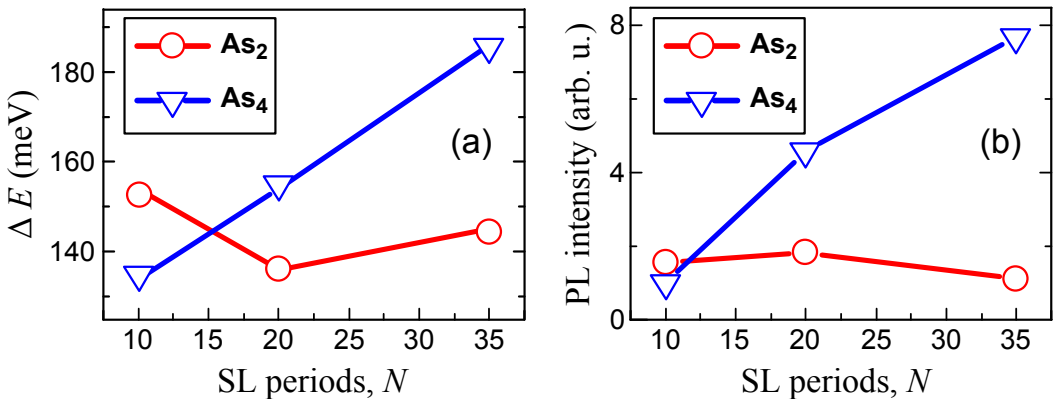

Figure 3.26 Dependencies of the energy separation ΔE between the InGaAs QR-related ground-state and QW-related 11H transitions on SL period number for samples grown using As_4 and As_2 sources (a). Variation of PL peak intensity with SL period N for As_4- and As_2-grown samples (b).

confinement in As_4-grown QRs is also evident in Fig. 3.24 from:

1. The appearance of extra PR feature (second excited state, `ES2`) around 1190 meV in the As_4-grown sample;

2. Increase in the energy spacing between QR ground (`GS`) and first excited (`ES1`) states for the As_4-grown sample.

The energy spacing between `GS` and `ES1` in As_4-grown QR is 57 meV, while that in As_2-grown QR is 39 meV. As discussed in [73], this increase in energy level spacing corresponds to the electron wavefunctions being more tightly confined in the As_4-grown QR structures. This could be an important factor for improving recombination efficiency and PL intensity in QR devices, such as SOAs. Indeed, as can be seen from Fig. 3.26(b), the PL intensity of QRs with larger SL period numbers improves significantly for larger period SLs, $N = 20$, 35, when grown using the As_4 source. It is apparent that the dependencies of PL intensity and the ΔE spacing on SL period for As_4-grown QR samples are related. It was suggested in Ref. [42] that the PL intensity enhancement should be attributed to lower impurity incorporation into the epitaxial layer during growth, owing to the cracker zone on the arsenic cell being cooler. Morover, the increase of the PL efficiency, alongside thermal decoupling effects [74], could be accounted for by changes in the oscillator strength of the optical transitions, which depends to a great extent on the potential profile of the QRs [39].

Through analyzing the intensities of the PR features (Figs. 3.23 and 3.24) we cannot directly determine the oscillator strengths of optical transitions, because the amplitude of the modulated reflectance depends on a number of parameters, such as the modulation efficiency, and the internal electric

fields. In such cases, only the relative intensity of different optical transitions can be compared. To estimate the relative oscillator strength of the transitions for As_2- and As_4-grown QRs, the PR modulus amplitudes were normalized to that of the InGaAs QW-related 11H transition. The PR modulus spectra, which are proportional to the oscillator strengths of the optical transitions, together with PL spectra for `QR35` samples, are shown in Fig. 3.27. It can be noted that the ground state transitions in the QR region are weaker in intensity compared to the interband optical transition from the first excited states (neighbouring PR features, as well as the broad PL shoulder). This can be explained by the different localization of electron and heavy-hole wavefunctions. The former are localized at the centre of the QR, whereas heavy-hole wavefunctions tend to localize at the sidewalls, hence the overlap of the wavefunctions is small [39]. As is evident from the Fig. 3.27, the amplitudes of PR modulus spectra, as well as the PL intensity, for the As_4-grown sample are considerably enhanced compared to the As_2-grown sample. Therefore, it is reasonable to assume that the increase of PL intensity in QRs grown under an As_4 flux is related to an increase of the oscillator strength of the optical transitions, which is most likely associated with an enhanced electron-hole wave function overlap for As_4-grown In-rich QRs. Comparative analysis of the PR modulus spectra for the `QR35` (Fig. 3.27) and `QR20` samples reveals that the ratio of both PL and PR intensities of QR-related transitions in As_4- and As_2-grown samples tends to increase with SL period. This experimental observation correlates with the PL intensity dependences shown in Fig. 3.26(b) and confirms our interpretation of the optical data.

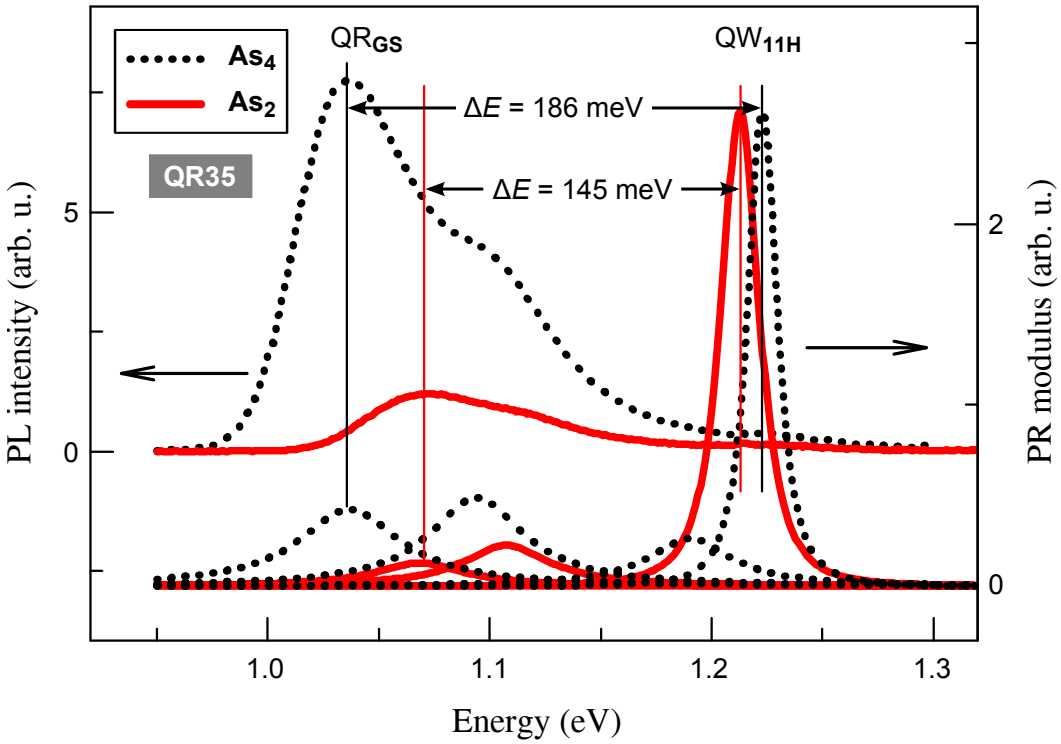

Figure 3.27 PL spectra and modulus of individual PR resonances for `QR35` samples consisting of a 35 period GaAs/InAs (3 ML/0.64 ML) SL grown using As_4 (dotted curves) and As_2 (solid curves) sources. The PR modulus data are normalized to that of 11H optical transitions of the InGaAs QW. ΔE denote energy separation between the InGaAs QR-related ground-state `GS` and QW-related 11H transitions.

3.3.5 Conclusions

In summary, the differences in the optical properties of As_2- and As_4-grown InGaAs QR samples have been examined by photoreflectance spectroscopy and photoluminescence techniques. It was found that

- compared with As_2-grown samples, a stronger PL intensity, a longer emission wavelength, and an increased energy spacing between the ground- and excited-states are observed for As_4-grown samples.
- The energy spacing $\triangle E$ between the QR and QW ground state transitions also increases for As_4-grown samples.
- These changes in optical properties can be explained in terms of enhanced carrier confinement in As_4-grown QRs owing to an increased indium composition contrast between the QR and surrounding QW layer.

It is suggested that different In and Ga diffusion lengths under As_2 and As_4 fluxes are responsible for the observed features.

In particular, for the QR structure `QR20` it was found that

✓ the red-shift by ≈ 20 meV for QR- and blue shift by ≈ 10 meV for QW-related transitions, as well as PL intensity enhancement by a factor of 2 have been observed, if As_4 source was used instead of As_2;

✓ changes of QR- and QW-related optical spectra from As_4- to As_2-grown samples could be assigned to the variation of In contents x_{QR} and x_{QW}, respectively;

✓ energy states of a model QR were numerically calculated using effective mass approximation. It was found, that the lowest-energy PR and PL features are due to transitions between heavy-hole and electron states, whilst higher-energy QR features involve light-holes.

The aforementioned findings allowed to formulate the following *statement for defence*

InGaAs quantum rods grown using As_4 source exhibit a stronger photoluminescence intensity, a longer emission wavelength, and a larger energy spacing between the ground- and excited-states, as compared to As_2-grown nanorods, due to enhanced carrier confinement. These features are attributed to an increase of indium composition contrast between InGaAs quantum rods and the surrounding InGaAs well.

3.4 Optical Anisotropy of Epitaxial InGaAs Quantum Rods

Alongside comparable TE and TM optical mode coupling, very favourable for SOAs, QRs have a large intrinsic dipole moment, which seems to be very promising for quantum memories and nonlinear electro-optic devices [75]. However, structural (TEM) analysis of such elongated nanostructures bring a clear evidence of in-plane shape anisotropy. Furthermore, very recent theoretical and experimental optical studies confirm the presence of optical anisotropy of QRs, suggesting that not only the shape anisotropy should be addressed therein. Indeed, it was assumed that material composition gradients, asymetric strain distribution, piezoelectrical effect and even bending of the stacking direction during growth are responsible for the features observed, owing to the huge estimations of optical anisotropy.

In this Section, optical polarization properties of two sets of quantum rod (QR) structures, grown on (001)-oriented GaAs substrate with SL periods $N = 10$, 20, and 35, are investigated [7.§]. Self-assembled nanostructures, comprising of InGaAs QRs immersed into 2-D InGaAs layer (QW), are examined by polarization-resolved photoreflectance (PR) and photoluminescence (PL) spectroscopy techniques [30], which already proved to be very productive for QR investigations [5.§, 6.§].

The effects of the QR height (number of SL periods deposited) along with the As source (As_2 or As_4) used in MBE growth on the polarization properties and electronic structure of InGaAs QRs are mostly considered. Special emphasis is placed on spectral features associated with interband optical transitions occurring in the InGaAs QRs and the surrounding InGaAs quantum well (QW) regions for As_2/As_4-grown nanorod structures.

While in the previous studies the polarization response of QDs and QRs was investigated for a single indefinite TE-mode [40], our polarization-resolved PR and PL measurements revealed a unique property of InGaAs QR that the TE response is anisotropic in the (001)-plane. Therefore, a single TE-mode is not sufficient to fully characterize the polarization response.

3.4.1 Polarized photoreflectance of InGaAs quantum rods

Room temperature PR and PL spectra for the As_4-grown sample `QR35` are shown in Fig. 3.28. The PR spectrum presents four groups of optical fea-

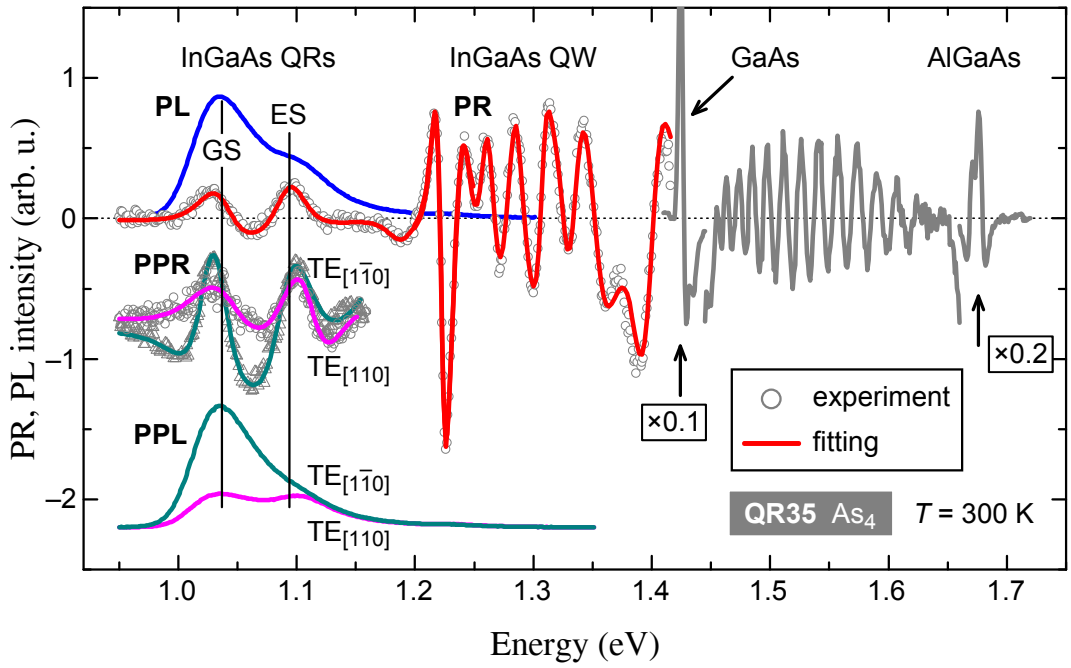

Figure 3.28 Room temperature photoreflectance (PR) and photoluminescence (PL) spectra of the As_4-grown sample QR35. Polarized PR (PPR) and PL (PPL) spectra show a significant in-(001)-plane polarization anisotropy in the region of InGaAs QR-related interband transitions.

tures, which correspond to various optical transitions in the QR structure investigated, and which were successfully modeled within the envelope function approximation [5.§, 6.§]. An optical feature at 1.67 eV is due to the bandgap transition in $Al_{0.2}Ga_{0.8}As$ layer. Pronounced oscillations in the spectral range of 1.42–1.67 eV can be attributed to the above-GaAs-barrier states. Optical features 1.2–1.4 eV correspond to the optical transitions occurring in the InGaAs QW, that surrounds QRs. Finally, optical features in the 1–1.2 eV region correspond to the ground and excited state transitions in QRs.

Characteristic rhombus shape of QRs clearly visible in a (001)-plane TEM images (see the Section "Quantum Structures Studied" in the Chapter "Samples and Experimental" for InGaAs QR structure TEM images) suggests an optical anisotropy to be considered. Due to this reason, we have analyzed linear polarization properties for the light propagation in the growth direction. As one can see from Fig. 3.28, linearly polarized PR (PPR) and PL (PPL) spectra revealed a significant in-(001)-plane polarization anisotropy in the spectral region of InGaAs QR-related interband transitions, which will be considered in-detail hereinafter.

Further, we focus on the spectral regions of the QR structures — low photon energy interband transitions within InGaAs QR and the surrounding

InGaAs QW.

3.4.2 Carrier confinement in InGaAs quantum rods

Firstly, we have studied the impact of As (As_2 and As_4) source used during MBE-growth on optical properties of QRs. A comparison of room temperature polarized PR (PPR) spectra at two perpendicular polarization angles for As_4- and As_2-grown `QR35` samples (Fig. 3.29) illustrates some following notable characteristics. Firstly, the low-energy QR-related features in experimental spectra are red-shifted for the As_4-grown structure as compared to the As_2-grown. Second characteristic, contrasting to the just-mentioned, is a blue-shift of the QW-related features for the As_4-grown sample in respect of those for the As_2-grown. Moreover, the intensity of a PL (not shown) and PR signal is significantly enhanced if the As_4 source is used instead of As_2.

The relative red-shift of QR-like and blue-shift of QW-like optical transitions for the As_4-grown QR sample was analyzed in terms of the carrier confinement, defined as the energy spacing ΔE between lowest QW-related transition and the QR ground-state transition.

By following the corresponding peak energies of PR modulus (dashed and dotted curves in Fig. 3.29), one can ascertain that the use of As_4 flux results in better carrier confinement in respect of As_2 — the energy spacings ΔE are of 195 meV and 160 meV, respectively. Such an increase in carrier confinement for As_4-grown QRs is also evident from significantly larger energy spacing between QR ground- (`GS`) and excited- (`ES`) states for the As_4-grown sample (61 meV), as compared to As_2-grown one (49 meV). Increased energy level spacing in the As_4-grown QR structures may be attributed to the electron wavefunctions being more tightly confined, as discussed in [73]. This could be an important factor for improving recombination efficiency and PL intensity in QR devices, such as SOAs.

In a view of the above-mentioned findings, it is suggested that better carrier confinement in As_4-grown QRs is due to an increased indium composition contrast between the InGaAs QRs and the surrounding InGaAs QW layer [6.§].

Another part of our study was devoted to the intriguing optical anisotropy properties of ground-state interband transitions in InGaAs QRs.

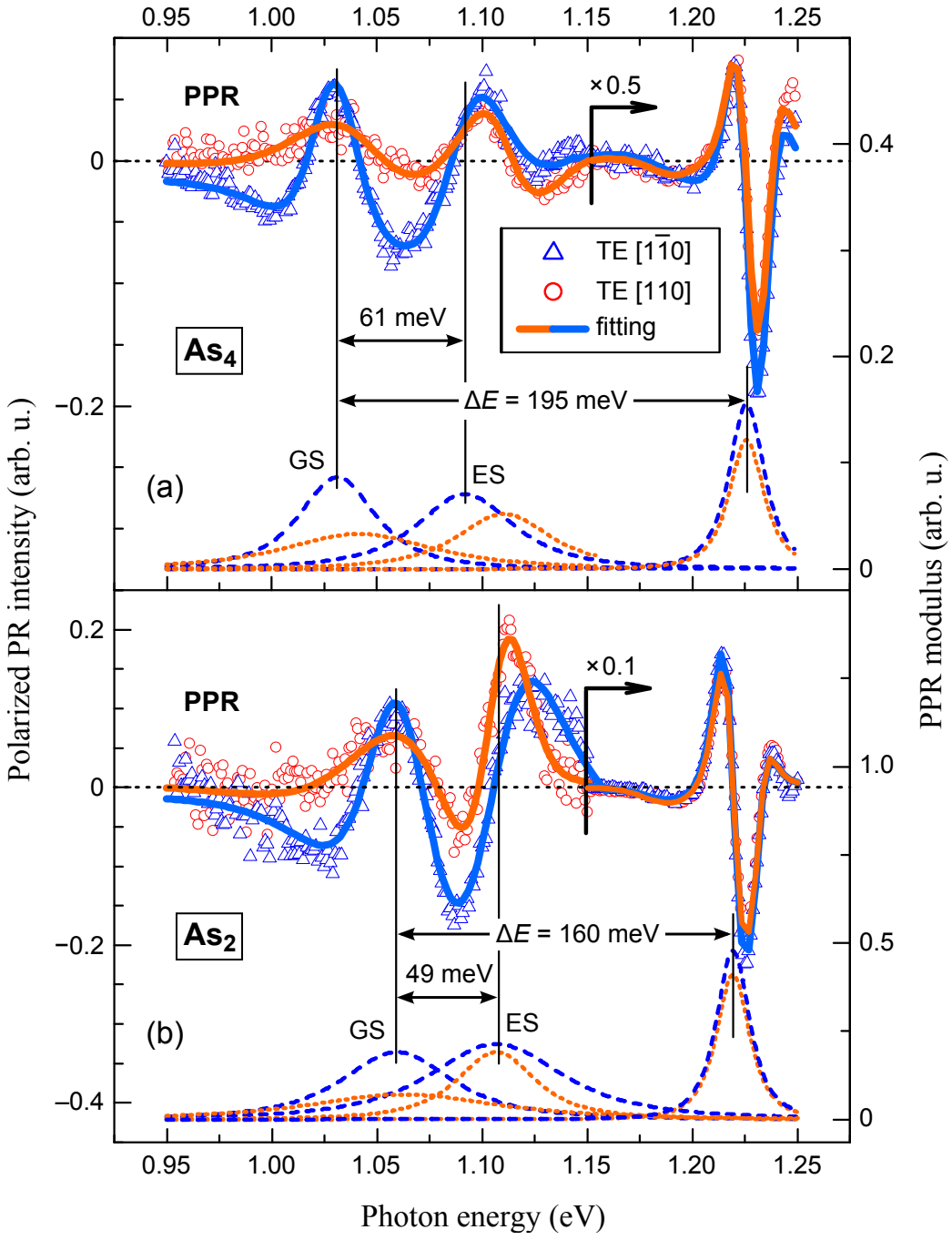

Figure 3.29 Room temperature polarized photoreflectance (PPR) spectra at two perpendicular polarization angles (symbols) for the (a) \ceAs4-grown and (b) As_2-grown QR35 samples. GS and ES denote optical transition energies in InGaAs QRs, involving ground- and excited-states, respectively. Modulus of individual PPR resonances are represented by dashed and dotted lines for electric vector $\boldsymbol{E}$ being parallel to the [1$\bar{1}$0] and [110] crystallographic axes, accordingly.

3.4.3 Polarization properties of InGaAs QRs and InGaAs QW

The in-(001)-plane optical anisotropy properties of InGaAs nanorods was explored by PPR and PPL techniques for two linear light polarizations — along the $[1\bar{1}0]$ and [110] crystal axes. Room temperature PPR spectra at two perpendicular polarization angles (Fig. 3.29) revealed significantly different PPR signal intensities for QR-related optical features both for As_4-, and As_2-grown samples. However, for the QW-related transitions only negligible polarization dependance was observed. Furthermore, optical anisotropy within QRs revealed by PPR technique was confirmed by PPL measurements (Fig. 3.28).

In order to get a deeper insight into the effect of QR aspect ratio on optical anisotropy properties of InGaAs QRs, we have systematically analyzed PPR and PPL response as a function of SL period number N, as discussed further.

Degree of polarization in InGaAs quantum rods

The in-(001)-plane polarization properties of optical transitions reflected in polarized PR and PL spectra (Figs. 3.28 and 3.29), were evaluated by a quantitative measure, *so called* degree of polarization,

$$\mathrm{DOP}_{[001]} = \frac{I_{[1\bar{1}0]} - I_{[110]}}{I_{[1\bar{1}0]} + I_{[110]}}. \tag{3.5}$$

Here $I_{[1\bar{1}0]}$ and $I_{[110]}$ denote signal amplitudes for $\boldsymbol{E} \parallel [1\bar{1}0]$ and $\boldsymbol{E} \parallel [110]$ light polarizations (two perpendicular polarizer positions), or alternatively for two transverse electric modes, $\mathrm{TE}_{[1\bar{1}0]}$ and $\mathrm{TE}_{[110]}$, respectively.

Figure 3.30shows room temperature polarized PL spectra at two perpendicular polarization angles (solid and dotted curves) alongside the calculated polarization degree (bubbles) for As_4- and As_2-grown `QR35` samples. According to definition (eq. (3.5)) we found that in-plane degree of polarization, $\mathrm{DOP}_{[001]}$, reaches value of $\approx 60\%$ for both `QR35` structures.

In order to investigate the effects of the QR height (number of SL periods deposited) on the polarization properties and electronic structure of InGaAs QRs, we have measured PPR and PPL optical response anisotropy of different in morphology InGaAs QR structures from (001)-plane. Figure 3.31 shows room temperature in-(001)-plane polarized PR and PL spectra at two perpendicular polarization angles for the As_2-grown QR samples: `QR10`

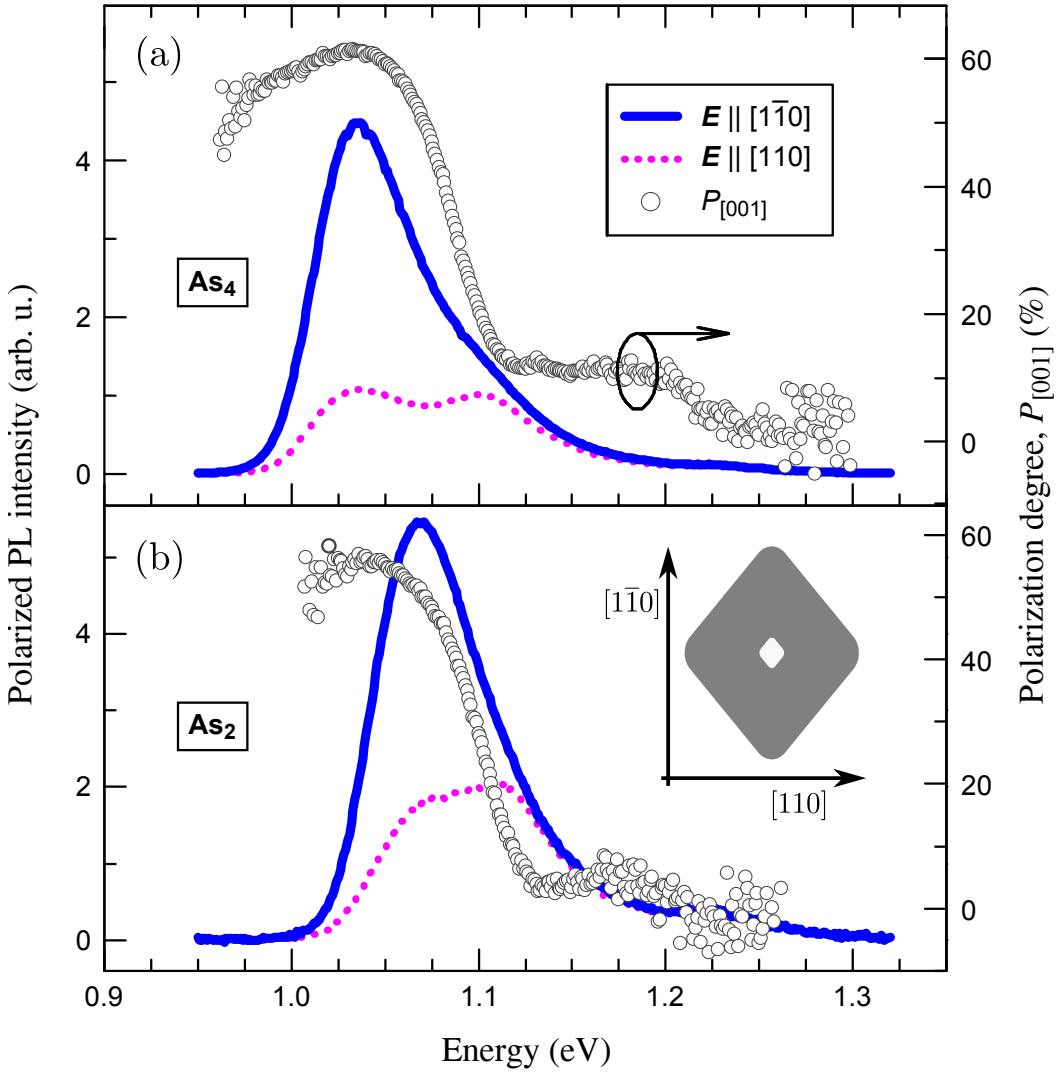

Figure 3.30 Room temperature polarized photoluminescence spectra at two perpendicular polarization angles (solid and dotted lines) for the `QR35` samples grown using (a) As_4 and (b) As_2 sources. Circles indicate optical anisotropy, represented by polarization degree, $P_{[001]}$. Inset: Schematic representation of a plan-view [in (001) plane] shape anisotropy in a QR along [1$\bar{1}$0] and [110] crystal axes.

(a), QR20 (b), and QR35 (c). From PPL data it was found that in-plane degree of polarization, $\mathrm{DOP}_{(001)}$, increases almost linearly with the SL period number N. In particular, for small aspect ratio QRs of 2.0 (QR10), degree of polarization is also small, $\mathrm{DOP}_{(001)} \approx 25\%$, and comparable to the DOP values for conventional self-assembled QDs. Increasing the SL period to $N = 20$ (aspect ratio of 3.2) results in increase of DOP value to $\mathrm{DOP}_{[001]} \approx 41\%$. Finally, for high aspect ratio QRs of 4.1 (QR35), in-(001)-plane DOP reaches value of $\approx 55\%$, close to the value ($\mathrm{DOP}_{(001)} \approx 60\%$) estimated for As_4-grown QR35 structure.

Similarly, the polarization anisotropy, estimated from the analysis of PPR modulus spectra, experiences an increase with SL period number N, however with a smaller slope. In particular, for the samples QR10, QR20, and QR35, we estimated DOP values of 37%, 43%, and 46%, respectively.

The significantly different DOP values obtained from PPR and PPL spectra (Fig. 3.31) may be related with the fact that PR is absorption-like spectroscopic method, which probes the maximum in the density of states, while the PL probes the states of the lowest energy. Another reason for different DOP values may be due to interference effects of PR signal [76].

In general, for low-dimensional structures PR signal intensity is associated with quantum-confined Stark effect (QCSE), the squared overlap integral of the electron and heavy-hole wavefunctions, $|M_{\mathrm{cv}}|^2$, modulation efficiency, and built-in electric field [66].

In particular, in QRs the lowest state electron wavefunction spans across the whole length of a QR, whereas hole wavefunctions of two lowest states are well-localized at the top and the bottom of QR. Such a confinement of holes is mainly driven by large heavy-hole effective mass and strain-related modification of confinement potential in the growth direction [37].

Bearing this in mind, the recorded PR signal of ground-state transition in QR is a superposition of two signals involving two well-confined hole states. Due to the difference in optical paths (the probed areas are spatially separated over the QR height) the contributed signals may arrive with a different phase and thus interfere constructively or destructively.

Thereby, it is tentatively suggested that under influence of electric field (QCSE) and localization of the lowest heavy-hole states at the top and the bottom of QR, the recorded PR intensity may be modified due to interference of two spatially separated signals. This presumption will be further elaborated by using different modulation sources in the PR experiment.

One more feature that can be traced from PPR spectra in Fig. 3.31 is

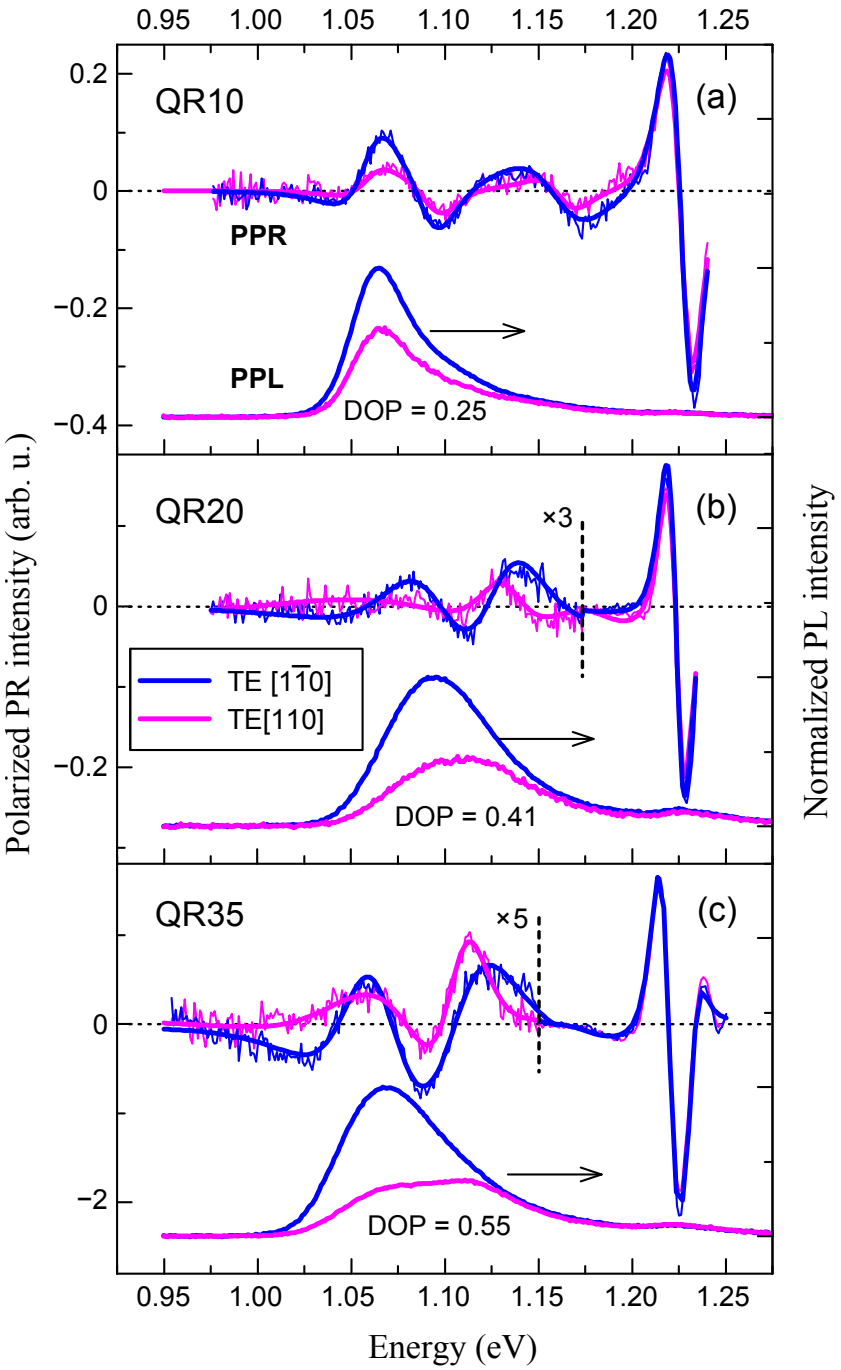

Figure 3.31 Room temperature in-(001)-plane polarized photoreflectance (PPR) and photoluminescence (PPL) spectra at two perpendicular polarization angles for the As_2-grown QR samples: `QR10` (a), `QR20` (b), and `QR35` (c). PPL-obtained optical anisotropy of `GS` interband transitions in QRs is indicated by the degree of polarization (DOP) values.

a decrease of QR-related transition intensities relatively to the lowest energy peak in QW, with the increase of SL period N. Such a behavior is attributed to a decrease in overlap integral of the electron and heavy-hole wavefunctions with increase of QR height.

A strong in-(001)-plane anisotropy, which has also been recently recorded for ultrahigh quantum posts [77], cannot be explained purely in terms of QR in-plane elongated shape along $[1\bar{1}0]$ direction as it normally account for up to 30%. It should be noted that the optical anisotropy is not entirely determined by the QD shape anisotropy. Another likely effects that may contribute to the giant polarization asymmetry are: material composition gradients (fluctuations), asymmetric strain distribution, piezoelectricity and in-plane modulation of InGaAs content — all should be considered on equal part. For example material composition fluctuations involves valence band mixing, causing $\leq 40\%$ polarization anisotropy, even in highly symmetrical QDs. However, the situation in QRs is even more complicated. Mukai *et al.* [78] have evaluated the internal structure of QRs and tracked the variation in in-plane lattice constants along $[1\bar{1}0]$ and [110] crystal axes by means of GIXD measurements. It was found that similar in height (tall) nanorods experience a reversal of lengths $L_{[1\bar{1}0]}$ and $L_{[110]}$ — $L_{[1\bar{1}0]} > L_{[110]}$ at the top of QR, whereas $L_{[1\bar{1}0]} < L_{[110]}$ at the QR bottom. Moreover, it was found [79] that the in-plane anisotropy of the PL intensity was clearly enhanced by increasing the stacking number in columnar QDs. As a result, TEM observations suggested that the polarization features might be governed by problems in the growth process such as the bending of the stacking direction during the formation of QDs with a high aspect ratio. However, a very recent theoretical predictions by Usman *et al.* in Ref. [48] performed on similar elongated QD (stacked QD) structures revealed that such intriguing (huge) optical anisotropy can be ascribed to the hole wavefunction $[1\bar{1}0]$-orientation, which suppresses the $\mathrm{TE}_{[110]}$ mode, and the light-heavy-hole band mixing, which favors an increase of the $\mathrm{TM}_{[001]}$ mode.

Our experimental findings suggest that PL polarization properties (intensity of TE- *versus* TM-mode) from the cleaved-facet surfaces should be different for the (110) and $(1\bar{1}0)$ facets, as is elaborated thereinafter.

When considering optical anisotropy from cleaved-facet surfaces [$(1\bar{1}0)$- and (110)-plane] of QR samples, degree of polarization can be defined by

$$\mathrm{DOP}_{(\mathrm{hkl})} = \frac{\mathrm{TE}_{\perp\text{-}z} - \mathrm{TM}_{\parallel\text{-}z}}{\mathrm{TE}_{\perp\text{-}z} + \mathrm{TM}_{\parallel\text{-}z}}, \tag{3.6}$$

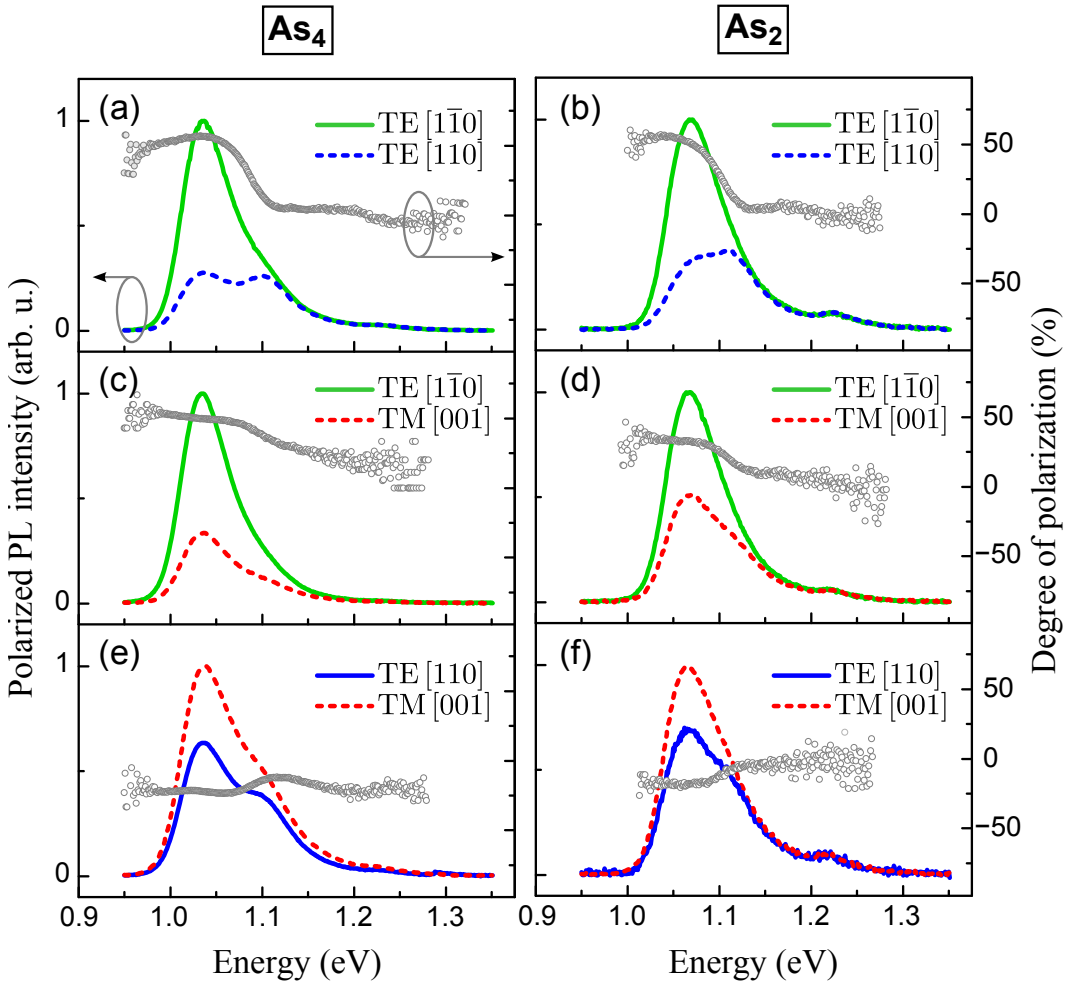

Figure 3.32 Room temperature linearly polarized PL spectra given by TE and TM modes for the QR35 samples grown using As_4 (a, c, e) and As_2 (b, d, f) sources. PL spectra are normalized to more intensive peak of GS transitions in InGaAs QRs. Circles indicate optical anisotropy, represented by the degree of polarization.

where z is QR growth direction and TE (TM) is the intensity of transverse electric (magnetic) mode. Here DOP is characterized by Miller indices of crystallographic facet plane.

Room temperature linearly polarized PL spectra at two perpendicular polarization angles (Fig. 3.32) shows that for high aspect ratio (4.1) QRs (QR35) a flip of DOP sign occurs for both As_4- and As_2-grown InGaAs QR structures. As a result, TM-mode is dominant from the (1$\bar{1}$0)-surface ($TM_{[001]} > TE_{[110]}$), while from the (110)-surface TE-mode is stronger ($TM_{[001]} < TE_{[1\bar{1}0]}$). It should be noted that DOP values for As_4-grown QRs [Figs. 3.32(c) and (e)] of $DOP_{(110)} = +50\%$ and $DOP_{(1\bar{1}0)} = -23\%$ exceed the corresponding DOP values of $DOP_{(110)} = +33\%$ and $DOP_{(1\bar{1}0)} = -18\%$ for As_2-grown QRs [Figs. 3.32(d) and (f)].

It should be noted that in a lenslike QDs optical transitions involving light-hole states are suppressed (by highly negative biaxial strain) and there-

fore the intensity of TM-mode is insignificantly small. As the QR height increases, biaxial strain reduces, simultaneously decreasing heavy- and light-hole subband splitting. Therefore, for high aspect ratio QRs the light- and heavy-hole bands become almost degenerate and thus manifest themselves by TE- and TM-modes of comparable intensity.

Thereby, it is suggested that light- and heavy-hole subband mixing favors an increase of the $TM_{[001]}$-mode. This is supported by calculated hydrostatic and biaxial strain profiles for different in height InAs/GaAs QD stacks reported in Ref. [48].

Finally, the evidence of sign reversal in degree of polarization estimated from the PPL spectra, fulfills the promise of QD shape engineering and shows a huge potential of QRs for demanded applications, such as polarization insensitive SOAs.

3.4.4 Conclusions

Polarized photoreflectance (PPR) and photoluminescence (PPL) spectroscopies were employed to study the electronic structure and optical anisotropy of InGaAs QR structures. From the experimental results it follows that the use of As_4 source during MBE growth results in a better carrier confinement and overall performance of the QR structures in respect of As_2 source. Moreover, optical measurements reveal strong (up to 60%) linear polarization anisotropy of the ground state optical transitions illustrating the importance of intrinsic structural anisotropy on optical properties of the InGaAs QRs. Finally, our spectroscopic findings provide the essential knowledge of the polarization properties of QRs, important for optoelectronic engineering.

The polarization properties of optical transitions observed in PPR and PPL spectra (Fig. 1) were evaluated by the in-plane polarization degree, $P_{(001)}$. It was found that

- ✓ in-(001)-plane polarization degree reaches a high value of about 60% for InGaAs QRs with $N = 35$. As a result, PL polarization properties (TE and TM modes) from the cleaved facet surfaces are different for the (110) and $(1\bar{1}0)$ facets;
- ✓ the TM mode was dominant from the $(1\bar{1}0)$ surface ($TM_{[001]} > TE_{[110]}$), while from the (110) surface TE mode prevailed ($TM_{[001]} < TE_{[1\bar{1}0]}$);
- ✓ in accordance with the theoretical predictions by Usman *et al.* in Ref. [48], such intriguing optical anisotropy can be ascribed to the hole wave-

function $[1\bar{1}0]$-orientation, which suppresses the $TE_{[110]}$ mode, and the light-heavy-hole band mixing, which favors an increase of the $TM_{[001]}$ mode.

The aforesaid findings allowed to formulate the following *statement for defence*

Transverse magnetic mode dominates from the $(1\bar{1}0)$-surface, while transverse electric mode is larger from the (110)-surface owing to a high in-(001)-plane polarization degree ($\approx 60\%$) of ground-state optical transitions in InGaAs quantum rod structures. These features are ascribed to hole wavefunction orientation along $[1\bar{1}0]$ direction together with light- and heavy-hole subband intermixing.

4 Analytical Model for Cylindrical Quantum Dots

Semiconductor nanotechnology based upon material (band gap) engineering and state-of-the-art growth technology (e.g., molecular beam epitaxy, metal-organic chemical vapour deposition, etc.) allows to develop materials by design with a great potential to adjust/tune their optical and electronic properties. The functionality of semiconductor nanostructures in a wide spectral region from ultraviolet (UV) to far-infrared, or terahertz (THz) is directly related to their energy level spectrum. Thus, knowledge of electronic structure and optical properties is crucial, in order to analyze and design new/advanced semiconductor quantum heterostructures for THz photonics and optoelectronics.

In the meantime the permanent interest in 2-dimensional (2-D) semiconductor quantum well heterostructures already yield a generation of new devices, exploiting these "quaint" quantum mechanical properties, attention is now turning towards low-dimensional solid state systems, providing higher degree of carrier confinement. The impetus at the moment is to understand the electronic and optical properties of 1-D quantum wires, 0-D quantum dots and even nanosystems, representing an exiting interjacent confinement, such as "quasi" 0-D quantum rods and quantum rings. The knowledge of low-dimensional electron behaviour would naturally reveal the potential of such semiconductor nanostructures to be incorporated into next generation electronic and photonic devices. Moreover, separate "pure" quantum systems can be combined, e.g. quantum dot/quantum ring on a quantum rod, expanding the degree of freedom and hiding numerous striking effects to be discovered someday...

Very elegant alternative to engineer modern functional elements at nanoscale is to use self-assembling (or Stranski-Krastanov, SK) quantum dots. SK dots have been studied extensively, owing to their intriguing atomic-like quantum confinement, which lead to a broad range of possible applications (see e.g. [1]). Non-trivial strain relaxation mechanisms usually result in

formation of flat (low aspect ratio), lens-shaped dots, scattered as two or more families in size, represented by a broad (Gaussian) lines in experimental spectra. Optical properties in terms of polarization insensitivity and size (volume of confinement) control can be significantly improved realizing high aspect ratio, or columnar quantum dots (nanorods, QRs), and quantum rings, respectively. However, in-plain optical anisotropy is common figure of merit for InGaAs-based structures due to better mobility (longer migration length) of In adatoms in [001] direction on the GaAs [44, 45].

From the theoretical perspective, self-assembling quantum systems are challenging, owing to the presence of (residual) strain, an inherent property, which drastically changes potential profile and hence modeling parameters. Moreover, the uncertainty of dot's material composition and geometry gives rise to even more free parameters to be considered. Typically, quantum well (QW) energy spectra calculations employ well-elaborated analytical envelope function methods [80]. In most cases, the added degrees of confinement, exhibited in lower dimensional systems, results in a greatly increased complexity in the Schrödinger equation, a cornerstone of theoretical methods, and therefore on cannot solve it for a QD purely analytically. Therefore, numerical methods are employed to simulate QD energy spectrum. Although numerical simulations give rather exact energy values, still analytical methods describing the behavior of QDs in external electric fields are needed. The lack of exact instruments of theoretical analysis stimulated us to create an analytical algorithm for energy spectra calculations of SK dots, which is promoted to be easy adjustable for similar-by-nature quantum systems, such as QRs and quantum rings.

The modeling of QD energy levels is essential tool to analyse the experimental optical spectra of the InGaAs QD structures studied recently [1–7.§]. We expect that implementing and development of such analytical model may succeed to a very helpful instrument in optimizing the well elaborated near- and mid-infrared QD-based photodetectors towards the pursuited THz-window operation.

In this Section, analytical approach for energy spectrum calculations of self-assembling QDs and QRs having cylindrical symmetry is presented. The given model is based on separation of variables approximation. Here, electron is represented by two quasi-particles, moving along z and ϱ directions and therefore each obtaining different effective masses. The algorithm presented models nanostructures with a rectangular potential profile consistently considering cases of constant effective mass, effective mass disconti-

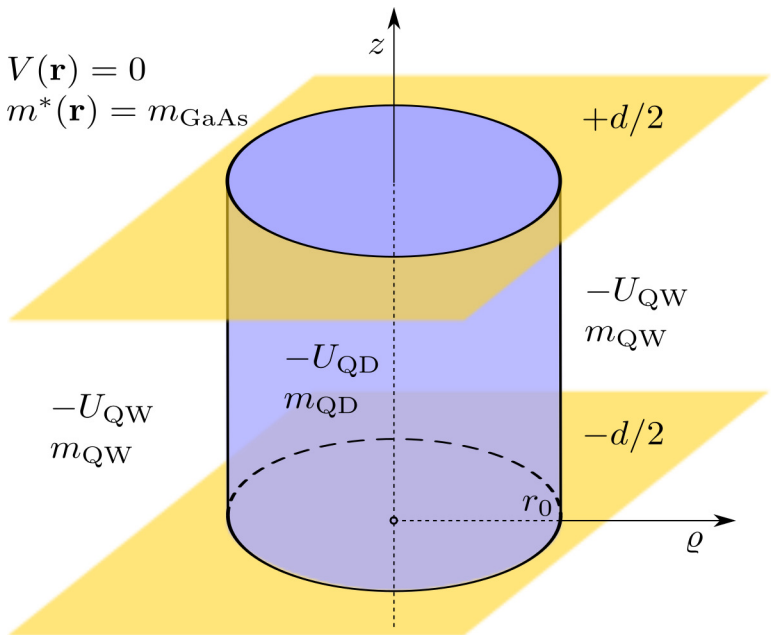

Figure 4.1 Potential $V(\mathbf{r})$ and effective mass $m(\mathbf{r})$ domains for cylindrical QD structure analyzed.

nuity, and energy band nonparabolicity (Kane model). Calculation results revealed that effective mass discontinuity and conduction band nonparabolicity effect energy levels significantly. In more detail, it is shown that the model is well-suitable for evaluating ground-state and lower excited-state interband transitions in QD/QR structures, i.e. when the electron remains tightly localized within QW. Nevertheless, application of the method for several QD/QR reference samples shows that in practice all bound states are reliably calculated by the suggested technique.

Analytical method with derived exact solutions for eigenstates is presented step-by-step hereinafter.

4.1 Algorithm for Variable Separation

Geometry of self-assembling QDs is dictated by the relaxation mechanisms of epitaxial layers during growth. Real SK dots have a typical shape of truncated cone or flat lens. Therefore, as a first approximation to analyze self-assembling QDs and QRs, a shape of cylinder was chosen (see Fig. 4.1).

The whole quantum system under consideration is represented by the equation of energy states E, or Schrödinger equation, given by

$$\left[-\frac{\hbar^2}{2m^*}\Delta + V(\boldsymbol{r})\right]\Psi(\boldsymbol{r}) = E\,\Psi(\boldsymbol{r}), \tag{4.1}$$

where $\hbar$ is reduced Planck's constant, $m^* = m(z, \varrho)$ is effective mass, Δ — Laplace operator (laplacian), $V(\mathbf{r})$ — potential energy, $\Psi(\mathbf{r})$ — wavefunction (eigenfunction), and E — energy (eigenvalue) of an electron. Laplacian Δ in cylindrical coordinate system (in concordance with the QD geometry chosen) has a form of

$$\Delta f = \frac{1}{\varrho}\frac{\partial}{\partial \varrho}\left(\varrho \frac{\partial f}{\partial \varrho}\right) - \frac{1}{\varrho^2}\frac{\partial^2 f}{\partial \varphi^2} + \frac{\partial^2 f}{\partial z^2}. \tag{4.2}$$

According to quantum mechanics, in a field of cylindrical symmetry, particle's angular momentum projection to the z-axis (axis of symmetry) is a conserved quantity, i.e. commutes with the hamiltonian, $\left[\hat{l}_z, \hat{H}\right] = 0$. Thereby, wavefunction dependence on azimuthal angle φ is defined by the eigenfunctions of angular momentum projection to the z-axis operator, Φ_m, indexed by azimuthal (or magnetic) quantum numbers m,

$$\Psi(\mathbf{r}) = \Psi(z, \varrho, \varphi) = \psi(z, \varrho)\, \Phi_m, \tag{4.3}$$

where

$$\Phi_m = \frac{1}{\sqrt{2\pi}} \exp(\mathrm{i}m\varphi), \quad m = 0, \pm 1, \pm 2, \ldots \tag{4.4}$$

Putting eigenfunction (4.3) into initial Schrödinger equation (4.1) brings to the equation for a reduced wavefunction $\psi(z, \varrho)$,

$$\hat{H}\, \psi(z, \varrho) = E\, \psi(z, \varrho), \tag{4.5}$$

where

$$\hat{H} = -\frac{\hbar^2}{2m(z, \varrho)}\left[\frac{\partial^2}{\partial z^2} + \frac{1}{\varrho}\frac{\partial}{\partial \varrho}\left(\varrho \frac{\partial}{\partial \varrho}\right) - \frac{m^2}{\varrho^2}\right] + V(z, \varrho). \tag{4.6}$$

Potential energy $V(z, \varrho)$ in Eq. (4.6) is the profile of the bottom of conduction band (CB). In a case of searching for hole states, potential energy $V(z, \varrho)$ is the profile of the top of valence band (VB). The abrupt change in energy of the CB or VB happens at the boundaries of semiconductor heterostructure layers. Our model does not take into account strain, which is present due to lattice mismatch between heterostructure layers, and wetting layer (thin layer just below QDs). Such being the case, potential profile accord with the finite 2-dimensional (2-D) quantum well (QW). Therefore, in concordance with Fig. 4.1, system potential and effective mass are defined as[1]

[1]Energy zero value is at the potential profile plateu in the barrier.

$$V(z,\varrho)=\begin{cases}-U_{\mathrm{QD}}, & \mathbf{r}\in\mathrm{QD},\\ -U_{\mathrm{QW}}, & \mathbf{r}\in\mathrm{QW},\\ 0, & \mathbf{r}\in\text{barrier};\end{cases}\qquad m(z,\varrho)=\begin{cases}m_{\mathrm{QD}}, & \mathbf{r}\in\mathrm{QD},\\ m_{\mathrm{QW}}, & \mathbf{r}\in\mathrm{QW},\\ m_{\mathrm{b}}, & \mathbf{r}\in\text{barrier}.\end{cases} \tag{4.7}$$

4.1.1 Adiabatic approximation

Variables z and ϱ are not independent, as is evident from Schrödinger equation 4.5. Here they are bound by potential $V(z,\varrho)$ as well as by effective mass $m^*=m(z,\varrho)$. Therefore, we can only separate variables approximately. As a first approximation, we will examine the case of constant effective mass, i.e., $m^*=m_{\mathrm{QD}}$.

The geometry of cylindrical quantum dot is defined by height d and base radius r_0 explicitly. Analyzing two different geometries — $d\ll r_0$ (the case of usual quantum dot) and $d\gg r_0$ (the case of quantum rod) — allows variable separation according to adiabatic algorithm.

Let us rewrite Eq. (4.5) in dimensionless units $\tilde{z}=z/d$ and $\tilde{\varrho}=\varrho/r_0$,

$$\left\{-\frac{\hbar^2}{2M_z}\frac{\partial^2}{\partial\tilde{z}^2}-\frac{\hbar^2}{2M_\varrho}\left[\frac{1}{\tilde{\varrho}}\frac{\partial}{\partial\tilde{\varrho}}\left(\tilde{\varrho}\frac{\partial}{\partial\tilde{\varrho}}\right)-\frac{m^2}{\tilde{\varrho}^2}\right]+V(\tilde{z},\tilde{\varrho})\right\}\psi(\tilde{z},\tilde{\varrho})=E\psi(\tilde{z},\tilde{\varrho}), \tag{4.8}$$

where $M_z\equiv m^*d^2$ and $M_\varrho\equiv m^*r_0^2$. Assuming the limit $d\ll r_0$ (quantum dot), one can see that Eq. (4.8) describes two 1-D quasiparticles — light (fast motion) z-particle with a mass M_z and heavy (slow motion) ϱ-particle having a mass M_ϱ — interacting with a potential $V(\tilde{z},\tilde{\varrho})$. In a case of quantum rod ($d\gg r_0$) terms "light" and "heavy" flip *vice versa* for corresponding quasiparticles.

Further we will seek for Schrödinger equation (4.5) solutions in a form of

$$\psi(z,\varrho)=Z_i(z)\,R_{nm}(\varrho),\quad E\equiv\varepsilon_{inm}=\varepsilon_i+\varepsilon_{nm}. \tag{4.9}$$

Note that as a matter of routine, adiabatic procedure would suppose an approximation $\psi(z,\varrho)=Z(z,\varrho)\,R(\varrho)$. However, such assumption is justified, as we are interested in localized QD states (when probability to find z-particle in a barrier is negligible, $P^{(z)}_{\mathrm{b},i}\ll 1$).[2]

[2] z-particle's probability in the barrier is defined as $P^{(z)}_{\mathrm{b},i}=\int_{-\infty}^{-d/2}\mathrm{d}z\,|Z_i|^2+\int_{d/2}^{\infty}\mathrm{d}z\,|Z_i|^2$.

Considering Eqs. (4.5) and (4.9) one can obtain that "light" (fastly moving) particle's eigenfunctions $Z_i(z)$ are solutions of equation

$$\hat{H}_z \, Z_i(z) = \varepsilon_i \, Z_i(z), \tag{4.10}$$

where

$$\hat{H}_z = -\frac{\hbar^2}{2m^*} \frac{\partial^2}{\partial z^2} + V(z). \tag{4.11}$$

Here potential $V(z)$ can be defined by Heaviside function $\Theta(z)$, $V(z) = -U_{\mathrm{QD}} \, \Theta(d/2 - |z|)$.

Similarly, "heavy" (slowly moving) particle's eigenfunctions $R_{nm}(\varrho)$ satisfy equation

$$\hat{H}_\varrho \, R_{nm}(\varrho) = \varepsilon_{nm} \, R_{nm}(\varrho), \tag{4.12}$$

where

$$\hat{H}_\varrho = -\frac{\hbar^2}{2m^*} \left[\frac{1}{\varrho} \frac{\partial}{\partial \varrho} \left(\varrho \frac{\partial}{\partial \varrho} \right) - \frac{m^2}{\varrho^2} \right] + V(\varrho). \tag{4.13}$$

Here $V(\varrho) = (U_{\mathrm{QD}} - U_{\mathrm{QW}}) \, \Theta(\varrho - r_0)$.

Solutions for Eqs. (4.10) and (4.12) are given in the following Subsection.

4.1.2 Separation of variables approximation

Let us keep effective mass constant ($m^* = m_{\mathrm{QD}}$) and define potential $V(z, \varrho)$ as

$$V(z, \varrho) = V(z) + V(\varrho), \tag{4.14}$$

where

$$V(z) = \begin{cases} U_z \equiv -U_{\mathrm{QD}}, & |z| < d/2, \\ 0, & |z| > d/2; \end{cases} \tag{4.15}$$

and

$$V(\varrho) = \begin{cases} 0, & \varrho < r_0, \\ U_\varrho \equiv U_{\mathrm{QD}} - U_{\mathrm{QW}}, & \varrho > r_0. \end{cases} \tag{4.16}$$

Thereby, potential $V(z, \varrho)$ obtains values, depicted in Fig. 4.2. A comparison of $V(z, \varrho)$ values for different areas with the real potential profile, given

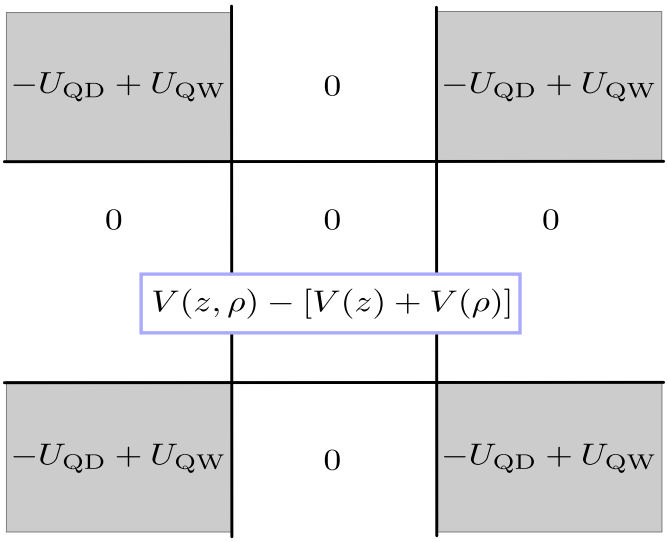

Figure 4.2 Scheme of potential $V(z) + V(\varrho)$ profile and areas of perturbation W (shaded).

in Fig. 4.2, clearly indicates four wrongly evaluated regions (shaded areas for $\{|z| > d/2,\, \varrho > r_0\}$ in Fig. 4.2). However, once again, we are interested only in localized QD states, which means that wavefunctions for such states will decay exponentially in these barrier regions. Thus, we expect that approximation assumed should give reasonable results.

Longitudinal z-motion states

We are used to think of a 3-dimensional world (and some of us, who are always in a hurry, add one more dimension — time). Even if we live in a room with low ceiling, still 2-dimensional freedom is sufficient, or we can lay down on the floor (with the high ceiling) and return to the normal conditions. Then the question arrives: How can one confine quantum particles (typically electrons or holes), e.g. in the dimension perpendicular to the material (layer) surface, whereas the movement in the other dimensions being not restricted; how can we create 2-dimensional electrons? Such situation realizes in a QW, a thin layer of a semiconductor medium, sandwiched between other semiconductor of a wider bandgap (examples: GaAs embedded in AlAs, or InAs within GaAs). The thickness of such a QW is typically $\sim$ 5–20 nm, or in other words, is comparable to the de Broglie wavelength of a particle (i.e. electron or hole). Such thin layers can be grown by molecular beam epitaxy (MBE) or metal–organic chemical vapor deposition (MOCVD) with control of the layer thickness down to monolayers. When electron travels from one semiconductor to the other, at the interface it experiences an abrupt change in potential energy and therefore

potential profile of a QW is represented as a square well of a finite depth (Fig. 4.3 (a)). Electron living in a QW experience dimensional quantization effects and thus can obtain only discrete energy values (live in the subbands) if moving in growth direction (usually marked by z-axis). However, such particle is free to move in-plane (in (x, y) plane) of the QW semiconductor layer, and, hence, be described by a well-known quadratic dispersion relation, $E = \hbar^2 k_{x,y}^2 / 2m^*$. As a result, energy spectrum of an electron, moving perpendicularly to the layers of a QW, should be calculated quantum mechanically. Calculated bound states and corresponding wavefunctions for a square finite potential well, which depth and width are denoted by U and d, respectively, are shown as an example in Fig. 4.3 (b). It is important to emphasize, that the eigenfunction penetration into the barrier becomes significantly deeper as an electron gains energy to approach the continuous (free particle) spectra. One can ascertain as well, that the exponential tails are always present (it is a finite probability for an electron to be in a barrier), no matter how thick the barrier layer is.

Fast motion Schrödinger equation (4.10) matches the common equation of 1-D particle in a potential well (Fig. 4.3 (b)). We can easily solve this equation employing well-known methods of analysis for a finite QW [2]. Eventually, wavefunction in a well shows an oscillating behavior and decays exponentially in left and right barriers (see Fig. 4.3 (b)),

$$Z_i = \begin{cases} A \exp(\kappa_\mathrm{b} z), & z < -d/2, \\ C \sin(\kappa_\mathrm{w} z + \pi i/2), & |z| < d/2, \\ (-1)^{i+1} B \exp(-\kappa_\mathrm{b} z), & z > d/2. \end{cases} \tag{4.17}$$

Here $\kappa_\mathrm{b} = \sqrt{2m^*(-\varepsilon_i)}/\hbar$, $\kappa_\mathrm{w} = \sqrt{2m^*(U_\mathrm{QD} + \varepsilon_i)}/\hbar$. U_QD and d are depth and width of a QW, and ε_i is the energy of the i-th state, $i = 1, 2, 3, \ldots$[3] Constants A and C are defined from two boundary conditions, which determine eigenfunction continuity at the material interfaces. Moreover, the continuity requirement states, that both eigenfunction and its logarithmic derivative should be continuous,

$$Z_i|_{\mp d/2-0} = Z_i|_{\mp d/2+0}, \qquad \left.\frac{Z_i'}{Z_i}\right|_{\mp d/2-0} = \left.\frac{Z_i'}{Z_i}\right|_{\mp d/2+0}. \tag{4.18}$$

The energy spectrum for a fastly moving z-particle is determined by dispersion equation

[3] In formula (4.17) the origin of z coordinate is in the middle-point of quantum well.

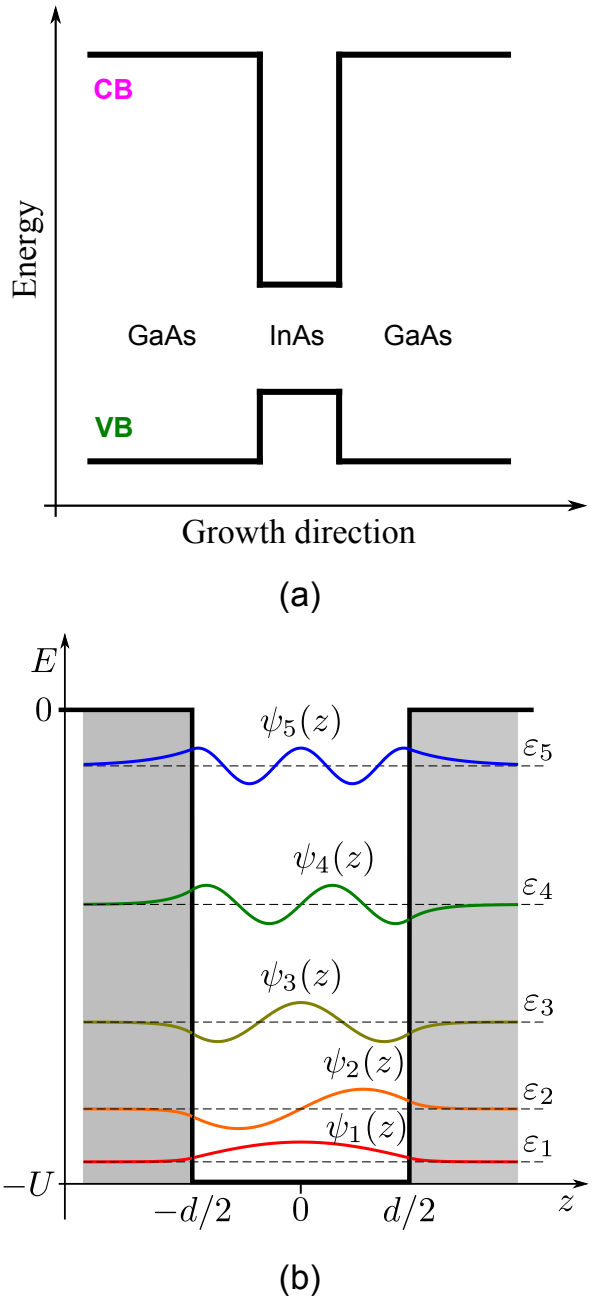

Figure 4.3 Finite potential well: Scheme of an InAs/GaAs QW with uppermost valence (VB) and lowermost conduction (CB) bands drawn (a) and its electron energy spectrum together with corresponding eigenfunctions (b). QW width and height are denoted by d and U, respectively.

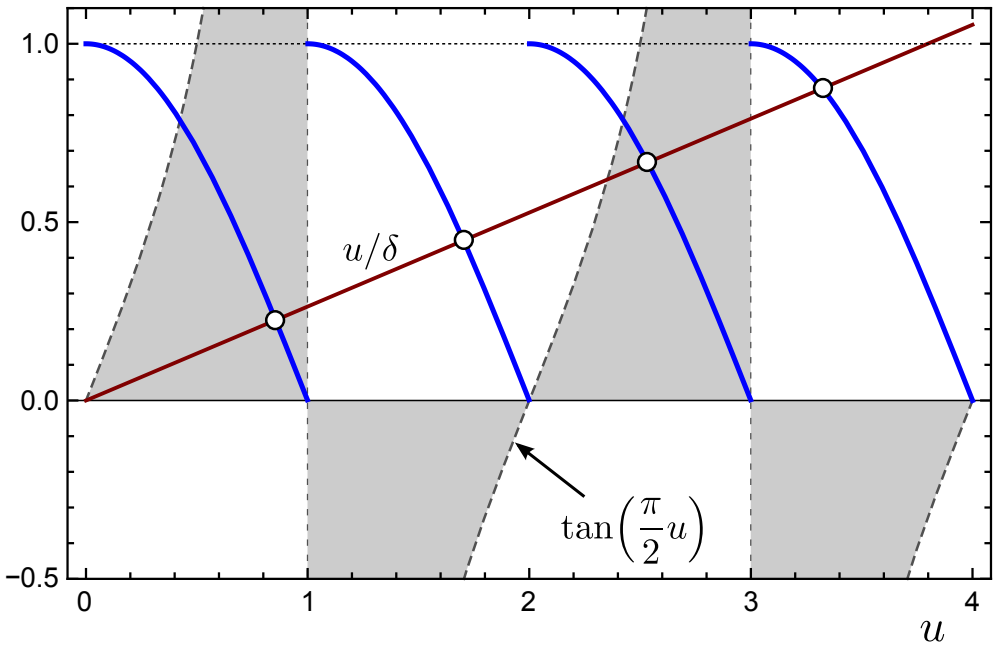

Figure 4.4 Graphical solution of finite quantum well dispersion equation (4.19). Energy values are determined from solid curve intersections (open circles).

$$\frac{u}{\delta} = \begin{cases} \left|\cos\left(\frac{\pi}{2}u\right)\right|, & \tan\left(\frac{\pi}{2}u\right) > 0, \\ \left|\sin\left(\frac{\pi}{2}u\right)\right|, & \tan\left(\frac{\pi}{2}u\right) < 0, \end{cases} \tag{4.19}$$

where $u = \delta\sqrt{1+\varepsilon_i/U_{\mathrm{QD}}}$ is a unitless variable (equation for eigenstate) and $\delta = \sqrt{2m^*U_{\mathrm{QD}}}\,d/\pi\hbar$ is a unitless parameter — the strength of a well. The solutions (energy levels) for a 1-D finite QW dispersion equation (4.19) can be obtained graphically, as shown in Fig. 4.4.

Transversal ϱ-motion states

We will now solve slow motion Schrödinger equation (4.12) in QD and barrier separately. Then we will match both solutions at the interface. This procedure is described properly in next two paragraphs.

The region of a QD ($\varrho < r_0$). In case radial electron coordinate is within the QD, $\varrho < r_0$, multiplying Eq. (4.12) by $-2m^*/\hbar^2$ and introducing notation $\beta = \sqrt{2m^*\varepsilon_{nm}}/\hbar$ yields

$$\frac{1}{\varrho}\frac{\partial}{\partial\varrho}\left(\varrho\frac{\partial R(\varrho)}{\partial\varrho}\right) + \left[\beta^2 - \frac{m^2}{\varrho^2}\right]R(\varrho) = 0, \tag{4.20}$$

which, by introducing unitless variable $u = \beta\varrho$, is reduced to the Bessel differential equation

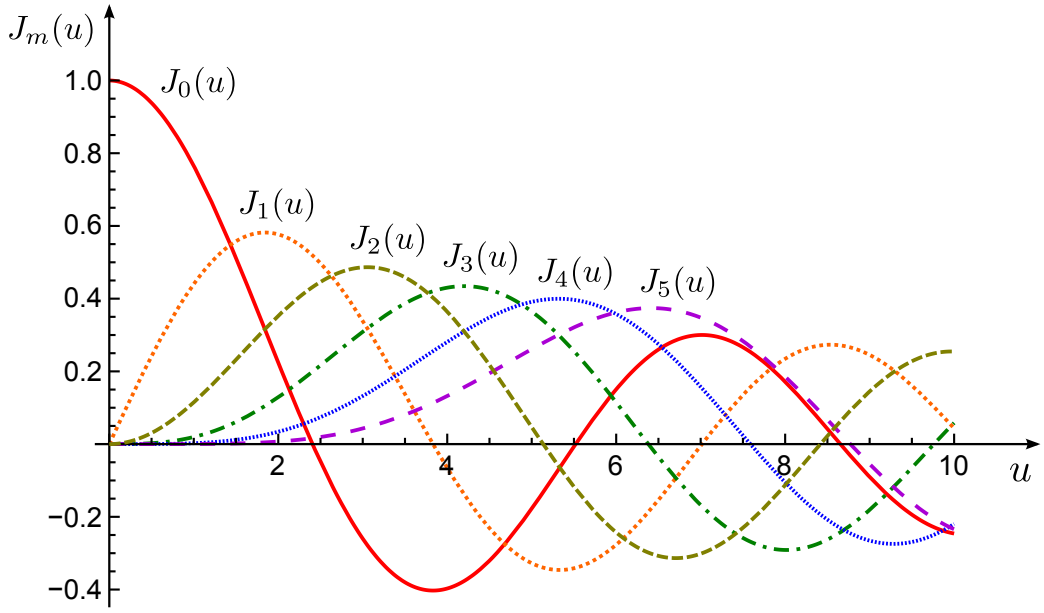

Figure 4.5 Bessel functions $J_m(u)$, with parameter m from eq. (4.21) obtaining integer values $m = 0, 1, \ldots, 5$.

$$u^2 R'' + uR' + (u^2 - m^2)R = 0. \tag{4.21}$$

The solution of a Bessel equation, which satisfies regularity requirement at the centre of a QD, $\varrho = 0$, is Bessel function $J_m(u)$, shown in Fig. 4.5. It is sometimes also called cylinder function or cylindrical harmonic. Thereby, radial function in QD is defined as

$$R(\varrho)|_{\varrho<r_0} = C_1\, J_m(\beta\varrho). \tag{4.22}$$

The region of a barrier ($\varrho > r_0$). In case radial electron coordinate is out of the QD, $\varrho > r_0$, multiplying Eq. (4.12) by $-2m^*/\hbar^2$ and introducing notation $\alpha = \sqrt{2m^*(U_\varrho - \varepsilon_{nm})}/\hbar$ yields

$$\frac{1}{\varrho}\frac{\partial}{\partial\varrho}\left(\varrho\frac{\partial R(\varrho)}{\partial\varrho}\right) + \left[-\alpha^2 - \frac{m^2}{\varrho^2}\right] R(\varrho) = 0. \tag{4.23}$$

After introducing unitless variable $u = \alpha\varrho$, the latter equation, is reduced to the modified Bessel differential equation

$$u^2 R'' + uR' - (u^2 + m^2)R = 0. \tag{4.24}$$

Solutions of this equation are the modified Bessel functions of the first and second kinds. However, only modified (hyperbolic) Bessel function of the second kind, $K_m(u)$, is regular in the asymptotic limit of $\rho \to \infty$. The

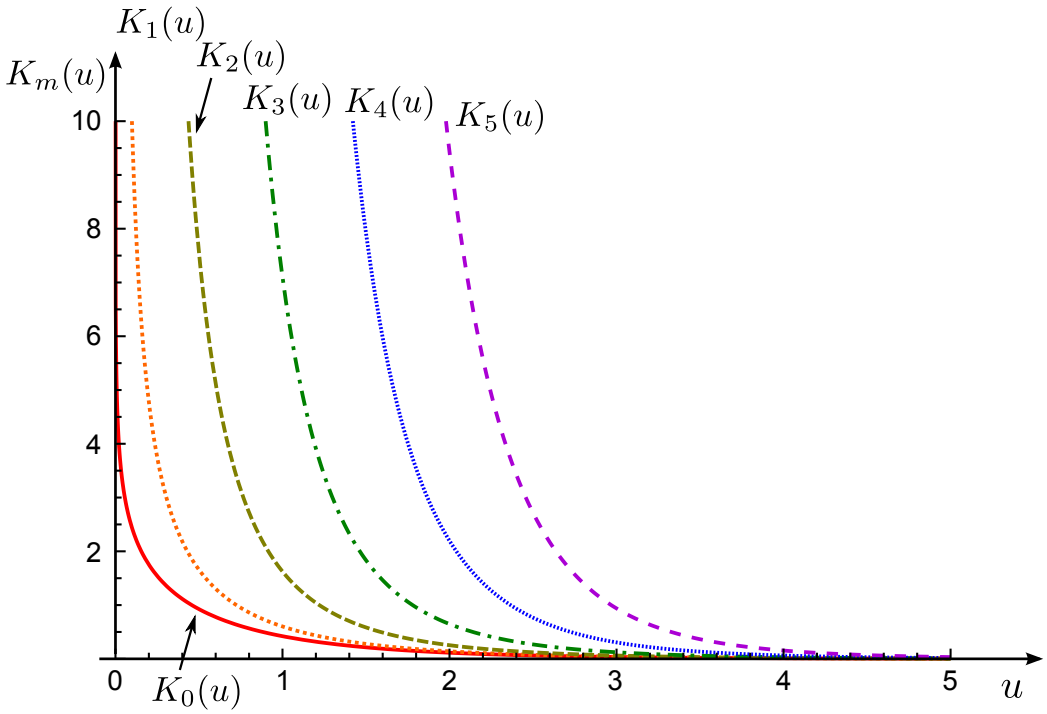

Figure 4.6 Modified (hyperbolic) Bessel functions of the second kind, $K_m(u)$, with parameter m from eq. (4.24) obtaining integer values in a range of $0 \leq m \leq 5$.

modified Bessel function of the second kind (shown in Fig. 4.6) is sometimes called the Basset function, or Macdonald function. Consequently, radial function in barriers is defined as

$$R(\varrho)|_{\varrho>r_0} = C_2\, K_m(\alpha\varrho). \tag{4.25}$$

Now we should match separate solutions for a radial function obtained in QD (4.22) and barrier (4.25) regions at the wall point of the QD, $\varrho = r_0$. Again, the requirements for the radial function are identical to the ones, we have stated for the "light" particle's (z-motion) eigenfunction (4.18). By employing boundary condition of logarithmic derivatives

$$\left.\frac{R'(\varrho)}{R(\varrho)}\right|_{r_0-0} = \left.\frac{R'(\varrho)}{R(\varrho)}\right|_{r_0+0}, \tag{4.26}$$

and taking into account the derivative identities [81]

$$\frac{\mathrm{d}}{\mathrm{d}u}u^m J_m(u) = u^m J_{m-1}(u), \qquad \frac{\mathrm{d}}{\mathrm{d}u}u^m K_m(u) = -u^m K_{m-1}(u), \tag{4.27}$$

one can see, that it is more convenient to match products $\varrho^m R(\varrho)$ instead of radial functions themselves. Therefore, we rewrite the boundary condition

(4.26) in a form of

$$\left.\frac{[\varrho^m R(\varrho)]'}{\varrho^m R(\varrho)}\right|_{r_0-0} = \left.\frac{[\varrho^m R(\varrho)]'}{\varrho^m R(\varrho)}\right|_{r_0+0}. \tag{4.28}$$

After putting the solutions (4.22) and (4.25) into (4.28), finally, we obtain the dispersion equation for energy levels of a QD,

$$\frac{J_{m-1}(\beta r_0)}{J_m(\beta r_0)} = -\frac{\alpha}{\beta}\,\frac{K_{m-1}(\alpha r_0)}{K_m(\alpha r_0)}. \tag{4.29}$$

We can rewrite this equation into more convenient form by setting up a unitless parameter $\delta = \sqrt{2m^* U_\varrho}\, r_0/\pi\hbar$ and a unitless variable $x = \delta\sqrt{\varepsilon_{nm}/U_\varrho}$,[4]

$$\frac{J_{m-1}(\pi x)}{J_m(\pi x)} = -\frac{\sqrt{\delta^2 - x^2}}{x}\,\frac{K_{m-1}\left(\pi\sqrt{\delta^2 - x^2}\right)}{K_m\left(\pi\sqrt{\delta^2 - x^2}\right)}. \tag{4.30}$$

The latter dispersion equation can be easily solved using iterational, graphical (see Fig.GraphDEsol in Subsection mass-disc) and other methods. As can be seen from Eq. (4.30), there is only single parameter δ (the strength of the well), which value defines the number of energy levels in a QD, i.e., $N = 1 + \mathrm{Int}[\delta]$, where Int[...] is the integer part of the number.

4.1.3 Corrections for energy levels

Variable separation approximation presented is based on potential $V(z, \varrho)$, defined as a sum of single variable dependent (partial) potentials $V(z)$ and $V(\varrho)$ (see Eq. (4.14)). Thereby, the real potential profile (given in Fig. 4.1) is evaluated wrongly in four regions $\{|z| > d/2,\ \varrho > r_0\}$, as indicated in Fig. 4.2. Now we will examine eigenvalues $\varepsilon^{(0)}_{inm}$, calculated within variable separation approximation. To this end, we will use perturbation procedure and calculate first-order correction $\varepsilon^{(1)}_{inm}$ to see, whether our algorithm (and assumptions therein) are adequate.

Real potential profile should not be defined by formula (4.14). Instead, one should keep in mind that variables in Schrödinger equation (4.5) are separable by the precision of operator $W(z, \varrho)$,

$$\hat{H} = \hat{H}_z + \hat{H}_\varrho + W, \qquad W = V(z, \varrho) - [V(z) + V(\varrho)], \tag{4.31}$$

[4] In case of s-type of states, $m = 0$, dispersion equation (4.29) turns into $-\frac{J_1(\pi x)}{J_0(\pi x)} = -\frac{\sqrt{\delta^2 - x^2}}{x}\,\frac{K_1\left(\pi\sqrt{\delta^2 - x^2}\right)}{K_0\left(\pi\sqrt{\delta^2 - x^2}\right)}$.

where

$$W(z,\varrho) = \begin{cases} -U_\varrho, & \{|z| > d/2,\ \varrho > r_0\}, \\ 0, & \text{otherwise.} \end{cases} \tag{4.32}$$

Taking into account the perturbing potential W, the first-order correction for electron energy levels, $\varepsilon^{(1)}_{inm}$, is given by

$$\begin{aligned} \varepsilon^{(1)}_{inm} &= \int \mathrm{d}^3 r\, |\psi(z,\varrho,\varphi)|^2\, W(z,\varrho) \\ &= -U_\varrho\, 2 \int_{d/2}^{\infty} \mathrm{d}z\, Z_i^2(z) \int_{r_0}^{\infty} \mathrm{d}\varrho\, \varrho\, R^2_{nm}(\varrho) \\ &= -U_\varrho\, P^{(z)}_{\mathrm{b},i}\, P^{(\varrho)}_{\mathrm{b},nm}, \end{aligned} \tag{4.33}$$

where $P^{(z)}_{\mathrm{b},i}$ and $P^{(\varrho)}_{\mathrm{b},nm}$ are probabilities to find z- and ϱ-particle in a barrier, respectively.[5]

4.1.4 Effective mass discontinuity

By now, we have calculated semiconductor heterostructure energy spectrum, assuming the mass of an electron is constant, $m^* = m_{\mathrm{QD}} = \mathrm{const}$, wherever it travels. However, electrons (and holes) when moving from one semiconductor layer to the other feel not only conduction (and valence) band discontinuity, but also abruptly acquire different effective mass (see Eq. (4.7) and Fig. 4.1). Therefore, neglecting the effective mass discontinuity may lead to substantial errors in energy level calculations.

Putting real potential profile $V(z,\varrho) = V(z) + V(\varrho) + W(z,\varrho)$ (see Eq. (4.31)) into Schrödinger equation (4.5) results in hamiltonian $\hat{H}$ defined as

$$\begin{aligned} \hat{H} = &- \frac{\hbar^2}{2m(z,\varrho)} \left[\frac{\partial^2}{\partial z^2} + \frac{1}{\varrho} \frac{\partial}{\partial \varrho} \left(\varrho \frac{\partial}{\partial \varrho} \right) - \frac{m^2}{\varrho^2} \right] + \\ &+ V(z) + V(\varrho) + W(z,\varrho). \end{aligned} \tag{4.34}$$

One can clearly see from (4.34) that variables are not separable due to

[5] Probabilities to find z- and ϱ-particle in a barrier under constant effective mass condition, $m^* = m_{\mathrm{QD}}$, are defined as follows,

$$P^{(z)}_{\mathrm{b},i} = \frac{1 - \frac{-\varepsilon_i}{U_{\mathrm{QD}}}}{1 + \frac{\pi\delta}{2}\sqrt{\frac{-\varepsilon_i}{U_{\mathrm{QD}}}}} \qquad P^{(\varrho)}_{\mathrm{b},nm} = \frac{\varepsilon_{nm}}{U_\varrho} \left\{ 1 - \frac{1}{\frac{K_{m-1}(\alpha r_0)}{K_m(\alpha r_0)} \left[\frac{K_{m-1}(\alpha r_0)}{K_m(\alpha r_0)} + \frac{2m}{\alpha r_0} \right]} \right\}.$$

effective mass dependence both on z and on ϱ, $m(z,\varrho)$, even if we would dismiss perturbation W.

In order to make variables separable in (4.34), we subtract and add kinetic energy operators

$$-\frac{\hbar^2}{2m(z)}\frac{\partial^2}{\partial z^2}, \qquad -\frac{\hbar^2}{2m(\varrho)}\left[\frac{1}{\varrho}\frac{\partial}{\partial\varrho}\left(\varrho\frac{\partial}{\partial\varrho}\right)-\frac{m^2}{\varrho^2}\right], \tag{4.35}$$

where

$$m(z)=\begin{cases} m_{\mathrm{QD}}, & |z|<d/2,\\ m_{\mathrm{b}}, & |z|>d/2; \end{cases} \qquad m(\varrho)=\begin{cases} m_{\mathrm{QD}}, & \varrho<r_0,\\ m_{\mathrm{QW}}, & \varrho>r_0. \end{cases} \tag{4.36}$$

Hereby, system hamiltonian turns into

$$\hat{H}=\hat{H}_z+\hat{H}_\varrho+\tilde{W}(z,\varrho), \tag{4.37}$$

where

$$\hat{H}_z \;=\; -\frac{\hbar^2}{2m(z)}\frac{\partial^2}{\partial z^2}+V(z) \tag{4.38}$$

and

$$\hat{H}_\varrho=-\frac{\hbar^2}{2m(\varrho)}\left[\frac{1}{\varrho}\frac{\partial}{\partial\varrho}\left(\varrho\frac{\partial}{\partial\varrho}\right)-\frac{m^2}{\varrho^2}\right]+V(\varrho). \tag{4.39}$$

Equation (4.37) now allows variable separation in case perturbation $\tilde{W}(z,\varrho)$ is small.

Hereinafter equation of states (4.5), considering hamiltonian (4.37) (when variables are separable), is solved. First of all, zero-order eigenvalues are obtained, which afterwards are validated by seeking for higher-order corrections employing perturbation procedure.

Dispersion equation for z-states

In concordance with (4.37) Schrödinger equation for z-particle is

$$\left[-\frac{\hbar^2}{2m(z)}\,\frac{\partial^2}{\partial z^2}+V(z)\right]Z_i(z)=\varepsilon_i\,Z_i(z). \tag{4.40}$$

By taking into account the effective mass discontinuity, we need to mod-

ify previously applied boundary conditions for the wavefunction derivative. The physical requirement for the probability flux density is to be continuous. One can keep in mind that the operator for a probability flux density is proportional to the wavefuncion derivative devided by a particle mass. Thus, the new requirement states that the wavefuncion derivatives devided by appropriate effective mass should match at the interface. Following this, for the "light" z-particle instead of (4.18) we apply the *so called* BenDaniel-Duke boundary conditions [82]

$$\left.\frac{Z_i'}{m(z)Z_i}\right|_{\mp d/2-0} = \left.\frac{Z_i'}{m(z)Z_i}\right|_{\mp d/2+0}. \tag{4.41}$$

According to (4.41), the dispersion equation for the fastly moving z-particle is given by

$$\frac{u/\delta}{\sqrt{\mu_z + (1-\mu_z)\,u^2/\delta^2}} = \begin{cases} \left|\cos\left(\frac{\pi}{2}u\right)\right|, & \tan\left(\frac{\pi}{2}u\right) > 0, \\ \left|\sin\left(\frac{\pi}{2}u\right)\right|, & \tan\left(\frac{\pi}{2}u\right) < 0, \end{cases} \tag{4.42}$$

where $\mu_z = m_{\mathrm{QD}}/m_{\mathrm{b}}$ is a ratio of effective masses, $u = \delta\sqrt{1+\varepsilon_i/U_{\mathrm{QD}}}$ is a unitless variable (equation for an energy of z-state) and $\delta = \sqrt{2m_{\mathrm{QD}}U_{\mathrm{QD}}}\,d/\pi\hbar$ is a unitless parameter, characterizing the strength of a well.

Dispersion equation for ϱ-states

Schrödinger equation for ϱ-particle, considering hamiltonian H_ϱ from (4.37) has a form of

$$\left(\hat{T}_\varrho + V(\varrho)\right) R_{nm}(\varrho) = \varepsilon_{nm}\, R_{nm}(\varrho), \tag{4.43}$$

where kinetic energy operator $\hat{T}_\varrho$ is defined by

$$\hat{T}_\varrho = -\frac{\hbar^2}{2m(\varrho)}\left[\frac{1}{\varrho}\frac{\partial}{\partial\varrho}\left(\varrho\frac{\partial}{\partial\varrho}\right) - \frac{m^2}{\varrho^2}\right]. \tag{4.44}$$

The boundary condition for the heavy ϱ-particle (4.26), taking into account effective mass discontinuity, should be exchanged to

$$\left[\frac{1}{m_{\mathrm{QD}}}\frac{R(\varrho)'}{R(\varrho)}\right]_{r_0-0} = \left[\frac{1}{m_{\mathrm{QW}}}\frac{R(\varrho)'}{R(\varrho)}\right]_{r_0+0}. \tag{4.45}$$

By employing derivative identities

$$\frac{\mathrm{d}}{\mathrm{d}u}J_m(u) = J_{m-1}(u) - \frac{m}{u}J_m(u), \qquad \frac{\mathrm{d}}{\mathrm{d}u}K_m(u) = -K_{m-1}(u) - \frac{m}{u}K_m(u), \tag{4.46}$$

the dispersion equation (4.29) and its unitless form (4.30) for the slowly moving ϱ-particle transform into

$$\frac{J_{m-1}(\beta r_0)}{J_m(\beta r_0)} = -\mu_\varrho \frac{\alpha}{\beta}\frac{K_{m-1}(\alpha r_0)}{K_m(\alpha r_0)} + (1-\mu_\varrho)\frac{m}{\beta r_0} \tag{4.47}$$

and

$$\frac{J_{m-1}(\pi x)}{J_m(\pi x)} = -\mu_\varrho \frac{\gamma}{x}\frac{K_{m-1}(\pi\gamma)}{K_m(\pi\gamma)} + (1-\mu_\varrho)\frac{m}{\pi x}, \tag{4.48}$$

respectively. Here $\mu_\varrho = m_{\mathrm{QD}}/m_{\mathrm{QW}}$ — effective mass ratio, $\gamma = \sqrt{\delta^2 - x^2}/\sqrt{\mu_\varrho}$ — unitless parameter, $\delta = \sqrt{2m_{\mathrm{QD}}U_\varrho}\, r_0/\pi\hbar$ — the strength of a well, and $x = \delta\sqrt{\varepsilon_{nm}/U_\varrho}$ is equation for an energy of ϱ-state.

Transversal ϱ-motion eigenstates from dispersion equation (4.48) can be obtained graphically, as illustrated in Fig. 4.7 by thick curve intersections (open circles).

4.1.5 Corrections for energy levels. Discontinuous effective mass

We have defined system hamiltonian by Eq. (4.37) and made variables separable within the precision of operator $\tilde{W}$, (by assuming $\tilde{W}$ is small perturbation). However, operator W, which comes from real potential profile definition (see Eq. 4.34), and operator $\tilde{W}$ match strictly only in the region of QD. Indeed, perturbation $\tilde{W}$ can be analyzed as a sum of three operators,

$$\tilde{W}(z,\varrho) = W(z,\varrho) + W_z^{(\mathrm{kin})}(z,\varrho) + W_\varrho^{(\mathrm{kin})}(z,\varrho), \tag{4.49}$$

where two last kinetic operators are defined by

$$W_z^{(\mathrm{kin})} = -\frac{\hbar^2}{2}\left[\frac{1}{m(z,\varrho)} - \frac{1}{m(z)}\right]\frac{\partial^2}{\partial z^2}, \tag{4.50}$$

and

$$W_\varrho^{(\mathrm{kin})} = -\frac{\hbar^2}{2}\left[\frac{1}{m(z,\varrho)} - \frac{1}{m(z)}\right]\left[\frac{1}{\varrho}\frac{\partial}{\partial\varrho}\left(\varrho\frac{\partial}{\partial\varrho}\right) - \frac{m^2}{\varrho^2}\right]. \tag{4.51}$$

Now one can clearly see (from the first angle brackets in Eqs. (4.50) and (4.51)) that perturbation operators $W_z^{(\mathrm{kin})}$ and $W_\varrho^{(\mathrm{kin})}$ obtain non-zero val-

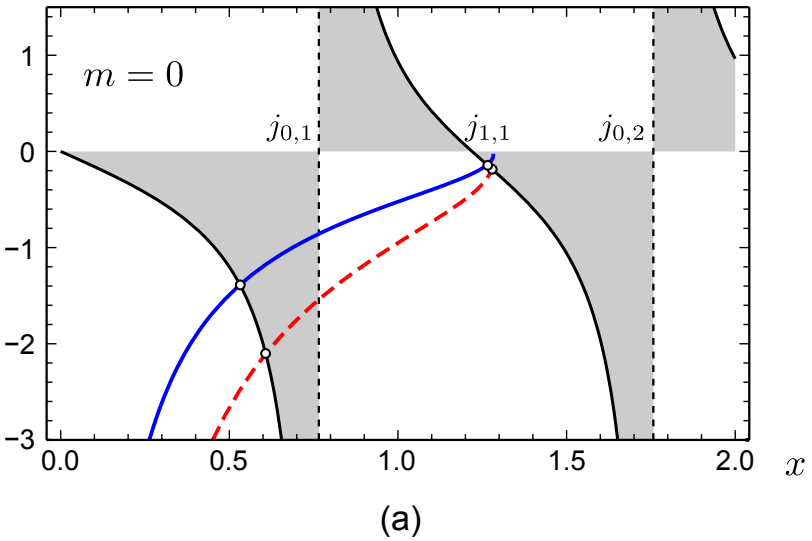

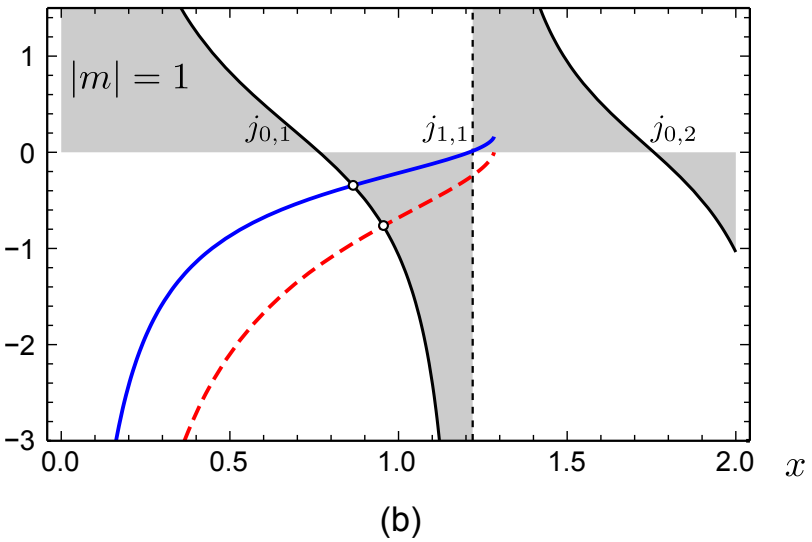

Figure 4.7 Graphical solutions of the dispersion equations: Taking into account (4.48) and disregarding (4.30) effective mass discontinuity, represented by thick solid and dashed curves, respectively. Solutions are provided for two azimuthal quantum number moduli: (a) $m = 0$ and (b) $m = \pm 1$. Strength of the QW was $\delta = 1.28$. $j_{m,n}$ denote n-th zero of a Bessel function $J_m(x)$. Energy values are determined from thick curve intersections (open circles)..

ues, when functions $m(z)$ and $m(\varrho)$ (defined in Eqs. (4.36)) "lie" effective mass values, i.e. when the difference in real and approximated reciprocal effective masses is non-zero,

$$\frac{1}{m(z,\varrho)} - \frac{1}{m(z)} = \begin{cases} \frac{1}{m_{\mathrm{QW}}} - \frac{1}{m_{\mathrm{QD}}}, & |z| < d/2,\ \varrho > r_0, \\ 0, & \text{otherwise;} \end{cases} \tag{4.52}$$

and

$$\frac{1}{m(z,\varrho)} - \frac{1}{m(\varrho)} = \begin{cases} \frac{1}{m_{\mathrm{b}}} - \frac{1}{m_{\mathrm{QD}}}, & \varrho < r_0,\ |z| > d/2, \\ \frac{1}{m_{\mathrm{b}}} - \frac{1}{m_{\mathrm{QW}}}, & \varrho > r_0,\ |z| > d/2, \\ 0, & \text{otherwise.} \end{cases} \tag{4.53}$$

Figure 4.8 illustrates the perturbated areas (filled in grey) for both z- and ϱ-motion particles.

As a result, zero-order eigenvalues obtained taking into account effective mass discontinuity and represented by formulas (4.42) and (4.48) should be examined under perturbation procedure, an instrument to reveal higher-order corrections. Hereinafter, we will seek for eigenvalue first-order corrections $\varepsilon^{(1)}_{inm}$.

Perturbation theory allows to calculate first-order energy level correction when zero-order eigenfunction is known. By definition, $\varepsilon^{(1)}_{inm}$ is obtained by integrating in a whole space perturbation operator being surrounded by zero-order eigenfunction and its complex conjugate form,

$$\begin{aligned} \varepsilon^{(1)}_{inm} &= \int \mathrm{d}^3 r\, \psi^{(0)*}_{inm}\, \tilde{W}(z,\varrho)\, \psi^{(0)}_{inm} \\ &= -U_\varrho\, P^{(z)}_{\mathrm{b},i}\, P^{(\varrho)}_{\mathrm{b},nm} + \varepsilon^{(1,\mathrm{kin})}_{z,inm} + \varepsilon^{(1,\mathrm{kin})}_{\varrho,inm}. \end{aligned} \tag{4.54}$$

Here first addend in a sum accounts for a contribution from perturbation $W(z,\varrho)$ (see Eq. (4.33)) with probabilities to find electron in a barrier, $P^{(z)}_{\mathrm{b},i}$ and $P^{(\varrho)}_{\mathrm{b},nm}$, derived taking into account discontinuous effective mass.[6] Terms $\varepsilon^{(1,\mathrm{kin})}_{z,inm}$ and $\varepsilon^{(1,\mathrm{kin})}_{\varrho,inm}$ correspond to contribution from perturbations $W^{(\mathrm{kin})}_z$ and $W^{(\mathrm{kin})}_\varrho$, respectively.

Let us find last two summands in Eq. (4.54). Term $\varepsilon^{(1,\mathrm{kin})}_{z,inm}$ is defined by

[6] Probabilities to find z- and ϱ-particle in a barrier, taking into account effective mass discontinuity, are defined as follows,

$$P^{(z)}_{\mathrm{b},i} = \frac{1-\frac{-\varepsilon_i}{U_{\mathrm{QD}}}}{1+\left[1-(1-\mu_z)\frac{-\varepsilon_i}{U_{\mathrm{QD}}}\right]\frac{\pi\delta}{2\sqrt{\mu_z}}\sqrt{\frac{-\varepsilon_i}{U_{\mathrm{QD}}}}} \qquad P^{(\varrho)}_{\mathrm{b},nm} = \frac{\frac{K_{m-1}(\alpha r_0)}{K_m(\alpha r_0)}\left[\frac{K_{m-1}(\alpha r_0)}{K_m(\alpha r_0)}+\frac{2m}{\alpha r_0}\right]-1}{\left(1+\mu_z^2\frac{\alpha^2}{\beta^2}\right)\frac{K_{m-1}(\alpha r_0)}{K_m(\alpha r_0)}\left[\frac{K_{m-1}(\alpha r_0)}{K_m(\alpha r_0)}+\frac{2m}{\alpha r_0}\right]-\frac{m^2}{\beta^2 r_0^2\left(1-\mu_\varrho^2\right)}},$$

where $\alpha = \sqrt{2m_{\mathrm{QD}}(U_\varrho - \varepsilon_{nm})}/\hbar$, $\beta = \sqrt{2m_{\mathrm{QD}}\varepsilon_{nm}}/\hbar$.

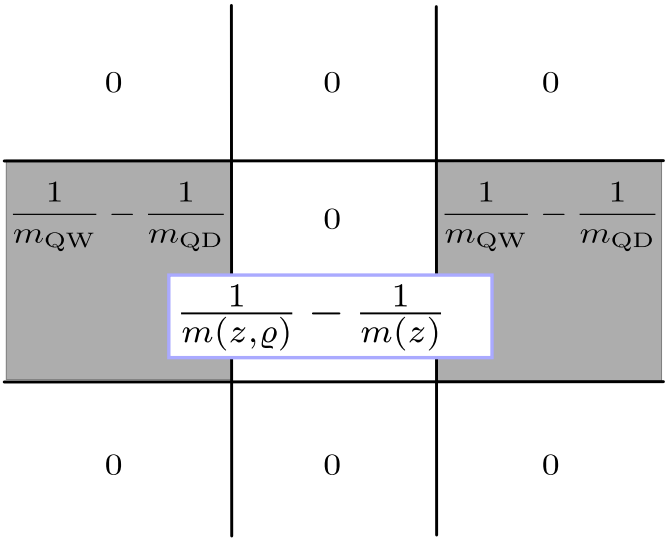

(a)

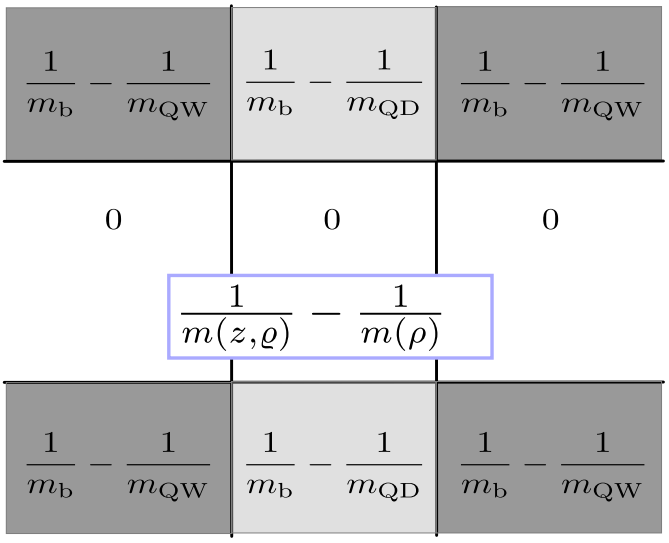

(b)

Figure 4.8 Scheme of effective mass, indicating wrongly evaluated zero-order eigenvalues, $\varepsilon_{inm}^{(0)}$, within shaded areas: (a) z-motion and (b) ϱ-motion perturbations..

$$\varepsilon_{z,inm}^{(1,\mathrm{kin})} = \int_{-d/2}^{d/2} \mathrm{d}z\, Z_i^{(0)*}\, W_z^{(\mathrm{kin})}\, Z_i^{(0)} \int_{r_0}^{\infty} \mathrm{d}\varrho\, \varrho \left| R_{nm}^{(0)} \right|^2. \tag{4.55}$$

Putting $W_z^{(\mathrm{kin})}$ formula (Eq. (4.50)) and employing Schrödinger equation (4.40) yields

$$\begin{aligned} \varepsilon_{z,inm}^{(1,\mathrm{kin})} &= (\mu_\varrho - 1)(U_{\mathrm{QD}} + \varepsilon_i) \int_{-d/2}^{d/2} \mathrm{d}z \left| Z_i^{(0)} \right|^2 P_{\mathrm{b},nm}^{(\varrho)} \\ &= -(1-\mu_\varrho)(U_{\mathrm{QD}} + \varepsilon_i) \left(1 - P_{\mathrm{b},i}^{(z)}\right) P_{\mathrm{b},nm}^{(\varrho)}. \end{aligned} \tag{4.56}$$

Term $\varepsilon_{\varrho,inm}^{(1,\mathrm{kin})}$ is defined by

$$\varepsilon_{\varrho,inm}^{(1,\mathrm{kin})} = \int_{-d/2}^{d/2} \mathrm{d}z \left| Z_i^{(0)} \right|^2 \int_{r_0}^{\infty} \mathrm{d}\varrho\, \varrho\, R_{nm}^{(0)*}\, W_\varrho^{(\mathrm{kin})}\, R_{nm}^{(0)}. \tag{4.57}$$

Inserting $W_\varrho^{(\mathrm{kin})}$ formula (Eq. (4.51)) and employing Schrödinger equation (4.43) yields

$$\begin{aligned} \varepsilon_{\varrho,inm}^{(1,\mathrm{kin})} = \quad & -\Bigg[(1-\mu_z)\, \varepsilon_{nm} \left(1 - P_{\mathrm{b},nm}^{(\varrho)}\right) \\ & -\left(1 - \frac{m_{\mathrm{QW}}}{m_{\mathrm{b}}}\right)(U_\varrho - \varepsilon_{nm})\, P_{\mathrm{b},nm}^{(\varrho)} \Bigg] P_{\mathrm{b},i}^{(z)}. \end{aligned} \tag{4.58}$$

4.1.6 Kane corrections

By now we have used envelope function (or effective mass) approximation (EFA) for calculations of energy spectra of semiconductor quantum heterostructures — dots and rods. Indeed, within EFA ($\mathbf{k}\cdot\mathbf{p}$ method) one can solve Schrödinger equation exactly only for a single quasimomentum $\hbar\mathbf{k_0}$, corresponding to CB minimum. However, 2-D electron levels in a QW are well-elevated from the bottom of a CB, therefore to be precise in our calculations we further consider Kane model, which accounts for band nonparabolicity effects.

As electrons recede from band minimum, successive bands ($n' \neq n$) start to influence $\{n, \mathbf{k}\}$ states. Modified EMA schemes, such as Kane model, score the contribution of several nearest bands accurately, whereas the following bands are addressed by perturbation procedure. Briefly, Kane model takes into account effective mass dependence upon the energy of electron

state, $m^* = m(\mathbf{r}; E)$. This is evident from effective Schrödinger equation (see e.g. Ref. [2]), which hamiltonian usually is written by

$$\hat{H} = -\frac{\hbar^2}{2m_E}\Delta + V(\mathbf{r}), \quad m_E \equiv m\,(1 + E/E_{\rm g}), \tag{4.59}$$

where $1/m = 2|P|^2/\hbar^2 E_{\rm g}$ and P - Kane parameter.[7]Now it is obvious from (4.59) that CB nonparabolicity effects become more and more significant as electron energy approaches the value of bandgap, $E_{\rm g}$.

In case of investigating VB spin-orbit splitting, $\Delta_{\text{s-o}}$, one then should use hamiltonian[8]

$$\hat{H} = -\frac{\hbar^2}{2m}\,\frac{1 + E/(E_{\rm g} + \frac{2}{3}\Delta_{\text{s-o}})}{(1 + E/E_{\rm g})[1 + E/(E_{\rm g} + \Delta_{\text{s-o}})]}\Delta + V(\mathbf{r}). \tag{4.60}$$

Finally, the recipe for energy level calculation can be simply illustrated by the self-explanatory scheme, depicting iterative procedure steps,

$$m^* = m(\mathbf{r}; E^{(0)}) \stackrel{\text{Schr.}}{\longrightarrow} E^{(1)} \longrightarrow m(\mathbf{r}; E^{(1)}) \stackrel{\text{Schr.}}{\longrightarrow} \ldots \tag{4.61}$$

4.1.7 Selection rules

One of the advantages of analytic solutions is a possibility to derive selection rules for optical transitions. The probability of the intraband optical transition from the initial state inm to the final one $i'n'm'$ is proportional to squared dipole matrix element,

$$w_{inm\to i'n'm'} \propto \left|\langle i'n'm'|\, e\boldsymbol{E}\boldsymbol{r}\,|inm\rangle\right|^2, \tag{4.62}$$

where $\boldsymbol{E}$ is an amplitude of the electric field and $|inm\rangle$ are the wave functions, which in the present scheme of QD description are

$$|inm\rangle = Z_i(z)R_{nm}(\varrho)\Phi_m(\varphi). \tag{4.63}$$

A simple analysis of the (4.62) integral yields that for the $\boldsymbol{E} \parallel z$ polarized

---

[7]Kane parameter is given by formula
$\int_{\rm cell} {\rm d}^3 r\, u_{\rm s}^* \frac{\partial}{\partial i} u_{{\rm P}i} \equiv -\frac{m_0}{\hbar^2} P, \quad i = x, y, z$

[8]In case of asymptotic boundary, $\Delta_{\text{s-o}} \ll E_{\rm g}$, efective hamiltonian (4.60) turns into (4.59); Effective mass m for CB electrons in formula (4.60) is defined by
$\frac{1}{m} = \frac{2|P|^2}{\hbar^2 E_{\rm g}}\,\frac{1+\frac{2}{3}\Delta_{\text{s-o}}/E_{\rm g}}{1+\Delta_{\text{s-o}}/E_{\rm g}}$.

light the intraband optical transitions should obey the selection rule

$$i' = i \pm 1, \pm 3 \ldots, \qquad n' = n, \quad m' = m. \tag{4.64}$$

While the selection rule for optical transitions induced by the in-plane polarized light, $\boldsymbol{E} \perp z$, is

$$i' = i, \qquad m' = m \pm 1. \tag{4.65}$$

4.2 Results of Energy Spectra Calculations

The supercell (elementary cell) of a quantum dot superlattice structures studied experimentally in [1–4.§] consist of truncated cone-shaped InAs quantum dots, formed above InAs wetting layer (WL), and embedded within GaAs or GaAs/AlAs matrix. Cone height is 2 nm, base and floor diameters are 20.4 nm and 13.4 nm, accordingly. Such topology of QD is similar to a low cylinder (or tablet), which radius, r_0, is defined as an arithmetic average of truncated cone base and floor radii [see Fig. 4.9(a)]. Hereby, choosing a cylindrical symmetry is rather adequate for QD spectrum analysis and compatible with the above-presented analytical algorithm.

Another set of QD structures studied experimentally consist of self-assembling InAs QDs embedded in GaAs or InGaAs/GaAs matrix. To adapt QD supercell geometry for adiabatic algorithm needs, lenslike QD is approximated by cylinder, matching their profile areas (retaining QD height value) as illustrated in Fig. 4.9(b). As a result, cylindrical QD height is 5 nm and radius is 7 nm.

Three sets of columnar QD structures, investigated most recently in [5–7.§], were also put under test within adiabatic model. A supercell of QR structures consists of InGaAs QR surrounded by InGaAs QW, having lower In content, and both QR and immersing QW are sandwiched between GaAs layers, as depicted in Fig. 4.9(c). According to TEM pictures, and assuming 1 ML equals the thickness of a half lattice constant, QR heights of 11 nm, 21 nm, and 37 nm were deduced, whereas radius is constant for all of them and equals 5 nm.

Let us calculate the electron energy spectrum of several cylindrical $In_xGa_{1-x}As$ reference samples $QD_{2:8}$, $QD_{5:7}$, $QR_{21:5}$, and $QR_{37:5}$ making use of the suggested calculation technique. The geometrical parameters and In-composition of the samples are summarized in Table 4.1. The reference samples chosen simulate the self-assembled lens-like QDs and QRs, which were MBE-grown

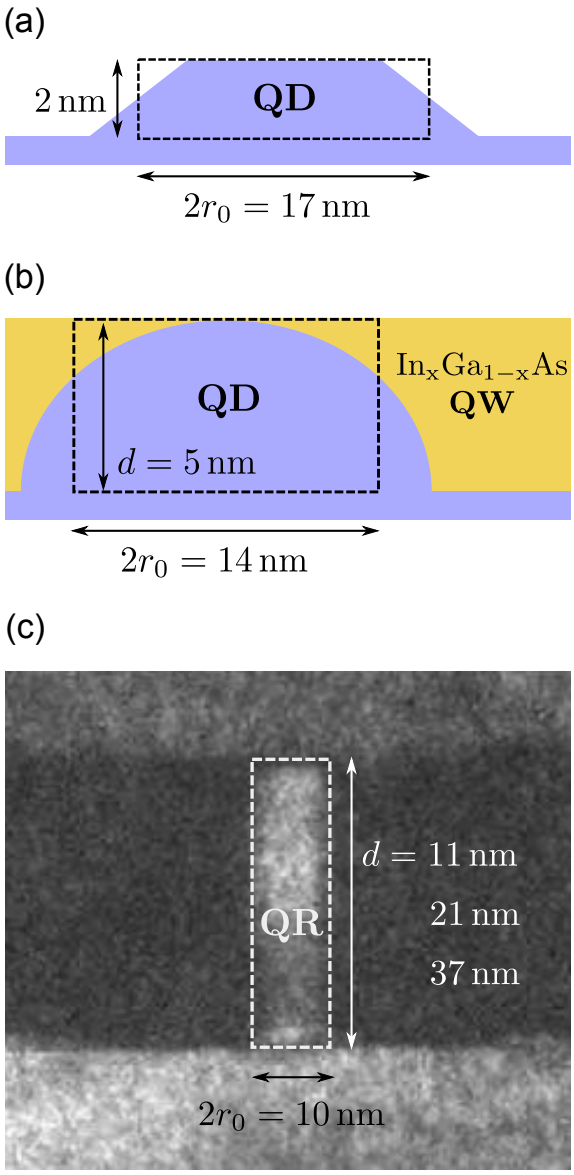

Figure 4.9 Schemes of quantum dot [(a) and (b)] and rod (c) structures under test, experimentally investigated in Refs. [1–7.§].

Table 4.1 Geometrical parameters and composition of $In_xGa_{1-x}As$ QD and QR reference samples: the height d, the radius r_0, the atomic composition of In in QD (QR) region x_{QD}, in the QW region x_{QW}, and in the $|z| > d/2$ barrier regions x_b.

QD geometry	d (nm)	r_0 (nm)	x_{QD}	x_{QW}	x_b
$QD_{2:8}$	2	8.45	1	0	0
$QD_{5:7}$	5	7	1	0.15	0
$QR_{21:5}$	21	5	0.4	0.18	0
$QR_{37:5}$	37	5	0.4	0.18	0

Table 4.2 Potential profile and effective masses of $In_xGa_{1-x}As$ QD and QR reference samples.

QD geometry	U_{QD} (meV)	U_{QW} (meV)	m^*_{QD} (m_0)	m^*_{QW} (m_0)	m^*_b (m_0)
$QD_{2:8}$	523	0	0.046	0.067	0.067
$QD_{5:7}$	523	109	0.046	0.063	0.067
$QR_{21:5}$	256	126	0.057	0.062	0.067
$QR_{37:5}$	256	126	0.057	0.062	0.067

by G. Strasser [3, 5, 6] and L. Li [7, 37], respectively.

The profiles of potential energy and effective mass in the reference samples were determined by the following scheme. The material parameters — energy gaps $E_{g(u)}$ and effective masses $m^*_{(u)}$ — of unstrained regions of samples were taken from Ref. [60]. The strain field was calculated within the framework of the isotropic elasticity theory [83, 84], which predicts an abrupt variation of the hydrostatic strain $\epsilon_h = \epsilon_{xx} + \epsilon_{yy} + \epsilon_{zz}$. Then, the average energy gaps (with respect to hh and lh valence bands) were calculated, $\overline{E}_g = E_{g(u)} + (a_c + a_v)\epsilon_h$, where a_c and a_v are the conduction and valence band deformation potentials. The conduction band offsets ΔE_c, which constitute the potential profile (4.7), were determined from the offsets of the energy gaps, $\Delta E_c = Q\Delta E_g$, making use of the $Q = 0.87$ ratio value, which was experimentally deduced for strained InGaAs-GaAs quantum wells [85,86]. To evaluate the strain-induced mass shifts, the $m^*_{(u)}(E_{g(u)})$ relation for unstrained InGaAs was employed. The determined potential profiles and effective masses are presented in Table 4.2.

The electron energy ε_{inm} spectra in the reference QDs and QRs are presented in Fig. 4.10. The s-, p-, and d-groups of QD levels correspond to the azimuthal quantum number $m = 0$, 1, and 2.

Figures 4.10(a), (c) and (d) present final results, the energy levels calculated taking into account both $\hat{W}(z, \varrho)$-coupling, and Kane corrections. Dotted and dashed levels in the $QD_{5:7}$ spectrum (Fig. 4.10(b)) present the electron energies calculated without the Kane corrections: dotted levels correspond to the zero-order energies $\varepsilon^{(0)}_{inm}$, dashed levels present the $\hat{W}(z, \varrho)$-corrected results $\varepsilon^{(0)}_{inm} + \varepsilon^{(1)}_{inm}$. As seen, the coupling corrections are larger for higher-energy levels and are small for the lower-energy ones, decreasing from several tens of meV to milielectronvolts. It should be noted that the potential and kinetic energy terms of the coupling operator $\hat{W}(z, \varrho)$ yield comparable corrections, of the same order of magnitude. The Kane corrections, as seen from Fig. 4.10(b), shift down the electron energy spectrum and decrease interlevel separations, in qualitative agreement with results of the calculations [87], where non-parabolicity effects were taken into accounted in the framework of 8-band $\boldsymbol{k} \cdot \boldsymbol{p}$ Hamiltonian. The Kane shifts, calculated within the present scheme, in general are larger than the $\hat{W}(z, \varrho)$-induced ones. They are first of all due to an increase of the effective mass in QD region, which leads to an increase of the wavefunction confinement within QD region and, therefore, to a subsequent decrease of the $\hat{W}(z, \varrho)$-corrections down to ~ 1 meV for all — both high-, and low-energy — levels. The same features of $\hat{W}(z, \varrho)$- and Kane-corrections qualitatively manifest themselves in all chosen reference QD and QR samples.

The energy spectrum structure of flat QDs, where $d < r_0$, is determined by quantization of the ϱ-motion. All four levels of the $QD_{2:8}$ and $QD_{5:7}$ dots correspond to the same, ground state $i = 1$ of the z-motion, with comparatively large size-quantization energy, and different nm-states of ϱ-motion, which correspond to a smaller size-quantization energy.

The ground ε_{110} level of the $QD_{2:8}$ is at the -178 meV, and the first excited ε_{111} is by 51 meV above. The positions can be compared with the IR experimental photocurrent spectral data [3, 5, 6] of the doped lens-like self-assembled QDs, which show 'the ground state $\rightarrow$ continuum' peak at ca. 220 meV and 'the ground $\rightarrow$ excited state' peak at ~ 60 meV. The discrepancy between calculated and experimental values can be removed adjusting parameters of the reference sample. However, it can be as well due to additional potential profile details, present in the real QDs and disregarded in $QD_{2:8}$.

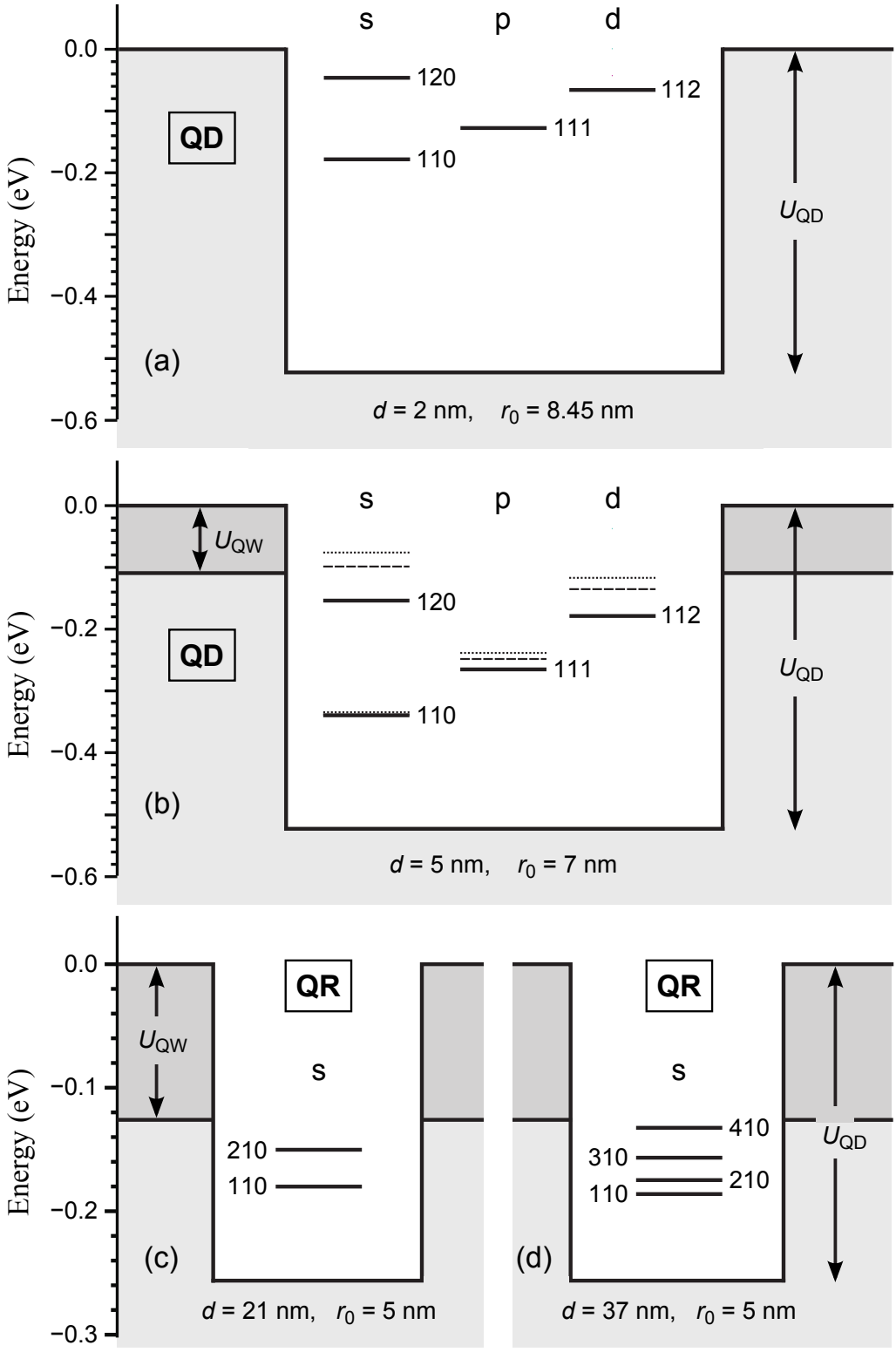

Figure 4.10 Electron energy spectra for two different quantum geometries — QD (a) and QR (b) — calculated under variable separation approximation. First-order corrections (solid lines) were obtained by perturbation procedure. Dashed lines denote zero-order calculations (given for QR spectra only).

The energy spectrum of the $QD_{5:7}$ reference sample has the same structure as that of the $QD_{2:8}$ dot, but levels are shifted down and energy separation between them are increased due to a larger height and a smaller radius of $QD_{5:7}$. One can trace the effect in the optical interband transitions: the photoluminescence (PL) peak of quantum dots, with parameters close to those of $QD_{2:8}$, is positioned at 1.00 eV, [1–4.§] while the main PL peak of the $QD_{5:7}$-like quantum dots [8.i, 1.n] is red-shifted to 0.95 eV.

The energy spectrum structure of quantum rods (Figs. 4.10(c) and (d)), which have opposite as compared to QDs aspect ratio $d > r_0$, is determined by quantization of the z-motion. All levels of the $QR_{21:5}$ and $QR_{37:5}$ rods correspond to the same, ground state ($n = 1,\ m = 0$) of the ϱ-motion with comparatively large size-quantization energy and different i-states of z-motion of a smaller size-quantization energy.

The ground state ε_{110} wavefunction of the $QR_{21:5}$ rod is presented in Fig. 4.11. As seen, it is well-localized in the QR region along the z-direction, but has a considerable in-plane spread into the ϱ-barrier. It should be noted that though the probability of the ϱ-barrier penetration is considerable, $P_{10} \approx 0.2$, the $\hat{W}(z, \varrho)$-shift of the energy level is very small, $\varepsilon_{110}^{(1)} < 1\,\text{meV}$.

With an increase of the QR height, the size-quantization energy of the z-motion decreases, the $QR_{37:5}$ levels shift down and the interlevel separation becomes smaller as compared to the $QR_{21:5}$ energy spectrum. This can be traced in the optical interband transitions [5–7.§]: the photoluminescence peak of quantum rods experience a red-shift at larger QR heights.

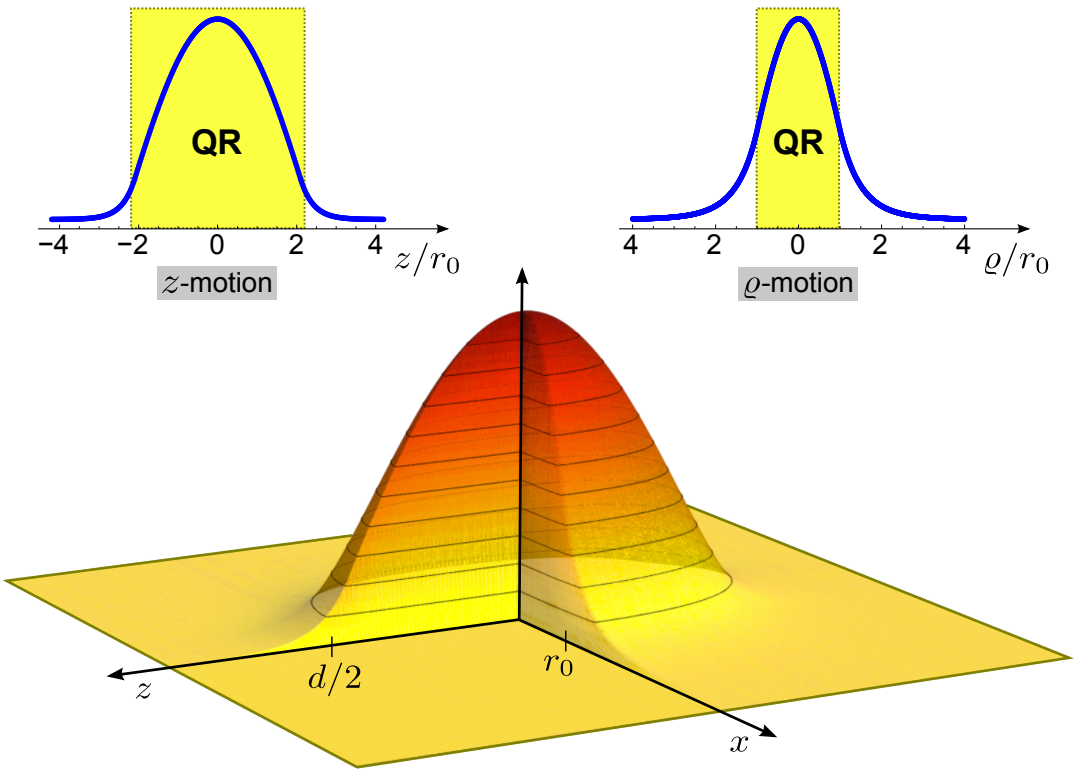

Figure 4.11 The ground-state wavefunction Ψ_{110} of the $\mathrm{QR}_{21:5}$ quantum rod with the $d = 21\,\mathrm{nm}$ height and $r_0 = 5\,\mathrm{nm}$ radius (bottom) together with the corresponding cross-sections along z- and ϱ-motion planes (top).

4.3 Conclusions

In summary, the analytical algorithm for electron energy spectrum calculations in cylindrical quantum dots. The method is based on a replacement of an actual hamiltonian with an approximate one, which allows for a separation of variables. The difference of the hamiltonians, both of their potential, and kinetic energy parts, act in regions outside quantum dot only and is treated as perturbation. Therefore, the suggested scheme is strictly justified for the electron states, which are well-localized within quantum dot. Application of the method for several quantum dot and quantum rod reference samples show that in practice all QD (QR) bound states can be reliably calculated by the suggested technique. The calculated energy spectra of the reference samples are in qualitative agreement with experimental data. Finally, modeling of QD/QR electron energy levels show that taking into account effective mass discontinuity, CB nonparabolicity, and strain results in significant changes of energy spectra and thereby are essential to reproduce and interpret experimentaly observed optical transitions.

The aforementioned findings allowed to formulate the following *statement for defence*

Analytical approach for electron energy spectrum calculations of cylindrical quantum dots is proposed. The method is based on the separation of variables approximation and provides reliable results both for ground- and excited-states of various InGaAs quantum dot structures.

Main Results and Conclusions

1. Studies of interband optical transitions and electronic structure of vertically stacked InAs quantum dot (QD) multilayers within GaAs matrix and GaAs/AlAs superlattice (SL) were performed by modulated reflectance — photoreflectance (PR) and contactless electroreflectance (CER) — techniques, supported by photoluminescence (PL) spectroscopy. Experimental results and numerical calculations show that the electronic structure of the considered QD systems is strongly affected by parameters of InAs QDs, InAs wetting layer (WL) and GaAs/AlAs SL.
   In particular, it was found that

   a) blue-shift (by about 50 meV) and intensity enhancement of the InAs WL-related PR/CER features in InAs/GaAs/AlAs QD-SL originate mainly due to off-centre position of the dot layers in the wells. In more detail, it was unambigously revealed by numerical calculations that interband transitions within InAs QD depend strongly on the dot position (distance) from the confining AlAs barrier layer.

   b) the appearance of multiple InAs WL-related features in the modulated reflectance spectra are attributed to the variation of the WL thickness in the stacked QD structures. The thickness of the InAs WL reduces from about 1.5 ML to 1 ML with vertical ordering in favor of larger QDs as a consequence of gradual buildup of the internal strain.

2. The comparative study of electronic energy spectra for InAs QDs embedded within InGaAs/GaAs/AlAs and GaAs/AlAs composite quantum wells (QWs) have been performed by spectroscopic PR and PL techniques together with the numerical calculations. From the analysis of spectroscopic data it was found that the use of InGaAs strain-reducing layer tunes the QD ground-state transition to lower energies by about 100 meV maintaining strong quantization of the electronic states.
   It was determined that

a) red-shift of the QD ground-state interband transitions is mainly caused by the partial strain relaxation within the capped InAs QDs and the increase of effective QD size due to decomposition of InGaAs cap layer during growth process.

b) actual value of $x = 0.13$ for the $In_xGa_{1-x}As$ strain-reducing layer is lower by 2% from the nominal In content.

3. The differences in the optical properties of variant in morphology InGaAs quantum rod (QR), surrounded by a InGaAs quantum well (QW), structures, grown using As_2 and As_4 sources, have been examined by PR and PL spectroscopy.
   It was found that

   a) as compared with As_2-grown InGaAs QRs, a stronger PL intensity, a longer emission wavelength, and an increased energy spacing between the ground- and excited-states are observed for As_4-grown QR structures.

   b) the energy spacing ΔE between the InGaAs QR and InGaAs QW ground-state interband transitions also increases for As_4-grown samples.

   c) the changes in optical properties can be explained in terms of enhanced carrier confinement in As_4-grown QRs owing to an increased indium composition contrast between InGaAs QRs and the surrounding InGaAs 2-D layer.

4. The anisotropy of optical response of epitaxial InGaAs QRs was studied by measuring polarization-resolved PR and PL spectra from cleaved-edge and in-plane surfaces.
   It was found that

   a) the in-(001)-plane polarization degree reaches a high value of about 60% for InGaAs QRs having $N = 35$ SL periods. As a result, PL polarization properties (TE and TM modes) are different for the (110)- and $(1\bar{1}0)$-facets.

   b) the transverse magnetic (TM) mode dominates from the $(1\bar{1}0)$-cleaved surfaces ($TM_{[001]} > TE_{[110]}$), whereas the transverse electric (TE) mode is larger from the (110)-facets ($TM_{[001]} < TE_{[1\bar{1}0]}$) .

5. To interpret experimental data of InGaAs quantum dot structures studied, a simple analytical method for electron energy spectrum calculations

in cylindrical QD/QR was proposed. The method is based on a replacement of an actual hamiltonian with an approximate one, which allows for a separation of variables.
It was found that

a) the potential and kinetic energy terms of the coupling operator (perturbation) $\hat{W}(z, \varrho)$ act in regions outside quantum dot only and yield comparable corrections, of the same order of magnitude

b) application of the method for several QD/QR reference samples shows that in practice all bound states are reliably calculated by the suggested technique.

c) the calculated energy spectra of the reference QD/QR samples qualitatively matches experimental data well.

References

[1] D. Bimberg, M. Grundmann, and N. N. Ledentsov, *Quantum dot heterostructures* (Wiley, Chichester, 1999).

[2] V. Karpus, *Dvimačiai elektronai* (Ciklonas, Vilnius, 2004) // in Lithuanian.

[3] L. Rebohle, F. F. Schrey, S. Hofer, G. Strasser, and K. Unterrainer, *Energy level engineering in InAs quantum dot nanostructures.* Appl. Phys. Lett. **81**, 2079 (2002).

[4] S. Hofer, H. Hirner, R. Bratschitsch, G. Strasser, and K. Unterrainer, *Photoconductive response of InAs/GaAs quantum dot stacks.* Physica E **13**, 190 (2002).

[5] L. Rebohle, F. F. Schrey, S. Hofer, G. Strasser, and K. Unterrainer, *Energy level engineering in InAs quantum dot stacks embedded in AlAs/GaAs superlattices.* Physica E **17**, 42 (2003).

[6] F. F. Schrey, L. Rebohle, T. Müller, G. Strasser, K. Unterrainer, D. P. Nguyen, N. Regnault, R. Ferreira, and G. Bastard, *Intraband transitions in quantum dot-superlattice heterostructures.* Phys. Rev. B **72**, 155310 (2005).

[7] L. H. Li, G. Patriarche, M. Rossetti, and A. Fiore, *Growth and characterization of InAs columnar quantum dots on GaAs substrate.* J. Appl. Phys. **102**, 033502 (2007).

[8] F. H. Pollak and H. Shen, *Modulation spectroscopy of semiconductors: bulk/thin film, microstructures, surfaces/interfaces and devices.* Mater. Sci. Eng. **R10** (7–8), 274–375 (1993).

[9] I. N. Stranski and L. Krastanow, *Abhandlungen der Mathematisch-Naturwissenschaftlichen Klasse IIb.* Akademie der Wissenschaften Wien **146**, 797–810 (1938).

[10] E. Bauer, *Phaenomenologische Theorie der Kristallabscheidung an Oberflaechen I.* Zeitschrift für Kristallographie **110,** 372–394 (1958).

[11] R. V. Kukta and L. B. Freund, *Minimum energy configuration of epitaxial material clusters on a lattice-mismatched substrate.* J. Mech. Phys. Solids **45** (11–12), 1835–1860 (1997).

[12] P. M. Petroff and S. P. DenBaars, *MBE and MOCVD growth and properties of self-assembling quantum dot arrays in III-V semiconductor structures.* Superlattices Microstruct. **15**, 15 (1994).

[13] D. Leonard, K. Pond, and P. M. Petroff , *Critical layer thickness for self-assembled InAs islands on GaAs.* Phys. Rev. B **50**, 11687–11692 (1994).

[14] J. Oshinowo, M. Nishioka, S. Ishicia, and Y. Arakawa, *Highly uniform lnGaAs/GaAs quantum dots (~15 nm) by metalorganic chemical vapor deposition.* Appl. Phys. Lett. **65** (11), 1421 (1994).

[15] E. -T. Kim, Z. Chen, and A. Madhukar, *Tailoring detection bands of InAs quantum-dot infrared photodetectors using $In_xGa_{1-x}As$ strain-relieving quantum wells.* Appl. Phys. Lett. **79**, 3341 (2001).

[16] D. Pan, E. Towe, and S. Kennerly, *Normal-incidence intersubband (In, Ga)As/GaAs quantum dot infrared photodetectors.* Appl. Phys. Lett. **73**, 1937 (1998).

[17] S. Maimon, E. Finkman, G. Bahir, S. E. Schacham, J. M. Garcia, and P. M. Petroff, *Intersublevel transitions in InAs/GaAs quantum dots infrared photodetectors.* Appl. Phys. Lett. **73**, 2003 (1998).

[18] L. Chu, A. Zrenner, M. Bichler, and G. Abstreiter, *Quantum-dot infrared photodetector with lateral carrier transport.* Appl. Phys. Lett. **79**, 2249 (2001).

[19] H. C. Liu, M. Gao, J. McCaffrey, Z. R. Wasilewski, and S. Fafard, *Quantum dot infrared photodetectors.* Appl. Phys. Lett. **78**, 79 (2001).

[20] J. -Y. Duboz, H. C. Liu, Z. R. Wasilewski, M. Byloss, and R. Dudek, *Tunnel current in quantum dot infrared photodetectors.* J. Appl. Phys. **93**, 1320 (2003).

[21] A. M. Adawi, E. A. Zibik, L. R. Wilson, A. Lemaître, J. W. Cockburn, M. S. Skolnick, M. Hopkinson, and G. Hill, *Comparison of intraband absorption and photocurrent in InAs/GaAs quantum dots.* Appl. Phys. Lett. **83**, 602 (2003).

[22] P. Boucaud and S. Sauvage, *Infrared photodetection with semiconductor self-assembled quantum dots.* C. R. Physique **4**, 1133–1154 (2003).

[23] S. Krishna, D. Forman, S. Annamalai, P. Dowd, P. Varangis,

T. Tumolillo, A. Gray, J. Zilko, K. Sun, M. Liu, J. Campbell, and D. Carothers, *Demonstration of a 320×256 two-color focal plane array using InAs/InGaAs quantum dots in well detectors.* Appl. Phys. Lett. **86**, 193501, (2005).

[24] B. F. Levine, *Quantum-well infrared photodetectors.* J. Appl. Phys. **74**, R1 (1993).

[25] L. Chu, M. Arzberger, G. Böhm, and G. Abstreiter, *Influence of growth conditions on the photoluminescence of self-assembled InAs/GaAs quantum dots.* J. Appl. Phys. **85**, 2355 (1999).

[26] J. S. Kim, P. W. Yu, J. -Y. Leem, M. Jeon, S. K. Noh, J. I. Lee, G. H. Kim, S. -K. Kang, J. S. Kim, and S. G. Kim, *Effects of high potential barrier on InAs quantum dots and wetting layer.* J. Appl. Phys. **91**, 5055 (2002).

[27] A. T. Winzer, R. Goldhahn, G. Gobsch, H. Heidemeyer, O. Schmidt, K. Eberl, *Optical properties of wetting layers in stacked InAs/GaAs quantum dot structures.* Physica E, **13**, 289–292 (2002).

[28] S. Anders, C. S. Kim, B. Klein, M. W. Keller, R. P. Mirin, and A. G. Norman, *Bimodal size distribution of self-assembled $In_xGa_{1-x}As$ quantum dots.* Phys. Rev. B **66**, 125309 (2002).

[29] J. Misiewicz, P. Sitarek, G. Sęk, and R. Kudrawiec, *Semiconductor heterostructures and device structures investigated by photoreflectance spectroscopy.* Materials Science-Poland, **21** (3), 263–320 (2003).

[30] B. Čechavičius, J. Kavaliauskas, G. Krivaitė, D. Seliuta, G. Valušis, M P. Halsall, M. J. Steer, and P. Harrison, *Photoreflectance and surface photovoltage spectroscopy of beryllium-doped GaAs/AlAs multiple quantum wells.* J. Appl. Phys. **98**, 023508 (2005).

[31] A. Fiore, J. X. Chen, and M. Ilegems, *Scaling quantum-dot light-emitting diodes to submicrometer sizes.* Appl. Phys. Lett. **81**, 1756 (2002).

[32] D. Bimberg and N. Ledentsov, *Quantum dots: lasers and amplifiers.* J. Phys.: Condens. Matter. **15** (24), R1063 (2003).

[33] S. Chakrabarti, A. D. Stiff-Roberts, X. H. Su, P. Bhattacharya, G. Ariyawansa, and A. G. U. Perera, *High-performance mid-infrared quantum dot infrared photodetectors.* J. Phys. D: Appl. Phys. **38**, 2135 (2005).

[34] S. Kiravittaya, A. Rastelli, and O. G. Shmidt, *Advanced quantum dot configurations.* Rep. Prog. Phys. **72**, 046502 (2009).

[35] M. Sugawara, H. Ebe, N. Hatori, M. Ishida, Y. Arakawa, T. Akiyama, K. Otsubo, and Y. Nakata, *Theory of optical signal amplification and processing by quantum-dot semiconductor optical amplifiers.* Phys. Rev. B **69**, 235332 (2004).

[36] J. He, R. Nötzel, P. Offermans, P. M. Koenraad, Q. Gong, G. J. Hamhuis, T. J. Eijkemans, and J. H. Wolter, *Formation of columnar (In,Ga)As quantum dots on GaAs(100).* Appl. Phys. Lett. **85**, 2771 (2004).

[37] L. H. Li, P. Ridha, G. Patriarche, N. Chauvin, and A. Fiore, *Shape-engineered epitaxial InGaAs quantum rods for laser applications.* Appl. Phys. Lett. **92**, 121102 (2008).

[38] T. Kita, N. Tamura, O. Wada, M. Sugawara, Y. Nakata, H. Ebe, and Y. Arakawa, *Artificial control of optical gain polarization by stacking quantum dot layers.* Appl. Phys. Lett. **88**, 211106 (2006).

[39] J. Andrzejewski, G. Sęk, E. O'Reilly, A. Fiore, and J. Misiewicz, *Eight-band $k \cdot p$ calculations of the composition contrast effect on the linear polarization properties of columnar quantum dots.* J. Appl. Phys. **107**, 073509 (2010).

[40] P. Ridha, L. H. Li, M. Mexis, P. M. Smowton, J. Andrzejewski, G. Sęk, J. Misiewicz, E. P. O'Reilly, G. Patriarche, and A. Fiore, *Polarization Properties of Columnar Quantum Dots: Effects of Aspect Ratio and Compositional Contrast.* IEEE J. Quantum Electron. **46** (2), 197 (2010).

[41] L. H. Li, M. Mexis, P. Ridha, M. Bozkurt, G. Patriarche, P. M. Smowton, P. Blood, P. M. Koenraad, and A. Fiore, *Control of polarization and dipole moment in low-dimensional semiconductor nanostructures.* Appl. Phys. Lett. **95**, 221116 (2009).

[42] L. H. Li, G. Patriarche, E. H. Linfield, S. P. Khanna, and A. G. Davies, *Effects of using As_2 and As_4 on the optical properties of InGaAs quantum rods grown by molecular beam epitaxy.* J. Appl. Phys. **108**, 103522 (2010).

[43] M. Motyka, G. Sęk, K. Ryczko, J. Andrzejewski, J. Misiewicz, L. H. Li, A. Fiore, and G. Patriarche, *Optical and electronic properties of GaAs-based structures with columnar quantum dots.* Appl. Phys. Lett. **90**, 181933 (2007).

[44] J. M. Garcia, D. Grandos, J. P. Silveira, and F. Briones, *In segregation effects during quantum dot and quantum ring formation on GaAs(001).* Microelectron. J. **35**, 7 (2004).

[45] J. H. Dai, J. H. Lee, and S. C. Lee, *Transition Mechanism of InAs Quantum Dot to Quantum Ring Revealed by Photoluminescence Spectra.* IEEE Photon. Technol. Lett. **20** (16), 1372 (2008).

[46] T. Inoue, M. Asada, N. Yasuoka, O. Kojima, T. Kita, and O. Wada, *Polarization control of electroluminescence from vertically stacked InAs/GaAs quantum dots.* Appl. Phys. Lett. **96**, 211906 (2010).

[47] T. Inoue, M. Asada, N. Yasuoka, T. Kita, and O. Wada, *Vertical stacking of InAs quantum dots for polarization-insensitive semiconductor optical amplifiers.* J. Phys.: Conf. Ser. **245** 012076 (2010).

[48] M. Usman, T. Inoue, Y. Harda, G. Klimeck, and T. Kita, *Experimental and atomistic theoretical study of degree of polarization from multilayer InAs/GaAs quantum dot stacks.* Phys. Rev. B **84**, 115321 (2011).

[49] L. H. Li, G. Patriarche, N. Chauvin, P. Ridha, M. Rossetti, J. Andrzejewski, G. Sęk, J. Misiewicz, and A. Fiore, *Controlling the Aspect Ratio of Quantum Dots: From Columnar Dots to Quantum Rods.* IEEE J. Sel. Top. Quantum Elect. **14** (4), 1204–1213 (2008).

[50] S. Datta, S. Ghosh, B.M. Arora, *Electroreflectance and surface photovoltage spectroscopies of semiconductor structures using an indium–tin–oxide-coated glass electrode in soft contact mode.* Rev. Sci. Instrum. **72**, 177 (2001).

[51] D. E. Aspnes, *Third-derivative modulation spectroscopy with low-field electroreflectance.* Surf. Sci. 37, 418 (1973).

[52] D. Seliuta, J. Kavaliauskas, B. Čechavičius, S. Balakauskas, G. Valušis, B. Sherliker, M. P. Halsall, P. Harrison, M. Lachab, S. P. Khanna, and E. H. Linfield, *Impurity bound-to-unbound terahertz sensors based on beryllium and silicon δ-doped GaAs/AlAs multiple quantum wells.* Appl. Phys. Lett. **92**, 053503 (2008).

[53] B. V. Shanabrook, O. J. Glembocki, and W. T. Beard, *Photoreflectance modulation mechanisms in GaAs-$Al_xGa_{1-x}As$ multiple quantum wells.* Phys. Rev. B **35**, 2540 (1987).

[54] R. Kudrawiec, G. Sęk, K. Ryczko, J. Misiewicz, and J. C. Harmand, *Photoreflectance investigations of oscillator strength and broadening of optical transitions for GaAsSb–GaInAs/GaAs bilayer quantum wells.* Appl. Phys. Lett. **84**, 3453 (2004).

[55] W. Rudno-Rudziński, G. Sęk, J. Misiewicz, T. E. Lamas, and A. A. Quivy, *The formation of self-assembled InAs/GaAs quantum*

dots emitting at 1.3 µm followed by photoreflectance spectroscopy. J. Appl. Phys. **101**, 073518 (2007).

[56] J. Bleuse, G. Bastard, and P. Voisin, *Electric-Field-Induced Localization and Oscillatory Electro-optical Properties of Semiconductor Superlattices.* Phys. Rev. Lett. **60**, 220–223 (1988).

[57] P. Voisin, J. Bleuse, C. Bouche, S. Gaillard, C. Alibert, and A. Regreny, *Observation of the Wannier-Stark Quantization in a Semiconductor Superlattice.* Phys. Rev. Lett. **61**, 1639–1642 (1988).

[58] B. Soucail, N. Dupuis, R. Ferreira, P. Voisin, A. P. Roth, D. Morris, K. Gibb, and C. Lacelle, *Electron minibands and Wannier-Stark quantization in an $In_{0.15}Ga_{0.85}As$-GaAs strained-layer superlattice.* Phys. Rev. B **41**, 8568-8571 (1990).

[59] K. J. Moore, G. Duggan, K. Woodbridge, and C. Roberts, *Exciton localization in $In_xGa_{1-x}As$-GaAs coupled quantum-well structures.* Phys. Rev. B **41**, 1095–1099 (1990).

[60] I. Vurgaftman, J. R. Meyer, and L. R. Ram-Mohan, *Band parameters for III–V compound semiconductors and their alloys.* J. Appl. Phys. **89**, 5815 (2001).

[61] V. Le Thanh, V. Yam, P. Boucaud, F. Fortuna, C. Ulysse, D. Bouchier, L. Vervoort, and J.-M. Lourtioz, *Vertically self-organized Ge/Si(001) quantum dots in multilayer structures.* Phys. Rev. B **60**, 5851–5857 (1999).

[62] P. B. Joyce, E. C. Le Ru, T. J. Krzyzewski, G. R. Bell, R. Murray, and T. S. Jones, *Optical properties of bilayer InAs/GaAs quantum dot structures: Influence of strain and surface morphology.* Phys. Rev. B **66**, 075316 (2002).

[63] P. B. Joyce, T. J. Krzyzewski, P. H. Steans, G. R. Bell, J. H. Neave, and T. S. Jones, *Variations in critical coverage for InAs/GaAs quantum dot formation in bilayer structures.* J. Crystal Growth **244** (1), 39 (2002).

[64] M. Motyka, R. Kudrawiec, and J. Misiewicz, *On the deepness of contactless electroreflectance probing in semiconductor structures.* Phys. Status Solidi A **204**, 354 (2007).

[65] J.-Y. Marzin and J.-M. Gérard, *Experimental probing of quantum-well eigenstates.* Phys. Rev. Lett. **62**, 2172 (1989).

[66] O. J. Glembocki and B. V. Shanabrook, in *Semiconductors and Semimet-*

als, edited by D. G. Seiler and C. L. Littler (Academic, New York, 1992), Vol. 67, p. 221.

[67] A. Barve, J. Shao, Y. D. Sharma, T. E. Vandervelde, K. Sankalp, S. J. Lee, S. K. Noh, and S. Krishna, *Resonant Tunneling Barriers in Quantum Dots-in-a-Well Infrared Photodetectors.* IEEE J. Quantum Electron. **46** (7), 1105–1114 (2010).

[68] Yu. I. Mazur, V. G. Dorogan, E. Marega, Jr., G. G. Tarasov, and G. J. Salamo, *Spectroscopic signature of strain-induced quantum dots created by buried InAs quantum dots in an InGaAs quantum well.* J. Appl. Phys. **110**, 054325 (2011).

[69] L. Höglund, K. F. Karlsson, P. O. Holtz, H. Pettersson, M. E. Pistol, Q. Wang, S. Almqvist, C. Asplund, H. Malm, E. Petrini, and J. Y. Andersson, *Energy level scheme of InAs/$In_xGa_{1-x}As$/GaAs quantum-dots-in-a-well infrared photodetector structures.* Phys. Rev. B **82**, 035314 (2010).

[70] S. Fafard, E. Fortin, and A. P. Roth, *Oscillatory behavior of the continuum states in $In_xGa_{1-x}As$/GaAs quantum wells due to capping-barrier layers of finite size.* Phys. Rev. B **45**, 13769 (1992).

[71] S. Fafard, E. Fortin, and A. P. Roth, *Effects of an electric field on the continuum energy levels in $In_xGa_{1-x}As$/GaAs quantum wells terminated with thin cap layers.* Phys. Rev. B **47**, 10588 (1993).

[72] T. Sugaya, T. Nakagawa, Y. Sugiyama, Y. Tanuma, and K. Yonei, *Difference in Diffusion Length of Ga Atoms under As_2 and As_4 Flux in Molecular Beam Epitaxy.* Jpn. J. Appl. Phys. **36**, 5670 (1997).

[73] Y. D. Jang, H. Lee, D. Lee, J. S. Kim, J. Y. Leem, and S. K. Noh, *The energy level spacing from InAs/GaAs quantum dots: Its relation to the emission wavelength, carrier lifetime, and zero dimensionality.* J. Appl. Phys. **99**, 096101 (2006).

[74] H. Y. Liu, I. R. Sellers, M. Hopkinson, C. N. Harrison, D. J. Mowbray, and M. S. Skolnick, *Engineering carrier confinement potentials in 1.3-μm InAs/GaAs quantum dots with InAlAs layers: Enhancement of the high-temperature photoluminescence intensity.* Appl. Phys. Lett. **83**, 3716 (2003).

[75] H. J. Krenner, C. E. Pryor, J. He, and P. M. Petroff, *A Semiconductor Exciton Memory Cell Based on a Single Quantum Nanostructure.* Nano Lett. **8** (6), 1750 (2008).

[76] A. J. Shields and P. C. Klipstein, *Line-shape model for the modulated reflectance of multiple quantum wells.* Phys. Rev. B **43**, 9118–9125 (1991).

[77] D. Alonso-Álvarez, B. Alén, J. M. Ripalda, J. M. Llorens, A. G. Taboada, F. Briones, M. A. Roldán, J. Hernández-Saz, D. Hernández-Maldonado, M. Herrera, and S. I. Molina, *Strain balanced quantum posts.* Appl. Phys. Lett. **98**, 173106 (2011).

[78] K. Mukai, K. Watanabe and Y. Kimura, *Grazing Incidence X-ray Diffraction Measurements of Columnar InAs/GaAs Quantum Dot Structures.* Jap. J. Appl. Phys., **49**, 04DH07 (2010).

[79] K. Mukai and K. Watanabe, *Polarization Symmetry of Vertical Photoluminescence from Columnar InAs/GaAs Quantum Dots.* e-J. Surf. Sci. Nanotech. 7, 537 (2009).

[80] G. Bastard, *Wave Mechanics Applied to Semiconductor Heterostructures* (Les Editions de Physique, Les Ulis, France, 1988).

[81] M. Abramowitz and I. A. Stegun eds., *Handbook of Mathematical Functions* (National Bureau of Standards, Washington, 1964).

[82] D. J. BenDaniel and C. B. Duke, *Space-Charge Effects on Electron Tunneling.* Phys. Rev. **152**, 683 (1966).

[83] J. R. Downes, D. A. Faux, and E. P. O'Reilly, *A simple method for calculating strain distributions in quantum dot structures.* J. Appl. Phys. **81**, 6700 (1997).

[84] J. H. Davies, *Elastic and piezoelectric fields around a buried quantum dot: A simple picture.* J. Appl. Phys. **84**, 1358 (1998).

[85] J.-Y. Marzin, M. N. Charasse, and B. Sermage, *Optical investigation of a new type of valence-band configuration in $In_xGa_{1-x}As$-GaAs strained superlattices.* Phys. Rev. B **31**, 8298 (1985).

[86] S. H. Pan, H. Shen, Z. Hang, F. H. Pollak, W. Zhuang, Q. Xu, A. P. Roth, R. A. Masut, C. Lacelle, and D. Morris, *Photoreflectance study of narrow-well strained-layer $In_xGa_{1-x}As/GaAs$ coupled multiple-quantum-well structures.* Phys. Rev. B **38**, 3375 (1988).

[87] N. Vukmirović, Ž. Gačević, Z. Ikonić, D. Indjin, P. Harrison, and V. Milanović, *Intraband absorption in InAs/GaAs quantum dot infrared photodetectors—effective mass versus $k \times p$ modelling.* Semicond. Sci. Technol. **21**, 1098 (2006).